

Effects of Interaction in Bose-Einstein Condensates

by

Kaiwen Xu

Submitted to the Department of Physics
in partial fulfillment of the requirements for the degree of

Doctor of Philosophy

at the

MASSACHUSETTS INSTITUTE OF TECHNOLOGY

June 2006

© Massachusetts Institute of Technology 2006. All rights reserved.

Author
Department of Physics
March 10, 2006

Certified by
Wolfgang Ketterle
John D. MacArthur Professor of Physics
Thesis Supervisor

Accepted by
Thomas J. Greytak
Professor of Physics, Associate Department Head for Education

Effects of Interaction in Bose-Einstein Condensates

by

Kaiwen Xu

Submitted to the Department of Physics
on March 10, 2006, in partial fulfillment of the
requirements for the degree of
Doctor of Philosophy

Abstract

This thesis discusses a series of studies that investigate the effects of interaction – essentially the s -wave scattering – in the various properties of Bose-Einstein condensates (BEC).

The phonon wavefunction in a BEC was measured using Bragg spectroscopy and compared with the well-known Bogoliubov theory. Phonons were first excited in a BEC of 3×10^7 condensed ^{23}Na atoms via small-angle two-photon Bragg scattering. Large angle Bragg scattering was then used to probe the momentum distribution. We found reasonable agreement with the theory.

With the same technique of Bragg diffraction, we studied the four-wave mixing process for matter waves. The BEC was split into two strong source waves and a weak seed wave. The s -wave scattering coherently mixed pairs of atoms from the sources into the seed and its conjugate wave, creating a pair-correlated atomic beams with “squeezed” number difference.

A Feshbach resonance was used to produce ultracold Na_2 molecules with initial phase-space density in excess of 20. Starting from an atomic BEC, a magnetic field ramp shifted a bound state from above the threshold of the unbound continuum to below, creating a molecular population with almost zero center-of-mass motion. A reverse field ramp dissociated the cold molecules into free atom pairs carrying kinetic energy dependent on the ramp speed. This dependence provided a measure of the coupling strength between the bound state and the continuum.

Condensates were loaded into optical lattices formed with retro-reflected single frequency lasers. Quantum phase transition from the superfluid state to Mott-insulator state was observed in a three dimensional lattice. The increased interaction and flattened dispersion relation led to strongly enhanced quantum depletion in the superfluid state.

Thesis Supervisor: Wolfgang Ketterle

Title: John D. MacAurthur Professor of Physics

To my family.

Acknowledgments

I remember a conversation I had during my first year at MIT with someone who just defended her PhD thesis. I asked her if she was excited about becoming a doctor and she said yes, but “at some point, you kind of outgrow the process” and finally getting the degree became rather a natural development. Now as I am writing this last part of my own thesis, it strikes me how true that statement was. Pursuing a PhD really is a lot more about the journey than the end, and I could not have made it through mine without the guidance and support from many people.

My personal journey started in the summer of 2000 when Wolfgang Ketterle offered me the opportunity to join his group at MIT. In Wolfgang, one could not have asked for a better research advisor. He has perhaps the most trusting style of managing a lab in terms of allowing us maximal latitude without losing touch with what takes place in each lab. His contagious optimism provided much needed boost to our morale in difficult times. My academic advisor, Dave Pritchard, has been extremely accommodating of my varied academic pursuits, be it quantum field theory or finance theory. Our registration day conversations were always a delight.

When I joined the “New Lab”, the senior people at the time were postdocs Roberto Onofrio, Chandra Raman and Johnny Vogels. I thank them for welcoming me into the group. Chandra and Johnny picked me up at the airport when I first arrived. Roberto left the group shortly after my arrival, but I was deeply impressed by his kindness and unique sense of humor. Johnny deserves a special acknowledgment as the mentor who taught me most about the machine and running the experiment. His “fearlessness” in the lab, while sometimes the source of frustration for other people, is also reflective of his intimate knowledge about the experiment and quick intuitive thinking. He is definitely one of the smartest people I have met.

In late 2002, I started collaborating with Jamil Abo-Shaeer, who became my partner in crime until his graduation in 2004. We struggled through many difficulties but also had a lot of fun working together. He was full of energy both inside and outside the lab. I particularly envy his ability to palm and dunk the basketball.

Also thanks to him, I became rather fluent in the useful vernacular for “venting frustrations”. Somewhat later, Takashi Mukaiyama joined the lab as a postdoc. He had the rare combination of quiet competence and thoughtfulness that made him an ideal labmate. I thank Takashi for everything he taught me as well as his parting gifts – a bike and a padlock.

Our current postdoc Yingmei Liu was my labmate during the last couple of projects. Her tireless work ethic and attention to details greatly improved the lab productivity. As a postdoc, Yingmei was a humble collaborator and willingly shouldered a lot of grunt work, without which much of the progress would not have been made. I wish her good luck and continued success.

Jit Kee Chin and Dan Miller are two junior (with respect to me) graduate students in the lab. I am thankful for their help in keeping the lab running. Even though I didn’t have the chance to work with them extensively, we shared the same office and many interesting conversations. Jit Kee’s “women-in-physics dinner” leftover and Dan’s creative ideas for practical jokes were among the highlights of my time here in building 26. They have now taken the New Lab into the “newer era” of Fermions, and I look forward to learning about their discoveries soon.

Widagdo Setiawan has been an undergraduate research assistant in our lab since the summer of 2004. His presence ensured that I would not be the only geek in the lab. I was often amazed by his quick learning abilities, and his contribution was instrumental to a lot of our success. I take the credit for hiring him as our UROP and expect to see great things from him in the future.

Ketterle group is a large family of some twenty students and postdocs in four labs. Over the years, I have greatly benefitted from my interaction with the people in other labs. In particular, Aaron Leanhardt and Claudiu Stan taught me a lot about the technical aspects of the experiments. The discussions I had with Yong-Il Shin and Martin Zwierlein often clarified confusing concepts and led to deeper understandings. Other people who have helped me in various ways include James Anglin, Micah Boyd, Gretchen Campbell, Ananth Chikkatur, Kai Dieckmann, Axel Görlitz, Deep Gupta, Todd Gustavson, Zoran Hadzibabic, Shin Inouye, Tom Pasquini, Till Rosenband,

Michele Saba, Andre Schirotzek, Dominik Schneble, Erik Streed, Christian Schunck, and Yoshio Torii.

Our former administrative assistant, the late Carol Costa, was an indispensable source of information and always went out of her way to make our lives easier. Her successor Ellenor Emery Barish did an admirable job in making sure we only missed Carol but not her work. I also thank David Foss, Al McGurl, Maxine Samuels from the RLE headquarters and Fred Cote from the student machine shop for their help during my stay at MIT.

Last but not least, I thank my mother Qiao and father Hongbing for always allowing me to pursue my interests ever since I was little. Making them proud has been an important motivation behind everything I have accomplished in my life. My sister Qi always has my best interest at heart and her presence at my thesis defense meant a great deal to me. My wife Heng is the love of my life. Her companionship has been a constant source of comfort throughout my PhD study especially in times of self-doubt and anxiety. I am deeply grateful for her understanding and tolerance of my often crazy schedules. I look forward to the next stage of our life together.

This work was supported by the National Science Foundation (NSF), the Army Research Office (ARO), , the Office of Naval Research (ONR), the Defense Advanced Research Projects Agency (DARPA), and the National Aeronautics and Space Administration (NASA).

Contents

1	Introduction	16
1.1	BEC – a macroscopic quantum phenomenon	16
1.2	No interaction no fun	18
1.2.1	Thomas-Fermi profile	18
1.2.2	Atom optics	19
1.2.3	Superfluid dynamics and quantum phase transition	19
1.3	Experiment setup	20
1.4	Outline of this thesis	21
2	Basic theory	23
2.1	Two body collision	23
2.1.1	Partial wave analysis	27
2.1.2	Pseudo potential	28
2.1.3	Resonant scattering	29
2.2	Bogoliubov theory	30
2.2.1	BEC with two-body interaction	30
2.2.2	Bogoliubov transformation	31
2.2.3	Sign of interaction	33
2.2.4	Superfluid flow	35
2.3	Gross-Pitaevskii equation	37
3	Momentum analysis using Bragg spectroscopy	40
3.1	Bragg spectroscopy – a “Swiss army knife”	41

3.2	Measuring phonon wavefunction	42
3.2.1	Experimental setup and time sequence	43
3.2.2	Measuring Bogoliubov amplitudes	44
3.3	Coherent collision and four-wave mixing	46
3.3.1	Experimental setup and time sequence	46
3.3.2	Bogoliubov approach for four-wave mixing	48
3.3.3	Dual Fock state and Heisenberg-limited interferometry	52
4	Quantum degenerate molecules	56
4.1	Magnetic Feshbach resonance	57
4.2	Experimental setup and time sequence	59
4.3	Quantum degenerate molecules	60
4.4	Molecule dissociation	64
4.4.1	Fermi's golden rule	65
4.4.2	Shape resonance	67
5	Bose-Einstein condensates in optical lattices	70
5.1	Bosons in lattice potential	71
5.1.1	Bose-Hubbard model	72
5.1.2	Shallow lattice	76
5.1.3	Deep lattice	78
5.1.4	Mott-insulator transition	79
5.2	Experimental Setup	82
5.3	Yellow lattice and photoassociative resonances	85
5.4	Enhanced quantum depletion	87
5.4.1	Quantum depletion in a BEC	88
5.4.2	BEc in free space	88
5.4.3	BEc in an optical lattice	89
5.4.4	Quantum depletion in time-of-flight	92
5.5	Lattice setup procedure	96
5.5.1	Laser system and optics layout	96

5.5.2	Lattice beam focusing and alignment	99
5.5.3	Lattice beam calibration	102
5.5.4	Crossed optical dipole trap	106
5.5.5	A few subtleties	106
5.6	Cheatsheet	108
5.6.1	Useful formulas	109
5.6.2	Some numbers	110
5.6.3	Scaling relations	111
6	Conclusion	114
6.1	Reminiscence	114
6.2	Looking ahead	116
A	Experimental Observation of the Bogoliubov Transformation for a Bose-Einstein Condensed Gas	118
B	Generation of Macroscopic Pair-Correlated Atomic Beams by Four-Wave Mixing in Bose-Einstein Condensates	123
C	Formation of Quantum-Degenerate Sodium Molecules	128
D	Dissociation and Decay of Ultracold Sodium Molecules	133
E	Sodium Bose-Einstein Condensates in an Optical Lattice	138
F	Observation of Strong Quantum Depletion in a Gaseous Bose-Einstein Condensate	145
	Bibliography	150

List of Figures

2-1	Dispersion relation of a BEC.	36
3-1	Two-photon Bragg scattering.	42
3-2	(Color) Bragg beams setup for phonon wavefunction measurement.	44
3-3	Momentum distribution of a condensate with phonons.	45
3-4	Bogoliubov amplitudes of phonons in a BEC.	47
3-5	(Color) Bragg beams setup for four wave mixing.	49
3-6	Time-of-flight images of atomic four-wave mixing.	50
3-7	The correlated exponential growth of seed wave and its conjugate.	53
4-1	(Color) Magnetic feshbach resonance.	58
4-2	(Color) Optical trap and magnetic field coils.	61
4-3	Molecule formation for various ramp speeds of magnetic field.	62
4-4	Ballistic expansion of a pure molecular cloud	63
4-5	Molecular phase space density vs. hold time.	64
4-6	Dissociation energy for different ramp speeds for ^{23}Na dimers.	66
4-7	Dissociation energy for different ramp speeds for ^{87}Rb dimers.	68
4-8	(Color) Magnetic shape resonance.	69
5-1	Band structure of an optical lattice	74
5-2	Tunneling ratio.	76
5-3	Effective mass and interaction.	78
5-4	The lowest band in deep lattice regime.	79
5-5	U and J as functions of lattice depth.	80

5-6	(Color) Incommensurate filling in an optical lattice.	83
5-7	(Color) Optical dipole trap and lattice beams setup.	84
5-8	Interference patterns in time-of-flight from a three dimensional lattice.	85
5-9	Atoms loss due to photoassociation resonance.	86
5-10	Quantum depletion density of a BEC in free space.	90
5-11	Quantum depletion for a BEC in a three dimensional optical lattice.	91
5-12	Time-of-flight images of atoms released from one, two and three dimensional lattices.	93
5-13	Masked gaussian fit to extract quantum depletion from time-of-flight images.	94
5-14	Quantum depletion of a BEC in a one, two and three dimensional optical lattice.	95
5-15	Optics table layout.	98
5-16	(Color) Collimation of lattice beam.	100
5-17	Kapitza-Dirac diffraction in a pulsed optical lattice.	103
5-18	Band populations of zero momentum state $ 0\rangle$	104
5-19	Energy gap between the lowest and the second excited bands at zero quasi-momentum.	105

List of Tables

4.1	Position B_{res} and width ΔB of the Feshbach resonances for ^{87}Rb . . .	67
5.1	Various constants for ^{23}Na , ^{87}Rb and ^6Li	111
5.2	U and J for 5 to 30 E_R three dimensional lattice.	112
5.3	Various quantities of interest for atoms in a three dimensional lattice.	113

Notations

k_B : Boltzmann constant

\hbar, h : Planck constant $h = 2\pi\hbar$

M : atomic mass

a_s : s -wave scattering length

N : total number of particles

ρ : atomic density $\rho = N/V$

Θ : diluteness factor $\Theta = \rho a_s^3$

\mathbf{p}, \mathbf{P} : single particle or total momentum

\mathbf{k}, \mathbf{K} : single particle or total momentum divided by \hbar

\mathbf{x}, \mathbf{X} : single particle or center of mass position

V : quantization volume

L : length of quantization volume in each dimension

d : number of dimensions

a^\dagger, a : atomic field operator

b^\dagger, b : quasiparticle field operator

Ψ : many-body wavefunction

χ : condensate wavefunction

ψ : order parameter

g : coupling constant $\frac{4\pi\hbar^2 a_s}{M}$

$\omega, \omega_{x,y,z}$: harmonic trap frequency

R_{TF} : Thomas-Fermi radius
 μ : chemical potential
 c_s : speed of sound in a condensate $\mu = Mc_s^2$
 λ_L : optical lattice wavelength
 E_R : photon recoil energy at λ_L
 a_L : optical lattice periodicity $a_L = \lambda_L/2$
 k_L : recoil momentum (wavenumber) $k_L = 2\pi/\lambda_L$
 q : quasi-momentum (wavenumber)
 \bar{q} : dimensionless quasi-momentum $\bar{q} = q/k_L$
 u_L : optical lattice depth in units of E_R
 I_L : laser peak intensity
 P_L : laser power
 w_L : laser $1/e^2$ beam waist
 ω_L : laser frequency (rad/s)
 ω_a : atomic transition frequency (rad/s)
 λ_a : atomic transition wavelength
 ω_{lh} : local harmonic frequency at the bottom of each lattice site
 ω_{tr} : harmonic trap frequency
 ω_{odt} : additional trap frequency due to the gaussian profile of the lattice beam
 Q_e : electron charge
 M_e : electron mass

c : speed of light

ε_0 : vacuum permittivity in SI units (8.85×10^{-12} F/m)

Γ_a : natural linewidth of the atom (rad/s)

Γ_{sc} : spontaneous Rayleigh scattering rate

n_{avg} : coarse-grained atomic density

n_{peak} : peak atomic density at the lattice potential minima

K_3 : three-body decay coefficient

Γ_3 : peak three-body decay rate $K_3 n_{\text{peak}}^2$

Chapter 1

Introduction

It has been a decade since the first observation of Bose-Einstein condensation (BEC) in a dilute gas of alkali atoms in 1995 [1, 2, 3]. Over the intervening years, the phenomenal growth of ultracold atomic research has contributed a tremendous wealth of knowledge to our understanding about quantum degenerate many-body systems [4, 5, 6]. BEC's have been achieved in many atomic species including ^{87}Rb [1], ^{23}Na [3], ^7Li [2], ^1H [7], ^{85}Rb [8], $^4\text{He}^*$ [9, 10], ^{41}K [11], ^{133}Cs [12], ^{174}Yb [13] and ^{52}Cr [14]. In addition, quantum degeneracy has also been observed in two species of fermions: ^{40}K [15] and ^6Li [16], which is now the subject of very active research.

Given the abundance of good introduction materials today, including the theses by the previous members of our group, I have decided to limit my own introduction mainly to the aspects relevant to this thesis. For a full primer and the history of BEC as well as the development of cooling and trapping techniques in general, I refer to those earlier works [17, 18].

1.1 BEC – a macroscopic quantum phenomenon

The concept of Bose-Einstein condensation predates the modern quantum mechanics [19, 20]. Since Einstein's original work in 1924, the physical significance of BEC seemed to rise and fall and rise again as a consistent quantum theory was developed and BEC's connection with superfluidity was made clear. This intertwined history

of BEC and quantum mechanics is a fascinating tale of how profound ideas lead to the discovery of new theories but the significance of the original ideas cannot be fully appreciated until the theories reach certain maturity.

After the initial success in the studies of superfluid liquid helium and superconductivity, the strong interaction of the conventional condensed matter systems made it prohibitively difficult to study Bose-Einstein condensation in details. The quest for gaseous BEC started in 1980's when new techniques for cooling and trapping neutral atoms were being developed. The first attempts were made with polarized hydrogen atoms on the grounds that the recombination rate into molecules could be made extremely low and the system would remain gaseous all the way down to zero temperature [21, 22]. The success in the laser cooling of alkali atoms prompted the alternative efforts in 1990's to search for BEC in metastable systems where recombination rate is low but finite [23, 24, 25]. In 1995, the confluence of laser cooling and evaporative cooling techniques led to the first observation of BEC in ^{87}Rb , ^7Li and ^{23}Na [1, 2, 3]. Three years later, hydrogen condensation was also achieved [7].

In a gaseous BEC, the condensate fraction typically exceeds 90 % and the system is essentially a giant matter wave of millions of particles¹. As a result, quantum mechanical effects become highly pronounced. Interesting phenomena such as condensate interference [26], super-radiance [27] and matter wave amplification [28, 29] were reported shortly after the realization of BEC. In many of these early discoveries, the (weak) atomic interaction did not play the central role and was either neglected or treated as a small correction to the main effect. The results discussed in this thesis, however, are among the experiments which investigated the effects of the atomic interaction.

¹Condensate size varies for different atomic species. Sodium condensate typically has several millions of atoms (up to a few tens of millions).

1.2 No interaction no fun

For experimentalists, the so called “good collisions” – elastic collisions preserving the internal states of the colliding particles – were crucial for realizing runaway evaporative cooling that ultimately made BEC a reality [30]. However, the effects of the interaction go far beyond the production of BEC. Despite the extremely low density of a gaseous condensate, the apparently tenuous interaction is responsible for many of its salient features, simply because all other energies in the condensate are even smaller!

1.2.1 Thomas-Fermi profile

The first signature of Bose-Einstein condensation was the absorption images taken during the ballistic expansion after the cloud was released from the magnetic trap. The bimodal density distribution consisting of a sharp parabola and a broader gaussian indicated the co-existence of the condensate and the thermal component [1, 3].

The condensate profile in time-of-flight comes from a rescaling of the parabolic Thomas-Fermi profile in the harmonic trap potential [31]. This is in contrast to the ground state of a non-interacting system: all atoms have a gaussian wavefunction, the size of which is determined by the balance between kinetic energy (delocalization) and potential energy (localization). At the typical BEC density, however, the meanfield interaction energy (divided by \hbar) is much greater than the trap frequency – this is called the *Thomas-Fermi regime* [see equation (2.69)]. As such, the spatial extent of the condensate wavefunction is much greater than the harmonic oscillator length, and the delocalization comes mainly from the repulsive interaction while the kinetic energy can be neglected ².

²Here we assume a repulsive interaction. In case of an attractive interaction, the condensate is further localized and the kinetic energy is the only delocalizing source and must be of the same magnitude as the interaction energy.

1.2.2 Atom optics

One of the great promises of BEC is making possible the kind of atom optics analogous to and even beyond what can be done with lasers, potentially at greater precisions [26, 32, 33, 34, 35, 36, 37]. Indeed, “atom laser” is now in the standard nomenclature of atomic physics. Beyond the apparent similarities, however, BEC’s differ from optical lasers in a number of important ways. Unlike photons, massive particles cannot be created or annihilated under the normal conditions of low energy experiments, and one cannot as easily crank up the intensity of matter waves as one would an optical laser. Furthermore, photons are for the most part non-interacting even at high intensities whereas atoms are almost always interacting. At high densities, the decoherence effect due to the interaction is a thorny issue in achieving high precision measurement ³.

On the other hand, the interaction in a BEC can be thought of as an inherent non-linearity, which for photons would require special non-linear optical media. Therefore wave mixing experiments can be performed with BECs in vacuum [38, 39], which could be used to realize various squeezed states. Novel schemes have been proposed to take advantage of such non-classical states and achieve Heisenberg limited spectroscopy, massive quantum entanglement, etc. [40, 41, 42, 43, 44].

1.2.3 Superfluid dynamics and quantum phase transition

The experimental observation of superfluidity in liquid ⁴He almost coincided with the realization [45, 46, 47] that Bose-Einstein condensation was behind the λ -transition discovered earlier from the specific heat measurement [48]. Over the years, the connection between BEC and superfluidity gained further support from both experimental evidences and theoretical studies [49, 50, 51, 52, 53, 54, 55], and is now widely accepted as one of the great triumphs of quantum statistical mechanics.

In today’s literature, BEC is quite often called “superfluid” almost interchangeably, but one would be remiss to take “superfluid” as a synonym for BEC. In fact,

³At higher still densities, inelastic three-body collisions cause atom losses.

BEC of non-interacting particles does not possess superfluidity. It is because of the interaction that the low-lying excitation spectrum of the BEC exhibits a linear dispersion relation, which leads to a non-vanishing *critical velocity* and superfluid flow (see discussion in Section 2.2).

What makes the gaseous BEC more interesting is the possibility to manipulate the interaction strength using Feshbach resonances [56, 57] or optical lattices. The strong inelastic collision loss near a Feshbach resonance limited its usefulness in experiments that required long coherent time [58]. Optical lattices have proven to be a viable tool that has enabled the observations of many intriguing phenomena such as quantum phase transition [59, 60], massively entangled state [61], Tonks-Girardeau gas [62, 63], long-lived Feshbach molecules [64, 65, 66], and enhanced quantum depletion [67]. In addition, Mott-insulator state of less than three atoms per lattice site provided a way to circumvent the collision loss problem near a Feshbach resonance.

1.3 Experiment setup

In this section, I briefly describe the laboratory in which I spent my five plus years as a graduate student. A detailed technical account of machine construction can be found in the thesis by the former graduate student Dallin Durfee [68].

All the experiments discussed in this thesis were performed on the second-generation BEC machine here at MIT, nicknamed “New Lab” despite the fact that the first generation machine (“Old Lab”) has long been upgraded to a dual-species system (now called “Lithium Lab”). In the past year or so, our lab also underwent a similar renovation to become the new ${}^6\text{Li}$ lab. The work discussed here, however, involved only a single species of ${}^{23}\text{Na}$.

The machine itself is of a classic design featuring a (horizontal) Zeeman slower and an Ioffe-Pritchard magnetic trap. Our machine differs from the three other BEC labs at MIT in that the BEC is produced in a glass cell that by design should provide improved optical access. As it turns out, the modest gain in optical access comes at a price. The fragility of the system, especially in times when we had to repair

the vacuum system or water cooling circuits, proved a source for endless fear and distress. Thankfully, the glass junction was strong enough to survive the replacement of gate-valve, and later the complete overhaul of the oven chamber, both of which required applying considerable force and torque – of course, care was taken to avoid direct impact on the glass cell.

Through much of my time in the lab, I have worked closely with two dye laser systems. A **Coherent 899** model pumped by a **Millennia Xs (Spectra-Physics)** produced all the light necessary for BEC production and detection. An older **Coherent 699** model pumped by a **Coherent Innova 110** argon-ion laser was first used for Bragg spectroscopy and later used in the initial attempts at setting up an optical lattice. The long hours spent in the lab cajoling the pair of lasers into stable performance were a significant part of my PhD career. Over the years, I have probably fiddled with, and in many cases, replaced every single part of the laser system – eventually I decided if nothing else, I could become a competent laser technician for a living! To me, this particular aspect of my lab life is also a microcosm of my personal development as an experimental physicist, i.e., learning to combine problem solving skills with an audacity to try different “knobs”.

1.4 Outline of this thesis

Chapter 2 reviews in some details the basic theories relevant to the experiments discussed in this thesis. These results are referred to throughout the thesis. The subsequent chapters discuss in chronological order a series of experiments to which I have made significant contribution. Chapter 3 discusses the experiments using Bragg spectroscopy as both excitation and detection tools to study the dynamics of the condensate in momentum space. These are two early experiments led by the former postdoc, Johnny Vogels, with whom I collaborated closely as a junior graduate student. Chapter 4 discusses the experiments on molecule formation using Feshbach resonances. The first experiment realized at the time the first quantum degenerate molecular sample, albeit with milliseconds lifetime. I played the leading role in this

experiment. The second experiment led by the former postdoc, Takashi Mukaiyama, studied the dissociation behavior of the ultracold molecules as well as the inelastic collision losses. My contribution was developing the theoretical model connecting the dissociation energy with the atom-molecule coupling responsible for the Feshbach resonance. Chapter 5 discusses our effort in setting up an optical lattice which became a technical challenge due to various practical issues. I first started this effort with the former graduate student Jamil Abo-Shaeer in late 2002, and later Takashi also joined the project. We were able to make some progress with a red-detuned dye laser but eventually switched to a high power infrared laser. The IR system was set up in collaboration with the postdoc Yingmei Liu. Chapter 6 concludes this thesis with some retrospection and future outlook. Appendices A-F include the reprints of the publications resultant from the work discussed in this thesis. Wherever it is possible, the discussion in the Chapters avoids repeating what is already covered in the publications.

Chapter 2

Basic theory

This chapter discusses some basic theories that are referred to throughout the subsequent chapters.

Exact solutions are few and far between when it comes to dealing with interacting many-body systems. In order to make some progress, approximate theories must be developed to focus on some aspects of the problems while ignoring others. A big reason why gaseous BEC is interesting to theorists is that because of the weak interaction, the approximate theories are often good enough to get quite close in predicting the experimental observations. In this chapter, I will present (and try to justify as much as possible) the series of approximations that led to the theoretical tools most used in my studies. Parts of the following discussion could be found in various textbooks (e.g. [69, 70, 71, 72]), but I made a conscious attempt to derive everything in a coherent manner, which hopefully helps elucidate key concepts that, from my own experience, are often talked about yet prone to misunderstandings. Emphasis is placed on consistency rather than mathematical rigor.

2.1 Two body collision

Much of this thesis is concerned with the role of atomic interaction in a Bose-Einstein condensate. In particular, we consider two-body interaction that is a conservative function of the separation between pairs of particles. This is well justified given the

low density of the typical gaseous condensate – about 100000 times thinner than the air. More than two-body encounters are much rarer and can be ignored. The non-relativistic Hamiltonian of N identical particles is therefore:

$$H = \sum_{i=1}^N \frac{\mathbf{p}_i^2}{2M} + \frac{1}{2} \sum_{i,j=1}^N U(\mathbf{x}_i - \mathbf{x}_j) \quad (2.1)$$

where \mathbf{p}_i and \mathbf{x}_i are the momentum and position of the i th particle, M the particle mass and $U(\mathbf{x})$ is the two-body interaction potential. Sometimes it is more convenient to work in the notations of second quantization:

$$H = \sum_{\mathbf{p}} \frac{\mathbf{p}^2}{2M} a_{\mathbf{p}}^{\dagger} a_{\mathbf{p}} + \frac{1}{2} \sum_{\substack{\mathbf{p}_1 + \mathbf{p}_2 \\ = \mathbf{p}_3 + \mathbf{p}_4}} \lambda(\mathbf{p}_1 - \mathbf{p}_3) a_{\mathbf{p}_3}^{\dagger} a_{\mathbf{p}_4}^{\dagger} a_{\mathbf{p}_1} a_{\mathbf{p}_2} \quad (2.2)$$

where the sum over momenta \mathbf{p} becomes an integral in the limit of infinite quantization volume. Throughout this thesis, unless otherwise noted, I choose to use an explicit quantization volume $V = L^d$ and periodic boundary condition for a d -dimensional system, but always assume the thermodynamic limit unless otherwise noted:

$$N, V \rightarrow \infty \quad (2.3)$$

$$N/V = n \quad (2.4)$$

where n is the (constant) finite density.

In addition, the low temperature ($\lesssim 1 \mu\text{K}$) justifies accounting for only the *low-lying* momentum states. Stated more precisely, if the effective range of interaction is R_e (the interaction strength is assumed to decrease faster than r^{-3} where r is inter-particle distance), the density n satisfies

$$nR_e^3 \ll 1 \quad (2.5)$$

and the temperature T satisfies:

$$k_B T \ll \frac{\hbar^2}{MR_e^2} \quad (2.6)$$

It is then reasonable to argue that the many-body wavefunction $\Psi(\mathbf{x}_1, \mathbf{x}_2, \dots, \mathbf{x}_N)$ is significant mostly for:

$$|\mathbf{x}_i - \mathbf{x}_j| \gg R_e \quad (2.7)$$

and one does not care about the exact details of U within R_e , as long as the asymptotic scattering behavior at large distances is adequately reproduced for low momentum ($\hbar k$) collisions:

$$k \ll \frac{1}{R_e} \quad (2.8)$$

Further approximations are based on an asymptotic analysis of the two-body scattering problem in the low momentum collision regime, starting with the Schrödinger's equation in the center-of-mass frame:

$$\left[-\frac{\hbar^2}{2(M/2)} \nabla^2 + U(\mathbf{x}) \right] \psi(\mathbf{x}) = E\psi(\mathbf{x}) \quad (2.9)$$

where $M/2$ is the reduced mass. $U(\mathbf{x})$ is assumed to approach 0 as $x \rightarrow \infty$ and treated as a perturbation. We look for eigenstates corresponding to an incident plane wave $|\mathbf{k}\rangle$:

$$\langle \mathbf{x} | \mathbf{k} \rangle = \frac{e^{i\mathbf{k}\cdot\mathbf{x}}}{\sqrt{V}} \quad (2.10)$$

with kinetic energy $\frac{\hbar^2 k^2}{M} = E$. The perturbation U couples this plane wave to other states of the system and create a scattered wave $|\varphi\rangle$ with asymptotic form:

$$\langle \mathbf{x} | \varphi \rangle = f(\theta, \phi) \frac{e^{ikr}}{r} \quad (2.11)$$

where r , θ and ϕ are the spherical coordinates of \mathbf{x} .

For convenience, define the “reduced” potential:

$$u(\mathbf{x}) = \frac{M}{\hbar^2} U(\mathbf{x}) \quad (2.12)$$

and rewrite Eq. (2.13) as:

$$(k^2 - \nabla^2) \psi(\mathbf{x}) = u(\mathbf{x})\psi(\mathbf{x}) \quad (2.13)$$

$$|\psi\rangle = |\mathbf{k}\rangle + |\varphi\rangle \quad (2.14)$$

The first order perturbation gives:

$$|\varphi\rangle = \frac{V}{(2\pi)^3} \int d\mathbf{k}' \frac{|\mathbf{k}'\rangle \langle \mathbf{k}'|u|\mathbf{k}\rangle}{k^2 - k'^2 + i0^+} \quad (2.15)$$

where $V/(2\pi)^3$ is the density of states as we have defined plane waves with a quantization volume V that goes to infinity in the continuum limit [see Eq. (2.10)]. The 0^+ ensures only outward scattering wave exists.

Eq. (2.15) evaluates to the following:

$$\varphi(\mathbf{x}) = -\frac{1}{4\pi\sqrt{V}} \int d\mathbf{x}' \frac{e^{ik|\mathbf{x}-\mathbf{x}'|}}{|\mathbf{x}-\mathbf{x}'|} u(\mathbf{x}') e^{i\mathbf{k}\cdot\mathbf{x}'} \quad (2.16)$$

which is the first order Born expansion and can also be obtained with the Green Function approach [71]. We are only concerned with asymptotic behavior at large x and Eq. (2.16) reduces to:

$$\varphi(\mathbf{x}) = \left(\frac{e^{ikx}}{\sqrt{V}x} \right) \left(-\frac{1}{4\pi} \int d\mathbf{x}' u(\mathbf{x}') e^{i\Delta\mathbf{k}\cdot\mathbf{x}'} \right) \quad (2.17)$$

where:

$$\Delta\mathbf{k} = \mathbf{k} - k\frac{\mathbf{x}}{x} \quad (2.18)$$

In general, the integral involving u is a function of scattering direction (θ, ϕ) . However, as $\Delta\mathbf{k}$ satisfies the low momentum criterion (2.8). Eq. (2.17) further reduces to:

$$\varphi(\mathbf{x}) = -a_s \frac{e^{ikx}}{\sqrt{V}x} \quad (2.19)$$

$$\begin{aligned} a_s &= \frac{1}{4\pi} \int d\mathbf{x}' u(\mathbf{x}') \\ &= \frac{M}{4\pi\hbar^2} \int d\mathbf{x}' U(\mathbf{x}') \end{aligned} \quad (2.20)$$

where the constant a_s has the dimension of length and is defined as the *scattering length*.

2.1.1 Partial wave analysis

Another way of analyzing the asymptotic scattering behavior is to use the partial waves that have well-defined angular momenta – conventionally labeled as $|l, m\rangle$. This is possible so long as the pair potential $U(\mathbf{x})$ is spherically symmetric hence the Hamiltonian is rotation-invariant. For a given momentum $|l, m\rangle$, the Schrödinger equation (2.13) reduces to the radial equation:

$$\frac{1}{r} \frac{\partial^2}{\partial r^2} r \rho_l(r) + k^2 \rho_l(r) = \left[\frac{l(l+1)}{r^2} + u(r) \right] \rho_l(r) \quad (2.21)$$

In absence of interaction ($u = 0$), $\rho_l(r)$ is the spherical Bessel function $j_l(kr)$, which has the following asymptotic behavior:

$$j_l(kr) \sim \frac{(kr)^l}{(2l+1)!!} \quad (2.22)$$

when $r \rightarrow 0$, and:

$$j_l(kr) \sim \frac{1}{kr} \sin(kr - l\frac{\pi}{2}) \quad (2.23)$$

when $r \rightarrow \infty$.

Since the right hand side of Eq. (2.21) vanishes at large r , $\rho_l(r)$ is asymptotically:

$$\rho_l(r) \propto \frac{1}{r} \sin(kr - l\frac{\pi}{2} + \delta_l) \quad (2.24)$$

where δ_l captures the effect of the interaction as a *phase shift* for the partial wave of angular momentum l .

To connect the partial waves with the scattered wave $|\varphi\rangle$ above in (2.11), first expand the free particle plane wave e^{ikz} in terms of the free partial waves:

$$e^{ikz} = \sum_{l=0}^{\infty} i^l \sqrt{4\pi(2l+1)} j_l(kr) Y_l^0(\theta) \quad (2.25)$$

where Y_l^0 is the spherical harmonic function. Notice that j_l consists of equal amount of incoming wave e^{-ikr}/r and outgoing wave e^{ikr}/r , and the effect of the interaction should therefore only modify the outgoing wave part, so as to create the scattered wave $|\varphi\rangle \sim e^{ikr}/r$. From (2.24), it means adding a phase shift of $2\delta_l$ to the outgoing wave part of $j_l(kr)$, and we have:

$$\varphi(\mathbf{x}) = \frac{e^{ikr}}{\sqrt{V}r} \sum_{l=0}^{\infty} \sqrt{4\pi(2l+1)} e^{i\delta_l} \sin \delta_l Y_l^0(\theta) \quad (2.26)$$

Ignoring the angle dependence of the integral of u in (2.17) is equivalent to saying only the s -wave ($l = 0$) gets a significant phase shift δ_0 . This is justified for small k , because $j_l(kr)$ is only significant when $kr > \sqrt{l(l+1)}$ [Eq. (2.22)] and therefore within the interaction range R_e , only the s -wave is significantly affected and accumulates a phase shift. It can be shown that as $k \rightarrow 0$, $\delta_0 \rightarrow -ka_s$ where a_s is the scattering length defined above.

2.1.2 Pseudo potential

The above analysis made clear the earlier statement that the details of $U(r)$ could be ignored at the low density and low temperature limit. A single parameter – s -wave scattering length a_s – captures for the most part the effect of the interaction as far as the “bulk” properties of the many-body wavefunction $\Psi(\mathbf{x}_1, \mathbf{x}_2, \dots, \mathbf{x}_N)$ are concerned. Eq. (2.20) implies that one may replace $U(r)$ with any short-range function whose spatial integration is equal to g :

$$g = \frac{4\pi\hbar^2 a_s}{M} \quad (2.27)$$

in particular:

$$U'(\mathbf{x}) = g\delta(\mathbf{x}) \quad (2.28)$$

where $\delta(\mathbf{x})$ is the Dirac δ -function. A more stringent form of contact pseudo-potential contains a regularization operator $\frac{\partial}{\partial r}r$, which can usually be left out as long as the wavefunction behaves “regularly” at small particle separations (see [70]).

Finally, the second quantization Hamiltonian (2.2) can be simplified with the coupling coefficients:

$$\lambda(\Delta\mathbf{p}) = \frac{1}{V} \int d\mathbf{x} U(\mathbf{x}) e^{i\Delta\mathbf{p}\cdot\mathbf{x}} \quad (2.29)$$

being replaced by a constant g/V .

2.1.3 Resonant scattering

Normally the first order results obtained above are quite sufficient for describing the effects of interaction in a condensate. A notable exception occurs when a bound state is energetically close to the continuum of unbound states *and* it couples to the continuum. Such situation causes resonant scattering phenomena including the magnetic Feshbach resonances discussed in Chapter 4 [56, 57].

Suppose the bound state $|\beta\rangle$ has energy E_β and the coupling between the bound state and the continuum is W . One must then include the second order terms related to the bound state in the scattered wave $|\varphi\rangle$:

$$|\varphi^{(2)}\rangle = \frac{V}{(2\pi)^3} \int d\mathbf{k}' \frac{|\mathbf{k}'\rangle \langle \mathbf{k}'| \left(\frac{M}{\hbar^2}\right) W |\beta\rangle \langle \beta| \left(\frac{M}{\hbar^2}\right) W |\mathbf{k}\rangle}{(k^2 - k'^2 + i0^+)(k^2 - ME_\beta/\hbar^2)} \quad (2.30)$$

To be more specific, consider the typical situation for a magnetic Feshbach resonance. The bound state energy is:

$$E_\beta = \Delta\mu(B - B_0) \quad (2.31)$$

where $\Delta\mu$ is the magnetic moment difference between the bound state and the continuum state, B is the magnetic field strength and the bound state is degenerate with the continuum threshold at $B = B_0$. In the strong field regime of our experiments, W is the V_-^{hf} part of the hyperfine interaction as defined in [73]. Eq. (2.30) evaluated in $|\mathbf{x}\rangle$ basis becomes:

$$\langle \mathbf{x} | \varphi^{(2)} \rangle = \left(\frac{e^{ikx}}{\sqrt{V}x} \right) \left(-\frac{MV}{4\pi\hbar^2} \frac{\langle k_x | W | \beta \rangle \langle \beta | W | \mathbf{k} \rangle}{\frac{\hbar^2 k^2}{M} - \Delta\mu(B - B_0)} \right) = -\Delta a_s \left(\frac{e^{ikx}}{\sqrt{V}x} \right)$$

where:

$$\Delta a_s = \frac{MV}{4\pi\hbar^2} \frac{\langle k_x^\pm | W | \beta \rangle \langle \beta | W | \mathbf{k} \rangle}{\frac{\hbar^2 k^2}{M} - \Delta\mu(B - B_0)} \quad (2.32)$$

$$\approx -\frac{M}{4\pi\hbar^2} \frac{V |\langle 0 | W | \beta \rangle|^2}{\Delta\mu(B - B_0)} \quad (2.33)$$

where Δa_s is the modification to the scattering length due to the bound state and the last approximate equality holds for $k \rightarrow 0$. (2.33) is the often quoted dispersive form of the scattering length near a Feshbach resonance [74, 73, 75, 76, 77, 78, 79]. It should be pointed out that the above result (2.32) only holds when the bound state is *close to being degenerate* with the colliding state but *not exactly*. Otherwise the scattering amplitude diverges and the perturbative approach fails. In this case, one should treat the problem exactly [69].

2.2 Bogoliubov theory

2.2.1 BEC with two-body interaction

At temperature T in thermal equilibrium, the density matrix of the system σ is given by [72]:

$$\sigma = \sum_i \frac{\exp(-\frac{E_i}{k_B T})}{\sum_j \exp(-\frac{E_j}{k_B T})} |\Psi_i\rangle \langle \Psi_i| \quad (2.34)$$

where i, j index the eigenstates of the many-body system and $|\Psi_i\rangle$ is the eigenstate of energy E_i . $|\Psi_i\rangle$ is either symmetric (boson) or anti-symmetric (fermion) under the exchange of any pair of particles. Bose-Einstein condensation occurs when at a finite temperature $T > 0$, the reduced single particle density matrix σ_1 :

$$\langle \mathbf{p}' | \sigma_1 | \mathbf{p}'' \rangle = \langle a_{\mathbf{p}'}^\dagger a_{\mathbf{p}''} \rangle \quad (2.35)$$

has one (or more) eigenvalue(s) n_M that satisfies [54]:

$$\lim_{N \rightarrow \infty} \frac{n_M}{N} = \text{Finite Constant} \quad (2.36)$$

An order parameter ψ can be defined as:

$$\psi = \sqrt{n_M} \chi_0 \tag{2.37}$$

where χ_0 is the eigenstate of σ_1 corresponding to the eigenvalue n_M – sometimes referred to as the *condensate wavefunction*.

2.2.2 Bogoliubov transformation

In absence of other external potentials, the Hamiltonian in (2.1) and (2.2) is invariant under spatial translation, which means the total momentum \mathbf{P} is a good quantum number for the eigenstates of the system. It immediately follows that the single particle density matrix σ_1 is diagonal with respect to the momentum basis $|\mathbf{p}\rangle$. Therefore, Bose-Einstein condensation occurs when there is a macroscopic occupation of a single momentum state.

N. N. Bogoliubov was the first to study in details the ground state properties of weakly interacting Bosons [80]. In deriving the theory, one first assumes the many body wavefunction contains $N_0 \sim N$ atoms in the zero momentum state and only small population in other momentum states – called “quantum depletion”. As a result, the field operators of zero momentum state a_0^\dagger, a_0 can be treated as complex numbers $\sim \sqrt{N_0}$ in solving the Heisenberg equations of motion for the field operators. Using a canonical transformation now named after Bogoliubov, one can diagonalize the equations and obtain the energy spectrum.

Bogoliubov started from the Hamiltonian (2.2), replacing the coupling factor $\lambda(\Delta\mathbf{p})$ with the constant g/V [see (2.27)], and made the further assumption that the population in the zero momentum state $N_0 \simeq N \gg 1$ ¹ which led to (1) operators a_0^\dagger and a_0 can be treated as complex numbers; (2) only interaction terms containing

¹For consistency, the notations here differ slightly from Bogoliubov’s original work [80].

at least two a_0^\dagger or a_0 need to be retained:

$$H = \sum_{\mathbf{p}} \frac{\mathbf{p}^2}{2M} a_{\mathbf{p}}^\dagger a_{\mathbf{p}} + \frac{1}{2} \frac{g}{V} \left(a_0^\dagger a_0^\dagger a_0 a_0 + 2 \sum_{\mathbf{p} \neq 0} a_{\mathbf{p}}^\dagger a_{-\mathbf{p}}^\dagger a_0 a_0 + 2 \sum_{\mathbf{p} \neq 0} a_0^\dagger a_0^\dagger a_{\mathbf{p}} a_{-\mathbf{p}} + 4 \sum_{\mathbf{p} \neq 0} a_0^\dagger a_0 a_{\mathbf{p}}^\dagger a_{\mathbf{p}} \right) \quad (2.38)$$

where the multiplicities of the interaction terms account for the commutativity of the field operators.

With the approximate Hamiltonian, one obtains the Heisenberg equations of motion for the field operators:

$$i\hbar \frac{da_0}{dt} = \frac{g}{V} a_0^\dagger a_0 a_0 \quad (2.39)$$

$$i\hbar \frac{da_{\mathbf{p}}}{dt} \Big|_{\mathbf{p} \neq 0} = T(\mathbf{p}) a_{\mathbf{p}} + \frac{g}{V} a_0 a_0 a_{-\mathbf{p}}^\dagger + 2 \frac{g}{V} a_0^\dagger a_0 a_{\mathbf{p}} \quad (2.40)$$

where $T(\mathbf{p} = \frac{\mathbf{p}^2}{2M})$ is the kinetic energy. Replacing $a_0^\dagger a_0$ with N_0 and μ being the meanfield energy gN_0/V , one gets from (2.39):

$$a_0(t) = a_0(0) e^{-i\frac{\mu}{\hbar}t} = \sqrt{N_0} e^{-i\frac{\mu}{\hbar}t} \quad (2.41)$$

Substituting (2.41) and $\hat{a}_{\mathbf{p}} = a_{\mathbf{p}} e^{-i\frac{\mu}{\hbar}t}$ into (2.40), one gets:

$$i\hbar \frac{d\hat{a}_{\mathbf{p}}}{dt} = \zeta(\mathbf{p}) \hat{a}_{\mathbf{p}} + \mu \hat{a}_{-\mathbf{p}}^\dagger \quad (2.42)$$

where:

$$\zeta(\mathbf{p}) = T(\mathbf{p}) + \mu \quad (2.43)$$

To diagonalize equation (2.42), we employ canonical transformation:

$$b_{\mathbf{p}} = u_{\mathbf{p}} \hat{a}_{\mathbf{p}} + v_{\mathbf{p}} \hat{a}_{-\mathbf{p}}^\dagger \quad (2.44)$$

$$b_{\mathbf{p}}^\dagger = u_{\mathbf{p}}^* \hat{a}_{\mathbf{p}}^\dagger + v_{\mathbf{p}}^* \hat{a}_{-\mathbf{p}} \quad (2.45)$$

where $u_{\mathbf{p}}$ and $v_{\mathbf{p}}$ satisfy:

$$|u_{\mathbf{p}}|^2 - |v_{\mathbf{p}}|^2 = 1 \quad (2.46)$$

in order for the commutation relation:

$$[b_{\mathbf{p}}, b_{\mathbf{p}}^\dagger] = 1 \quad (2.47)$$

to hold. From Eq. (2.42) and its complex conjugate replacing \mathbf{p} with $-\mathbf{p}$, one gets:

$$i\hbar \frac{db_{\mathbf{p}}}{dt} = (u_{\mathbf{p}}\zeta(\mathbf{p}) - v_{\mathbf{p}}\mu) \hat{a}_{\mathbf{p}} + (u_{\mathbf{p}}\mu - v_{\mathbf{p}}\zeta(\mathbf{p})) \hat{a}_{-\mathbf{p}}^\dagger \quad (2.48)$$

One then forces the right hand side of (2.48) to be proportional to $b_{\mathbf{p}}$, and solves for $u_{\mathbf{p}}$ and $v_{\mathbf{p}}$ subject to (2.46) and obtain:

$$u_{\mathbf{p}} = \frac{\mu}{\sqrt{\mu^2 - |\zeta(\mathbf{p}) - \epsilon(\mathbf{p})|^2}} \quad (2.49)$$

$$v_{\mathbf{p}} = \frac{\mu}{\sqrt{\mu^2 - |\zeta(\mathbf{p}) - \epsilon(\mathbf{p})|^2}} \quad (2.50)$$

where:

$$\epsilon(\mathbf{p}) = \sqrt{T^2(\mathbf{p}) + 2T(\mathbf{p})\mu} \quad (2.51)$$

is the eigenenergy corresponding to quasiparticle $b_{\mathbf{p}}$ ($b_{\mathbf{p}}^\dagger$). Eqs. (2.44) and (2.45) along with (2.49) and (2.50) are the famed *Bogoliubov transformation*.

2.2.3 Sign of interaction

It should be noted that $T(\mathbf{p})$, μ and $\zeta(\mathbf{p})$ are generally real, and the above Bogoliubov transformation only works if $\epsilon(\mathbf{p})$ is real as well, in which case Eqs. (2.49) and (2.50)

reduce to the more commonly used forms:

$$\begin{aligned}
u_{\mathbf{p}} &= \sqrt{\frac{T(\mathbf{p}) + \mu + \epsilon(\mathbf{p})}{2\epsilon(\mathbf{p})}} \\
&= \frac{\epsilon(\mathbf{p}) + T(\mathbf{p})}{2\sqrt{T(\mathbf{p})\epsilon(\mathbf{p})}} \tag{2.52}
\end{aligned}$$

$$\begin{aligned}
v_{\mathbf{p}} &= \sqrt{\frac{T(\mathbf{p}) + \mu - \epsilon(\mathbf{p})}{2\epsilon(\mathbf{p})}} \\
&= \frac{\epsilon(\mathbf{p}) - T(\mathbf{p})}{2\sqrt{T(\mathbf{p})\epsilon(\mathbf{p})}} \tag{2.53}
\end{aligned}$$

If $\epsilon(\mathbf{p})$ becomes imaginary, i.e. $T^2(\mathbf{p}) + 2T(\mathbf{p})\mu < 0$, then there is no u and v that can achieve the aforementioned diagonalization [the denominators of Eqs. (2.49) and (2.50) vanishes]. This is no surprise as the original Hamiltonian is Hermitian and cannot have imaginary eigenvalues.

Note that as $T(\mathbf{p})$ is continuous starting from zero, the sign of the interaction g determines whether $\epsilon(\mathbf{p})$ is ever imaginary for certain (small enough) momenta \mathbf{p} .

In case of repulsive interaction ($g > 0$), $\epsilon(\mathbf{p})$ is always real and the Bogoliubov transformation gives the low-lying excitation spectrum of a stable condensate. The quasiparticle operators $b_{\mathbf{p}}$ ($b_{\mathbf{p}}^\dagger$) correspond to the eigenmodes of the system, called *phonons*. The ground state wavefunction $|\Psi_0\rangle$ can be obtained by requiring:

$$b_{\mathbf{p}} |\Psi_0\rangle = 0 \tag{2.54}$$

for all \mathbf{p} and turns out to be:

$$|\Psi_0\rangle \propto |n_0 = N\rangle \prod_{\mathbf{p} \neq 0} \frac{1}{u_{\mathbf{p}}} \sum_{j=0}^{\infty} \left(-\frac{v_{\mathbf{p}}}{u_{\mathbf{p}}}\right)^j |n_{\mathbf{p}} = j, n_{-\mathbf{p}} = j\rangle \tag{2.55}$$

where $n_{\mathbf{p}}$ is the number of particles in (single particle) momentum state $|\mathbf{p}\rangle$. Note that in (2.55) the total number of particles N is not conserved, which is a result of treating a_0 and a_0^\dagger as complex numbers. The number conserving version can be obtained by subtracting the *quantum depletion* – population in non-zero momentum

states – from N for n_0 .

In case of attractive interaction ($g < 0$), for sufficiently small $|\mathbf{p}|$, no phonon operators can be constructed with the Bogoliubov transformation. Physically, this means no stationary condensate wavefunction as described above exists, where $N_0 \sim N$ particles are in the zero-momentum state. If one starts with a stable condensate with repulsive interaction and suddenly switches the sign of interaction, the particles in the zero-momentum state will collide into the low-lying momentum states. The so-called “quantum evaporation” corresponds to such a situation [81].

2.2.4 Superfluid flow

Eq. (2.51) gives the dispersion relation for the low-lying excitations of the condensate – here I shall only consider the case of repulsive interaction and stable condensate. It is often convenient to define a natural momentum unit for a condensate $p_s = Mc_s$ where c_s is the speed of sound given by:

$$Mc_s^2 = \mu \tag{2.56}$$

There are two momentum regimes depending on the magnitude of the momentum as compared to p_s , as shown in Fig. 2-1:

Phonon regime when $|\mathbf{p}| \ll p_s$;

Free-particle regime when $|\mathbf{p}| \gg p_s$.

In the phonon regime, the dispersion relation becomes linear:

$$\epsilon(\mathbf{p}) = c|\mathbf{p}| \tag{2.57}$$

and in the free-particle regime, the dispersion relation becomes the usual quadratic form plus a meanfield offset:

$$\epsilon(\mathbf{p}) = \frac{\mathbf{p}^2}{2M} + \mu \tag{2.58}$$

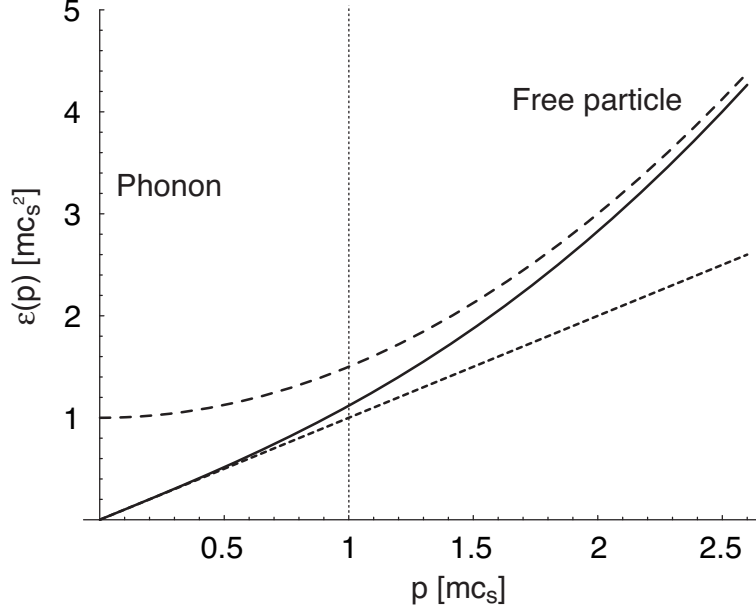


Figure 2-1: Dispersion relation of a BEC: The momentum is in units of $p_s = mc_s$ where c_s is the speed of sound. p_s separates the two regimes in which the dispersion relation is either linear or quadratic.

It is exactly the linear dispersion near zero-momentum that gives rise to superfluidity. To see this [70], consider a condensate having a massive velocity of \mathbf{V} that is interacting with a stationary obstacle. In the rest frame of the condensate, a quantum of excitation at momentum \mathbf{p} corresponds to energy $c_s|\mathbf{p}|$. In the rest frame of the obstacle, this excitation causes $\Delta E = c_s|\mathbf{p}| + \mathbf{V} \cdot \mathbf{p}$. Since the obstacle remains stationary and does no work, ΔE must be zero, and we have:

$$c_s|\mathbf{p}| = -\mathbf{V} \cdot \mathbf{p} \leq |\mathbf{V}||\mathbf{p}| \quad (2.59)$$

This inequality cannot be satisfied if $|\mathbf{V}| < c_s$. Therefore, when the massive flow speed is less than the speed of sound, the stationary obstacle cannot excite the condensate and cause its flow to slow down. c_s is the *critical velocity* of the superfluid flow [82, 83, 84, 85, 86], and was observed in a gaseous condensate as one of the first proofs of superfluidity [87, 88, 89].

In contrast, for a BEC of non-interacting particles, the dispersion relation remains quadratic at zero momentum and there is no finite critical velocity, hence no superfluidity.

2.3 Gross-Pitaevskii equation

A related but somewhat different approach to deriving the condensate wavefunction is based on the Hartree-Fock method [71], which is especially useful when it is necessary to account for the trapping potential. This approach leads to the well-known Gross-Pitaevskii (GP) equation [4, 5]. The time-dependent form of GP equation is often used for direct (in other words, brute-force) simulation of condensate dynamics, sometimes with modifications such as rotating reference frame and phenomenological damping factor [90, 91, 92].

Briefly, by taking the many-body wavefunction as a multiplication of N identical single particle wavefunctions $\Psi(\mathbf{x}_1, \mathbf{x}_2, \dots, \mathbf{x}_N) = \chi(x_1)\chi(x_2)\dots\chi(x_N)$, and minimizing the functional:

$$\mathcal{H}(\chi) = N \int d\mathbf{x} \chi^*(\mathbf{x}) \left(-\frac{\hbar^2}{2M} \nabla^2 + U_{ex}(\mathbf{x}) \right) \chi(\mathbf{x}) + \frac{N(N-1)}{2} g \int d\mathbf{x} |\chi(\mathbf{x})|^4 \quad (2.60)$$

subject to the normalization constraint:

$$\int d\mathbf{x} |\chi(\mathbf{x})|^2 = 1 \quad (2.61)$$

leads to the GP equation:

$$-\frac{\hbar^2}{2M} \nabla^2 \chi + U_{ex} \chi + g(N-1) |\chi|^2 \chi = \frac{\lambda}{N} \chi \quad (2.62)$$

where $U_{ex}(\mathbf{x})$ is the external trapping potential and λ is the Lagrangian multiplier. A cleaner form is obtained by using the *order parameter* defined as $\psi(\mathbf{x}) = \sqrt{N} \chi(\mathbf{x})$

and the *chemical potential* $\mu = \lambda/N$, also noting $N - 1 \simeq N$ for large N :

$$-\frac{\hbar^2}{2M}\nabla^2\psi + U_{ex}\psi + g|\psi|^2\psi = \mu\psi \quad (2.63)$$

Incidentally, to see why μ is called the chemical potential, one can rewrite the constrained functional minimization problem in terms of ψ . Noting that N is the “target” value for the constraint, it immediately follows that the minimized \mathcal{H}^* and the corresponding μ^* (i.e. the ground state energy) satisfies: $\mu^* = \partial\mathcal{H}^*/\partial N$.

In the Thomas-Fermi regime, the meanfield energy:

$$g|\psi|^2 = \frac{4\pi\hbar^2 a_s n}{M} \quad (2.64)$$

dominates over the kinetic energy, ignoring the kinetic energy term in 2.63 altogether leads to the equation for the Thomas-Fermi profile of the condensate:

$$U_{ex} + g|\psi|^2 = \mu \quad (2.65)$$

which for a harmonic trap $U_{ex}(\mathbf{x}) = \frac{1}{2}M(\omega_x^2 x^2 + \omega_y^2 y^2 + \omega_z^2 z^2)$ gives the density profile $n(x, y, z)$:

$$n(x, y, z) = g^{-1} \left(\mu - \frac{1}{2}M(\omega_x^2 x^2 + \omega_y^2 y^2 + \omega_z^2 z^2) \right) \quad (2.66)$$

Therefore a trapped condensate has an inverse-parabolic density distribution with Thomas-Fermi radii:

$$R_{TF,i}^2 = \frac{2\mu}{M\omega_i^2} \quad (2.67)$$

where $i = x, y, z$. This is a very good approximation and the small deviation is at the edge of the condensate where the density is rounded off instead of abruptly going to zero [4]. For a given N , μ is determined by the normalization condition that $N = \int d\mathbf{x} n(\mathbf{x})$:

$$\mu(N) = \frac{\hbar\tilde{\omega}}{2} \left(\frac{15Na_s}{\tilde{a}_{HO}} \right)^{\frac{2}{5}} \quad (2.68)$$

where $\tilde{\omega} = (\omega_x\omega_y\omega_z)^{1/3}$ is the geometric-mean trap frequency and $\tilde{a}_{HO} = \sqrt{\frac{\hbar}{M\tilde{\omega}}}$ is the

mean harmonic oscillator length.

Finally note that in the Thomas-Fermi regime:

$$\mu = \frac{1}{2}M\omega^2 R_{TF}^2 \gg \hbar\omega \quad (2.69)$$

which is equivalent to:

$$R_{TF} \gg \sqrt{\frac{\hbar}{M\omega}} = a_{HO} \quad (2.70)$$

which means the condensate wavefunction has a spatial extension much greater than the single particle ground state in the harmonic trap.

Chapter 3

Momentum analysis using Bragg spectroscopy

This chapter discusses two experiments using the technique of two-photon Bragg scattering to both prepare (excite) and probe the condensates:

- J.M. Vogels, K. Xu, C. Raman, J.R. Abo-Shaeer, and W. Ketterle, *Experimental Observation of the Bogoliubov Transformation for a Bose-Einstein Condensed Gas*, Phys. Rev. Lett. **88**, 060402 (2002). Included in Appendix A.
- J.M. Vogels, K. Xu, and W. Ketterle, *Generation of Macroscopic Pair-Correlated Atomic Beams by Four-Wave Mixing in Bose-Einstein Condensates*, Phys. Rev. Lett. **89**, 020401 (2002). Included in Appendix B.

The experiments always deal with condensates of finite size confined in a (usually) harmonic trapping potential, whereas the Bogoliubov theory derived in Section 2.2 assumes a homogeneous system with translational symmetry whose eigenstates have well defined momenta. Nevertheless, the main results of the theory work quite well for understanding many processes in a trapped condensate, including some of the experiments described in this thesis. Oftentimes, a *local density approximation* is sufficient to account for the inhomogeneity, and as long as the dynamics in question occurs on timescales much faster than the trap period, the presence of the trap can be largely ignored.

Both experiments described in this chapter used Bragg spectroscopy to analyze the “momentum” distribution of condensate wavefunctions, whose static and dynamic properties were directly related to the atomic interaction. The momentum states in the following discussion should be understood as wavepackets of the condensate size $\Delta R \sim R_{TF}$, and have a momentum “uncertainty” $\Delta P \sim \hbar/R_{TF}$. In addition, momentum states different by more than ΔP are approximately orthogonal – sometimes called “quasimodes” [93, 44, 94].

3.1 Bragg spectroscopy – a “Swiss army knife”

Despite its name, Bragg spectroscopy is more than just a spectroscopic technique. It has proven an extremely versatile tool in the studies of ultracold atomic systems. Since 1988, two-photon Bragg diffraction of atoms from a moving optical lattice has been used as a *coherent beamsplitter* for atomic samples much like an optical beamsplitter for light [95], and was first applied in a Bose-Einstein condensate in 1999 [96, 97]. Subsequently, the Bragg spectroscopy was extensively used both as an *exciter* and as a *probe* to study the condensate dynamics by measuring the momentum distribution of the condensate or, more precisely, the *dynamic structure factor* [85, 98, 99].

As a *beamsplitter*, the two-photon Rabi frequency is typically high and exceeds the inhomogeneous “linewidth” of the atoms, so that the collective effect (such as the meanfield) can be ignored and all atoms are coherently split in the momentum space. Large fraction – 50 % ($\pi/2$ -pulse) to 100 % (π -pulse) – of the atomic population are routinely transferred between momentum states. As an *exciter* or a *probe*, the Bragg beams are typically operated in the perturbative regime where a linear response theory provides a good description of the process [99]. For the two experiments discussed in this Chapter [100, 39], we utilized all three aforementioned functions of Bragg spectroscopy.

There are various ways to look at the two-photon Bragg scattering process, some more rigorous and generally applicable than others. Here, I choose to adopt a practical “experimentalist” view of a scatterer under the influence of two *far-detuned* laser

beams as illustrated in Fig. 3-1¹. The scatterer coherently absorbs a photon from the higher frequency beam and subsequently emits one into the lower frequency beam. The total energy and momentum must be conserved, and therefore the resonant condition is given by:

$$\Delta\omega_{\text{res}} = \omega(\mathbf{q} + \Delta\mathbf{k}) - \omega(\mathbf{q}) \quad (3.1)$$

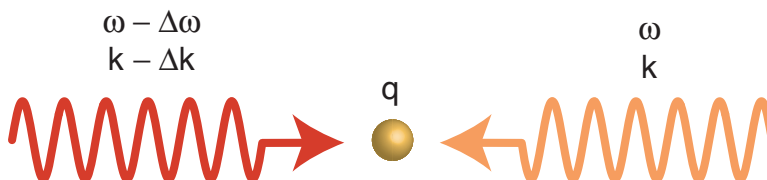


Figure 3-1: Two-photon Bragg scattering: The yellow ball can be a single particle or a many-body system such as a BEC, that has an initial momentum \mathbf{q} . The resonant condition is satisfied when the frequency difference $\Delta\omega$ between the two Bragg beams exactly matches the energy cost to transfer momentum $\Delta\mathbf{k}$ to the scatterer.

Usually the dispersion relation ($\omega(\mathbf{q})$) for the scatterer approaches the quadratic free-particle asymptote for large momentum q such as in Fig. 2-1. The resonant condition then becomes (for large Δk):

$$\Delta\omega_{\text{res}} = \frac{\hbar}{2M}(\Delta\mathbf{k}^2 + \mathbf{q} \cdot \Delta\mathbf{k}) + \delta(\mathbf{q}) \quad (3.2)$$

where $\delta(\mathbf{q})$ includes $\omega(\mathbf{q})$, $\frac{\hbar q^2}{2M}$ and any other *small* offset (such as the meanfield shift) that depends on \mathbf{q} . The linear term $\mathbf{q} \cdot \Delta\mathbf{k}$ should be much greater than $\delta(\mathbf{q})$ in order for the momentum distribution to be (linearly) mapped into the frequency domain. For this reason, the momentum transfer Δk is typically set to be as large as possible when measuring the momentum distribution through Bragg spectroscopy.

3.2 Measuring phonon wavefunction

The Bogoliubov theory showed that because of the interaction, the elementary excitations in a BEC are phonons corresponding to the quasi-particle creation/annihilation

¹*Far-detuned* means the two-photon Rabi frequency of the stimulated Bragg scattering process is much greater than the spontaneous Rayleigh scattering.

operators given in Eqs. (2.44) and (2.45). From the ground state wavefunction (2.55), it is straightforward to calculate that for l phonons at momentum \mathbf{p} ($b_{\mathbf{p}^\dagger}^l |\Psi_0\rangle$), there are $lu_{\mathbf{p}}^2 + v_{\mathbf{p}}^2$ free particles moving with momentum \mathbf{p} and $(l+1)v_{\mathbf{p}}^2$ moving with momentum $-\mathbf{p}$. The finite population $v_{\mathbf{p}}^2$ present in the ground state corresponds to the quantum depletion and will be further discussed in Chapter 5. Since both $u_{\mathbf{p}}^2$ and $v_{\mathbf{p}}^2$ become $\gg 1$ for small momentum p , we expect to see a significant populations in both the $+\mathbf{p}$ and $-\mathbf{p}$ directions.

3.2.1 Experimental setup and time sequence

In the first experiment [100], we used the Bragg spectroscopy to excite phonons in the condensate and subsequently probe the resulted momentum distribution [101]. The setup of the Bragg beams is illustrated in Fig. 3-2. We first turned on a pair of small angle (30 mrad) Bragg beams 1 and 2 for 3 ms, exciting phonons at low momentum $q/M = 1.9$ mm/s (the speed of sound c_s for our experiment was at least twice higher). Subsequently, a pair of large angle Bragg beams were pulsed for 500 μ s to probe the momentum distribution of the system – the large momentum transfer $Q/M = 59$ mm/s was at least 10 times greater than c_s . The trap was then switched off and the atoms expanded ballistically for 40 ms before an absorption image was taken. In the experiment, we actually retro-reflected a laser beam that contained both ω and $\omega - \Delta\omega_p$ for the large angle Bragg scattering, resulting in out-coupling of atoms in both direction – a technicality largely out of convenience. All the Bragg pulses were applied when the condensate was held in a magnetic trap whose radial and axial trapping frequencies were 37 and 7 Hz respectively.

Fig. 3-3 shows three absorption images taken when the probe frequency was resonant with the atoms in $+q, 0, -q$ momentum states with respect to the direction of the large momentum transfer \mathbf{Q} . Note that in the center of the images, aside from the remnant of the initial condensate, there is a shadow of atoms on one side of the condensate corresponding to the phonons that were adiabatically converted into free

²We see from the normalization condition (2.46) that the total momentum is still $l\mathbf{p}$, consistent with the phonon picture.

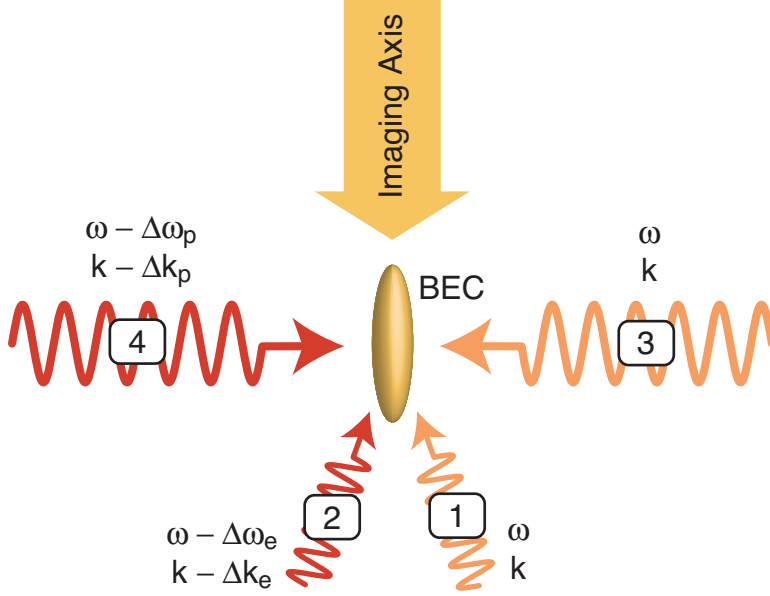


Figure 3-2: (Color) Bragg beams setup for phonon wavefunction measurement: The small angle beams 1 and 2 were used to excite phonons at $\mathbf{q} = \Delta\mathbf{k}_e$, while the large angle beams 3 and 4 were used to measure the momentum distribution $\mathbf{Q} = \Delta\mathbf{k}_p$. Absorption images were taken along the long axis of the condensate.

particles during the ballistic expansion. This is a consequence due to the condensate being in the Thomas-Fermi regime, where the density drops on a timescale (inverse radial trap frequency which is 37 Hz) much slower than the inverse of the phonon energies (about 400 Hz) [102]. Precisely for this reason, we had to use the large angle Bragg beams to perform *in-situ* momentum analysis³.

3.2.2 Measuring Bogoliubov amplitudes

To measure the Bogoliubov amplitude, we kept the probe frequency $\Delta\omega_p$ fixed at 94 kHz, which was chosen to resonantly detect free atoms with $+q$ momentum (by kicking them into the $-Q + q$ momentum state). The excitation frequency $\Delta\omega_e$ was tuned to excite phonons, and the atoms out-coupled to the $-Q + q$ states were counted as a measure of the phonon amplitude. As shown in Fig. 3-4, two resonances were found in the scanning of $\Delta\omega_e$ (one positive and one negative) corresponding to the

³This subtlety is revisited in Chapter 5.

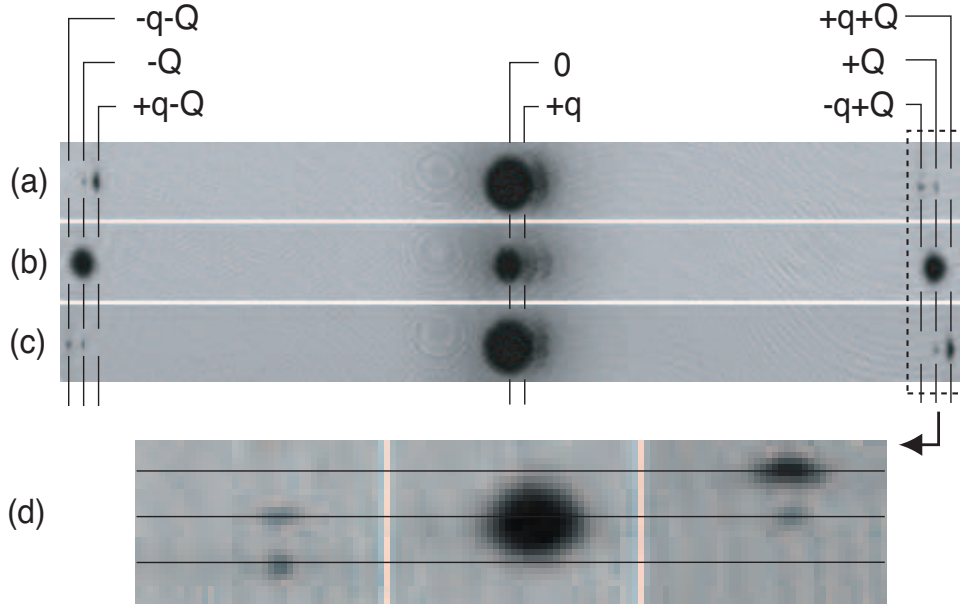


Figure 3-3: Momentum distribution of a condensate with phonons: After the small angle Bragg beams excited $+q$ phonons into the condensate, the large angle Bragg beams probed the momentum distribution. Absorption images after 40 ms time of flight in (a), (b), and (c) show the condensate in the center and outcoupled atoms to the right and left for probe frequencies of 94, 100, and 107 kHz, respectively. The small clouds centered at $+q$ are phonons which were converted into free particles. The size of the images is 25×2.2 mm. (d) The outlined region in (a) - (c) is magnified, and clearly shows outcoupled atoms with momenta $Q \pm q$, which implies that phonons with wavevector q/\hbar have both $+q$ and $-q$ free particle momentum components.

phonon excitations at two momenta $+q$ and $-q$ that contained u_q^2 and v_q^2 units of free atoms in $+q$ state.

The relative heights of the two peaks gives the ratio of u_q^2/v_q^2 , which increases as $q/p_s = q/(Mc_s)$ is increased. Due to limited optical access, it was difficult for us to change the phonon momentum q , which required changing the angle between the small angle Bragg beams. Instead, we performed the same measurement for condensates at peak densities $1.0 \times 10^{14} \text{ cm}^{-3}$ and $0.5 \times 10^{14} \text{ cm}^{-3}$, which correspond to the speed of sound $c_s = 5 \text{ mm/s}$ and 3.5 mm/s respectively. The result is consistent with the Bogoliubov theory calculation (dashed lines in Fig. 3-4. Somewhat later, a different group was able to map out the entire excitation spectrum by varying the angle between the exciting beams [103, 104].

3.3 Coherent collision and four-wave mixing

The long range coherence of BEC in the context of atom optics is analogous to that of laser, which prompted the term *atom laser*. In the same context, the interaction terms in the Hamiltonian (2.2) are identical to the four-wave mixing Hamiltonian in non-linear optics:

$$H_{\text{FWM}} \propto a_3^\dagger a_4^\dagger a_1 a_2 \quad (3.3)$$

This led to the matter-wave mixing experiments with BEC, which was first reported in 1999 [38]. The second experiment described in this Chapter was the effort by our lab based on the same idea. Due to the much larger size of our condensate, a maximum gain in excess of 20 was observed which implied an approximate dual Fock state [105].

3.3.1 Experimental setup and time sequence

Fig. 3-5 shows the setup of four Bragg beams used as atomic beamsplitters. The condensate was initially in mode 1 (zero momentum state). The beams 1 and 2 were pulsed for $20 \mu\text{s}$ to seed mode 3 with about 1 to 2 % of total atoms. Subsequently,

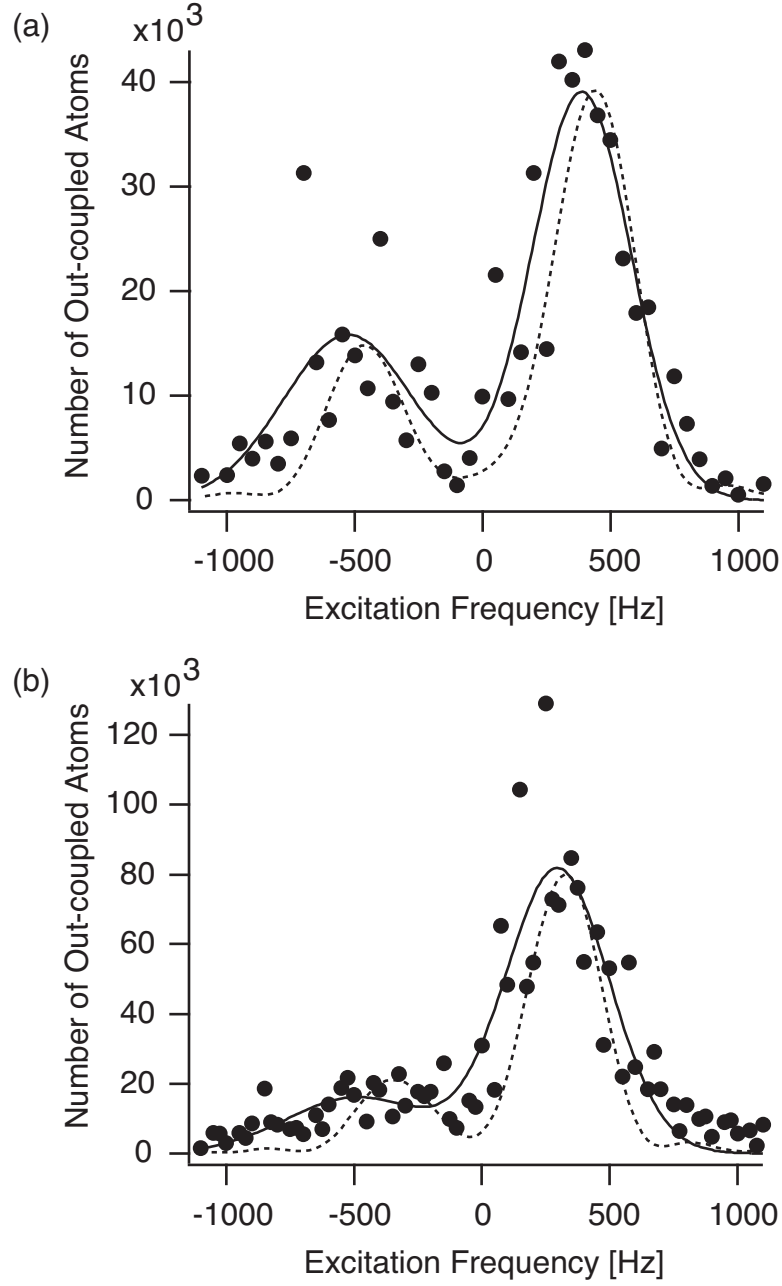


Figure 3-4: Bogoliubov amplitudes of phonons in a BEC: The relative height of the two peaks reflect the ratio of $u_{\mathbf{q}}^2/v_{\mathbf{q}}^2$, which increases as p/p_s increases. (a) and (b) are data for condensates at peak densities of $1.0 \times 10^{14} \text{ cm}^{-3}$ ($c_s = 5 \text{ mm/s}$) and $1.0 \times 10^{14} \text{ cm}^{-3}$ ($c_s = 5 \text{ mm/s}$) respectively.

the beams 1 and 3 were pulsed for 40 μs to split half of the condensate into mode 2. The three waves then underwent four-wave mixing, during which the seed wave and its conjugate (mode 4) grew exponentially while the source waves (mode 1 and 2) became depleted. In order to observe the amplification in mode 3 and 4 *in-situ*, a 40 μs readout pulse was used to couple out a (fixed) fraction of the atoms in mode 3 and 4 at various points during the four-wave mixing. These “read-out” atoms did not mix with the other waves as phase-matching condition (i.e. energy and momentum conservation was no longer satisfied. The All Bragg pulses were applied when the condensate was held in the magnetic trap whose radial and axial trap frequencies are 80 and 20 Hz respectively. After the readout pulse, the magnetic trap was shut off and absorption images were taken after 43 ms time-of-flight, as shown in Fig. 3-6.

3.3.2 Bogoliubov approach for four-wave mixing

Assuming the initial source waves 1 and 2 remain dominant over the entire process of the wave mixing, we can adopt a similar approximation as the Bogoliubov theory and retain in the Hamiltonian (2.2) only terms containing $a_{1,2}$ and $a_{1,2}^\dagger$:

$$\begin{aligned}
H = & \sum_i \frac{\hbar^2 k_i^2}{2M} a_i^\dagger a_i \\
& + \frac{g}{2V} (a_1^\dagger a_1^\dagger a_1 a_1 + a_2^\dagger a_2^\dagger a_2 a_2) + \frac{2g}{V} a_1^\dagger a_2^\dagger a_1 a_2 \\
& + \sum_{i,j \neq 1,2} \frac{2g}{V} (a_1^\dagger a_2^\dagger a_i a_j + \text{c.c.}) \\
& + \sum_{i \neq 1,2} \frac{2g}{V} (a_1^\dagger a_i^\dagger a_1 a_i + a_2^\dagger a_i^\dagger a_2 a_i)
\end{aligned} \tag{3.4}$$

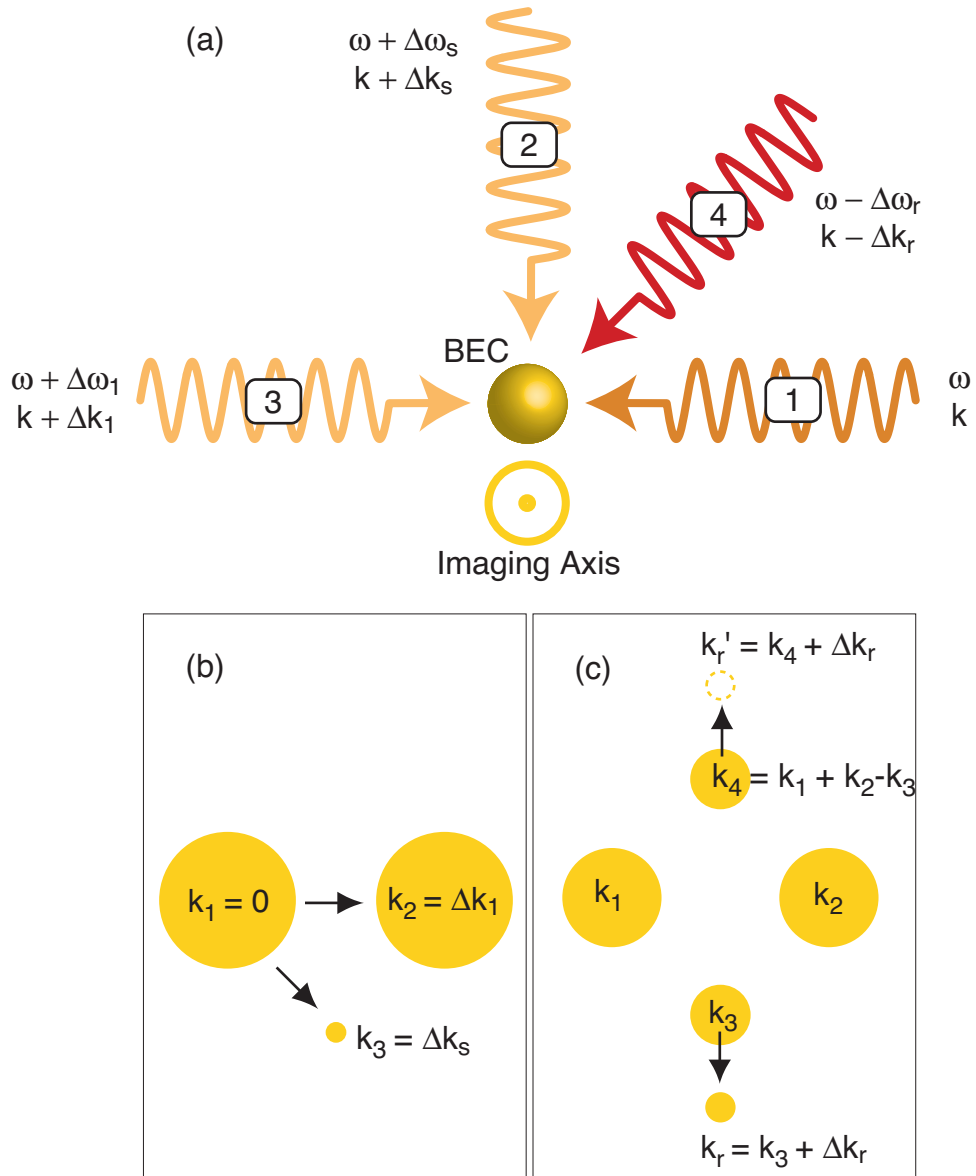


Figure 3-5: (Color) Bragg beams setup for four wave mixing: (a) The beam 1 was paired up with the beams 2, 3 and 4 sequentially to split the atoms into source waves, seed wave and then read out the growth in the seed and source waves. The detunings were set to satisfy the resonant Bragg condition. (b) and (c) show the initial waves and the subsequent four-wave mixing including the readout.

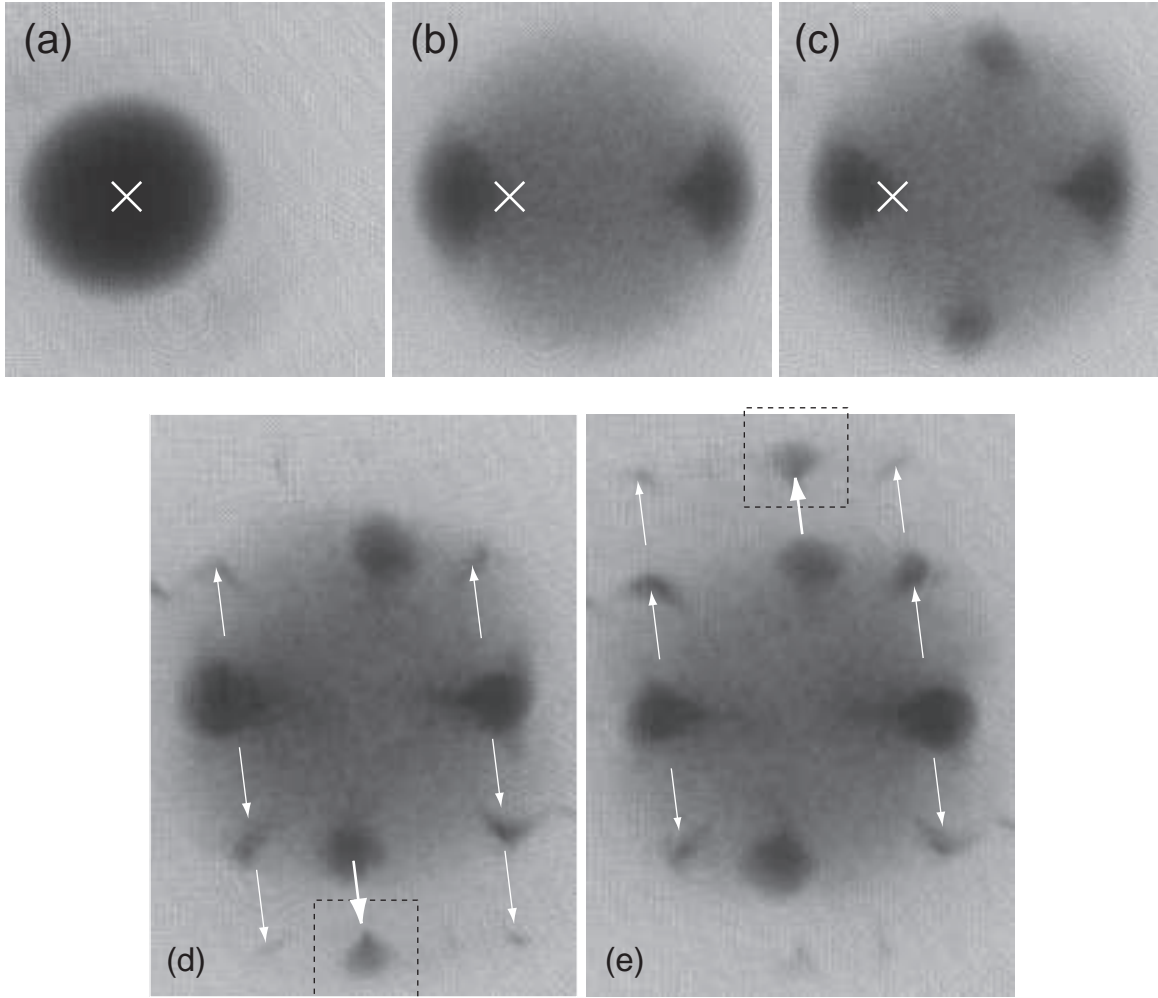


Figure 3-6: Time-of-flight images of atomic four-wave mixing: (a) Only a 1 % seed was present (barely visible). (b) only the two source waves were created and the collisions result in a *s*-wave halo. (c) All three waves were present and the four-wave mixing greatly enhanced the number of atoms in the seed and its conjugate waves. The white cross marks the location of the initial condensate. (d) and (e) are examples of the readout pulses coupling out a small fraction of the seed and its conjugate waves. The readout pulses were $40 \mu\text{s}$ in order to take a “snapshot” of the amplification, resulting in off-resonant out-coupling to other wave packets indicated by the white arrows. Our signal is in the dashed square boxes. The time of flight is 43 ms.

where $g = \frac{4\pi\hbar^2 a_s}{M}$. We further neglect the depletion of the source waves and treat $a_{1,2}$ and $a_{1,2}^\dagger$ as complex numbers that evolve as:

$$a_1(t) = e^{-i\omega_1 t} a_1(0) = e^{-i\omega_1 t} \sqrt{N_1} \quad (3.5)$$

$$a_2(t) = e^{-i\omega_2 t} a_2(0) = e^{-i\omega_2 t} \sqrt{N_2} \quad (3.6)$$

$$\hbar\omega_1 = \frac{\hbar^2 k_1^2}{2M} + \mu_1 + 2\mu_2 \quad (3.7)$$

$$\hbar\omega_2 = \frac{\hbar^2 k_2^2}{2M} + \mu_2 + 2\mu_1 \quad (3.8)$$

$$\mu_i = \frac{g}{V} N_i \quad i = 1, 2 \quad (3.9)$$

where N_1 and N_2 are the number of atoms in the source modes 1 and 2, assumed to be constant for the duration of the wave mixing.

The equations of motion for mode 3 and 4 are:

$$i\hbar \frac{da_3}{dt} = \hbar\omega_3 a_3 + 2\frac{g}{V} a_1 a_2 a_4^\dagger \quad (3.10)$$

$$i\hbar \frac{da_4}{dt} = \hbar\omega_4 a_4 + 2\frac{g}{V} a_1 a_2 a_3^\dagger \quad (3.11)$$

$$\hbar\omega_{3,4} = \frac{\hbar^2 k_{3,4}^2}{2M} + 2\mu_1 + 2\mu_2 \quad (3.12)$$

With a change of variable:

$$\hat{a}_{3,4} = e^{i\omega_{3,4} t} a_{3,4} \quad (3.13)$$

Eqs. (3.10) and (3.11) simplify to:

$$i\hbar \frac{d\hat{a}_3}{dt} = 2\sqrt{\mu_1 \mu_2} e^{i\Delta\omega t} \hat{a}_4^\dagger \quad (3.14)$$

$$i\hbar \frac{d\hat{a}_4}{dt} = 2\sqrt{\mu_1 \mu_2} e^{i\Delta\omega t} \hat{a}_3^\dagger \quad (3.15)$$

$$\hbar\Delta\omega = \hbar(\omega_3 + \omega_4 - \omega_1 - \omega_2) \quad (3.16)$$

$$= \frac{\hbar^2 k_3^2}{2M} + \frac{\hbar^2 k_4^2}{2M} - \frac{\hbar^2 k_1^2}{2M} - \frac{\hbar^2 k_2^2}{2M} + \mu_1 + \mu_2 \quad (3.17)$$

which can be solved to give:

$$\hat{a}_3(t) = \left(\frac{\lambda_2 e^{\lambda_1 t}}{\lambda_2 - \lambda_1} + \frac{\lambda_1 e^{\lambda_2 t}}{\lambda_1 - \lambda_2} \right) \hat{a}_3(0) + i \frac{2\sqrt{\mu_1 \mu_2}}{\hbar(\lambda_2 - \lambda_1)} \hat{a}_4^\dagger(0) \quad (3.18)$$

$$\hat{a}_4(t) = \left(\frac{\lambda_2 e^{\lambda_1 t}}{\lambda_2 - \lambda_1} + \frac{\lambda_1 e^{\lambda_2 t}}{\lambda_1 - \lambda_2} \right) \hat{a}_4(0) + i \frac{2\sqrt{\mu_1 \mu_2}}{\hbar(\lambda_2 - \lambda_1)} \hat{a}_3^\dagger(0) \quad (3.19)$$

$$\lambda_{1,2} = \frac{1}{2} \left(i\Delta\omega \pm \sqrt{\frac{16\mu_1\mu_2}{\hbar^2} - \Delta\omega^2} \right) \quad (3.20)$$

Since we initially have N_{seed} atoms in mode 3 and no atoms in mode 4, the above solutions (3.18) and (3.19) give the time evolution of N_3 and N_4 :

$$\langle \hat{N}_3(t) \rangle = \left| \cosh(\lambda t) - \frac{i\Delta\omega}{2\lambda} \sinh(\lambda t) \right|^2 N_{\text{seed}} + \left| \frac{2\sqrt{\mu_1\mu_2}}{\hbar\lambda} \sinh(\lambda t) \right|^2 \quad (3.21)$$

$$\langle \hat{N}_4(t) \rangle = \left| \frac{2\sqrt{\mu_1\mu_2}}{\hbar\lambda} \sinh(\lambda t) \right|^2 (N_{\text{seed}} + 1) \quad (3.22)$$

$$\lambda = \sqrt{\frac{4\mu_1\mu_2}{\hbar^2} - \frac{\Delta\omega^2}{4}} \quad (3.23)$$

When $\hbar\Delta\omega < 4\sqrt{\mu_1\mu_2}$, both N_3 and N_4 grow exponentially together at the growth rate λ ; when $\hbar\Delta\omega > 4\sqrt{\mu_1\mu_2}$, the cosh and sinh functions become cos and sin and N_3 and N_4 become oscillatory instead. The maximum growth rate λ is achieved when the *energy mismatch* $\Delta\omega = 0$ as expected.

In our experiment, the Bragg beams were set up to minimize the energy mismatch (Fig. 3-5). The number of atoms out-coupled by the readout pulse in our experiment indeed showed an initial exponential growth, which leveled off after a couple of hundred microseconds when the source waves became significantly depleted, as shown in Fig. 3-7.

3.3.3 Dual Fock state and Heisenberg-limited interferometry

In quantum mechanics, the evolution of any dynamic system can be thought of as the accumulation of phase differences among various eigenstates. *Interferometry* is the class of measurement based on interfering two (or more) alternative dynamic paths and mapping the cumulative *phase* difference between the paths into some

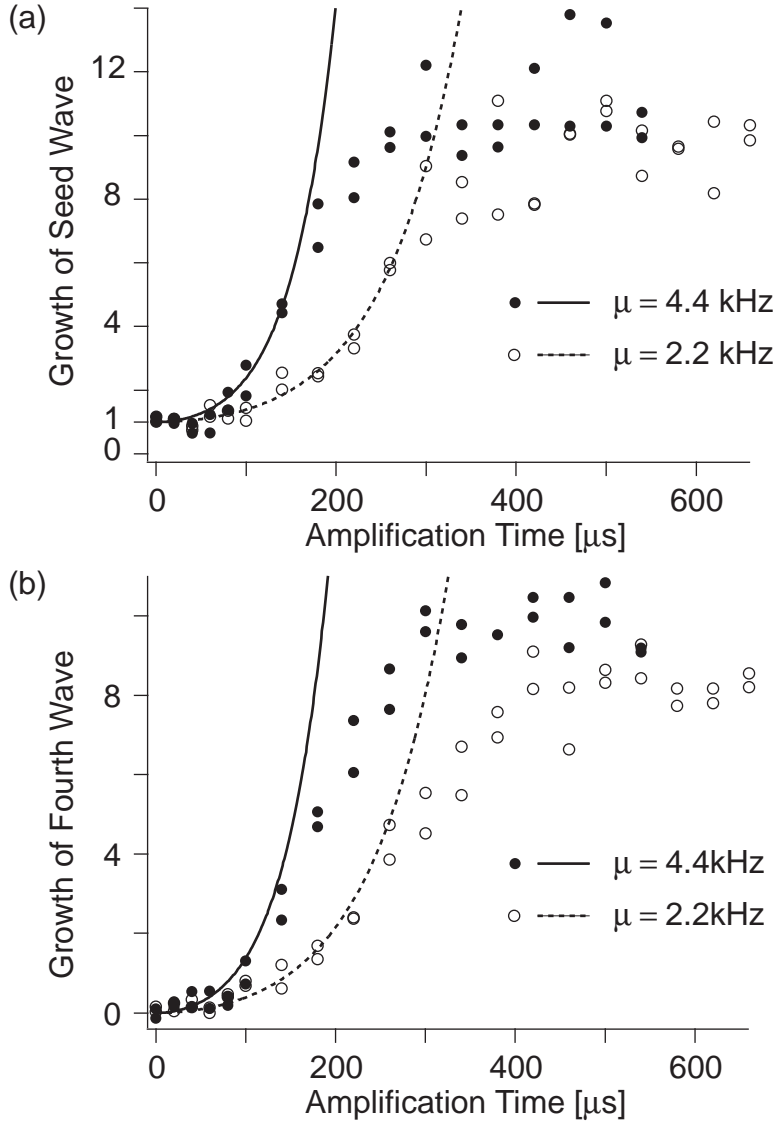


Figure 3-7: The correlated exponential growth of seed wave and its conjugate: The growth of (a) the seed wave in mode 3 and (b) its conjugate in mode 4. The growth rate is determined by the meanfield energy [Eq. (3.21) and (3.22)]. The atom counts (in the dashed square boxes in Fig. 3-6) are normalized by the initial value for the seed wave. The solid and dashed lines are fits to the initial growth according to Eq. (3.21) and (3.22), which give growth rates of $(170 \mu\text{s})^{-1}$ and $(100 \mu\text{s})^{-1}$ respectively.

sort of time-dependent *intensity*, thereby obtaining the eigenenergies⁴. The quantum nature of light or particle waves gives rise to *shot noise* in the intensity measurement. Typically, the intensity of a classical wave has a Poissonian fluctuation:

$$\Delta N \sim \sqrt{N} \quad (3.24)$$

where N is the total counts corresponding to the integrated intensity within the measurement window⁵. Therefore, the accuracy of the phase (and frequency) measurement is also subject to this $1/\sqrt{N}$ shot noise.

In principle, if the states involved in the interferometry are *squeezed* in amplitude [105], the phase measurement resolution should only be limited by the total number count N [106]:

$$\Delta\phi \sim \frac{1}{N} \quad (3.25)$$

which is called the *Heisenberg limit*. Various schemes based on such non-classical squeezed states have been proposed over the year. In particular, one class of schemes require the use of dual Fock state which is of the form:

$$|\psi\rangle = \sum_N c_N |N, N\rangle \quad (3.26)$$

where the occupation in a pair of (input) modes are identical [40, 41, 107, 42].

In our experiment, due to the initial seed N_{seed} in mode 3, the number difference between mode 3 and 4 is not exactly zero, but does stay constant – $\hat{N}_3 - \hat{N}_4$ commutes with the Hamiltonian (3.4):

$$|\psi'\rangle = \sum_{N, N'} c_1 |N_3 = N, N_4 = N'\rangle \quad (3.27)$$

$$\Delta(N_3 - N_4) \sim \sqrt{N_{\text{seed}}} \quad (3.28)$$

⁴It is the energy difference to be exact, as a global energy offset leads to a global phase that is not physically observable.

⁵The inverse of measurement (time) window determines the bandwidth for the measurement of intensity variation, from which the eigen frequency is calculated.

Therefore, a gain of 20 implies a squeezing factor of $\sqrt{40}$. However, it should be noted that such squeezing is only true because we have ignored the secondary terms in the Hamiltonian (3.4) which correspond to secondary collisions that would degrade the squeezing factor. This limitation is in principle a technical one – as long as the meanfield gain factor $\lambda_{1,2}$ are sufficiently large, the compromising effect of secondary collisions could be suppressed. In addition, mode selectivity that enhances the gain in the desired modes would eliminate the need for the initial seed. Mode selectivity in optics is typically achieved by cavities. In case of atoms, the analog of which for atoms are atomic waveguides [108, 109, 110, 111, 112]. Similarly, extreme geometries could also lead to some mode selectivity [94].

Chapter 4

Quantum degenerate molecules

This chapter discusses two experiments studying the formation and decay of ultracold molecules produced from an atomic condensate using a magnetic Feshbach resonance:

- K. Xu, T. Mukaiyama, J.R. Abo-Shaeer, J.K. Chin, D.E. Miller, and W. Ketterle *Formation of Quantum-Degenerate Sodium Molecules*, Phys. Rev. Lett. **91**, 210402 (2003). Included in Appendix C.
- T. Mukaiyama, J.R. Abo-Shaeer, K. Xu, J.K. Chin, and W. Ketterle, *Dissociation and Decay of Ultracold Sodium Molecules*, Phys. Rev. Lett. **92**, 180402 (2004). Included in Appendix D.

One of the first interesting discoveries about ultracold atomic gases is the observation of Feshbach resonances [56, 57, 113]. Because of the low temperature and narrow kinetic energy spread of the cloud, the highest bound states of the two-body potential could be tuned very close to the unbound colliding states, resulting in resonant scattering. It was immediately suggested as a way to vary the interaction strength in BEC, which proved to be more difficult in practice due to the strong inelastic collision losses near the Feshbach resonance [58]. In past three years, however, much progress has been made in a different way of using the resonances, namely creating ultracold molecule samples from an atomic condensate (or a degenerate Fermi gas).

Molecules, due to their complicated internal level structure, are difficult to cool using the conventional laser cooling techniques, which are typically the precursor to

evaporative cooling in order to reach quantum degeneracy. Alternative techniques such as buffer gas loading [114], Stark deceleration [115] or cavity cooling [116] have been successful to some extent, but still fall short of achieving the requisite phase-space density for BEC. Feshbach resonances provided a solution to convert ultracold atoms into molecules thereby circumventing the problem of directly cooling the molecules.

This Chapter describes the efforts in our lab to create and study ultracold (quantum degenerate) molecules using a Feshbach resonance. Although such molecules are short-lived due to inelastic collisions, we were able to use them to experimentally probe the coupling between the atomic and molecular states that underlies the Feshbach resonance.

4.1 Magnetic Feshbach resonance

I start this Chapter by making explicit the general formalism of resonant scattering phenomena in Chapter 2 as applied to the specific case of inducing a Feshbach resonance with an external magnetic field. Fig. 4-1 illustrates the typical situation. The *collision channel* (red) and *bound state channel* (green) are each labeled by the atom pair's hyperfine configuration in the far distance limit, denoted as $|c\rangle$ and $|b\rangle$ respectively. At zero field, the *continuum thresholds* of these channels are separated according to the atomic hyperfine structure. Each channel has a Born-Oppenheimer potential associated with it, which gives rise to a discrete set of bound states.

When a magnetic field is applied, the potentials of two channels with different magnetic moment can be shifted with respect to each other, along with their continuum threshold and bound states. Suppose this is the case for channels $|c\rangle$ and $|b\rangle$, whose magnetic moment difference is:

$$\Delta\mu = \mu_b - \mu_c \tag{4.1}$$

Then it is possible to shift one of the highest bound states of channel $|b\rangle$ (typically a

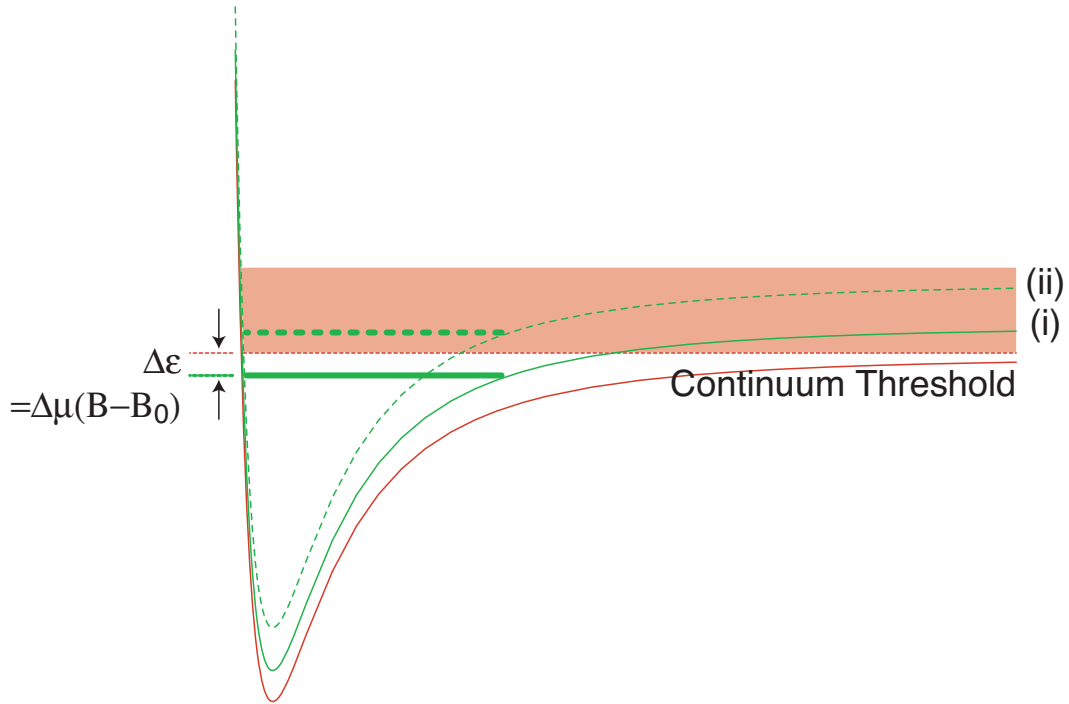


Figure 4-1: (Color) Magnetic feshbach resonance: Color red represents the unbound collision channel and color green represents the bound state channel. Shaded area represents the colliding continuum. $\Delta\epsilon$ is the energy separation between the bound state and continuum threshold (in a condensate, atoms lie very close to the threshold), tunable by the magnetic field B . The bound state is degenerate with the threshold at B_0 . For the purpose of illustration, the potentials are not drawn to actual scale.

couple of gigahertz below the threshold) close to the continuum threshold of channel $|c\rangle$. If there is a coupling between the two channels, the resonant scattering behavior would occur.

Since $\Delta\mu/h \sim 1$ MHz/G, a magnetic field $B_0 \lesssim 1000$ G would be sufficient to induce such a magnetic Feshbach resonance, which is indeed the case for the Feshbach resonance experiments in ^{23}Na . For heavier atoms such as ^{87}Rb and ^{133}Cs that have larger hyperfine splittings, even lower magnetic field is required to induce Feshbach resonances [113, 117].

Eq. 2.33 is typically rewritten in a dispersive form [73]:

$$a_s(B) = a_s^{(\text{bg})} \left(1 - \frac{\Delta B}{B - B_0} \right) \quad (4.2)$$

$$a_s^{(\text{bg})} \Delta B = \frac{MV}{4\pi\hbar^2\Delta\mu} |\langle c|W|b\rangle|^2 \quad (4.3)$$

4.2 Experimental setup and time sequence

The main components of the experiment is illustrated in Fig. 4-2, along with the time sequence for creating and detecting the molecules. The optical dipole trap had an axial trap frequency $\omega_z = 2\pi \times 2.2$ Hz and radial trap frequencies $\omega_{x,y} = 2\pi \times 290$ Hz, which gave Thomas-Fermi radii of $R_z = 650$ μm and $R_{x,y} = 5$ μm and a peak density of 1.7×10^{14} cm^{-3} for a condensate of 5×10^6 ^{23}Na atoms.

The Feshbach resonance used for molecule formation is at about $B_0 = 907$ G, corresponding to the resonant collision between atoms in the lowest hyperfine state $|m_S = -1/2, m_I = +3/2\rangle$ which connects to the $|F = 1, m_F = +1\rangle$ state at zero field. An adiabatic radio-frequency sweep was applied to transfer all the atoms from the initial $|F = 1, m_F = -1\rangle$ state into the $|F = 1, m_F = +1\rangle$ state. Since the true bound state exists below B_0 , we first ramped the field to just under B_0 with the small coils adding about 10 G magnetic field opposite to the high field direction, and then switched off the small coils to jump across the resonance quickly (~ 1 μs). At this point, the (quasi) bound state was above the continuum threshold. The magnetic field was subsequently ramped back down across the resonance. Due to the atom-

molecule coupling, part of the atomic population was transferred into the molecular state following the Landau-Zener avoided crossing.

A “blast” light pulse ($20 \mu\text{s}$) was applied in the radial direction to quickly remove the remnant atoms, in order to minimize the inelastic collision between the molecules and atoms which would lead to the heating and loss of molecules. The magnetic field was sufficiently detuned from the resonance so that only the atoms were resonant with the blast pulse while the molecules were largely transparent due to the small Frank-Condon factor and remained intact.

After some time of flight, we ramped the magnetic field back up in $100 \mu\text{s}$ and moved the molecular state into the continuum, which again became a quasi-bound state. The molecules were quickly dissociated into free atoms and then imaged at the high field. The imaging occurred $500 \mu\text{s}$ after the dissociation which was short enough to ensure that the spatial extent of the cloud reflected mostly the momentum distribution of the molecules, which could be used to define a nominal “temperature”.

4.3 Quantum degenerate molecules

The slower the ramp down speed, the more atoms should be converted into molecules. However, the inelastic collision loss is greatly enhanced near the Feshbach resonance. In a slow ramp, the molecule atom mixture spends too much time near the resonance and most of the molecules are lost to relaxation into deeper bound states.

Fig. 4-3 shows the situation for different ramp speeds with or without the “blast” pulse to remove the remnant atoms. Based on the estimation of Landau-Zener factor, the “ideal” conversion efficiencies for ramping the magnetic field by 10 G in $50 \mu\text{s}$, $200 \mu\text{s}$, 1 ms and 4 ms are 5 %, 20 %, 60 % and 98 % respectively. However, due to the inelastic collisions with the atoms, slow ramps did not produce more molecules than a fast ramp followed by a “blast” pulse, in which case the molecules were also significant “colder”.

In fact, these molecules appeared so cold in time-of-flight that we suspected they might be quantum degenerate – Fig. 4-4. A quantitative analysis of the phase space

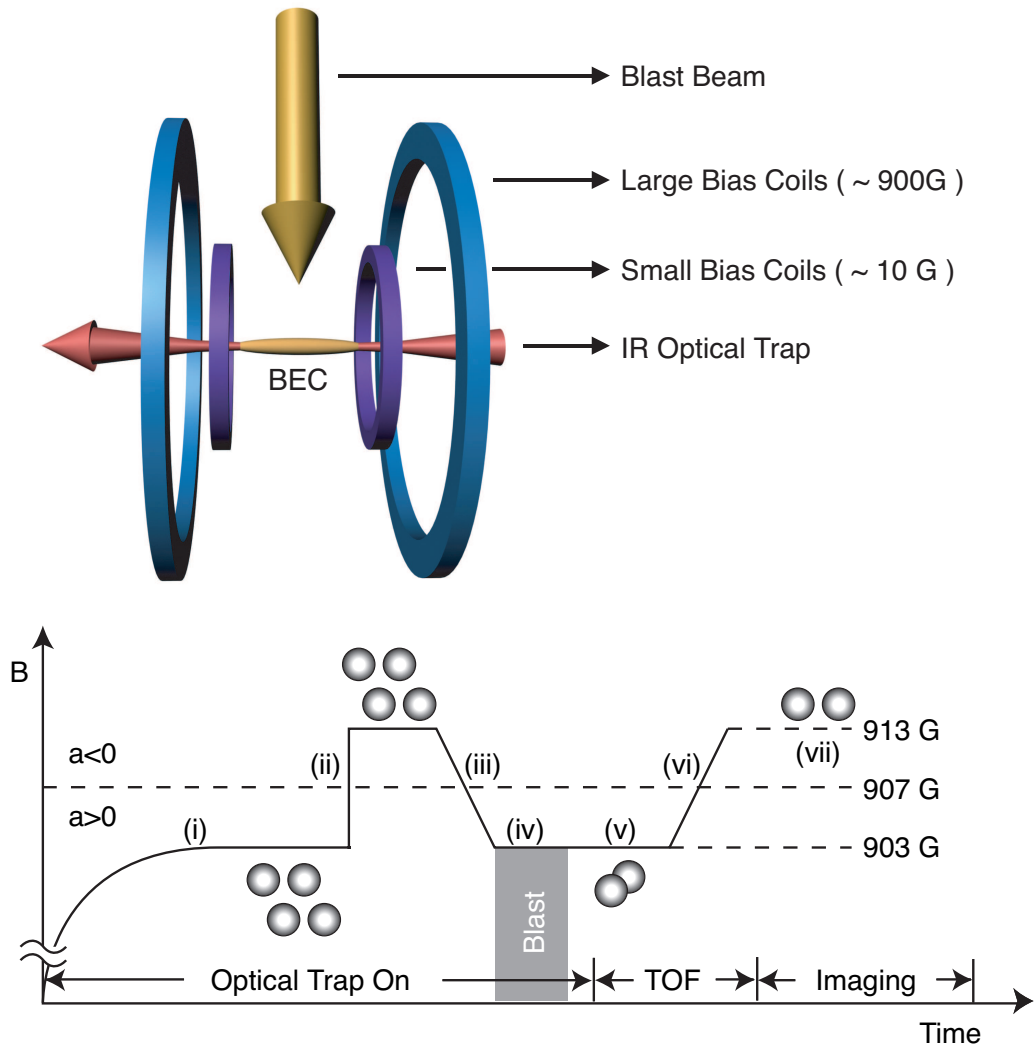


Figure 4-2: (Color) Optical trap and magnetic field coils: The large coils provide most of the magnetic field. They are ramped up during stage (i) and kept a constant level actively stabilized by a feedback servo. During (ii) through (vii), the small coils provide the fast field switch/ramp for jumping over the Feshbach resonance, ramping back down (creating molecules) and then ramping back up (dissociating and detecting molecules).

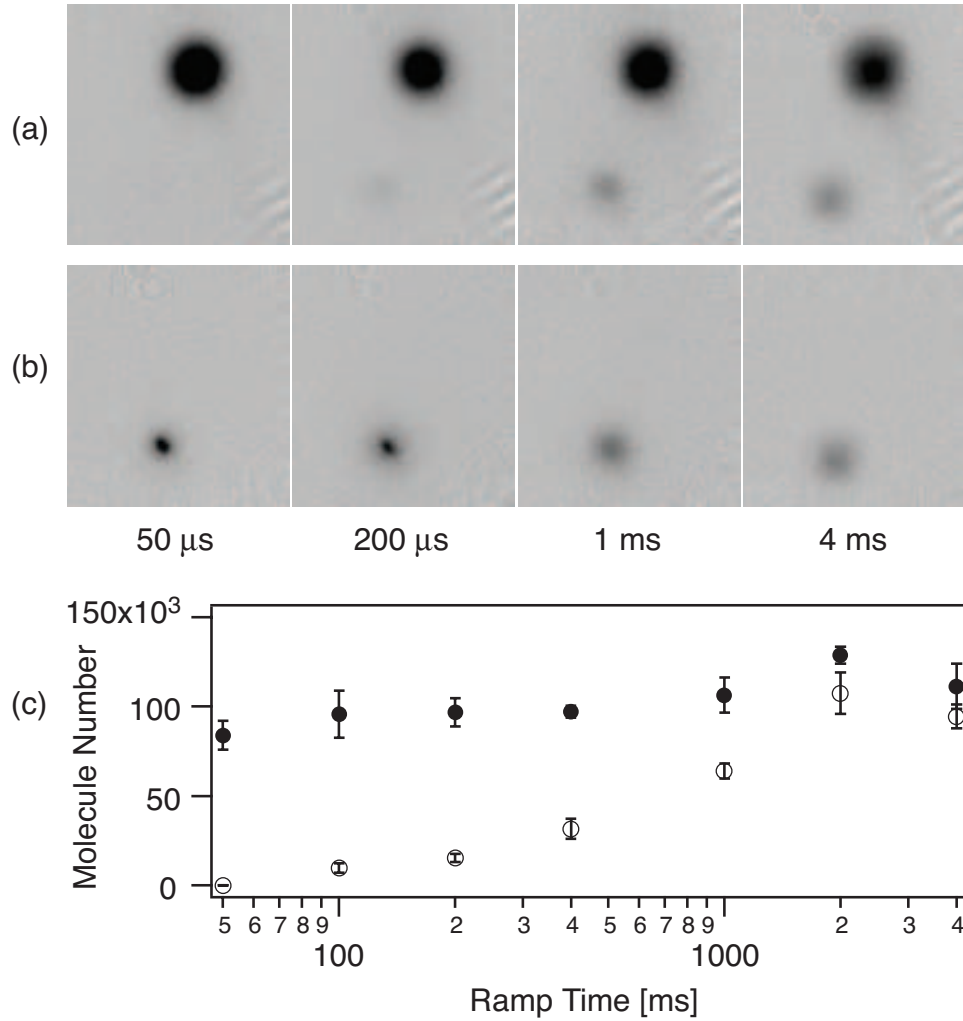


Figure 4-3: Molecule formation for various ramp speeds of magnetic field: During a given time, the magnetic field was ramped by 10 G. (a) and (b) are the absorption images taken after 14 ms time-of-flight. The molecules (bottom) were radially separated from the atoms (top) by a field gradient of 2.8 G/cm. (a) Without applying the “blast” pulse, the atoms remained in the trap. (b) With the “blast” pulse, the atoms were quickly removed after the field ramp. (c) Number of molecules as a function of ramp time for (a) (open circles) and (b) (closed circles).

density could be obtained by counting the molecules and calculating the peak density based on the trap geometry, in addition to fitting the time-of-flight images to obtain the momentum distribution (see details in [118]). Our analysis confirmed that the peak phase space density exceeded 20, which is significantly above the critical value of 2.6 for an ideal Bose gas.

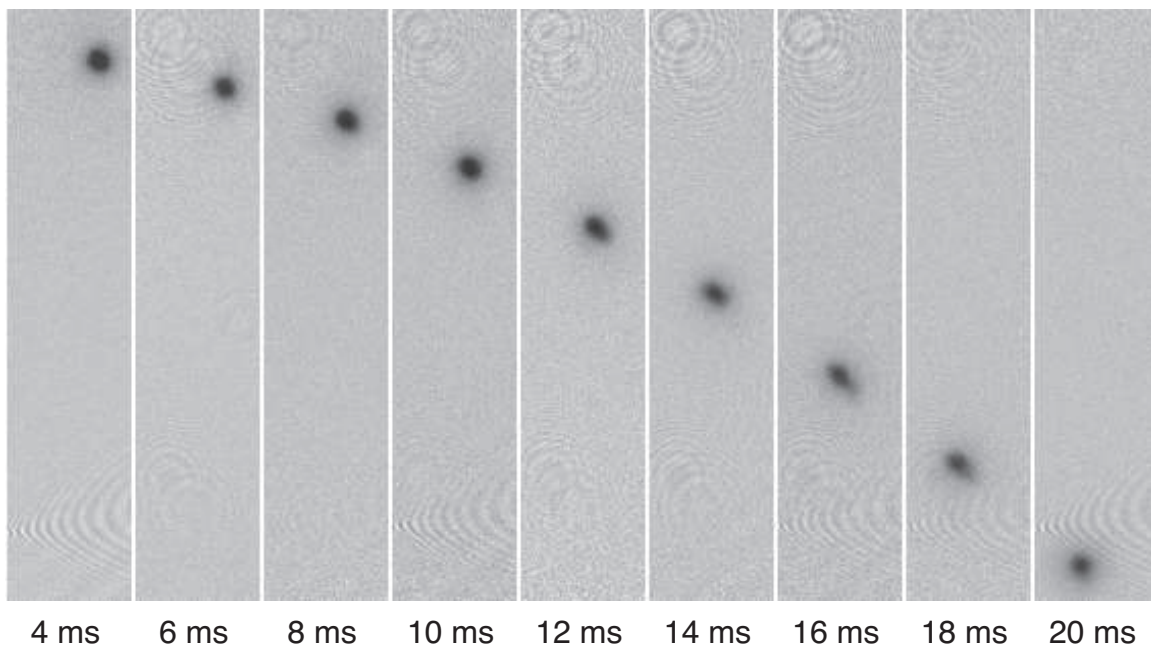


Figure 4-4: Ballistic expansion of a pure molecular cloud: These are the absorption images of molecular clouds (reconverted into free atoms) taken after various times of flight. The expansion velocity corresponds to a temperature of ~ 30 nK. The images were taken along the long weak axis of the optical dipole trap and the field of view is $3.0 \text{ mm} \times 0.7 \text{ mm}$.

Despite the high phase space density which indicated quantum degeneracy, we stopped short of calling these molecules “molecular BEC” because the high inelastic collision rate quickly heated the cloud in a few milliseconds even at a density less than $4 \times 10^{12} \text{ cm}^{-3}$, as shown in Fig. 4-5. This lifetime is much shorter than the axial trap frequency of the optical trap, making it impossible to reach any (quasi) thermal equilibrium, which we believed to be a reasonable requirement for BEC. Somewhat later, molecular BEC’s were realized in ultracold Fermi gases [119, 120, 121]. The ${}^6\text{Li}_2$ BEC exhibited remarkably long lifetimes near the broad Feshbach resonance

[119, 121], which was attributed to Fermi statistics [122]. In $^{40}\text{K}_2$ [120], however, the “BEC” was produced in a few milliseconds and only radial equilibrium could be achieved, which was similar to our situation. A notable difference is that for Fermi clouds, the ramp speed of the magnetic field could not have been as short as $50 \mu\text{s}$ as the initial atomic cloud had at most unity phase space density. For an atomic BEC, the molecules simply inherit the initial zero center-of-mass motion of the atom pairs.

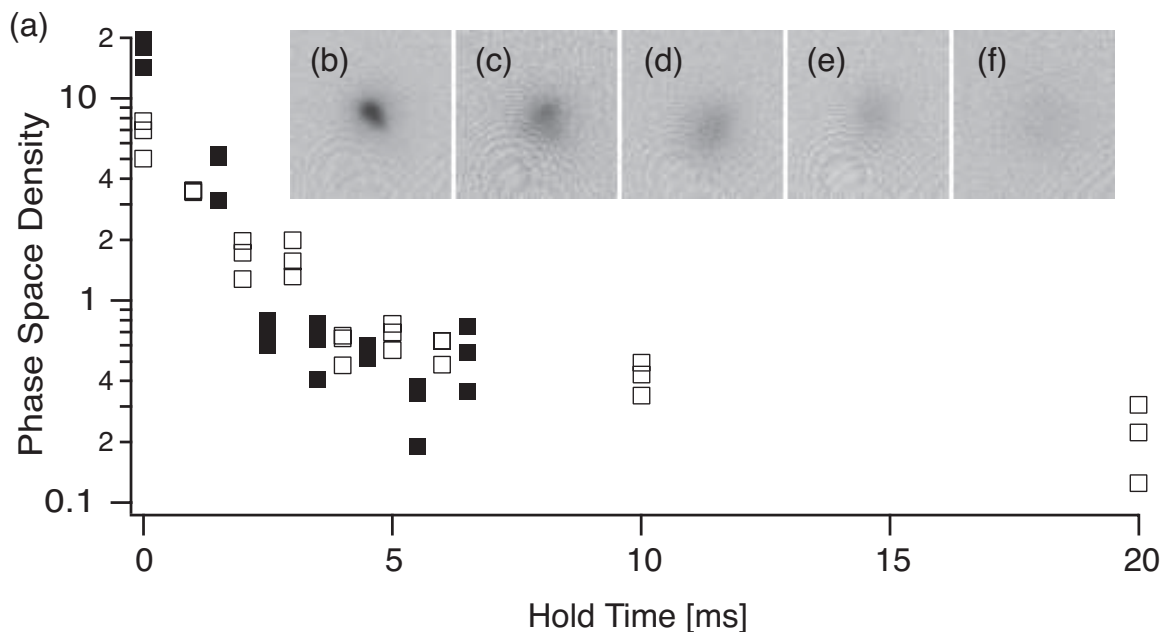


Figure 4-5: Molecular phase space density vs. hold time: (a) The phase space densities of the molecules decreases significantly after a few milliseconds holding in the optical trap. (b - c) are the absorption images of the molecular clouds after (b) 0 ms, (c) 2 ms, (d) 5 ms, (e) 10 ms, (f) 20 ms hold time in the trap. The field of view is $0.8 \text{ mm} \times 0.8 \text{ mm}$.

4.4 Molecule dissociation

If after the molecule formation and the removal of the remnant atoms, we immediately dissociate the molecules with a reverse field ramp before the time of flight, the added dissociation energy will appear in addition to the initial kinetic energy of the molecules. Intuitively, the dissociation rate is proportional to the atom-molecule coupling strength $|\langle c|W|b \rangle|^2$ in Eq. (4.3). For a given coupling strength, the faster

the ramp speed of the magnetic field, the deeper the quasi-bound state would move into the continuum before the molecules were fully dissociated. Therefore the (mean) dissociation energy as a function of the ramp speed can be a direct measure of the atom-molecule coupling strength.

4.4.1 Fermi's golden rule

More specifically, for the s -wave molecular state involved in the Feshbach resonance, the coupling is predominantly to the s -wave unbound states. In the low momentum limit, the coupling strength:

$$|\langle c|W|b\rangle|^2 = \frac{4\pi\hbar^2\Delta\mu}{MV} a_s^{(\text{bg})} \Delta B \quad (4.4)$$

is essentially a constant proportional to the Frank-Condon factor between the bound state and the zero momentum (threshold) state.

The dissociation rate is given by the Fermi's golden rule [71]:

$$\Gamma_{\text{diss}} = D(\epsilon) |\langle c|W|b\rangle|^2 \quad (4.5)$$

$$D(\epsilon) = \frac{V}{(2\pi)^2} \left(\frac{M}{\hbar^2}\right)^{3/2} \epsilon^{1/2} \quad (4.6)$$

where $D(\epsilon)$ is the density of states at the kinetic energy ϵ *in the center-of-mass frame*, corresponding to atom pairs with kinetic energy $\epsilon/2$ in the lab frame.

Let $m(\epsilon)$ be the molecular population which is unity at $\epsilon = 0$ (at the continuum threshold). As the magnetic field is ramped up and ϵ increases at the rate $\Delta\mu|\dot{B}|$, the molecules dissociate into atoms at a rate given by (4.5):

$$\begin{aligned} \frac{dm(\epsilon)}{d\epsilon} &= -\frac{dm(\epsilon)}{dt} (d\epsilon/dt)^{-1} = -\frac{\Gamma_{\text{diss}}m(\epsilon)}{\Delta\mu|\dot{B}|} \\ &= -C\epsilon^{1/2}m(\epsilon) \\ C &= \frac{2a_s^{(\text{bg})}\Delta B}{\hbar|\dot{B}|} \sqrt{\frac{M}{\hbar^2}} \end{aligned} \quad (4.7)$$

which can be solved for $m(\epsilon)$:

$$m(\epsilon) = e^{-\frac{2}{3}C\epsilon^{3/2}} \quad (4.8)$$

Finally, the mean dissociation energy is given by:

$$\delta E = \int_0^\infty \frac{\epsilon}{2} [-dm(\epsilon)] = 0.591 \left(\sqrt{\frac{\hbar^2}{M}} \frac{\hbar |\dot{B}|}{2a_s^{(\text{bg})} \Delta B} \right)^{2/3} \quad (4.9)$$

Note that Eq. (4.9) shows that the dissociation is proportional to the 2/3-power of the field ramp speed $|\dot{B}|$, and the proportionality constant contains no other free parameters aside from $a_s^{(\text{bg})} \Delta B$. Fig. (4-6) shows our data, from which we obtained a fit value of $a_s^{(\text{bg})} \Delta B = 3.64$ G nm. The know theoretical calculations agreed with our measurement to within 10 % [123, 124].

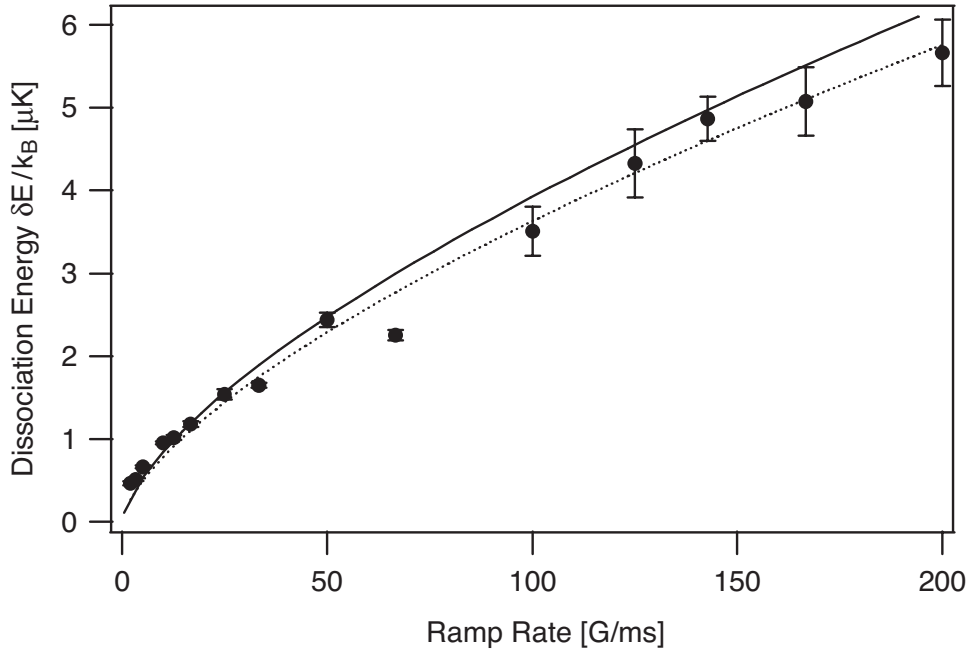


Figure 4-6: Dissociation energy for different ramp speeds for ^{23}Na dimers: The solid line corresponds to the (slightly larger) theory value of $a_s^{(\text{bg})} \Delta B$ for $\Delta B = 0.98$ G and $a_s^{(\text{bg})} = 3.4$ nm [123, 124]. The dotted line is a fit curve with the fitting parameter $a_s^{(\text{bg})} \Delta B = 3.64$ G nm.

Shortly after the publication of our result, Rempe group in Germany performed the same measurement of Feshbach resonance widths for ^{87}Rb [125]. Their measurement

was done more carefully for resonances as narrow as 1 mG, as shown in Fig. 4-7 and Table 4.1. It is worth noting that the field stability for their experiment is 4 mG (which is in fact excellent for such high magnetic fields), so any static method would not have the resolution to resolve the narrow Feshbach resonances. In contrast, the dynamic method based on molecule dissociation maps the resonance width into a large kinetic energy spread, which corresponds to a large magnetic field range where the molecules dissociate. This is somewhat analogous to the situation of large Δk Bragg spectroscopy discussed in Section 3.1.

B_{res} (G)	ΔB_{fit} (mG)	ΔB_{th} (mG)
632	1.3(2)	1.5
685	6.2(6)	17
912	1.3(2)	1.3
1007	210(20)	170(30)

Table 4.1: Position B_{res} and width ΔB of the Feshbach resonances for ^{87}Rb : ΔB_{fit} is the best-fit value obtained from the measurement in Fig. 4-7. ΔB_{th} is the theoretical prediction from Ref. [117]. This Table is taken from [125].

4.4.2 Shape resonance

For narrow resonances such as in ^{87}Rb , it is possible to ramp the magnetic field fast enough across the resonance (without significant dissociation in the process) to a particular value of ϵ and measure the dissociation rate of the molecules at that particular point in the continuum. This is demonstrated in the ring-shaped dissociated cloud in [125].

However as mentioned earlier, for s -wave molecules, the dissociation rate is almost independent of ϵ [Eq. (4.4)] as the quasi-bound state couples mostly to the s -wave free states which is almost uniform in short distances. The situation changes for rotating molecules [126, 127] which can couple strongly to the d, g, i, \dots -waves (p, f, h, \dots -waves are prohibited due to bosonic symmetry). As illustrated in Fig. 4-8, the centrifugal barrier gives rise to quasi-bound d, g, i, \dots -waves that have large amplitudes in short distances. When the molecular state is tuned near these quasi-bound waves,

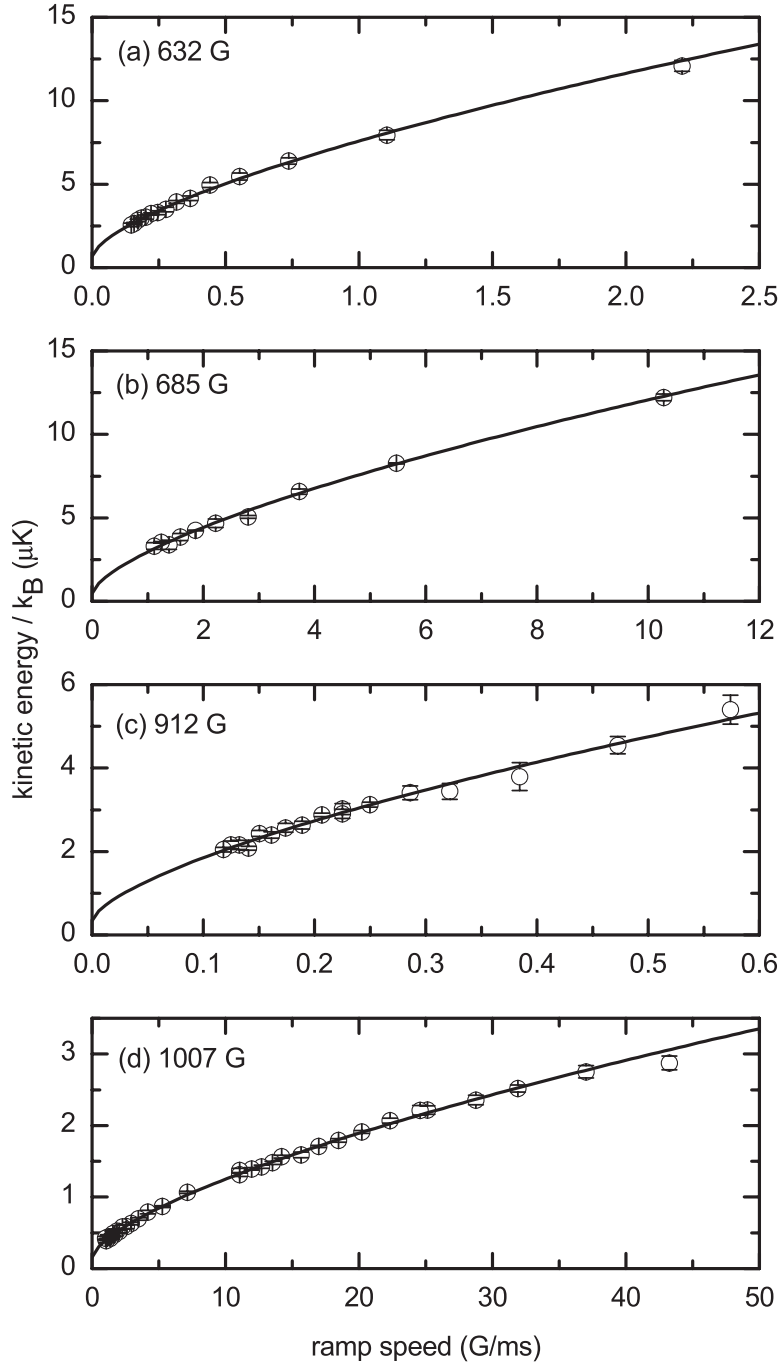


Figure 4-7: Dissociation energy for different ramp speeds for ^{87}Rb dimers: The four Feshbach resonances of ^{87}Rb are much narrower than the one we measured for ^{23}Na , and could not have been measured accurately with static methods. This figure is taken from [125].

the dissociation rate is enhanced and no longer uniform. Such phenomenon is called a *shape resonance* and was observed in ^{87}Rb [127].

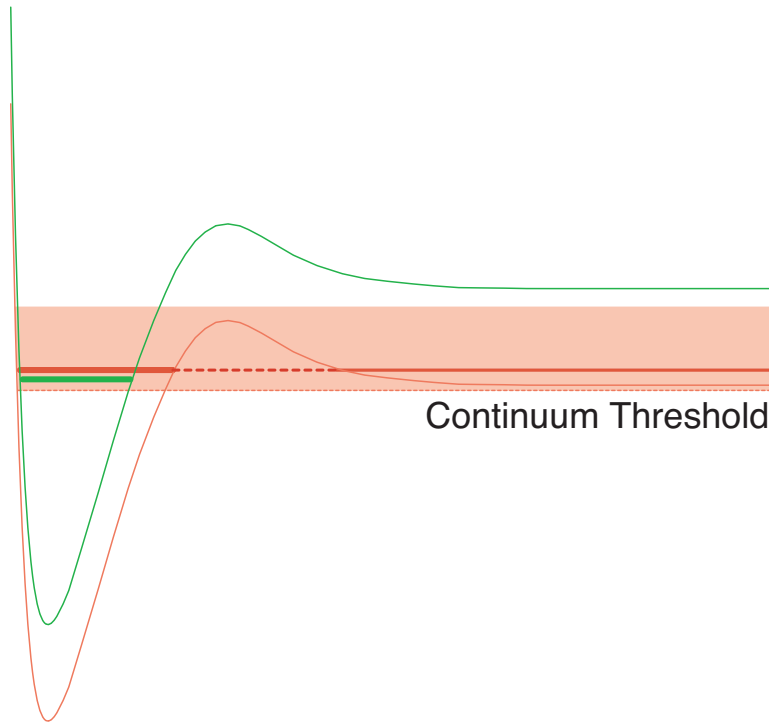


Figure 4-8: (Color) Magnetic shape resonance: The two-body potential includes the centrifugal part due to the finite angular momentum. A quasi-bound state has stronger overlap with the bound state in short distances than the other continuum states, resulting in a stronger decay rate when the bound state is tuned close to the quasi-bound state. For the purpose of illustration, the potentials are not drawn to actual scale.

Chapter 5

Bose-Einstein condensates in optical lattices

This chapter discusses two experiments with condensates in optical lattices:

- K. Xu, Y. Liu, J.R. Abo-Shaeer, T. Mukaiyama, J.K. Chin, D.E. Miller, and W. Ketterle, *Sodium Bose-Einstein condensates in an optical lattice*, Phys. Rev. A **72**, 043604 (2005). Included in Appendix E.
- K. Xu, Y. Liu, D.E. Miller, J.K. Chin, W. Setiawan, and W. Ketterle, *Observation of Strong Quantum Depletion in a Gaseous Bose-Einstein Condensate*, preprint: *cond-mat/0601184* (submitted to Phys. Rev. Lett). Included in Appendix F.

In recent years, optical lattices have become an important tool in the study of strongly correlated systems with ultracold atomic gases. The interference of two far-detuned laser beams forms a periodic optical potential called *optical lattice*. Simply by changing the lattice beam intensity, one can vary the interaction strength as well as the tunneling rate. In addition, the well-developed band theory for condensed matter systems is readily applicable to BEC in an optical lattice, providing powerful tools for theoretical investigations.

Earlier experiments usually involved a one dimensional optical lattice and observing the time-of-flight interference pattern and the collective motion of the condensate

along the direction of the lattice beam. The single-particle band structure was manifest as an enhanced effective mass for small velocities [128, 129] and Bloch oscillation for larger velocities [130]. For a very deep lattice, some evidence of number squeezing due to the atomic interaction was observed [59]. Somewhat later, two and three dimensional lattices were applied which led to the discoveries of more interesting states. The quantum phase transition from a superfluid state to a Mott-insulator was first observed in a ^{87}Rb condensate [131, 60]. Massive entanglement was achieved via controlled coherent collision in a Mott-insulator [61]. Tonk-Girardeau regime was explored in one dimensional quantum gases confined in a two dimensional lattice [62, 63, 132, 133]. The inelastic collision loss of Feshbach molecules (see Chapter 4) could be suppressed in a Mott-insulator, enabling the study of coherent molecule formation and dissociation [64, 65, 66]. As described in this Chapter, we recently studied the quantum depletion in an optical lattice, mapping out the intermediate regime between gaseous BECs and quantum fluids such as superfluid liquid helium [67].

I start this chapter with a review of some useful results from the band structure theory relevant to understanding most of the experiments involving ultracold atoms in an optical lattice. I then proceed to discussing the two published results, mainly focusing on a few subtleties not fully discussed in the papers. The rest of this Chapter is devoted to a detailed account of the technical issues encountered in setting up the optical lattice and the ways in which we worked around them. This is intended as a future reference for posterity in the lab.

5.1 Bosons in lattice potential

To avoid confusion, *d-dimensional lattice* refers to having d (orthogonal) standing waves with the other $(3 - d)$ dimensions free of lattice beams ($d = 1, 2, \text{ or } 3$). This should be differentiated from a *d-dimensional gas* in an optical lattice which is usually achieved by having $(3 - d)$ very deep lattices to “freeze out” $(3 - d)$ degrees of freedom. For simplicity, all lattice beams are assumed to have the same wavelength λ_L and to

be orthogonal with respect to each other.

5.1.1 Bose-Hubbard model

Including the lattice potential $U_L(\mathbf{x})$, the Hamiltonian (2.1) now reads:

$$H = \sum_{i=0}^N h_i + \frac{1}{2} \sum_{i,j=1}^N U(\mathbf{x}_i - \mathbf{x}_j) \quad (5.1)$$

$$h = -\frac{\hbar^2}{2M} \nabla^2 + U_L(\mathbf{x}) (+U_{ex}(\mathbf{x})) \quad (5.2)$$

where U_{ex} is other slow-varying potentials such as the atom trap. $U_L(\mathbf{x})$ has a spatial periodicity of $a_L = \lambda_L/2$ in each dimension with a pair of lattice beams present.

A natural unit for energies is the photon recoil energy defined as:

$$E_R = \frac{\hbar^2 k_L^2}{2M} \quad (5.3)$$

$$\begin{aligned} k_L &= \frac{2\pi}{\lambda_L} \\ &= \frac{\pi}{a_L} \end{aligned} \quad (5.4)$$

The single particle Hamiltonian h (without U_{ex}) is invariant under translation of a_L in the lattice direction – say \hat{z} :

$$U_{L,z}(z) = \frac{u_L}{2} E_R (1 - \cos 2k_L z) \quad (5.5)$$

where u_L is the lattice depth measure in units of E_R . It follows from Bloch theorem that the eigenstates of h can be chosen to have definite quasi-momenta \mathbf{q} and form a band structure:

$$\phi_{q,n}(\mathbf{x} + a_L \hat{z}) = e^{iq a_L} \phi_{q,n}(\mathbf{x}) \quad (5.6)$$

$\phi_{q,n}(\mathbf{x})$ is called the Bloch function and $n = 0, 1, 2, \dots$ labels the different energy bands in increasing order. Since $\exp\left[i\left(\frac{2\pi}{a_L}\right)a_L\right] = 1$, physically distinct q should span a range no more than $2k_L$. Typically this range is defined as $[-k_L, +k_L)$ – called the first *Brillouin zone*. k_L defines a natural unit for quasi-momenta.

Once again I choose to work with a quantization volume V with periodic boundary conditions:

$$V = (a_L N_L)^d L^{3-d} \quad (5.7)$$

where the lengths along the d lattice dimensions are chosen to be integer multiples of a_L and N_L is the number of lattice sites along each lattice dimension.

It is useful to develop an intuitive feel for how the band structure should look like. Fig. 5-1 shows the band structures for various lattice depths. The free particle case ($u_L = 0$) is simply obtained from the quadratic kinetic energy:

$$\begin{aligned} E_{q,n_j} &= E_R \left(2j + \frac{q}{k_L} \right)^2 \\ j &= 0, \pm 1, \pm 2, \dots \\ n_j &= \begin{cases} 2|j| - 1 & \text{if } qj > 0 \text{ or } q = 0, j > 0 \\ 2|j| & \text{if } j = 0 \text{ or } qj < 0 \text{ or } q = 0, j < 0 \end{cases} \end{aligned} \quad (5.8)$$

where E_{q,n_j} is the eigenenergy corresponding to the n_j th band at quasi-momentum q . The Bloch functions in this case are simply the plane waves $|\phi_{q,n_j}\rangle = |2jk_L + q\rangle$.

At finite lattice depths, U_L couples only the plane waves at the same quasi-momentum. In fact, due to its sinusoidal form (5.5), the only non-zero matrix elements due to U_L are:

$$\langle 2jk_L + q | U_L | 2jk_L + q \rangle = \frac{u_L}{2} \quad (5.9)$$

$$\langle 2(j+1)k_L + q | U_L | 2jk_L + q \rangle = -\frac{u_L}{4} \quad (5.10)$$

Gaps open up near the center and the edges of the Brillouin zone where different bands meet, causing avoided crossings. The deeper the lattice, the flatter the bands. In the limit of completely flat bands (zero tunneling, see discussion below), the bands are separated by the local harmonic trap frequency at each lattice site.

In some cases, it is more convenient to work with a different set of orthonormal

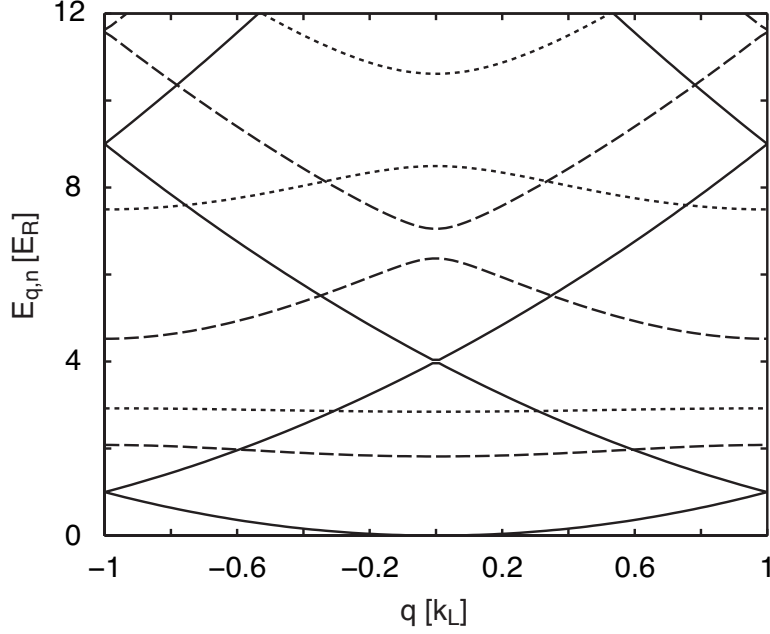


Figure 5-1: Band structure of an optical lattice: The first few energy bands for $0 E_R$ (solid lines), $5 E_R$ (dashed lines), $10 E_R$ (dotted lines).

basis called *Wannier functions* [134]:

$$w_{s,n}(\mathbf{x}) = \frac{1}{\sqrt{N_L}} \sum_q \phi_{q,n}(\mathbf{x}) e^{-isa_L q} \quad (5.11)$$

$w_{s,n}$ are localized wavepackets at the s th lattice site ($s = 0, \pm 1, \pm 2, \dots, \pm N_L/2$) and have identical forms except a spatial offset:

$$w_{s,n}(\mathbf{x} + sa_L \hat{z}) = w_{0,n}(\mathbf{x}) = w_n(\mathbf{x}) \quad (5.12)$$

In the limit of very deep lattices, $w_{s,n}$ approach the wavefunctions of a harmonic oscillator – for the typical experimental conditions, however, $w_{s,n}$ are more delocalized.

The Bloch states can be expanded in $w_{s,n}$ basis:

$$\phi_{q,n}(\mathbf{x}) = \frac{1}{\sqrt{N_L}} \sum_q w_{s,n}(\mathbf{x}) e^{isa_L q} \quad (5.13)$$

Adopting the second quantization notations, (5.1) can be rewritten as:

$$\begin{aligned}
H &= \sum_{s_1, n_1, s_2, n_2} \langle s_2, n_2 | h | s_1, n_1 \rangle a_{s_2, n_2}^\dagger a_{s_1, n_1} \\
&= +\frac{1}{2} \sum_{\substack{s_1, n_1, s_2, n_2 \\ s_3, n_3, s_4, n_4}} \langle s_3, n_3, s_4, n_4 | U | s_1, n_1, s_2, n_2 \rangle a_{s_4, n_4}^\dagger a_{s_3, n_3}^\dagger a_{s_1, n_1} a_{s_2, n_2} \quad (5.14)
\end{aligned}$$

$|s, n\rangle$ refers to $w_{s, n}$. Note that because of (5.12), we have:

$$\begin{aligned}
\langle s, n | h | s, n \rangle &= \int_V d\mathbf{x} w_n^*(\mathbf{x}) h w_n(\mathbf{x}) \\
&= \epsilon_n \quad (5.15)
\end{aligned}$$

$$\begin{aligned}
\langle s + \Delta s, n | h | s, n \rangle &= \int_V d\mathbf{x} w_n^*(\mathbf{x} + \Delta s a_L \hat{z}) h w_n(\mathbf{x}) \\
&= -J_n(\Delta s) \quad (5.16)
\end{aligned}$$

$$\begin{aligned}
\langle s, n, s, n | U | s, n, s, n \rangle &= g \int_V d\mathbf{x} |w_n(\mathbf{x})|^4 \\
&= U_n \quad (5.17)
\end{aligned}$$

We call ϵ_n the offset energy, $J_n(\Delta s)$ the tunneling rate between sites separated by Δs sites, and U_n the onsite interaction energy – for the n th band.

The typical temperature in the BEC experiments is much lower than the gap between the lowest band and the first excited band $\epsilon_1 - \epsilon_0$. Therefore one can retain in (5.14) only the terms involving the lowest band ($n = 0$). Due to the localized nature of the Wannier functions, the tunneling rate $J_0(\Delta s)$ between non-adjacent sites for a lattice of a few E_R deep is much smaller compared with that between adjacent sites (see Fig. 5-2). Therefore, one can keep only the tunneling rate between nearest neighbors $J_0 = J_0(\pm 1)$. Finally, because of the small spatial overlap between the Wannier functions, one can ignore the interaction terms $\langle s_3, 0, s_4, 0 | U | s_1, 0, s_2, 0 \rangle$ where s_i 's are not the same. The resulted approximate Hamiltonian is called the *Bose-Hubbard* model [135, 136, 137, 131]:

$$H = -J \sum_{|s-s'|=1} a_{s'}^\dagger a_s + \frac{1}{2} U \sum_s \hat{n}_s (\hat{n}_s - 1) \quad (5.18)$$

where $\hat{n}_s = a_s^\dagger a_s$ and we have dropped the subscript 0 from J_0 and U_0 .

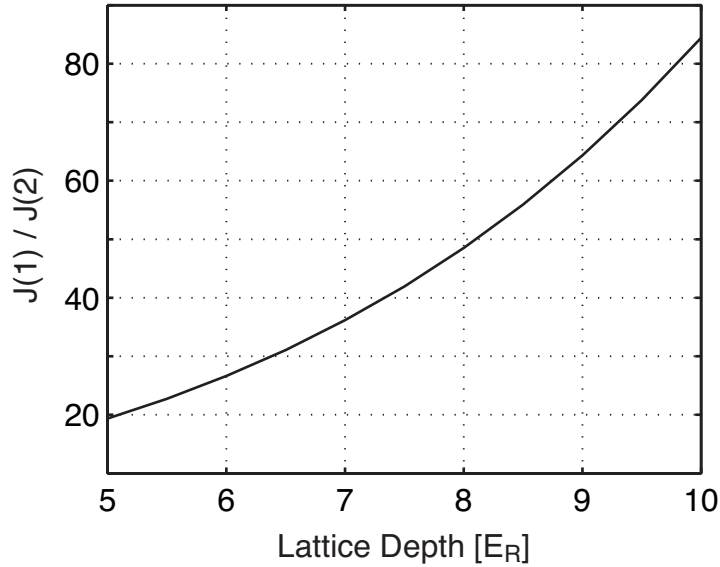


Figure 5-2: Tunneling ratio: The ratio between $J_0(1)$ (nearest neighbors) and $J_0(2)$ (next nearest neighbors) is plotted as a function of the lattice depth. For lattice depths greater than $5 E_R$, the tunneling between nearest neighbors essentially determines the dispersion curve (see discussion in Section 5.1.3).

Finally, if there is an external trapping potential [U_{ex} Eq. (5.2)], an extra term:

$$H_{ex} = \sum_s \epsilon_{ex} \hat{n}_s \quad (5.19)$$

$$\epsilon_{ex} = \int_V d\mathbf{x} w_0^*(\mathbf{x}) U_{ex}(\mathbf{x}) w_0(\mathbf{x}) \quad (5.20)$$

should be added to (5.18).

5.1.2 Shallow lattice

For a shallow lattice ($u_L \lesssim 1$), the Bloch states can be calculated by treating the lattice potential as a perturbation. In particular, for the lowest band $\phi_q(\mathbf{x}) = \phi_{q,0}(\mathbf{x})$,

only three plane waves $|q\rangle, |q + 2k_L\rangle, |q - 2k_L\rangle$ need to be considered:

$$h = \begin{pmatrix} \bar{q}^2 & -\frac{u_L}{4} & -\frac{u_L}{4} \\ -\frac{u_L}{4} & (\bar{q} - 2)^2 & 0 \\ -\frac{u_L}{4} & 0 & (\bar{q} + 2)^2 \end{pmatrix} \quad (5.21)$$

where $\bar{q} = q/k_L$ is the dimensionless quasi-momentum and we have dropped the common diagonal term $u_L/2$ in (5.9).

In terms of the Hamiltonian (2.2), the presence of the lattice has two effects, namely flattening the dispersion relation $T(\mathbf{p})$ and increasing the interaction strength $\lambda(\Delta\mathbf{p})$ (in the lattice, p becomes the quasi-momentum q). In the shallow lattice limit where the population concentrate at the bottom of the lowest band, the change in dispersion relation can be captured by the effective mass M^* :

$$M^* = \hbar^2 \left[\frac{\partial^2}{\partial q^2} T(q) \right]^{-1} \quad (5.22)$$

and the effective interaction strength $\lambda(\Delta\mathbf{p})$ is approximately constant (in s -wave scattering limit):

$$\lambda^* = g \int_V d\mathbf{x} |\phi_0(\mathbf{x})|^4 \quad (5.23)$$

By diagonalizing the matrix (5.21) near $q = 0$, we can get closed form solution for M and λ in a d -dimensional lattice:

$$M^* = M \left[1 - 8 \frac{\sqrt{4 + \frac{u_L^2}{8}} - 2}{\sqrt{4 + \frac{u_L^2}{8}} \left(\sqrt{4 + \frac{u_L^2}{8}} - 2 \right)} \right]^{-1} \quad (5.24)$$

$$\lambda^* = \frac{g}{V} \left[1 + \frac{2\alpha^2(4 + \alpha^2)}{(1 + 2\alpha^2)^2} \right]^d \quad (5.25)$$

$$\alpha = \frac{u_L}{4 \left(4 + \frac{u_L^2}{8} \right)}$$

Eqs. (5.24) and (5.25) work fairly well for lattice depths up to $\sim 5 E_R$. Fig. 5-3 plots the above approximate formulas in comparison with the exact band calculations for

a three dimensional lattice ($d = 3$).

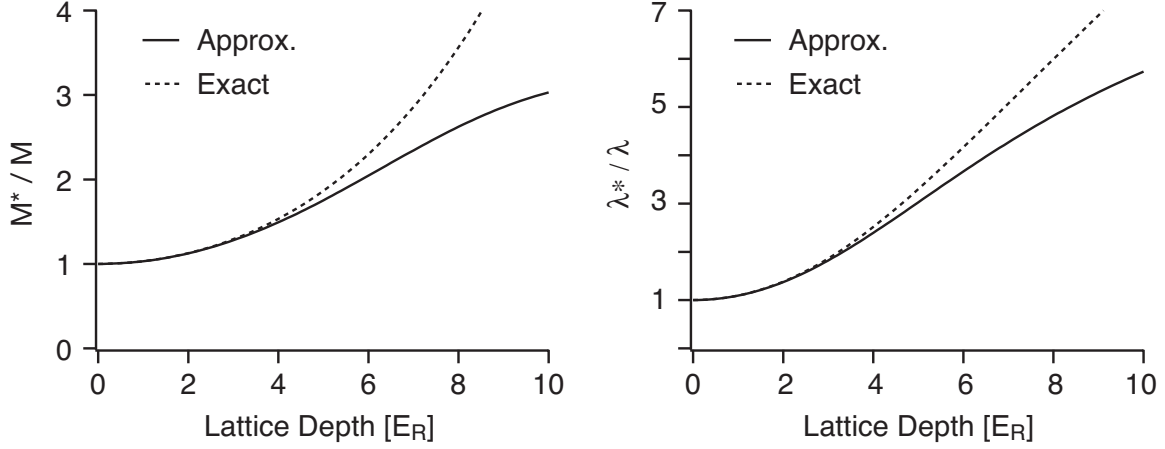


Figure 5-3: Effective mass and interaction: The approximate formulas are accurate up to $\sim 5 E_R$. The band structure calculations were done numerically with 20 plane waves.

5.1.3 Deep lattice

In the deep lattice regime ($\gtrsim 5 E_R$), the single particle part of Bose-Hubbard Hamiltonian (5.18) has the tridiagonal form:

$$\langle s' | h | s \rangle = -J(\delta_{s,s'+1} + \delta_{s,s'-1}) \quad (5.26)$$

where δ_i, j is the Kronecker delta. Therefore the eigenenergy E_q corresponding to the Bloch function $\phi_q(\mathbf{x})$ has a closed form:

$$E_q = -2J \cos(qa_L) \quad (5.27)$$

It immediately follows that the width of the lowest energy band (in each lattice direction) ΔE_0 is directly proportional to the tunneling rate J :

$$\Delta E_0 = 4J \quad (5.28)$$

and the effective mass M^* (at zero quasi-momentum) is inversely proportional to J :

$$M^* = \frac{\hbar^2}{2a_L^2} J^{-1} \quad (5.29)$$

It should be noted that these closed form solutions exist because we have ignored the tunneling beyond the nearest neighbors. The agreement of (5.27) with the exact shape of the lowest band provides a test for whether this approximation is justified.

Fig. 5-4 shows such a comparison.

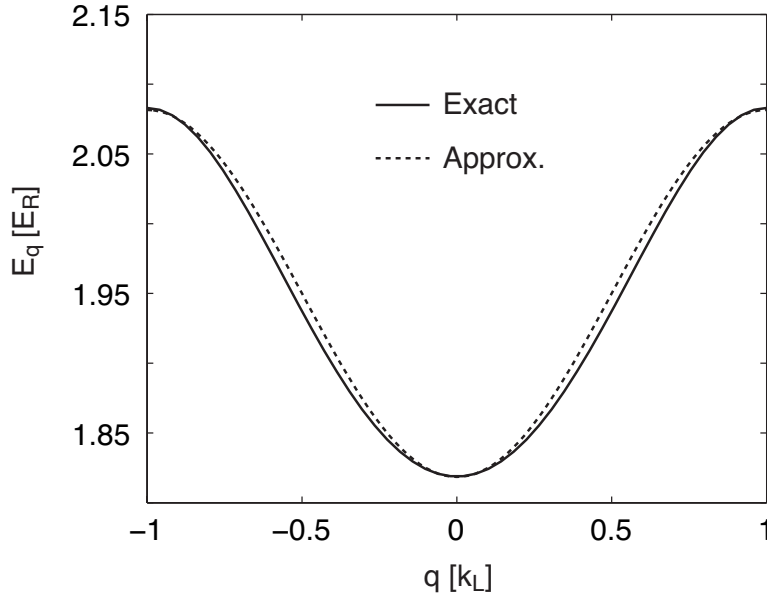


Figure 5-4: The lowest band in deep lattice regime: At $5 E_R$, $J = 0.0658 E_R$ and the approximate formula (5.27) is close to the exact solution. A constant is added to account for the omitted energy offset $\epsilon_0 = 1.95 E_R$ in (5.15).

5.1.4 Mott-insulator transition

As discussed above, for lattice depths greater than $5 E_R$, the Bose-Hubbard model (5.18) is a good approximation and the system dynamics is determined by two parameters – tunneling rate J and on-site interaction U , which are both functions of the lattice depth u_L . The results of J and U from the band structure calculation are plotted in Fig. 5-5 for ^{23}Na in a three dimensional lattice using 1064 nm laser.

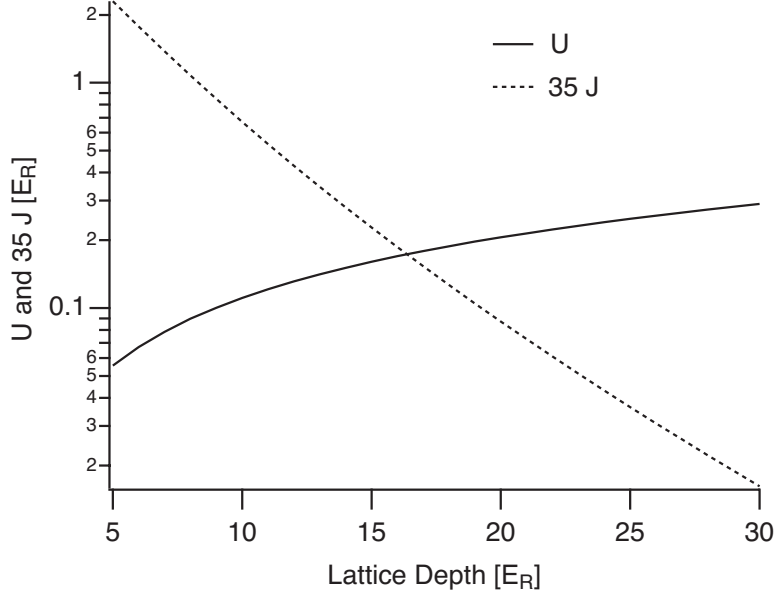


Figure 5-5: U and J as functions of lattice depth: J is rescaled by a factor of 35, so that at the crossing point of J and U , the corresponding lattice depth gives the critical value for Mott-insulator transition in a three dimensional optical lattice at unit filling $n = 1$ (see discussion in text). In the natural unit E_R , J is independent of atomic mass and wavelength, whereas U is proportional to a_s/λ_L [Eq. 5.53]. Here U is calculated for ^{23}Na using $a_s = 2.75$ nm and $\lambda_L = 1064$ nm. The exponential suppression of J causes the critical depth u_L^* to depend weakly on the scattering length and occupancy number n . In this case, $u_L^* = 16.3, 18.5, 20.0, 21.2, 22.1, 22.9, 23.6$ for $n = 1, 2, 3, 4, 5, 6, 7$ respectively.

Since both J and U are positive real numbers, it immediately follows from the Bose-Hubbard model that in order to minimize the energy, the “tunneling terms” ($\propto J$) tend to delocalize the atoms to create coherence between neighboring sites $\langle a_{s+1}^\dagger a_s \rangle$, whereas the “interaction terms” ($\propto U$) tend to localize the atoms and decrease the coherence ¹. A more detailed meanfield study predicts a *quantum phase transition* from a superfluid state (delocalized) to a Mott-insulator state [135, 136, 137, 131], at the transition point:

$$\left(\frac{U}{J}\right)_c = 2d \left[2n + 1 + 2\sqrt{n(n+1)} \right] \quad (5.30)$$

where $2d$ represents the number of nearest neighbors in a d -dimensional optical lattice, and n denotes the number of atoms per lattice site.

From Fig. 5-5, J decreases exponentially as the lattice depth u_L increases :

$$J \sim e^{-0.3u_L} \quad (5.31)$$

while U increases roughly linearly with u_L for *three dimensional lattice* [see Eq. (5.54) in Section 5.6]:

$$U \sim 1.33 + 0.7u_L \quad (5.32)$$

The Mott-insulator transition occurs for the lattice depth where the two curves cross, roughly $16.3 E_R$ for ^{23}Na in a 1064 nm three dimensional lattice at unit filling ($n = 1$). Note that while U depends linearly on the scattering length a_s , a factor of 2 increase in a_s only reduces the critical depth by roughly $2 E_R$. This is because of the exponentially fast suppression of J . Therefore, unless one can change the scattering length by a large factor (for example, near a Feshbach resonance), the quantum phase transition occurs around the same lattice depth between 10 to $20 E_R$. For the same reason, the linear dependence of the critical U/J in Eq. (5.30) on the occupancy number per lattice site n only changes the critical lattice depth by a few E_R .

It should be pointed out that a perfectly localized Mott-insulator state can only

¹For a given total number of atoms, the minimal interaction energy is achieved for commensurate fillings.

be achieved for commensurate filling of integer n if there is no other external potential U_{ex} present. This is illustrated in Fig. 5-6(a) where there is one extra atom after every site is occupied by an atom. Since all the states $|\cdots, n_{s-1} = 1, n_s = 2, n_{s+1} = 1, \cdots\rangle$ ($s = 1, 2, \cdots$) are degenerate and coupled by the tunneling matrix element J , the ground state cannot be the perfectly localized situation. With a smooth trap however – “smooth” means the energy offset due to the trap between adjacent lattice sites is small compared to U – the atoms can distribute into shells of Mott-insulator at different filling factors as in Fig. 5-6(b) [138].

5.2 Experimental Setup

The basic configurations for both the dye laser lattice and the IR lattice were the same on the BEC machine side. Fig. 5-7 illustrates the positions of the various beams relative to the condensate. All laser beams were transported through optical fibers from another laser table, and actively stabilized to computer generated reference signals through feedback servos. The optics setup before the fibers and the servo components are illustrated in Fig. 5-15 in Section 5.5.

In our experiments, the condensates were loaded from the magnetic trap into the nearly spherical crossed optical dipole trap in about a second. The atoms were held in a tight optical trap for varied amount of time to control the final atom number through three body collisions. The optical trap was then decompressed to the final trap frequencies, which were chosen such that the intraband excitation was minimized during the lattice ramping (see Section 5.5.5). A vertical magnetic field gradient was applied to compensate for gravity and eliminate sagging in the weak optical trap. The condensate had negligible thermal fraction as the evaporation continued in the optical trap for a few seconds.

The lattice ramping sequence of both the optical trap and the lattice beams was controlled by programming the functional form of the computer analog outputs that were used as the reference signals to servo the optical powers. The feedback servos for the lattice beams allowed for a ramping time constant $\tau_{\text{ramp}} \sim 1$ ms.

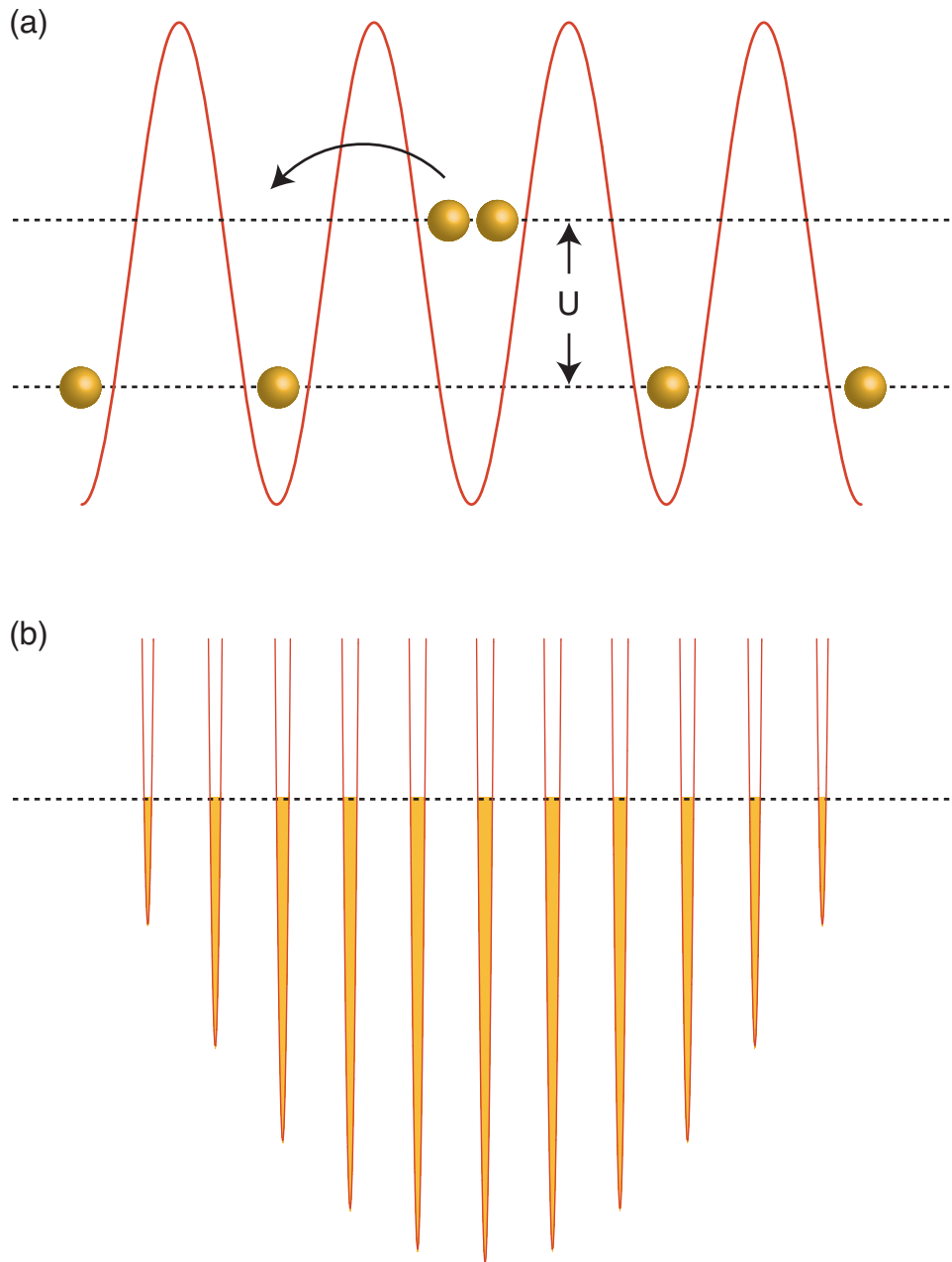


Figure 5-6: (Color) Incommensurate filling in a homogenous optical lattice: (a) The extra atom is free to hop to any lattice site without changing the energy of the system. (b) With a smooth trapping potential, atoms could distribute such that each lattice site is filled up to a constant chemical potential, resulting in a Thomas-Fermi profile in the case of a harmonic trap. Figures are for illustration purposes and not drawn to scale.

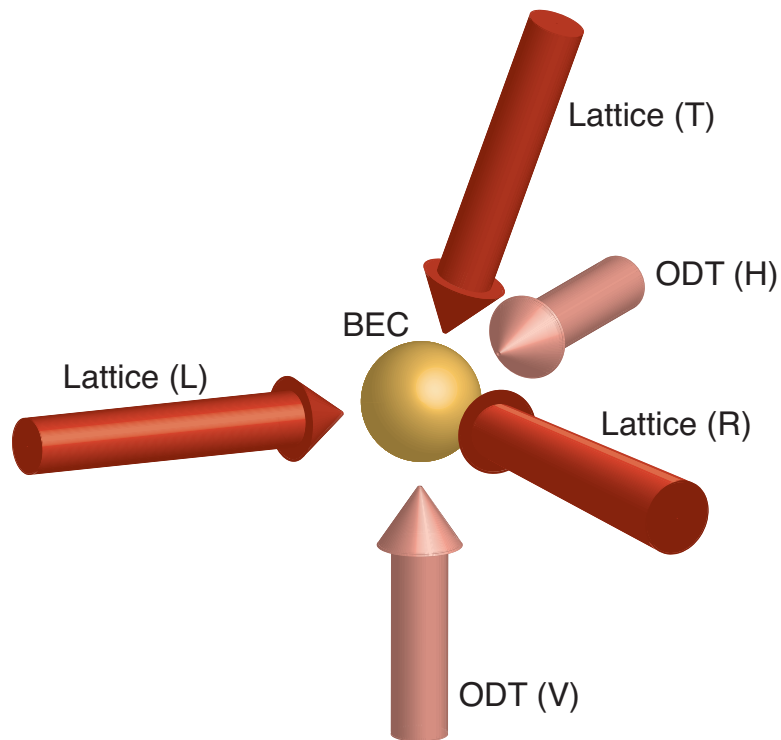


Figure 5-7: (Color) Optical dipole trap (ODT) and lattice beams setup: Three lattice beams – Left (L), Right (R) and Top (T) are retro-reflected to form standing waves. Two ODT beams – Horizontal (H) and Vertical (V) are crossed to form a round trap.

5.3 Yellow lattice and photoassociative resonances

Our first optical lattice using a red-detuned dye laser eventually proved barely good enough to observe the superfluid-to-Mott insulator transition, with a lattice ramp sequence of a few milliseconds [139]. During the ramp-up and ramp-down of the lattice, we observed the disappearance and re-emergence of the interference pattern in time-of-flight, as shown in Fig. 5-8. The heating of the system out of the ground state during the lattice ramping process could be characterized by the fraction of atoms outside the condensate at the end of the ramp sequence, and turned out to be $\sim 20\%$ for the parameters of our experiment.

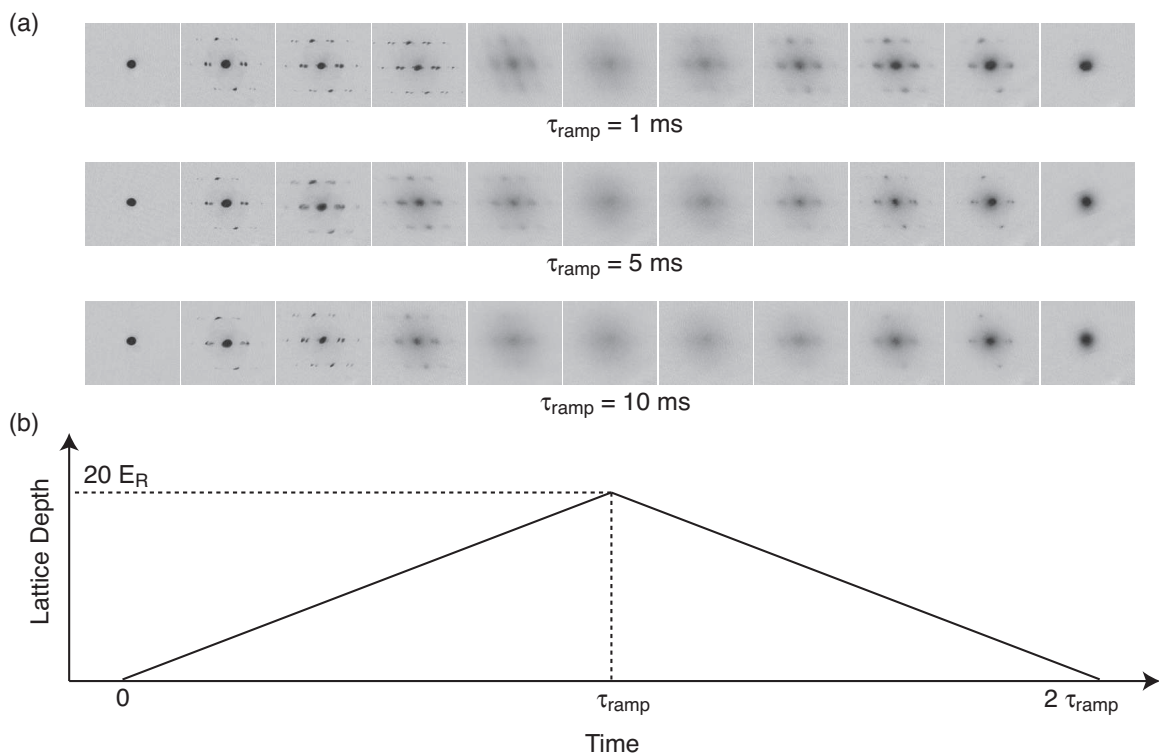


Figure 5-8: Interference patterns in time-of-flight from a three dimensional lattice: (a) The images from left to right are for lattice depths 0, 4, 8, 12, 16, 20, 16, 12, 8, 4, 0 E_R . The time of flight is 7 ms and the field of view is $1000 \mu\text{m} \times 1200 \mu\text{m}$. The peak occupancy here is around 5, which means the Mott-insulator transition should occur between 14 and 20 E_R . (b) The lattice depth is ramped linearly.

The spontaneous scattering ($\sim 20 \text{ s}^{-1}$) and the three-body collision loss ($\sim 16 \text{ s}^{-1}$) placed severe limits on the duration of the experiment. The three-body loss could be

reduced by lowering the total number of atoms, although at the time we were limited by our imaging and atom counting resolutions – we failed to observe a reproducible signal in our attempt to create Feshbach molecules at low atom numbers (so as to have two atoms per lattice site). The time limit also precluded other more conclusive diagnostic techniques such as the gap measurement [60, 140, 141] or radio-frequency spectroscopy [142, 143].

In the process of optimizing our yellow (reddish orange to be exact) lattice, we stumbled upon some lattice wavelengths near which large atom losses were observed. One of such loss features is shown in Fig. 5-9. With some theoretical help from NIST scientists Kevin Jones and Eite Tiesinga, we confirmed these losses were due to single-photon photoassociations. A sequence of previously unobserved resonance peaks due to $(1)^1\Sigma_g^+$ state were identified. Detailed discussion can be found in [139].

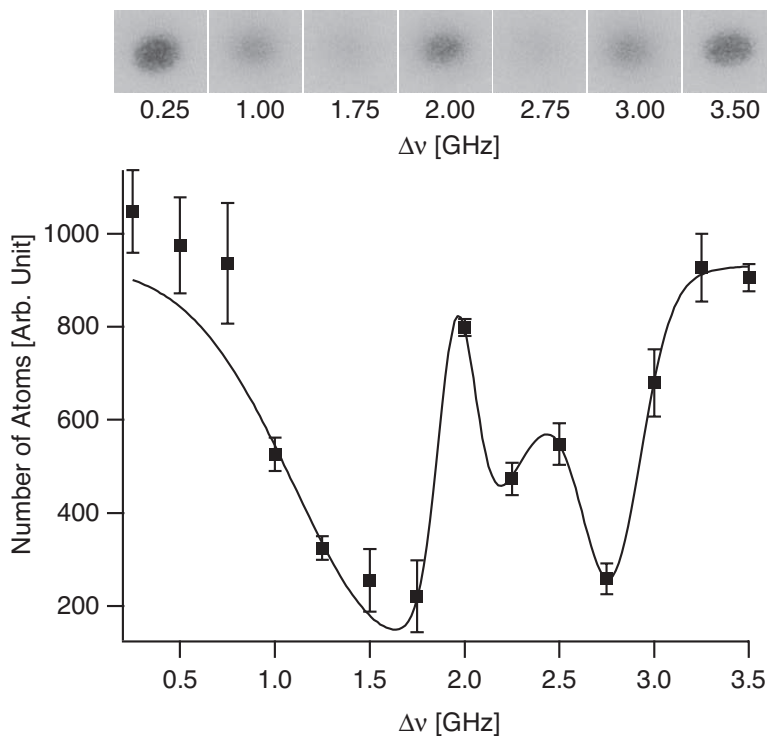


Figure 5-9: Atoms loss due to photoassociation resonance: The top row shows the remaining atom cloud after the lattice was ramped up in 1 ms to peak intensity 280 W/cm^2 in each beam and then ramped down in 1 ms. The zero of the frequency axis corresponds to lattice wavelength 594.490 nm as measured by a wavemeter accurate $\sim 1 \text{ GHz}$.

5.4 Enhanced quantum depletion

Shortly after Wolfgang was awarded the 2001 Nobel prize in physics for the discovery of gaseous BEC, Laszlo Tisza gave a commemorating talk at the Center for Ultracold Atoms entitled “The History of the Two-Fluid Concept and a New Look at the Bose-Einstein Condensation”. It was a popular talk without much technical depth, by someone who was in the thick of things when the first understandings of superfluid helium were developed. For me, there were two things from the talk that stood out. First is the difficulty of understanding the role of Bose-Einstein condensation in the superfluidity of a strongly interacting system such as liquid helium. This is one of the main reasons why gaseous BEC has garnered such widespread interest across the condensed matter physics community. Second is the distinction Tisza emphasized between *superfluid fraction* and *condensate fraction*. Superfluid fraction is related to finite temperature and typically approaches unity in a superfluid as the temperature decreases to absolute zero. Condensate fraction is related to interaction and can be (significantly) less than unity even at zero temperature. In general condensate fraction is not directly correlated with the superfluid fraction. One extreme (as mentioned in Chapter 1) is the absence of superfluidity but unity condensate fraction for an ideal gas of bosons at zero temperature. In the case of superfluid helium, the opposite is true – at low enough temperature, He II fraction approaches unity while the condensate fraction is only about 10 % [54, 70].

Gaseous BECs of alkali atoms are superfluid which has been demonstrated theoretically [80] and experimentally [87, 88, 89, 144, 145, 146]. The thermal (non-superfluid) fraction for the typical experiments can be made extremely small. Due to the weak interaction, the quantum depleted (non-condensate) fraction is also small. Therefore, people often use the terms “condensate” and “superfluid” interchangeably, which may have prompted Tisza’s comment on their distinction. In principle, the quantum depletion for gaseous condensates can be increased by increasing the atomic density, but three body recombination dramatically reduces the lifetime for density above 10^{15} cm^{-3} [147]. In our recent work, we showed that the intermediate regime between

quantum gases (low quantum depletion) and He II (high quantum depletion) could be reached in an optical lattice.

5.4.1 Quantum depletion in a BEC

The quantum depleted fraction in a weakly interacting condensate can be calculated within the Bogoliubov theory developed in Chapter 2. In particular, from the Bogoliubov transformation [inverse of Eqs. (2.52) and (2.53)] and the ground state wavefunction [Eq. (2.55)], the population in momentum state $|\mathbf{p}\rangle$ turns out to be:

$$v_{\mathbf{p}}^2 = \frac{T(\mathbf{p}) + \mu - \sqrt{T^2(\mathbf{p}) + 2\mu T(\mathbf{p})}}{2\sqrt{T^2(\mathbf{p}) + 2\mu T(\mathbf{p})}} \quad (5.33)$$

Note that $v_{\mathbf{p}}^2$ increases as the meanfield energy μ increases, or as the kinetic energy $T(\mathbf{p})$ decreases – in the limit of $T(\mathbf{p}) \rightarrow 0^+$, $v_{\mathbf{p}}^2$ diverges as:

$$v_{\mathbf{p}}^2 \sim \frac{1}{\sqrt{T(\mathbf{p})}} \quad (5.34)$$

and in the limit of $T(\mathbf{p}) \rightarrow \infty$, $v_{\mathbf{p}}^2$ approaches zero:

$$v_{\mathbf{p}}^2 \sim \frac{1}{T^2(\mathbf{p})} \quad (5.35)$$

The total quantum depleted fraction is given by:

$$N_{qd} = \frac{V}{(2\pi\hbar)^3} \int_V d\mathbf{p} v_{\mathbf{p}}^2 \quad (5.36)$$

5.4.2 BEC in free space

In free space, the kinetic energy and meanfield energy are given by:

$$T(\mathbf{p}) = \frac{p^2}{2M} \quad (5.37)$$

$$\begin{aligned} \mu &= \frac{4\pi\hbar^2 a_s}{M} \rho \\ &= Mc_s^2 \end{aligned} \quad (5.38)$$

Eq. (5.36) becomes:

$$N_{qd} = \frac{V}{(2\pi)^3} \left(\frac{Mc_s}{\hbar} \right)^3 \int_0^\infty d\hat{p} (4\pi\hat{p}^2) \frac{1 + \frac{\hat{p}^2}{2} - \sqrt{\hat{p}^2 + \frac{\hat{p}^4}{4}}}{2\sqrt{\hat{p}^2 + \frac{\hat{p}^4}{4}}} \quad (5.39)$$

$$\begin{aligned} &= \frac{V}{(2\pi)^3} (4\pi a_s \rho)^{3/2} \frac{8\pi}{3} \\ &= 1.505 \sqrt{\rho a_s^3} N \end{aligned} \quad (5.40)$$

where $\hat{p} = p/(Mc_s)$ is the momentum measured in the natural unit $p_s = Mc_s$, $\rho = N/V$ is the atomic density.

Fig. 5-10 plots the integrand in (5.39) – quantum depletion density function vs. dimensionless momentum \hat{p} . Due to the diminishing density of states near zero momentum, the quantum depletion density is actually peaked around p_s which makes physical sense. The total quantum depleted fraction is $1.505\sqrt{\rho a_s^3}$, where:

$$\Theta = \rho a_s^3 \quad (5.41)$$

is the *diluteness factor* that characterizes the density and interaction strength of the condensate. For gaseous condensates, Θ is normally quite small which leads to negligible quantum depletion. ^{23}Na BEC at the typical density of 10^{14} cm^{-3} , for instance, has a quantum depletion of merely 0.2 %.

5.4.3 BEC in an optical lattice

As discussed in Sections 5.1.2 and 5.1.3, the presence of an optical lattice effectively flattens the dispersion curve (kinetic energy) and increases the meanfield interaction. Therefore one expects to see enhanced quantum depletion.

For a shallow lattice, the change in the dispersion relation is captured by an increased effective mass M^* as in Eq. (5.22), while the increase in the meanfield is given by λ^* as in Eq. (5.23). The quantum depletion can be obtained from the free

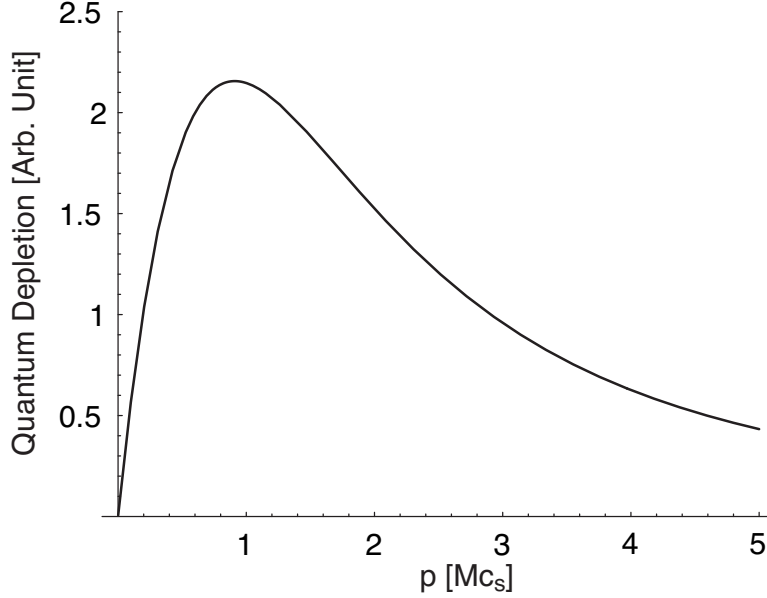


Figure 5-10: Quantum depletion density of a BEC in free space: The quantum depletion peaks around $p_s = Mc_s$ and mostly distributes at momenta $\gtrsim p_s$ (greater than 80 %).

space case (5.40) with the scattering length replaced by an effective one:

$$a_s^* = \left(\frac{\lambda^* M^*}{g/V} \right) a_s \quad (5.42)$$

Fig. 5-11 shows the results for two different per lattice site occupancy numbers $n = 1$ and $n = 7$ for ^{23}Na $|F = 1, m_F = -1\rangle$ condensate ($a_s = 2.75$ nm) in a three dimensional optical lattice of 1064 nm.

For a deep lattice, the quantum depletion starts to populate the entire first Brillouin zone, while the large gap between the lowest and the next excited bands prevents any significant population beyond the lowest band. In this case, the free space formula with an effective scattering length overestimates the quantum depletion as the *available states* for the free space result are not limited to the first Brillouin zone. In addition, the dispersion relation for a deep lattice ($u_L \gtrsim 5$) is sinusoidal as in Eq. (5.27). Therefore a single effective mass (at zero quasi-momentum) is insufficient to capture the shape of the entire first band. For lattice depths between 5 and 20 E_R ,

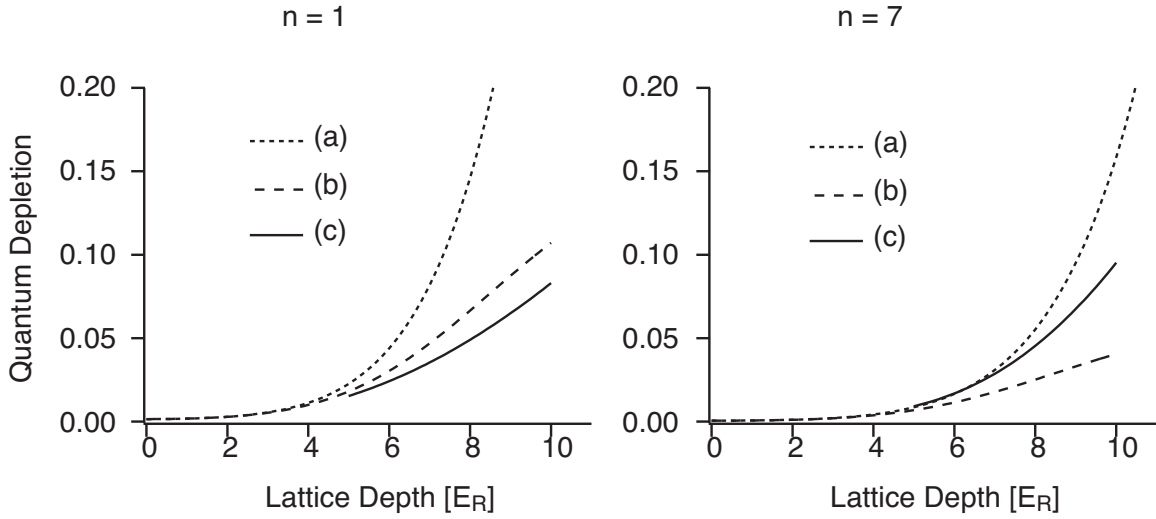


Figure 5-11: Quantum depletion for a BEC in a three dimensional optical lattice: Curves (a) and (b) are from the free space formula (5.40) using the effective scattering length defined in (5.42), where M^* and λ^* are obtained from (a) exact band structure calculation (b) perturbation calculation Eqs. (5.24) and (5.25). Curve (c) is the deep lattice calculation with only the first Brillouin zone populated by quantum depletion. In the regime where the first Brillouin zone is not saturated ($u_L \lesssim 5$), the perturbation result (b) is very close to the band structure calculation (a). All calculations are done for ^{23}Na BEC in $|F = 1, m_F = -1\rangle$ state and lattice wavelength 1064 nm.

we can numerically integrate Eq. (5.36) using:

$$T(\mathbf{q}) = 4J \sum_{i=1}^3 \sin^2 \left(\frac{q_i \lambda_L}{4} \right) \quad (5.43)$$

$$\mu = nU \quad (5.44)$$

and the result is also shown in Fig. 5-11 which connects smoothly with the shallow lattice results around $5 E_R$.

5.4.4 Quantum depletion in time-of-flight

For this experiment, we worked with an infra-red optical lattice at 1064 nm, where the heating due to the spontaneous light scattering was no longer an issue. Due to our limited atom counting resolution, the peak occupancy number was set to around $n = 7$, which corresponds to three body decay rate $\lesssim 6 \text{ s}^{-1}$. The lattice ramp time was set to $\tau_{\text{ramp}} = 50 \text{ ms}$. Fig. 5-12 shows the time-of-flight images after the lattice and optical trap are switched off (in $< 1 \mu\text{s}$) at various lattice depths.

We measured the quantum depletion directly from the absorption images taken in time-of-flight. This is incidentally another effect due to the optical lattice. For bare condensates in a harmonic trap, the quantum depletion (mostly in momentum states $p \gtrsim p_s$, see Fig. 5-10) is adiabatically reabsorbed into the condensate as the density decreases on the timescale of the trap period which is much longer than the inverse of the meanfield energy (times \hbar) in the typical Thomas-Fermi regime. In contrast, the optical lattice on-site trap frequency (for $u_L \gtrsim 5$) is much greater than the meanfield energy (“anti” Thomas-Fermi limit) and the time-of-flight image becomes a snapshot of the momentum distribution of the system at the switch-off of the lattice and trap potential.

To measure the quantum depletion, we used a “masked two dimensional gaussian fit” to extract the number of atoms outside the interference peaks in the time-of-flight images, an example of which is shown in Fig. 5-13. The measurement was done for one, two and three dimensional lattices, and the results are shown in Fig. 5-14. In a

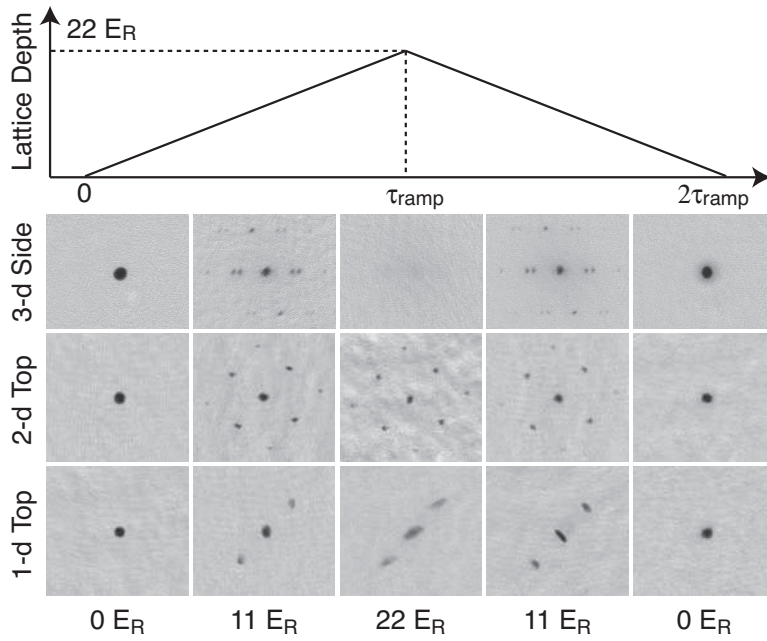


Figure 5-12: Time-of-flight images of atoms released from one, two and three dimensional lattices: The lattice depths for the sequence of images are, from left to right: 0, 11, 22, 11, 0 E_R . The time-of-flight is 10 ms; the field of view is $1075 \mu\text{m} \times 861 \mu\text{m}$ for the 3-d lattice imaged from the side, and $1185 \mu\text{m} \times 1079 \mu\text{m}$ for the 1-d and 2-d lattices imaged from the top. τ_{ramp} here is 50 ms.

three dimensional lattice, quantum depletion *in excess of 50 %* was observed. In one and two dimensional lattices, the dispersion relation is only flattened in the lattice beam directions:

$$T(\mathbf{q}) = 4J \sum_{i=1}^d \sin^2 \left(\frac{q_i \lambda_L}{4} \right) + \frac{4E_R}{\pi^2} \sum_{i=d}^3 \left(\frac{q_i \lambda_L}{4} \right)^2 \quad (5.45)$$

where dimensions 1 through d are assumed to have a lattice beam present. For the lattice depths in our experiment, the quantum depletion remains small for one and two dimensional lattices, consistent with our measurement.

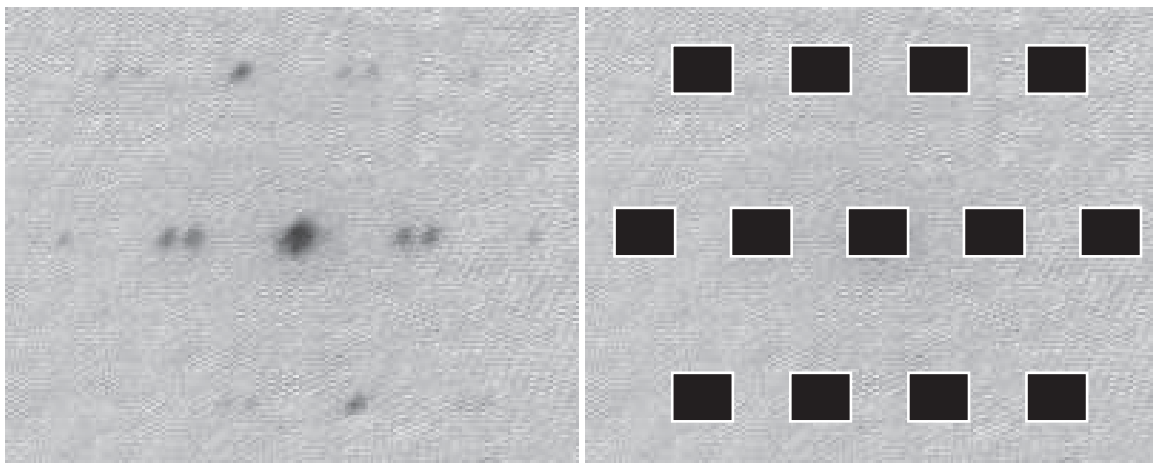


Figure 5-13: Masked gaussian fit to extract quantum depletion from time-of-flight images: In this example, the interference peaks (i.e. the zero quasi-momentum fraction) in the left image are masked off by small rectangles as in the right image, and then a two dimensional gaussian fit is used to extract the number of atoms outside the interference peaks which is taken as the quantum depletion (with a small heating correction [67]).

For three dimensional lattice, the superfluid to Mott-insulator transition is expected to occur at lattice depths between 16 to 24 E_R for occupancy numbers $n = 1$ to 7. The Mott-insulator fraction is also shown in Fig. 5-14 which shows a much steeper transition than the gradual increase of quantum depletion (see detailed discussion in [67]). For one and two dimensional lattices, we do not expect to observe a Mott-insulator transition at these lattice depths.

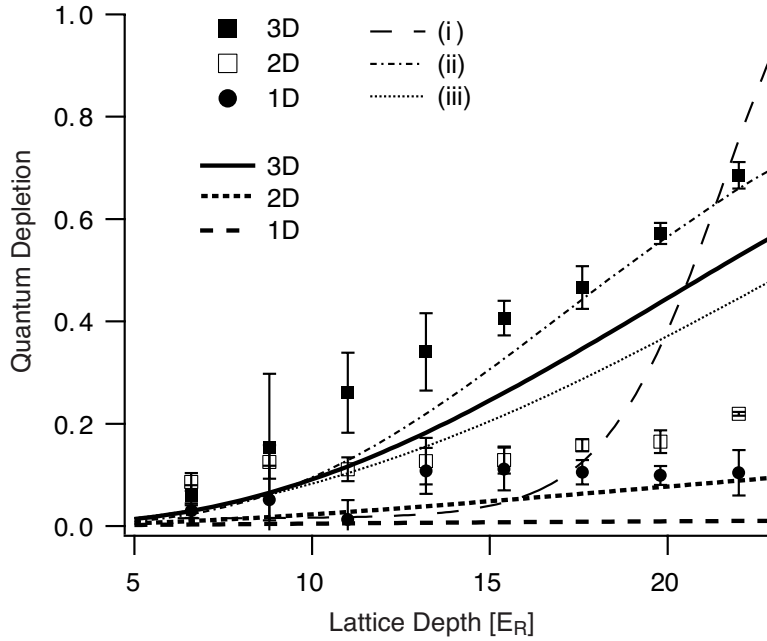


Figure 5-14: Quantum depletion of a BEC in a one, two and three dimensional optical lattice: the data points with statistical error bars are measured from the time-of-flight images. The three thick curves are the theoretical calculation using Bogoliubov theory and local density approximation assuming a Thomas-Fermi density profile for the condensate with peak occupancy number $n = 7$. For comparison, also shown are (thin curves): (i) the Mott-insulator fraction and (ii) quantum depletion for a *homogeneous* system of occupancy number $n = 1$ and (iii) $n = 7$. See detailed discussion in [67]

5.5 Lattice setup procedure

This section serves as a “working manual” for the setup and calibration of the optical lattice in our lab. The focus is on the IR lattice which shares the same basic configuration with the earlier dye laser lattice, but presents some additional difficulties due to the invisibility as well as the high power involved. While the “tricks” discussed are particular to our machine configuration, they may provide some useful hints for other situations.

5.5.1 Laser system and optics layout

The procedure for setting up an optical lattice is now fairly standard. Most of the existing setups use the same “tricks” discussed below. The main difficulty arises from the limited choices of lasers with appropriate wavelength and adequate power to form an optical lattice deep enough to achieve quantum phase transition. There are three factors to consider when choosing the lattice laser:

1. the laser must be sufficiently detuned from the atomic transition to limit the heating from spontaneous light scattering;
2. the laser must have enough power (at the given detuning) to reach the necessary lattice depth – this usually means exceeding the critical depth for the quantum phase transition;
3. the laser linewidth must be sufficiently narrow to achieve a stable interference pattern.

From the discussion in Section 5.1.4, Compared to heavier atoms like ^{87}Rb , the higher recoil energy for ^{23}Na requires higher *absolute* lattice depth to reach the critical point of the quantum phase transition. In addition, the optical AC stark shift is proportional to $(\omega_a^2 - \omega_L^2)^{-1}$ – ω_L is the laser frequency and ω_a the atomic transition frequency (rad/s). Commonly available IR options include 850 nm laser diode and 1064 nm Nd:YAG crystal laser. The atomic transition wavelength is 780 nm for ^{87}Rb

compared with 589 nm for ^{23}Na . Therefore ^{87}Rb requires about 10 times less power than ^{23}Na to achieve the critical lattice depth (about $14 E_R$ for ^{87}Rb) with a 1064 nm lattice laser. Laser diodes (tens of milliwatts) are sufficiently powerful for lattice experiments with ^{87}Rb ² but not for ^{23}Na without some kind of power amplifier.

The lack of single-frequency high power IR laser was the major reason for our initial attempt at using a dye laser several nanometers detuned to set up the optical lattice. Eventually, **IPG Photonics** was able to produce a high power IR laser based on a single frequency seed and a fiber amplifier (**Model: YAR-20K-1064-SF**), which outputs 20 W maximum CW power with a linewidth of ~ 100 kHz. In addition, IPG also provided us with a small amount of high-power single-mode optical fibers designed to work with such high powers. This IR laser system enabled us to obtain enough light from a single source for the three lattice beams and a crossed optical dipole trap (see below). Fig. 5-15 shows the optics table layout.

The *high power optical fiber* from IPG is a specially designed fiber that has a light conducting cladding. Normal single-mode fiber can only conduct light through the core and any light that leaks into the cladding escapes the fiber after a short distance. The IPG fiber cladding has a high index of refraction and acts as a multi-mode fiber for light leaked out of the fiber. This prevents local dissipation of very high laser power that leads to excessive heating. However, due to this property, we could not use the usual fiber alignment procedure of maximizing the output power (monitored with a photo diode) – one almost always gets > 95 % light through but most likely the light is being conducted through the cladding and the output shows the speckle pattern typical of a multi-mode fiber. The trick is to use some high index of refraction material to coat a section of the output end so as to “lead” the multi-mode light out of the fiber before it hits the end of the fiber and shows up on the photo diode.

To get more than 80 % of single-mode light through proved to be much more difficult, as expected. We followed a systematic procedure as the following:

1. The fiber has a specified $1/e^2$ beam waist $5.3 \mu\text{m}$ for perfect mode-matching

²Although diode lasers were used for some earlier experiments, Ti:Sapphire lasers are more commonly used to achieve deeper lattices.

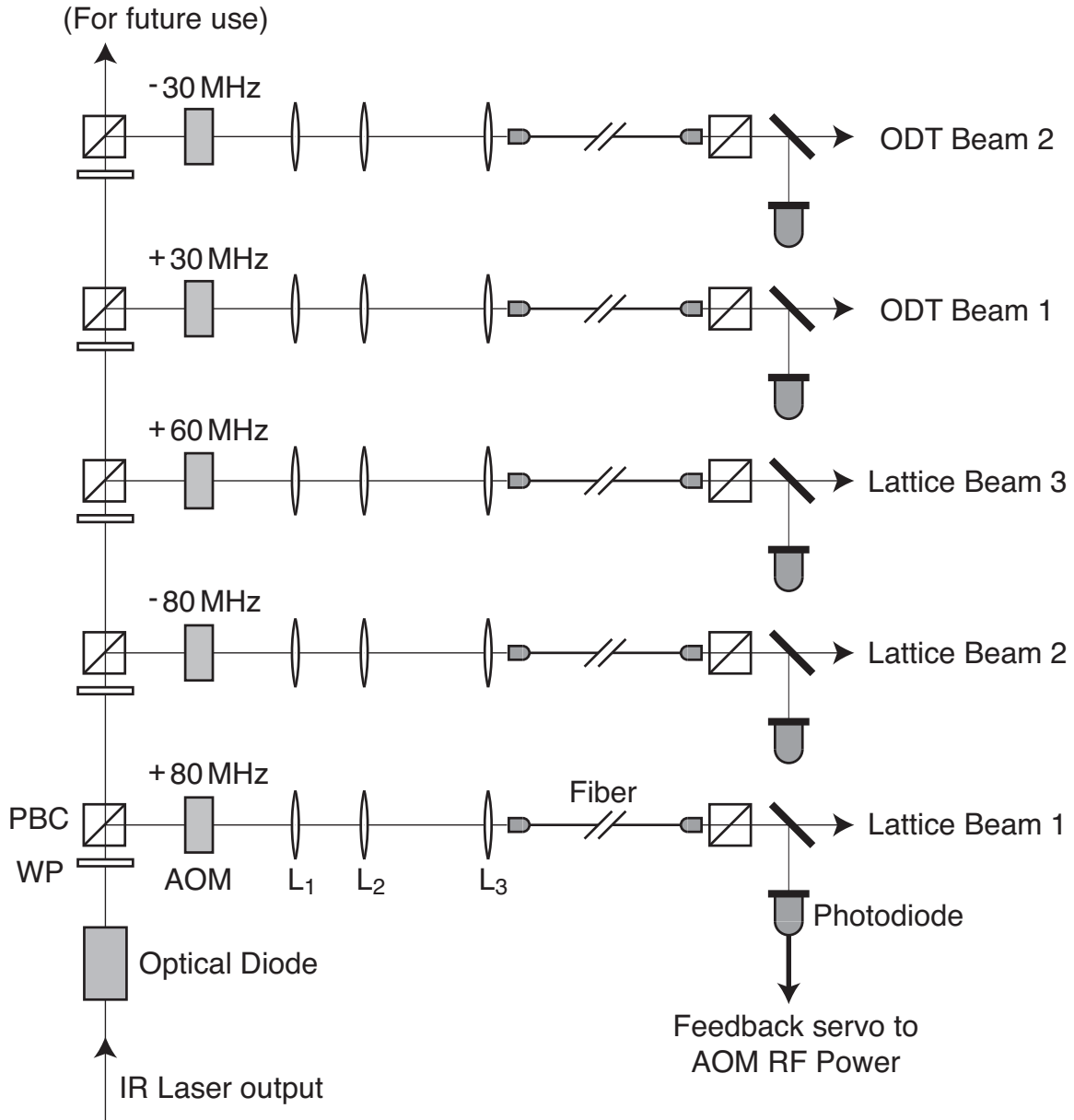


Figure 5-15: Optics table layout: The IR laser output is split into five beams with polarizing beam cubes (PBC) and half waveplates (WP). Three are for the optical lattice, and two for a crossed optical dipole trap. The acousto-optical modulators (AOM) shift the frequencies of the beams at least 20 MHz apart to eliminate cross interference between different beams. An optical diode (**Model: OFR 50-3-1064-VHP**) is used to prevent the back-reflected lattice light from damaging the IR laser. At the output of the fiber, a PBC is used to clean up the polarization after which a pick-off window sends a few percent of light to a photo diode to monitor the laser power. The photodiode signal is used for stabilizing the laser power to a reference level (typically generated by a computer analog output) through a proportional-integral (PI) feed back servo.

(independently checked with a beam profiler (**Model: BeamOn-VIS (USB2) CCD** from **Duma Photonics**). We can calculate the size of the collimated light entering the fiber coupler (**F230FC-C** from **Thorlabs** focal length 4.5 mm) needs to be 288 μm .

2. Using a two-lens telescope (L_1 and L_2 in Fig. 5-15), resize the beam into a *slightly diverging* size of somewhat smaller than 288 μm . It is important that the beam is approximately collimated but not exactly so that we can find the needed size 288 μm over a couple of centimeters.
3. Place the fiber output coupler near the spot where the beam size is correct, and add lens L_3 as close to the output coupler as possible. L_3 should be a long focal length convex lens to flatten the wave front of the beam at the desired size. This part requires swapping several lengths to find the best one. Despite the discrete selections of focal length, we were able to mode match quite well and obtain nearly 90 % of single mode light through the fiber.

In addition, the fiber tips are angle-cleaved instead of polished. The surface of a cleaved fiber tip looks mirror-like under the microscope, and is necessary for achieving high coupling efficiency. We used a popular version of cleaver **York FK12**. Cleaved fiber tips must be handled with great care, and we found it most convenient to work with the universal fiber connector **BFTU** in conjunction with the **30126D1** FC connector, both from **Thorlabs**, to terminate the cleaved fiber ends.

5.5.2 Lattice beam focusing and alignment

After the fiber (and the PBC in Fig. 5-15), the lattice beams are again resized and focused at the condensate by a telescope L_1 and L_2 as in Fig. 5-16. We chose *short focal length* for $L_{1,2}$ ($\approx s_1$) compared with the distance between L_2 and the BEC (s_2), such that a small displacement of L_2 (compared to s_1) could move s_2 over a wide range. This way, the beam size after L_2 is somewhat decoupled from adjusting its focus onto the condensate. We chose the beam size at L_2 based on the target lattice

beam waist $w_L \approx 100 \mu\text{m}$ (see discussion below) at the BEC and the measured distance s_2 . Gaussian optics formulas should be used to account for the Rayleigh range ($\sim 3 \text{ cm}$). The third lens (L_3) is placed at about a focal length away from the BEC (again accounting for the finite Rayleigh range). The retro-reflection mirror (M) is immediately after L_3 which re-collimates the beam.

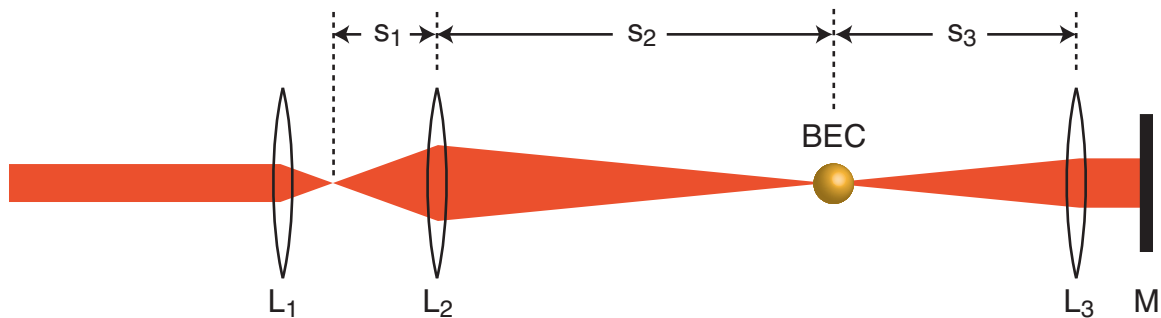


Figure 5-16: (Color) Collimation of lattice beam: Telescope lenses L_1 and L_2 have short focal length (~ 25 to 60 mm) and collimate the beam to the desired size (see text). Due to the short focal length, a small displacement of L_2 further away from L_1 changes focus of the lattice beam over a wide range, covering the location of BEC.

Note that the the measurement of distances s_i (~ 20 to 30 cm) usually has a couple of centimeters uncertainty, which is comparable to the Rayleigh range for the desired lattice beam size. Besides, the optics cannot be placed at arbitrary spots due to space constraint. It is therefore not practical to simply rely on the distance measurement and calculation. In practice, one of L_1 and L_2 is mounted on a translation stage with micrometer to scan the focus of the lattice beam, and achieve the best spatial mode overlap between the incident and reflected beams. We then measure the beam waists at an equal distance away from the BEC, which is easy as the BEC machine has symmetric configurations. From the two measured beam waists and the distance between the two points, we calculate the beam waist at the BEC ³. Typically we would try a few combinations of L_1 and L_2 before settling on a pair giving the closest to target beam waist at the condensate.

The *spatial mode match* between the incident and retro-reflected beam is achieved

³We can also learn from this measurement whether the beam focus is actually on the BEC, which is not so important as the Rayleigh range is much greater than the size of the condensate.

by adjusting the position of lens L_2 and maximizing the light going back through the fiber picked off by a 50/50 beam splitter. For each L_2 location, the retro mirror M is tweaked to keep the pointing of the retro beam optimized. During this mode matching process, the laser power is actively stabilized at a constant level.

Finally, we align the lattice beam with the condensate. The alignment was made more difficult by the fact that none of our lattice beams were aligned along the imaging axes due to limited optical access. We could not use the camera to coarse-align the lattice beam onto the condensate. Given the small size of the beam ($\sim 100 \mu\text{m}$ at BEC), it is actually non-trivial to get the beam close enough to the condensate so that the optical potential starts to affect the atoms, which is the signal for the fine alignment of the beams. We developed the following procedure to first align the incident beam to the condensate (one at a time without the retro beam), after which the above mode matching technique can be used to overlap the retro-reflection with the incident beam:

1. Some small amount of dye laser light tuned to sodium atomic resonance was sent through the lattice fiber. The fiber was multi-mode for yellow light and the IR optics worked poorly, but we only cared about the direction of the light. With atomic beam shutter open and the camera running in “focusing” mode, we were able to “see” the beam as the fluorescence from the atomic beam, and adjust it onto the in-trap BEC location on the camera. We then placed two irises to mark the beam path on either side of BEC.
2. After the initial step, the lattice beam should be within a couple of millimeters from the BEC. BEC released from the trap was able to hit the lattice beam in $\gtrsim 50$ ms ballistic expansion and be trapped or deflected by the lattice beam (increase laser power to enhance the effect if necessary). **Note:** A magnetic field gradient was applied during the time of flight to cancel out the gravity, so that atoms could expand in all directions for a long time without falling out of the picture (as lattice beam could be anywhere including above the in-trap BEC location). Eventually, the lattice beam could be tuned to trap all the atoms

into a tightly squeezed “tube” ($\lesssim 20 \mu\text{m}$ radially).

3. The beam was further fine tuned with the micrometer mount (**SN100-F2M** from **Newport**) such that the location of the atom “tube” was within $10 \mu\text{m}$ from the initial BEC in-trap location on the camera. This step provided very high sensitivity – a quarter of the smallest graduation on the micrometer knob.
4. The two irises were adjusted to mark the updated beam path. Afterwards, as long as the atom trap does not move too much, we can skip the first two steps, simply align the beam to the irises and use step 3 for fine adjustment.

5.5.3 Lattice beam calibration

To calibrate the depth of the lattice beam with respect to the lattice power, we have tried three different methods that complement each other and provide some consistency check:

- Optical dipole trap frequency measurement,
- Kapitza-Dirac diffraction,
- Intensity modulation spectroscopy (Bragg).

The first method is the easiest to implement but also the most inaccurate. The idea is that the laser power P_L can be measured with a photodiode. If in addition we have the optical dipole trap frequency ω_{odt} due to the lattice beam (with retro-reflection blocked), then the beam waist w_L can be calculated. However, to get the lattice depth, we have to figure out the contrast of the standing wave which is difficult to know accurately – the retro-reflected beam is attenuated by uncoated/dirty optics (such as our glass cell) and the mode-match could be imperfect. We simply assume a perfect contrast so that the standing wave AC stark shift is 4 times higher than the incident wave alone, which usually sets an upper bound for the true lattice depth ⁴.

⁴There is a chance that the retro-reflected beam has a tighter focus at the condensate, but usually the mode-matching is quite good and the power loss reduces the contrast more.

For trap frequency measurement, with the atoms trapped in the lattice beams (one at a time), we “kick” the atoms radially with a magnetic field gradient pulse to induce dipole oscillation and record the location after a fixed time of flight – again gravity is cancelled out during the entire process (except when applying the vertical kick) to prevent it from dragging atoms out of the lattice beams (especially for the vertical beam).

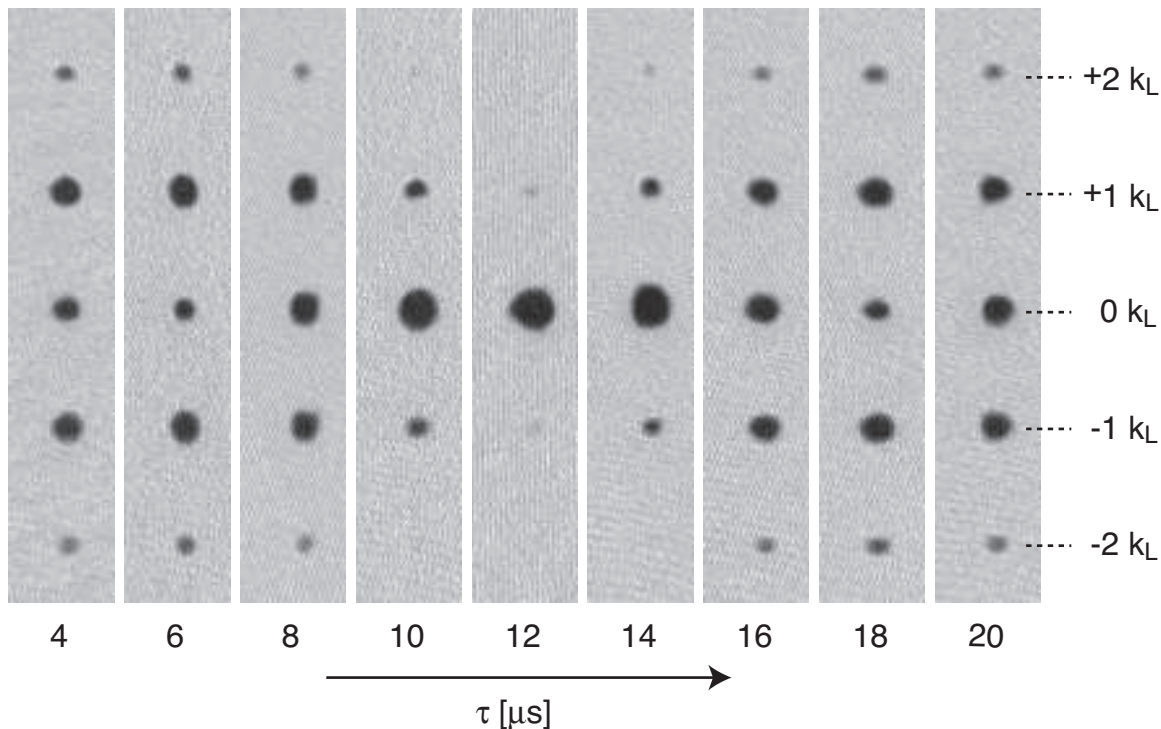


Figure 5-17: Kapitza-Dirac diffraction in a pulsed optical lattice: The population in central peak shows an oscillation in time, whose frequency corresponds to the gap between the lowest and the second excited bands (see discussion in text). For this sequence, the oscillation period $\sim 12 \mu\text{s}$ which corresponds to $u_L = 15.6$. The time of flight is 10 ms and the field of view is $1237 \mu\text{m} \times 220 \mu\text{m}$.

The second method – “Kapitza-Dirac diffraction” [140] – is also very convenient, and much more reliable. Simply by pulsing on the lattice beam (using an AOM as switch) at a fixed (unknown) depth u_L for various length of time ($\sim \mu\text{s}$), one would observe a time-varying diffraction pattern as in Fig. 5-17. The size of the central peak shows an oscillation, which is easily understood as following: During the lattice pulse, the eigenstates of the system are the Bloch functions. The system is

initially in the zero momentum state $|0\rangle$ which can be decomposed into populations in the Bloch states of $n = 0, 2, 4, \dots$ bands at zero quasi-momentum⁵. These bands subsequently evolve at their own eigen frequencies, so the population in $|0\rangle$ should contain oscillating terms at various gap frequencies. Fig. 5-18 shows the populations as a function of the lattice depth, which mostly concentrate in the $n = 0$ and $n = 2$ band for $u_L < 20$. Therefore the population in the $|0\rangle$ state oscillates predominantly at the gap frequency $E_{0,2} - E_{0,0}$. Fig. 5-19 shows $E_{0,2} - E_{0,0}$ as related to u_L and one can infer the lattice depth from the observed Kapitza-Dirac frequency.

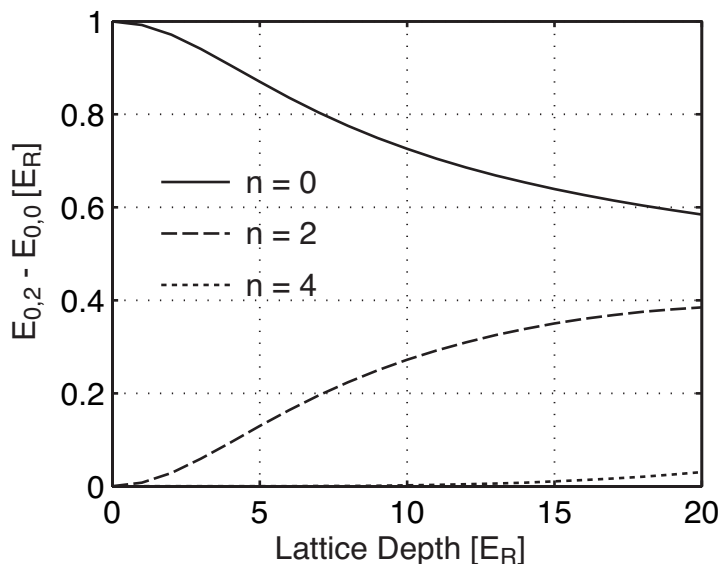


Figure 5-18: Band populations of zero momentum state $|0\rangle$: For lattice depths up to $20 E_R$, the populations concentrate largely in the lowest ($n = 0$) and the second excited bands ($n = 2$). Therefore the oscillation frequency corresponds to the energy gap between the two bands.

Due to the microsecond pulses involved, this method does require a relatively stable laser power from shot to shot without active stabilization (since the stabilization servo has a much longer time constant). However, with the fiber laser system and a cycle time of around 30 seconds, such stability is not hard to achieve. In addition, one should avoid calibrating at very shallow lattices ($< 5 E_R$) as the sensitivity to lattice depth becomes lower and longer pulses are required to observe the oscillation

⁵Symmetry dictates zero population in the $n = 1, 3, \dots$ bands.

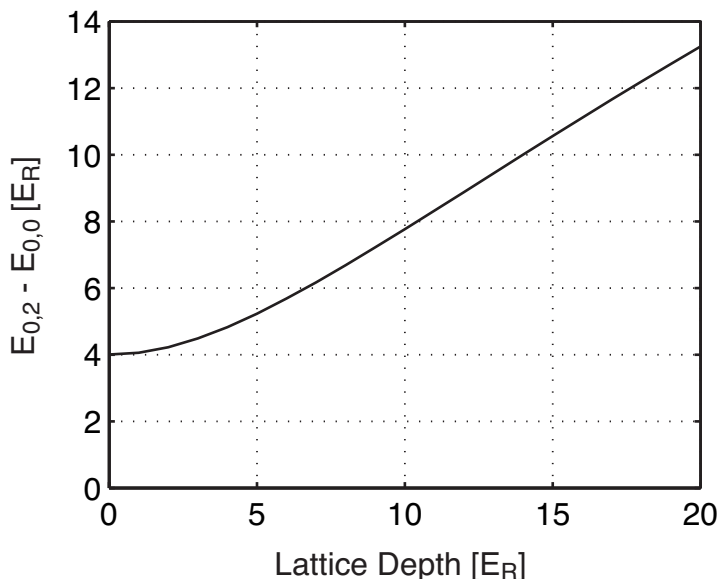


Figure 5-19: Energy gap between the lowest and the second excited bands at zero quasi-momentum: For lattice depths between 10 to 20 E_R , the energy gap is almost a linearly function of lattice depth with a slope ~ 0.55 .

which is susceptible to noise and decoherence effects (due to, for example, the inhomogeneity of the system). On the other hand, at very deep lattice ($> 20 E_R$), the population becomes significant for more than two bands and the signal contains multiple harmonics and cannot be fit to a single oscillation. A range of 10 to 20 E_R could be easily pre-selected with the “trap frequency measurement” method.

The third method is essentially “Bragg spectroscopy” for BEC in the optical lattice [60, 140]. It was somewhat complicated to set up and in our case, did not work noticeably better than the second technique. It was seldom used as consistency check or when laser power was not stable enough (as was often the case with the dye laser lattice system). Instead of pulsing on the lattice, we adiabatically loaded the BEC into the zero-quasi-momentum state at some *actively stabilized* lattice depth, which is then dithered at various frequencies to excite the atom into the second excited band⁶. We typically dithered at about 5 to 10% total lattice depth⁷ for about 1 ms,

⁶The dithering does not couple to the first excited band for symmetry reasons.

⁷This corresponds to about a couple of E_R modulation depth for $u_L \sim 10$. The Rabi frequency of such a dither is about 20 to 30% of the modulation depth for $u_L \lesssim 20$.

after which the lattice was adiabatically ramped down instead of being abruptly shut off. The population in the excited band appeared as $\pm 2\hbar k_L$ momentum peaks in time-of-flight when the dithering frequency is near the band gap $E_{0,2} - E_{0,0}$. Note that the ramp-down of the lattice must not be too slow or the trap potential would distort the momentum distribution and make it difficult to see the signal. We found 1 ms ramp time to be sufficiently slow to allow the lower band Bloch state to convert adiabatically back to the zero momentum state.

5.5.4 Crossed optical dipole trap

The alignment of the crossed optical dipole trap (ODT) is much easier as both beams are along the imaging axis. We used the camera in “focusing” mode to coarse align the light onto the condensate. For fine alignment, we used the phase contrast imaging [148] ($8\times$ magnification) to look at the condensate trapped with the magnetic trap and one ODT beam on at a time. The ODT provided much tighter confinement and “sucked” the atoms into a small circle whose location was matched to the condensate location in the magnetic trap only. The phase contrast imaging does not “see” the thermal component (which is quite optically dense in the trap) and improves the alignment resolution.

5.5.5 A few subtleties

Lattice beam size : As the lattice depth is proportional to light intensity, a tighter focus w_L would reduce the required laser power. However, the gaussian profile of the lattice beam adds an extra confining potential which tends to localize the atoms toward the center. At the same lattice depth u_L , the peak density is proportional to $w_L^{-6/5} N^{-2/5}$ [see Eqs. (5.63) and (5.64) below]. Since many experiments require relatively low occupancy numbers per lattice site (one or two), we can not reduce w_L too much without having to work with very small number of atoms N (see the numbers in Table 5.3), which requires very good imaging to have decent signal to noise ratio.

Adiabatic BEC loading : Because of the large energy gap between the lowest and the next excited bands, it is relatively easy to maintain “inter-band” adiabaticity during the lattice ramp – any ramp time $\gtrsim 1$ ms is slow enough. However, the “intra-band” adiabaticity is not as easy to maintain, especially as the lattice deepens, the band width actually decreases exponentially. A mismatch between the meanfield energy and the trapping potential (both of which increase with the lattice depth as well) would cause a phase to develop across the condensate or, put plainly, the condensate would tend to “slosh” [138]. This leads to intra-band heating. However, due to the almost linear dependence of \hat{U} on the lattice depth [Eq. (5.54)] in a three dimensional lattice, so long as the initial and final equilibrium condensate sizes are equal, the meanfield and the trapping potential would remain closely matched during the entire ramp process. The final trapping potential is mostly due to the lattice beams and is fairly isotropic. Due to the limited axial trap frequency for our magnetic trap ($\lesssim 40$ Hz), we could not make the magnetic trap spherical over a wide range of trap frequencies. This is one of the reasons for us to setup a crossed dipole trap whose trap frequencies are chosen to match the initial and final condensate sizes.

Lattice beam polarization : Because of the fine structure separation Δ_{hf} (about 500 GHz between ^{23}Na D1 and D2 lines), if the lattice laser detuning from the atomic transition is comparable to Δ_{hf} , one cannot consider D1 and D2 lines to be degenerate. In that case, the optical potential not only depends on the laser intensity but also on the polarization. Such an effect was actually used to create a moving optical lattice [149] For example, for atoms in the $|F = 1, m_F = -1\rangle$ state, the optical potential due to D1 and D2 lines are:

$$\text{D1} \propto \frac{1}{6}|\mathcal{E}_-|^2 + \frac{5}{18}|\mathcal{E}_+|^2 \quad (5.46)$$

$$\text{D2} \propto \frac{1}{6}|\mathcal{E}_-|^2 + \frac{1}{18}|\mathcal{E}_+|^2 \quad (5.47)$$

where \mathcal{E}_\pm are the electric field with σ^\pm helicity. However, if the polarization is not purely transverse to the quantization axis of the atoms, there could be non-vanishing coupling to the other hyperfine states ($|F = 2, m_F = 0, -2\rangle$). This coupling goes to

zero when D1 and D2 lines are degenerate (compared to the laser detuning), or when the polarization of the light is purely linear. We have used linear polarization for all lattice beams (as well as the crossed dipole trap beams) so far in our experiments – the dye laser lattice system, in particular, operated at a detuning not much greater (about 10 times) than the D1 and D2 separation.

5.6 Cheatsheet

This section is intended as a quick reference for calculating various quantities relevant to optical lattice experiments. I first list some useful formulas, and then tabulate some numbers and scaling relations. The numbers are calculated for the atomic species (^{23}Na , ^{87}Rb and ^6Li) and lattice wavelength (1064 nm) found in the MIT labs. Using the scaling relations, one can easily obtain relevant quantities for other atomic species or lattice wavelengths.

Previously undefined symbols used below:

I_L : laser peak intensity

P_L : laser power

w_L : laser $1/e^2$ gaussian beam waist

Q_e : electron charge

M_e : electron mass

c : speed of light

ϵ_0 : vacuum permittivity in SI units (8.85×10^{-12} F/m)

Γ_a : natural linewidth of the atom (rad/s)

λ_a : atomic transition wavelength

n_{avg} : coarse-grained atomic density

n_{peak} : peak atomic density at the lattice potential minima

K_3 : three-body decay coefficient

Γ_3 : peak three-body decay rate $K_3 n_{\text{peak}}^2$

ω_{tr} : harmonic trap frequency

5.6.1 Useful formulas

- Recoil Energy E_R :

$$E_R = \frac{h^2}{2M\lambda_L^2} \quad (5.48)$$

- Optical AC stark shift (SI units are used):

$$\Delta U_{\text{AC}} = I_L \left[\frac{\Gamma_a}{\omega_a^2 - \omega_L^2} \frac{3\pi c^2}{\omega_a^2} \right] \quad (5.49)$$

$$= I_L \left[\frac{Q_e^2}{2M_e \varepsilon_0 c (\omega_a^2 - \omega_L^2)} \right] \quad \text{for alkali atoms} \quad (5.50)$$

Multiply by a factor of 4 for a standing wave with perfect contrast.

- Spontaneous Rayleigh scattering rate (SI units are used):

$$\Gamma_{\text{sc}} = I_L \left[\frac{\Gamma_a^2}{(\omega_a^2 - \omega_L^2)^2} \frac{6\pi c^2}{\hbar \omega_a} \left(\frac{\omega_L}{\omega_a} \right)^3 \right] \quad (5.51)$$

Multiply by a factor of 4 for a standing wave with perfect contrast.

- Gaussian beam profile (r distance from center):

$$I_L(r) = I_L(0) e^{-2\frac{r^2}{w_L^2}} = \frac{2P_L}{\pi w_L^2} e^{-2\frac{r^2}{w_L^2}} \quad (5.52)$$

- On-site interaction U in Eq. (5.17) as a function of (dimensionless) lattice depth

u_L :

$$U(u_L) = E_R \left(\frac{16a_s}{\pi\lambda_L} \right) \hat{U}(u_L) \quad (5.53)$$

$$\begin{aligned} \hat{U}(u_L) &= a_L^3 \int_V d\mathbf{x} |w_n(\mathbf{x})|^4 \\ &\simeq 1.33 + 0.7u_L \quad \text{for three dimensional lattice.} \end{aligned} \quad (5.54)$$

$\hat{U}(u_L)$ is a dimensionless number depending only on u_L and reflects the enhancement of interaction due to the lattice.

- Local harmonic frequency at the bottom of each lattice site:

$$\omega_{\text{lh}} = 2\sqrt{u_L} \left(\frac{E_R}{\hbar} \right) \quad (5.55)$$

- Local harmonic oscillator length $a_{\text{lh}} = \sqrt{\frac{\hbar}{M\omega_{\text{lh}}}}$:

$$a_{\text{lh}} = \frac{\lambda_L}{2\pi u_L^{1/4}} \quad (5.56)$$

- Optical dipole trap (ODT) frequency due to the gaussian profile of the lattice beam:

$$\omega_{\text{odt}} = \omega_{\text{lh}} \left(\frac{\lambda_L}{\sqrt{2\pi}w_L} \right) \quad (5.57)$$

This is due to one lattice beam. Trap frequencies should be added in quadrature.

5.6.2 Some numbers

- Table 5.1 lists some useful atomic constants.
- Table 5.2 lists U and J for three-dimensional cubic lattice 5 to 30 E_R deep.
- Table 5.3 lists various quantities for $N = 10^5$ atoms in a 20 E_R three dimensional lattice, and the lattice beams have $1/e^2$ waist equal to 100 μm .

	²³ Na	⁸⁷ Rb	⁶ Li
a_s [nm]	2.75	5.45	–
M [amu]	22.9898	86.9092	6.0151
Γ_a [2π MHz]	10.01	5.98	5.92
λ_a [nm]	589	780	671
E_R/h [Hz]	7666	2028	29299
K_3 [10^{-30} cm ⁶ s ⁻¹]	1.1	5.8	–

Table 5.1: Various constants for ²³Na, ⁸⁷Rb and ⁶Li: 1 amu= $1.66053886 \times 10^{-27}$ kg, and the lattice wavelength is 1064 nm. Scattering lengths are given for ²³Na pair both in $|F = 1, m_F = -1\rangle$ hyperfine state, ⁸⁷Rb pair both in $|F = 1, m_F = -1\rangle$ or one in $|F = 1, m_F = -1\rangle$ and one in $|F = 2, m_F = 2\rangle$ [114]. ⁶Li scattering length between $|F = 1/2, m_F = \pm 1/2\rangle$ is highly variable as the experiments typically take place near the broad Feshbach resonance [150]. The natural linewidths are taken from [151].

5.6.3 Scaling relations

$$E_R \propto \frac{1}{M\lambda_L^2} \quad (5.58)$$

$$U \propto \frac{a_s}{\lambda_L} \quad (5.59)$$

$$\Delta U_{AC} \propto \frac{I_L}{\omega_a^2 - \omega_L^2} \quad (5.60)$$

$$\Gamma_a \propto \omega_a^2 \quad \text{approximately for alkali atoms} \quad (5.61)$$

$$\Gamma_{sc} \propto \frac{I_L \omega_L^3}{(\omega_a^2 - \omega_L^2)^2} \quad (5.62)$$

$$\omega_{odt} \propto \frac{\sqrt{u_L}}{M\lambda_L w_L} \quad (5.63)$$

$$n_{avg} \propto \left(\frac{M\omega_{tr}}{\hbar} \right)^{6/5} \frac{N^{2/5}}{d_s^{3/5} \hat{U}^{3/5}} \quad (5.64)$$

$$R_{TF} \propto \frac{(Na_s)^{1/5}}{(M\omega_{tr})^{2/5}} \quad (5.65)$$

u_L	\hat{U}	J/E_R	U/E_R (^{23}Na)	U/E_R (^{87}Rb)
5	4.2173536	0.065767347	0.05551383	0.107192159
6	5.099319748	0.050773027	0.067123319	0.129609026
7	5.96420995	0.039417172	0.078508033	0.151591875
8	6.808026905	0.030799256	0.089615357	0.173039108
9	7.630290247	0.024226709	0.100438966	0.193938513
10	8.432083331	0.019182452	0.110993122	0.214317627
11	9.215050505	0.015284695	0.121299468	0.234218245
12	9.980926877	0.012252082	0.131380845	0.253684467
13	10.73134008	0.009876701	0.141258677	0.272757663
14	11.46774231	0.008004102	0.15095208	0.291474743
15	12.19140073	0.006518816	0.160477734	0.309867915
16	12.90341171	0.005333916	0.16985007	0.327965044
17	13.60472252	0.004383499	0.179081558	0.345790209
18	14.29615382	0.003617253	0.188183	0.363364266
19	14.97841986	0.002996508	0.197163798	0.38070537
20	15.65214588	0.00249135	0.206032182	0.397829414
21	16.31788253	0.002078495	0.214795401	0.414750392
22	16.97611773	0.001739714	0.223459876	0.431480707
23	17.62728641	0.001460653	0.232031334	0.448031412
24	18.2717784	0.001229954	0.240514905	0.464412417
25	18.90994499	0.001038582	0.248915214	0.480632649
26	19.54210425	0.000879316	0.257236447	0.496700193
27	20.16854549	0.000746359	0.265482412	0.512622403
28	20.78953294	0.000635039	0.273656588	0.528405994
29	21.40530887	0.000541571	0.281762164	0.544057125
30	22.01609618	0.000462884	0.289802074	0.55958146

Table 5.2: U and J for 5 to 30 E_R three dimensional lattice: \hat{U} and J are calculated numerically with 20 plane waves and 10 lattice sites (convergence checked for both parameters). \hat{U} is defined in Eq. (5.53). U for ^6Li is not listed because in typical experiments, the scattering length could be tuned over a wide range with Feshbach resonance.

	P_L [mW]	ω_{odt} [$2\pi \text{ s}^{-1}$]	$n_{\text{avg}} \left(\frac{\lambda_L}{2}\right)^3$ (number of atoms per site)	n_{peak} [10^{14} cm^{-3}]	R_{TF} [μm]	Γ_{sc} [s^{-1}]
^{23}Na	543	232	5.5	19.2	11.8	0.009
^{87}Rb	52.2	61.4	3.6	12.7	13.5	0.007
^6Li	1810	888	–	–	–	0.041

Table 5.3: Various quantities of interest for atoms in a three dimensional lattice: The ODT frequency is obtained from Eq. (5.57) multiplied by $\sqrt{2}$ to account for the crossed lattice beams. The scattering rate Γ_{sc} is for a single standing wave with perfect contrast. The numbers are calculated for $N = 10^5$ atoms in a $20 E_R$ three dimensional lattice at 1064 nm with $1/e^2$ waist equal to $100 \mu\text{m}$. ^6Li scattering length is variable near the Feshbach resonance, which gives varied cloud size and density. One can use the scaling relations in this section to obtain the corresponding quantities for other values of N , w_L and u_L and different atomic species.

Chapter 6

Conclusion

6.1 Reminiscence

This is literally the last chapter of my PhD career. I cannot help but feel a bit nostalgic about my five plus years at MIT, which for better or worse have led me into a rather different career path than I had in mind growing up. I suppose a little reminiscence is in order.

Back in 2000 at the MIT open house, I became pretty excited about the prospect of getting into a new field which seemed to be growing at an explosive pace. At the time, the gaseous BEC was barely five years old and only a handful of labs around the world had a working BEC machine. The development in the ensuing years far exceeded my (admittedly uninformed) expectations. A Nobel prize was awarded for the achievement of BEC in 2001 – I was one year into graduate school and still learning my ways around the lab. I remember thinking to myself then whether the “best time” had passed, but the field certainly has not slowed down since. New labs with better designed machines quickly emerged and made possible new experiments that required more refined technical capabilities and explored previously unattainable regimes. According to the latest count on the atom traps online database (<http://www.uibk.ac.at/c/c7/c704/ultracold/atomtraps.html>), there are now about 50 groups worldwide having achieved BEC. The breadth of the research also expanded to quantum degenerate Fermi systems, which at present are the most actively

researched subjects.

As a junior graduate student, I did my share of grunt work that probably taught me more about being an experimentalist than working on the scientific projects. In addition to electronics and laser maintenance, notable undertakings included building a new magnetic trap and “fiberizing” our laser table. The trap – fully built and bench-tested – still sits around somewhere in the lab waiting to be called to duty. In the meantime, it serves as a quiet reminder of the importance to keep a good record of benchmarks. The “fiberized” laser table made our BEC production almost turn-and-key.

The field grew fast and became increasingly competitive. Consequently, our experiments also grew in complexity – the difference between our recent work compared to three years ago in terms of technical difficulty is quite startling. Many parts have to work simultaneously for an experiment to succeed, and we seemed to be constantly trying to fix things faster than they broke. Mishaps with key components like the water chiller (heavy lifting) or the gate-valve (venting the main chamber) provided extra “excitement”. For all the hectic runs and seemingly endless chores, it was a challenge to keep one’s sanity and continue to think about and learn physics. Looking back, I feel reasonably content with the way I have spent my time and energy. The few breakthroughs in my studies would not have happened without a conscientious effort to think through some difficult problems.

In light of the rapid progress of the field in general, my personal success seems rather modest, which in part contributed to my decision to explore different directions post-PhD. That said, I’d like to think I have nonetheless done my small part in contributing to the large body of work on condensate physics. Through this thesis, I hope to have tied together and put into perspective the few projects to which I made substantial contributions.

6.2 Looking ahead

The lab is now entering a new era as the second lab at MIT capable of producing dual-species quantum gases (^{23}Na and ^6Li). As complicated as our previous experiments eventually became, the added layers of complexity still constituted no more than incremental improvements to an existing system. In comparison, constructing a new system with fundamentally different capabilities is much more likely to open up new regimes and research directions. Adding fermionic ^6Li to an optical lattice certainly presents intriguing possibilities.

^6Li has proven to be the most “benign” species for working with Feshbach resonances. Most BEC systems suffer from strong inelastic collision losses near a Feshbach resonance which limited the density or the time duration of the experiments [152, 153, 118, 125, 154, 155, 156]. Fermions are generally longer-lived due to their different quantum statistics [122, 157, 158], but the exact lifetimes are still quite different – there are only two data points now, namely ^{40}K (a few milliseconds [159, 120, 160]) and ^6Li (hundreds of milliseconds [161, 162, 119, 121, 163]). In addition, the strong Feshbach resonance for ^6Li is ~ 300 G wide [150], which makes it possible to map out the details of various interaction regimes with modest magnetic field resolution. The long lifetime of ^6Li near this resonance allows the system to equilibrate. Unlike the quantum degenerate $^{23}\text{Na}_2$ molecules described in Chapter 4, $^6\text{Li}_2$ can form true molecular condensates ¹.

Across the Feshbach resonance, the scattering length changes sign, corresponding to a bound state being shifted from below the continuum threshold to above. By slowly ramping the magnetic field, it is possible to adiabatically connect the molecular BEC (positive scattering length) regime to the BCS regime (negative scattering length) [164, 165, 162, 163, 166, 167, 168, 169, 170, 171, 172, 173, 174, 175], where superfluidity can only arise through Cooper pairing. Observing the BCS-type superfluidity had been the “Holy Grail” in the studies of quantum degenerate Fermi systems since the very beginning. The recent observation of vortex lattice in ^6Li pro-

¹In contrast, “condensation” for $^{40}\text{K}_2$ was only achieved in two dimensions [120].

vided a spectacularly definite proof [176]. Rather than reaching the end of the road, one can hope to learn much more from these ultracold Fermi gases. In many ways, they represent the closest thing to the conventional superconductors while (approximate) theories may still be able to model the experiments accurately – much like when the gaseous BEC was first realized. The critical temperature compared to the Fermi temperature is much higher for these degenerate Fermi gases², which may shed light on the natures of high-temperature superconductors. Combining different tools such as optical lattices and Feshbach resonances in addition to having two atomic species could lead us into even more exotic regimes.

On the other hand, many challenges lie ahead. Like what happened with BEC, after the initial slew of results brought on by the realization of a new system, the research becomes more difficult and requires deeper understandings of the physics and/or more specialized engineering efforts. Oftentimes we started setting up an experiment with a particular agenda but could not make it work as planned despite our best effort. As an experimentalist, it is important to keep in mind that failing to see what one expects to see could very well be interesting physics. Therefore one should not get too caught up in the original agenda.

² T_c/T_F is ~ 0.3 for ${}^6\text{Li}$, similar to high temperature conductors and more than 100 times higher than normal superconductors.

Appendix A

Experimental Observation of the Bogoliubov Transformation for a Bose-Einstein Condensed Gas

This appendix reprints Ref. [100]: J.M. Vogels, K. Xu, C. Raman, J.R. Abo-Shaeer, and W. Ketterle, *Experimental Observation of the Bogoliubov Transformation for a Bose-Einstein Condensed Gas*, Phys. Rev. Lett. **88**, 060402 (2002).

Experimental Observation of the Bogoliubov Transformation for a Bose-Einstein Condensed Gas

J. M. Vogels, K. Xu, C. Raman,* J. R. Abo-Shaeer, and W. Ketterle[†]

Department of Physics, MIT-Harvard Center for Ultracold Atoms, and Research Laboratory of Electronics, Massachusetts Institute of Technology, Cambridge, Massachusetts 02139

(Received 11 September 2001; published 28 January 2002)

Phonons with wave vector q/\hbar were optically imprinted into a Bose-Einstein condensate. Their momentum distribution was analyzed using Bragg spectroscopy with a high momentum transfer. The wave function of the phonons was shown to be a superposition of $+q$ and $-q$ free particle momentum states, in agreement with the Bogoliubov quasiparticle picture.

DOI: 10.1103/PhysRevLett.88.060402

PACS numbers: 05.30.Jp, 03.75.Fi, 32.80.-t, 67.40.Db

The pioneering work of Bogoliubov in 1947 constitutes the first microscopic theory that attributes superfluidity to Bose-Einstein condensation [1]. As described by Einstein, noninteracting bosons condense [2], but they are not superfluid. However, Bogoliubov showed that with weak interactions the condensate will exhibit superfluidity. Repulsive interactions change the elementary excitations at long wavelengths from free particles into phonons which, according to the Landau criterion, lead to superfluidity [3]. The main step in the nonperturbative treatment is the Bogoliubov transformation

$$\begin{aligned} b_{+q}^\dagger &:= u_q a_{+q}^\dagger + v_q a_{-q}, \\ b_{+q} &:= u_q a_{+q} + v_q a_{-q}^\dagger, \end{aligned} \quad (1)$$

which expresses the creation and annihilation operators b_q^\dagger and b_q for Bogoliubov quasiparticles in terms of creation and annihilation operators a_q^\dagger and a_q for free particles in momentum states q . This transformation also plays a crucial role in general relativity, where it connects the particle operators in different reference frames [4]. In this paper we experimentally verify the Bogoliubov transformation by generating quasiparticles with momentum $+q$ and observing that they are a superposition of $+q$ and $-q$ momentum states of free particles.

Following a recent suggestion of Brunello *et al.* [5], we perform an experiment that combines the two regimes of Bragg spectroscopy, where the momentum imparted to the atoms is either smaller [6] or larger [7] than the sound velocity c times the mass m of the atoms. An optical lattice moving through the condensate at the sound velocity imprinted phonons with wavelengths equal to the spatial period of the lattice [6]. This was accomplished by intersecting two laser beams at a small angle and choosing their frequency difference to be equal to the phonon frequency. The momentum analysis of the phonon wave function was performed by a second Bragg pulse consisting of counterpropagating laser beams that transferred a large momentum Q (two photon recoils) to atoms with initial momentum p . In the limit $Q \gg p$, mc , the resonance frequency ν is equal to the kinetic energy

transferred: $h\nu = Q^2/2m + Qp/m$, where the second term is simply the Doppler shift [7–9]. The resulting frequency spectrum shows three peaks corresponding to the three momentum components (0 , $+q$, and $-q$) of a condensate with phonons (see Fig. 2 below) [5].

The Bogoliubov spectrum for the energy of elementary excitations is [10]

$$\varepsilon(q) = \sqrt{q^2 c^2 + \left(\frac{q^2}{2m}\right)^2}, \quad (2)$$

where $c = \sqrt{4\pi\hbar^2 a n}/m$, a is the scattering length, and n is the density. The amplitudes u_q and v_q in Eq. (1) are given by

$$u_q, v_q = \pm \frac{\varepsilon(q) \pm \frac{q^2}{2m}}{2\sqrt{\varepsilon(q) \frac{q^2}{2m}}}. \quad (3)$$

The nontrivial aspect of the Bogoliubov transformation manifests itself only at low momenta ($q \ll mc$), where both amplitudes u_q and v_q are significant. In this regime, the excitations are characterized by $u \sim -v \sim \sqrt{mc/2q} \gg 1$ and $\varepsilon(q) \sim qc$. Such excitations are phonons, each involving many particles moving in both directions. At high momenta ($q \gg mc$), $u_q \sim 1$, $v_q \sim 0$, and $\varepsilon(q) = q^2/2m + mc^2$. These excitations are free particles with an energy shift equal to the chemical potential $\mu = mc^2$.

The phonon creation operator b_{+q}^\dagger [Eq. (1)] is a superposition of the creation operator a_{+q}^\dagger for particles moving in the $+q$ direction and the annihilation operator a_{-q} for particles moving in the $-q$ direction, yet the creation of a phonon in the condensate implies an increase of particles moving in both the $+q$ and $-q$ direction. Indeed, simple operator algebra shows that a condensate with l excitations, $b_{+q}^\dagger/\sqrt{l}! |\Psi_0\rangle$, contains $lu_q^2 + v_q^2$ free particles moving with momentum $+q$ and $(l+1)v_q^2$ free particles with momentum $-q$. In its ground state the condensate contains v_q^2 pairs of atoms with momenta $+q$ and $-q$. These pairs constitute the quantum depletion in the condensate wave function [10]

$$|\Psi_0\rangle = \prod_{q \neq 0} \frac{1}{u_q} \sum_{j=0}^{\infty} \left(\frac{-v_q}{u_q} \right)^j |n_{-q} = j, n_{+q} = j\rangle, \quad (4)$$

where the remaining atoms are in the $q = 0$ momentum state. When a_{+q}^\dagger and a_{-q} act on Ψ_0 , terms with large occupation numbers j are enhanced: $a_{+q}^\dagger |n_{-q} = j, n_{+q} = j\rangle = \sqrt{j+1} |n_{-q} = j, n_{+q} = j+1\rangle$, $a_{-q} |n_{-q} = j, n_{+q} = j\rangle = \sqrt{j} |n_{-q} = j-1, n_{+q} = j\rangle$. In addition, $-q$ and $+q$ atoms occur only in pairs in the ground state. Together, these two effects cause both a_{+q}^\dagger and a_{-q} to increase the number of atoms in both the $-q$ and $+q$ states.

The experiments were performed with condensates of 3×10^7 sodium atoms in a magnetic trap with radial and axial trapping frequencies of 37 and 7 Hz, respectively [11]. The condensate had a peak density of $1.0 \times 10^{14} \text{ cm}^{-3}$ corresponding to a chemical potential of $\mu = h \times 1.5 \text{ kHz}$, a sound velocity of $c = 5 \text{ mm/s}$, and a Thomas-Fermi radial radius of $32 \text{ }\mu\text{m}$. The Bragg beams for the optical lattices were generated from a common source of laser light 1.7 GHz red-detuned from the $3S_{1/2}|F=1\rangle$ to $3P_{3/2}|F'=0,1,2\rangle$ transitions. The lattices were moved radially through the cloud. This was done to avoid the high collisional density along the axial direction, where outcoupled atoms would have undergone elastic collisions with the condensate [12]. The Bragg beams for imprinting the phonons were at an angle of 32 mrad with respect to one another, resulting in a lattice spacing of $\sim 9 \text{ }\mu\text{m}$ and a recoil momentum of $q = m \times 1.9 \text{ mm/s}$. The beams propagated at an angle of 0.4 rad with respect to the longitudinal axis of the condensate and were linearly polarized perpendicular to it. The frequency difference (“excitation frequency”) between the two beams was chosen to be 400 Hz, corresponding to the frequency of the phonons. The excitation pulse had to be long enough to ensure sufficient frequency resolution in order to selectively excite $+q$ phonons, and no $-q$ phonons (see below). However, the excitation pulse also had to be shorter than the transit time of phonons through the condensate, since phonons accelerate when they move through regions of varying density. We chose small-angle Bragg beams 3 ms in duration with intensity 0.05 mW/cm^2 , corresponding to a two-photon Rabi frequency of 50 Hz.

The momentum analysis of the phonons was performed with two counterpropagating beams that imparted a recoil momentum of $Q = m \times 59 \text{ mm/s}$ onto the outcoupled atoms. The beams were polarized parallel to the longitudinal axis of the condensate to suppress super-radiant emission [13]. A frequency difference (“probe frequency”) of 100 kHz between the two beams corresponded to the kinetic energy needed for atoms initially at rest to reach this recoil momentum. To gain recoil momentum $+Q$, atoms with initial momentum $+q$ were resonant at 107 kHz (Fig. 1a). Atoms with momentum $-q$ were reso-

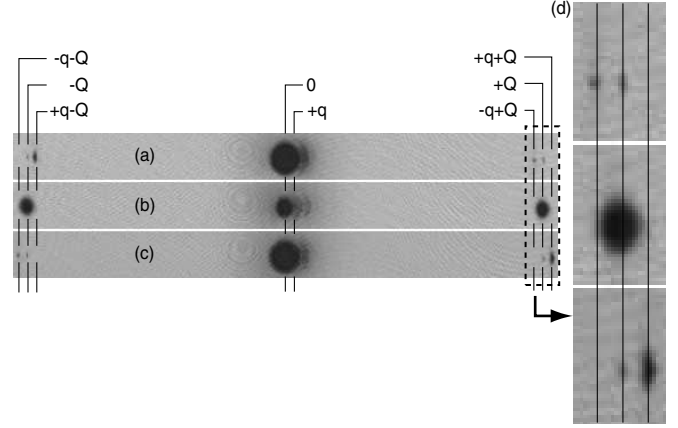


FIG. 1. Momentum distribution of a condensate with phonons. After imprinting $+q$ phonons into the condensate, momentum analysis via Bragg spectroscopy transfers a momentum $\pm Q$ (two-photon recoil) to the atoms. Absorption images after 40 ms time of flight in (a), (b), and (c) show the condensate in the center and outcoupled atoms to the right and left for probe frequencies of 94, 100, and 107 kHz, respectively. The small clouds centered at $+q$ are phonons that were converted to free particles. The size of the images is $25 \times 2.2 \text{ mm}$. (d) The outlined region in (a)–(c) is magnified, and clearly shows outcoupled atoms with momenta $Q \pm q$, implying that phonons with wave vector q/\hbar have both $+q$ and $-q$ free particle momentum components.

nant at 94 kHz (Fig. 1b). In our experiment, a retro-reflected beam containing both optical frequencies resulted in two optical lattices moving at the same speed in opposite directions. This led to simultaneous outcoupling of $+q$ and $-q$ atoms in opposite directions. These large-angle Bragg beams were pulsed on for 0.5 ms. The probe pulse had to be long enough to selectively excite atoms with $\pm q$ momentum, but also shorter than h/μ for the mean-field energy to be negligible during the readout. Each frequency component had an intensity of 0.7 mW/cm^2 , corresponding to a two-photon Rabi frequency of 700 Hz. Subsequently, the trap was turned off and a resonant absorption image was taken after 40 ms of ballistic expansion.

Figure 1 shows typical absorption images for various probe frequencies. The quasiparticle nature of the phonons was directly evident (see outlined region) in the time-of-flight distribution through the presence of the peaks at momenta $\pm q + Q$. These peaks had well-defined momentum because the outcoupled atoms left the condensate quickly (during this time the atoms’ velocity changed by less than the speed of sound [14]). This “photograph” of the Bogoliubov transformation is the central result of this paper.

We now discuss the different momentum components distinguishable in Fig. 1: (i) The original condensate is in the center. (ii) The condensate is asymmetrically extended towards positive momenta. This is due to imprinted phonons of momentum q that were converted to free particles during the ballistic expansion. Previously this signature was used to determine the structure factor of a condensate [6]. There is no momentum component in the

opposite direction, because we did not create $-q$ phonons (see below). The smearing of the observed momentum distribution may be caused by acceleration due to the inhomogeneous density distribution of the condensate when the trap was switched off. (iii) The two components with momentum $+Q$ and $-Q$ are atoms outcoupled from the condensate at rest. The symmetry of the $\pm Q$ peaks, as well as the position of the main condensate, served as an indicator as to whether the condensate was undergoing dipole oscillation during the experiment. Images that showed such “sloshing” (caused by technical noise) were excluded from further analysis. (iv) Atoms at $+q + Q$ (Fig. 1c) and $+q - Q$ (Fig. 1a) are coupled out from the $+q$ component of the phonons. (v) Atoms at $-q - Q$ (Fig. 1c) and $-q + Q$ (Fig. 1a) are coupled out from the $-q$ component of the phonons.

Quantitative information was obtained by scanning the probe frequency and measuring the number of outcoupled atoms in the three peaks around $-Q$ (See Fig. 1). Without phonons only the condensate peak is observed. The excitation of phonons at wave vector $+q$ creates momentum sidebands at momentum $\pm q$. The $-q$ peak is expected to be smaller by a factor v_q^2/u_q^2 . This effect is evident in Fig. 2, but with a poor signal-to-noise ratio.

The excitation of the phonons was characterized by scanning the frequency difference of the small-angle Bragg beams (Fig. 3a) and measuring the number of outcoupled atoms at $+q - Q$. The probe frequency was kept at 94 kHz because the momenta of the excited phonons remained fixed. The observation of two distinct peaks (corresponding to $+q$ at 400 Hz and $-q$ phonons at -400 Hz) confirms that there was sufficient resolution to excite only $+q$ phonons and suppress the off-resonant excitation of $-q$ phonons. The higher peak represents the u component of $+q$ phonons excited at positive excitation frequencies. When the excitation frequency became negative, $-q$

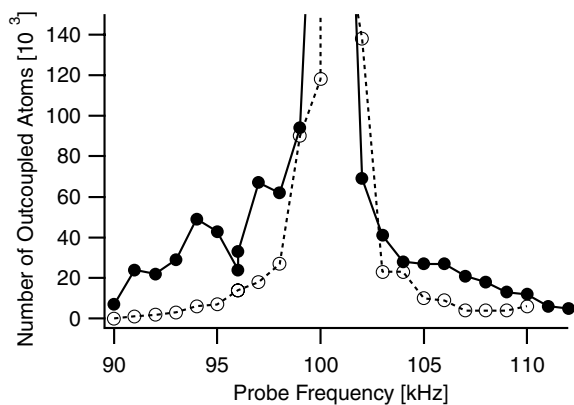


FIG. 2. Bragg spectrum of a condensate with (●) and without (○) phonon excitation. The number of outcoupled atoms vs the probe frequency is shown. The excitation of phonons creates sidebands on both sides of the central condensate peak. At about 100 kHz, the absorption images were saturated due to high optical density.

phonons were excited. This second peak represents the v component of the phonons.

According to Eq. (3) the ratio of the two peaks, v_q^2/u_q^2 , should be smaller at lower density. This is confirmed in Fig. 3b, which shows the excitation spectrum at low density. The density was lowered by a factor of 2 by weakening the axial trap frequency to 4 Hz and reducing the number of atoms in the condensate by a factor of 3. The scatter in the data could be due to residual sloshing, shot-to-shot fluctuations in the size of the condensate, or non-linear effects (see below).

The dashed line is the theoretical prediction with no free parameters (except the vertical scale). It was obtained by integrating Eq. (3) over the inhomogeneous density distribution of the condensate and by accounting for the finite length of the square excitation pulse, which broadens the line and causes the extra sidelobes at about 900 Hz. The theory assumes the validity of a perturbative approach, i.e., that the excitation pulse is weak.

Ideally, both Bragg pulses should affect only a few percent of the atoms, as in previous experiments [6,7].

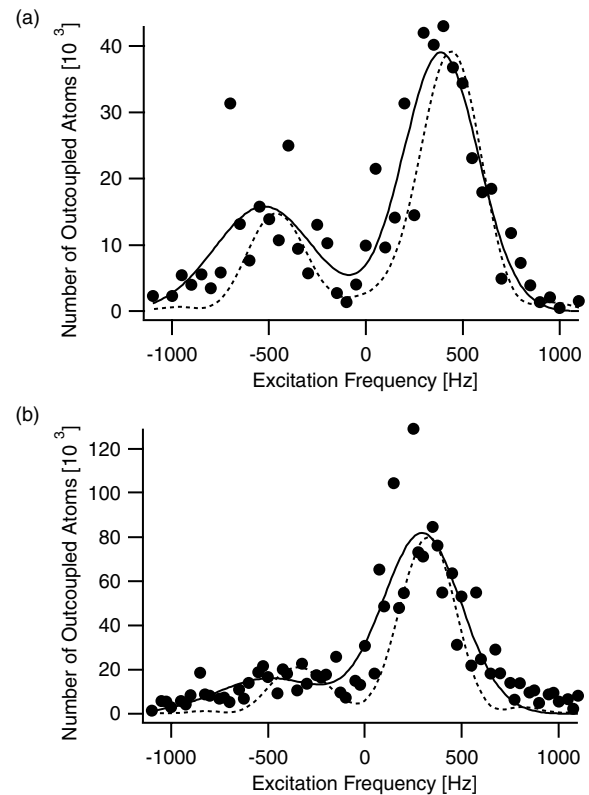


FIG. 3. Phonon excitation spectrum. Atoms with initial momentum $+q$ were detected by setting the probe frequency to 94 kHz and measuring the number of atoms with momentum $-Q + q$. The two peaks reflect that phonons with $+q/\hbar$ and $-q/\hbar$ wave vectors have free particle components with momentum $+q$. Spectra were taken at (a) high density ($1.0 \times 10^{14} \text{ cm}^{-3}$) and (b) low density ($0.5 \times 10^{14} \text{ cm}^{-3}$). The solid line, a fit to the sum of two Gaussians, is intended to guide the eye. The dashed line is the theoretical prediction.

However, because our signal was the product of the two outcoupling efficiencies, we needed to work at much higher outcoupled fractions. We estimate that the excitation pulse transferred 10% of the condensate atoms into the phonon state, and that the probe pulse outcoupled 40% of these atoms on resonance.

Both Bragg processes (stimulated Rayleigh scattering) should depend only on the product of the two intensities. Therefore, changing the sign of the excitation frequency should not affect the number of phonons generated (assuming a stationary condensate). However, when the sign of the excitation frequency was changed in our experiment, the observed number of phonons differed. This is most likely due to superradiance [13], which is sensitive to the individual intensities. Therefore, the asymmetry in phonon number was eliminated by ensuring equal intensities in the two beams. Additionally, there was a substantial loss ($\sim 50\%$) of condensate atoms due to superradiant Rayleigh scattering. Both superradiant effects could be further suppressed using light further detuned from resonance. However, in our case this would have required an additional laser. Given these experimental limitations, the agreement between experiment and theory in Fig. 3 is satisfactory.

In this work we have used large-angle Bragg pulses to analyze the momentum structure of the phonon wave function. In principle, this could have also been achieved by removing the mean-field interaction within a time $\hbar/\varepsilon(q)$ and then probing the velocity distribution of the particles. This is not possible with ordinary ballistic expansion because the reduction of the interactions is too slow, taking place on a time scale of the trapping period. However, the use of a Feshbach resonance [15] would provide an effective method for suddenly reducing the mean-field interaction.

In conclusion, we have experimentally analyzed the phonon wave function in a Bose-Einstein condensate. Following recent theoretical work [5], the two-component character of Bogoliubov quasiparticles was observed in the frequency domain (Fig. 2). In addition, the momentum components of the phonon wave function were discriminated by their final momenta after the probe pulse (Fig. 1). By combining momentum and frequency

selectivity, we were able to directly photograph the Bogoliubov transformation (Fig. 1d), demonstrating the power of Bragg spectroscopy to analyze nontrivial wave functions. This method may also be applicable to studying the many-body and vortex states [8] of dilute atomic Bose-Einstein condensates.

This work was funded by ONR, NSF, ARO, NASA, and the David and Lucile Packard Foundation. We are grateful to A. Brunello and S. Stringari for insightful discussions.

*Current address: School of Physics, Georgia Institute of Technology, Atlanta, Georgia 30332.

†Group website: http://cua.mit.edu/ketterle_group/

- [1] N. N. Bogoliubov, J. Phys. (USSR) **11**, 23 (1947).
- [2] A. Einstein, Sitzungsber. Preuss. Akad. Wiss. Bericht **3**, 18 (1925).
- [3] L. D. Landau, J. Phys. (USSR) **5**, 71 (1941).
- [4] N. Birell and P. Davies, *Quantum Fields in Curved Space* (Cambridge University Press, Cambridge, UK, 1982).
- [5] A. Brunello, F. Dalfovo, L. Pitaevskii, and S. Stringari, Phys. Rev. Lett. **85**, 4422 (2000).
- [6] D. M. Stamper-Kurn, A. P. Chikkatur, A. Görlitz, S. Inouye, S. Gupta, D. E. Pritchard, and W. Ketterle, Phys. Rev. Lett. **83**, 2876 (1999).
- [7] J. Stenger, S. Inouye, A. P. Chikkatur, D. M. Stamper-Kurn, D. E. Pritchard, and W. Ketterle, Phys. Rev. Lett. **82**, 4569 (1999).
- [8] F. Zambelli, L. Pitaevskii, D. M. Stamper-Kurn, and S. Stringari, Phys. Rev. A **61**, 063608 (2000).
- [9] P. B. Blakie, R. J. Ballagh, and C. W. Gardiner, cond-mat/0108480.
- [10] K. Huang, *Statistical Mechanics* (Wiley, New York, 1987).
- [11] R. Onofrio, D. S. Durfee, C. Raman, M. Köhl, C. E. Kulewicz, and W. Ketterle, Phys. Rev. Lett. **84**, 810 (2000).
- [12] A. P. Chikkatur, A. Görlitz, D. M. Stamper-Kurn, S. Inouye, S. Gupta, and W. Ketterle, Phys. Rev. Lett. **85**, 483 (2000).
- [13] S. Inouye, A. P. Chikkatur, D. M. Stamper-Kurn, J. Stenger, D. E. Pritchard, and W. Ketterle, Science **285**, 571 (1999).
- [14] E. W. Hagley, L. Deng, M. Kozuma, J. Wen, K. Helmerson, S. L. Rolston, and W. D. Phillips, Science **283**, 1706 (1999).
- [15] S. Inouye, M. R. Andrews, J. Stenger, H.-J. Miesner, D. M. Stamper-Kurn, and W. Ketterle, Nature (London) **392**, 151 (1998).

Appendix B

Generation of Macroscopic Pair-Correlated Atomic Beams by Four-Wave Mixing in Bose-Einstein Condensates

This appendix reprints Ref. [39]: J.M. Vogels, K. Xu, and W. Ketterle, *Generation of Macroscopic Pair-Correlated Atomic Beams by Four-Wave Mixing in Bose-Einstein Condensates*, Phys. Rev. Lett. **89**, 020401 (2002).

Generation of Macroscopic Pair-Correlated Atomic Beams by Four-Wave Mixing in Bose-Einstein Condensates

J. M. Vogels, K. Xu, and W. Ketterle*

*Department of Physics, MIT-Harvard Center for Ultracold Atoms,
Research Laboratory of Electronics, Massachusetts Institute of Technology, Cambridge, Massachusetts 02139*

(Received 13 March 2002; published 24 June 2002)

By colliding two Bose-Einstein condensates, we have observed strong bosonic stimulation of the elastic scattering process. When a weak input beam was applied as a seed, it was amplified by a factor of 20. This large gain atomic four-wave mixing resulted in the generation of two macroscopically occupied pair-correlated atomic beams.

DOI: 10.1103/PhysRevLett.89.020401

PACS numbers: 05.30.Jp, 03.75.Fi, 32.80.-t, 67.40.Db

In a gaseous Bose-Einstein condensate (BEC), all the atoms occupy the ground state of the system [1]. Once BEC has been achieved, the initial well-defined quantum state can be transformed into other more complex states by manipulating it with magnetic and optical fields. This can result in a variety of time-dependent macroscopic wave functions [1], including oscillating condensates, multiple condensates moving relative to each other, an output coupler, and rotating condensates with vortex lattices. Such macroscopically occupied quantum states represent classical matter-wave fields in the same way an optical laser beam is a classical electromagnetic wave. The next major step involves engineering nonclassical states of atoms that feature quantum entanglement and correlations. These states are important for quantum information processing, subshot noise precision measurements [2], and tests of quantum nonlocality.

Quantum correlations in the BEC ground state have been observed in a BEC held in optical lattices [2–4]. The repulsive interactions between the atoms within each lattice site force the occupation numbers to equalize, resulting in a number squeezed state. Alternatively, correlations in a BEC can be created in a dynamic or transient way through interatomic collisions. At the low densities typical of current experiments, binary collisions dominate, creating correlated pairs of atoms. Because of momentum conservation, the pair-correlated atoms scatter into modes with opposite momenta in the center-of-mass frame, resulting in squeezing of the number difference between these modes [5–7]. Our work is an implementation of the suggestions in Refs. [5,6]. However, we use elastic scattering processes instead of spin flip collisions to create pair correlations because the elastic collision rate is much higher than the spin flip rate. This was essential to observe large amplification before further elastic collisions led to losses.

Elastic scattering between two BEC's produces a collisional halo [8], where the number of atoms moving into opposing solid angles is the same, corresponding to number squeezing. Once these modes are occupied, the scattering process is further enhanced by bosonic stimulation. The onset of such an enhancement was observed in Ref. [8].

In this paper, we report strong amplification, corresponding to a gain of at least 20. Based on a theoretical prediction [6], which drew an analogy to optical superradiance [9], we expected to obtain a highly anisotropic gain using our cigar-shaped condensate. However, this mechanism of mode selection proved to be irrelevant for our experiment, because atoms do not leave the condensate during amplification (see below). Instead, we preselected a single pair-correlated mode by seeding it with a weak third matter wave, and observed that up to 40% of the atoms scattered into it. Because the scattered atoms are perfectly pair correlated, the only fluctuations in the number difference between the two beams stem from number fluctuations in the initial seed. Therefore, an observed gain of 20 implies that we have improved upon the shot-noise limit by a factor of $\sqrt{40}$, although this was not directly observed. Such a four-wave mixing process with matter waves had only been observed previously with a gain of 1.5 [10,11].

This experiment was performed with sodium condensates of ~ 30 million atoms in a cigar-shaped magnetic trap with radial and axial trap frequencies of 80 and 20 Hz, respectively. Such condensates had a mean field energy of 4.4 kHz, a speed of sound of 9 mm/s, and radial and axial Thomas-Fermi radii of 25 and 100 μm , respectively. The second condensate and the seed wave were generated by optical Bragg transitions to other momentum states. Figure 1 shows the geometry of the Bragg beams. Four laser beams were derived from the same laser that was 100 GHz red detuned from the sodium D_2 line. The large detuning prevented optical superradiance [9]. All beams propagated at approximately the same angle of ~ 0.35 rad with respect to the long axis of the condensate, and could be individually switched on and off to form beam pairs to excite two-photon Bragg transitions [12] at different recoil momenta.

The seed wave was created by a weak 20 μs Bragg pulse of beams with momenta \mathbf{p}_3 and \mathbf{p}_2 , which coupled 1%–2% of the atoms into the momentum state $\mathbf{k}_s = \mathbf{p}_3 - \mathbf{p}_2$, with a velocity ~ 15 mm/s. Subsequently, a 40 μs $\pi/2$ pulse of beams \mathbf{p}_1 and \mathbf{p}_2 splits the condensate into two strong source waves with momenta $\mathbf{k}_1 = 0$

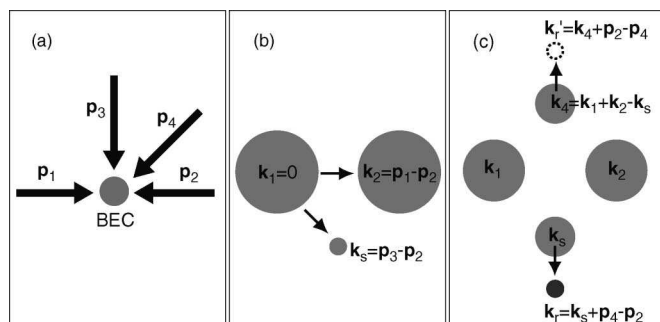


FIG. 1. Arrangement of laser beams to generate three atomic wave packets: (a) Four Bragg beams intersected at the condensate. (b) Two source waves and a small seed were created with Bragg beam pairs. (c) The four-wave mixing process amplified the seed and created a fourth wave. Both were subsequently read out with another Bragg pulse. The figures are projections on a plane perpendicular to the condensate axis. All wave packets move within this plane.

and $\mathbf{k}_2 = \mathbf{p}_1 - \mathbf{p}_2$ (see Fig. 1b), corresponding to a relative velocity of ~ 20 mm/s. The four-wave mixing process involving these three waves led to an exponential growth of the seed wave, while a fourth conjugate wave at momentum $\mathbf{k}_4 = \mathbf{k}_1 + \mathbf{k}_2 - \mathbf{k}_s$ emerged and also grew exponentially (Fig. 1c). The Bragg beams were arranged in such a way that the phase matching condition was fulfilled [the sum of the kinetic energies of the source waves (~ 11 kHz) matched the energy of the seed and the fourth wave]. The effect of any energy mismatch on the process will be discussed later. The four-wave mixing process was analyzed by absorption imaging [1]. Figure 2c shows the key result of this paper qualitatively: A small seed and its conjugate wave were amplified to a size where a significant fraction of the initial condensate atoms had been transferred into this pair-correlated mode.

To study this process, we applied “readout” beams \mathbf{p}_2 and \mathbf{p}_4 for $40 \mu\text{s}$, interrupting the amplification after a variable growth period between 0 and $600 \mu\text{s}$. {Turning off the trap after a variable amount of time is insuf-

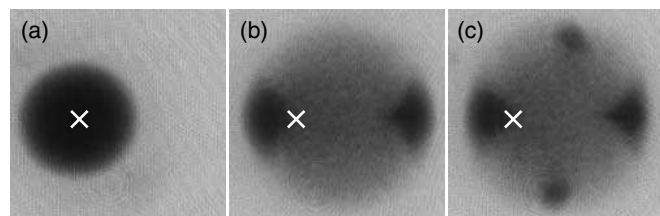


FIG. 2. High-gain four-wave mixing of matter waves. The wave packets separated during 43 ms of ballistic expansion. The absorption images [1] were taken along the axis of the condensate. (a) Only a 1% seed was present (barely visible), (b) only two source waves were created and no seed, and (c) two source waves and the seed underwent the four-wave mixing process where the seed wave and the fourth wave grew to a size comparable to the source waves. The gray circular background consists of spontaneously emitted atom pairs that were subsequently amplified to around 20 atoms per mode. The crosses mark the center position of the unperturbed condensate. The field of view is 1.8 mm wide.

ficient in this case because the density decreases on the time scale of the trapping period [$1/(80 \text{ Hz})$], while the amplification occurs more rapidly.} The frequency difference between the two readout beams was selected such that a fixed fraction of the seed (fourth) wave was coupled out to a different momentum state $\mathbf{k}_r = \mathbf{k}_s + \mathbf{p}_4 - \mathbf{p}_2$ ($\mathbf{k}'_r = \mathbf{k}_4 + \mathbf{p}_2 - \mathbf{p}_4$) (Fig. 1c). \mathbf{k}_r or \mathbf{k}'_r did not experience further amplification due to the constraint of energy conservation and therefore could be used to monitor the atom number in the seed (fourth) wave during the four-wave mixing process (Fig. 3).

The growth of the 2% seed and the fourth wave are shown in Fig. 4. As expected, the growth rates were found to increase with the mean field energy. Eventually, the amplification slowed down and stopped as the source waves were depleted. This is in contrast to Ref. [10,13], where the mixing process was slow (due to much lower mean field energy), and the growth time was limited by the overlap time of the wave packets. In our experiment, the overlap time was ≥ 1.8 ms, whereas the growth stopped already after $\leq 500 \mu\text{s}$.

A simple model describes the salient features of the process. The Hamiltonian of a weakly interacting Bose condensate is given by [11]

$$H = \sum_{\kappa} \frac{\hbar^2 \kappa^2}{2m} \hat{a}_{\kappa}^{\dagger} \hat{a}_{\kappa} + \frac{2\pi \hbar^2 a}{mV} \sum_{\substack{\kappa_1 + \kappa_2 \\ = \kappa_3 + \kappa_4}} \hat{a}_{\kappa_1}^{\dagger} \hat{a}_{\kappa_2}^{\dagger} \hat{a}_{\kappa_3} \hat{a}_{\kappa_4}, \quad (1)$$

where κ denotes the wave vectors of the plane wave states, m is the mass, V is the quantization volume, \hat{a}_{κ_i} is the annihilation operator, and $a = 2.75$ nm is the scattering length. If two momentum states \mathbf{k}_1 and \mathbf{k}_2 are highly occupied relative to all other states (with occupation numbers N_1 and N_2), the initial depletion of \mathbf{k}_1 and \mathbf{k}_2 can be neglected. Therefore, the only interactions are mean field interactions (self-interactions) and scattering involving \mathbf{k}_1 and \mathbf{k}_2 . In the Heisenberg picture, the difference between the

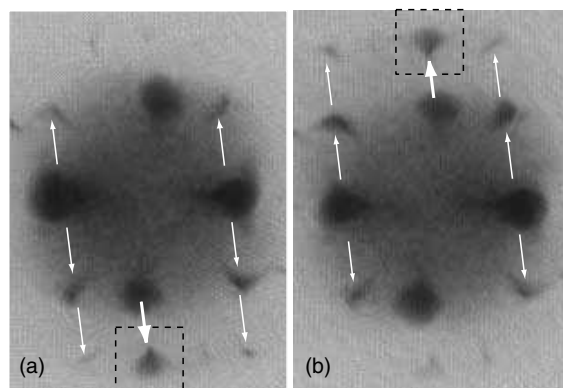


FIG. 3. Absorption images after a readout pulse was applied to (a) the seed wave and (b) the fourth wave. The thick arrows indicate the readout process. The readout pulse was kept short ($40 \mu\text{s}$), resulting in a large Fourier bandwidth and off-resonant coupling to other wave packets indicated by the narrow arrows. However, this did not affect the readout signal (atoms in the dashed box).

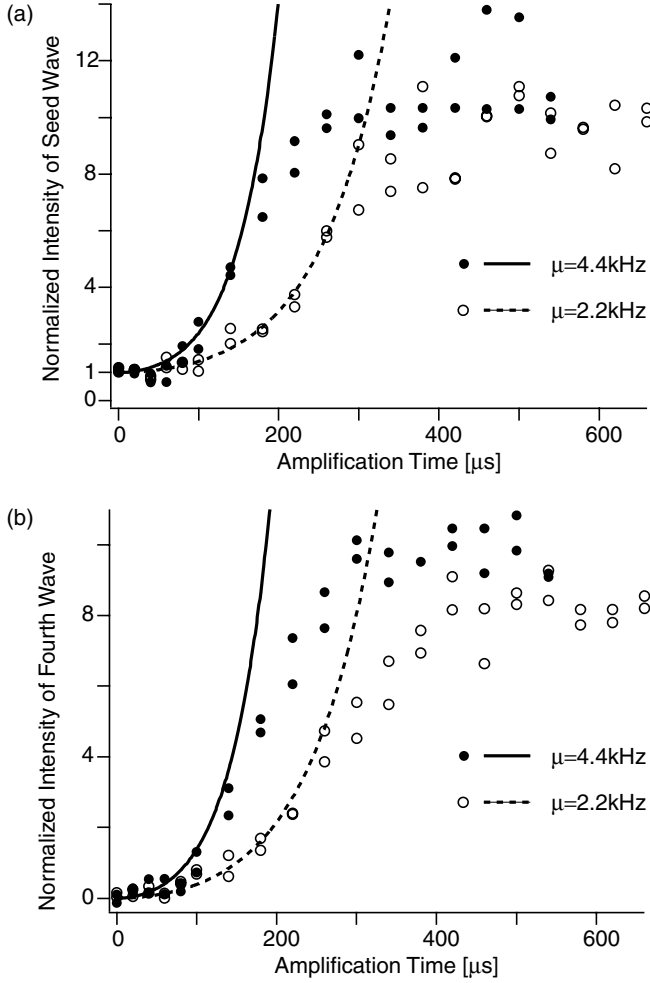


FIG. 4. Generation of pair-correlated atomic beams. The growth of (a) a 2% seed and (b) its conjugate fourth wave are shown for two different chemical potentials μ . The intensities of the waves were determined by counting the number of atoms in the dashed boxes in Fig. 3 and were normalized to the intensity of the initial seed. The solid lines and dashed lines are fits to the initial growth according to Eq. (4) with growth rates of $(170 \mu\text{s})^{-1}$ and $(100 \mu\text{s})^{-1}$, respectively.

occupations of the mode pairs $\Delta\hat{n} = \hat{a}_{\kappa_1}^\dagger \hat{a}_{\kappa_1} - \hat{a}_{\kappa_2}^\dagger \hat{a}_{\kappa_2}$ is time independent for any $\kappa_1 + \kappa_2 = \mathbf{k}_1 + \mathbf{k}_2$. Therefore, the fluctuations in the number difference $\langle \Delta\hat{n}^2 \rangle - \langle \Delta\hat{n} \rangle^2$ remain constant even though the occupations grow in time. The result is two-mode number squeezing. This is equivalent to a nondegenerate parametric amplifier; the Hamiltonians for both systems are identical [14].

When calculating the occupations $\langle \hat{a}_{\kappa_1}^\dagger \hat{a}_{\kappa_1} \rangle$, $\langle \hat{a}_{\kappa_2}^\dagger \hat{a}_{\kappa_2} \rangle$ and the correlation $\langle \hat{a}_{\kappa_1} \hat{a}_{\kappa_2} \rangle$, the relevant physical parameters are

$$\bar{\mu} = \sqrt{\mu_1 \mu_2}, \quad \mu_i = \frac{4\pi\hbar^2 a}{mV} N_i \quad (i = 1, 2),$$

$$\Delta\omega = \frac{\hbar\kappa_1^2}{2m} + \frac{\hbar\kappa_2^2}{2m} - \frac{\hbar\mathbf{k}_1^2}{2m} - \frac{\hbar\mathbf{k}_2^2}{2m} + \frac{\mu_1}{\hbar} + \frac{\mu_2}{\hbar}, \quad (2)$$

where $\bar{\mu}$ is the (geometric) average mean field energy of the two source waves, and $\hbar\Delta\omega$ is the energy mismatch for the scattering of atoms from states \mathbf{k}_1 and \mathbf{k}_2 to states

κ_1 and κ_2 . One obtains exponential growth for κ_1 and κ_2 if $\bar{\mu} > \hbar\Delta\omega/4$, and the growth rate is given by

$$\eta = \sqrt{\left(\frac{2\bar{\mu}}{\hbar}\right)^2 - \left(\frac{\Delta\omega}{2}\right)^2}. \quad (3)$$

For our initial conditions with s atoms in the seed wave \mathbf{k}_s and an empty fourth wave \mathbf{k}_4 , the correlation $\langle \hat{a}_{\mathbf{k}_s} \hat{a}_{\mathbf{k}_4} \rangle$ starts to grow as

$$\langle \hat{a}_{\mathbf{k}_s} \hat{a}_{\mathbf{k}_4} \rangle = \frac{2\bar{\mu}\sqrt{4\bar{\mu}^2 \cosh(\eta t)^2 - \frac{\Delta\omega^2}{4}}}{\eta^2} \times \sinh(\eta t)(s + 1).$$

This leads to exponential growth of the occupation numbers [10,13]:

$$\langle \hat{a}_{\mathbf{k}_s}^\dagger \hat{a}_{\mathbf{k}_s} \rangle = \left[\frac{2\bar{\mu}}{\hbar\eta} \sinh(\eta t) \right]^2 (s + 1) + s, \quad (4)$$

$$\langle \hat{a}_{\mathbf{k}_4}^\dagger \hat{a}_{\mathbf{k}_4} \rangle = \left[\frac{2\bar{\mu}}{\hbar\eta} \sinh(\eta t) \right]^2 (s + 1).$$

Equations (3) and (4) show that, for a large mean field energy $\bar{\mu}$, $\Delta\omega$ can be quite large without suppressing the four-wave mixing process. When $\Delta\omega > 4\bar{\mu}/\hbar$, one has to replace the hyperbolic sine functions in Eq. (4) with sine functions and η in Eq. (3) with $\sqrt{(\Delta\omega/2)^2 - (2\bar{\mu}/\hbar)^2}$. The occupations in states \mathbf{k}_s and \mathbf{k}_4 still grow initially, but then they begin to oscillate. The above solution also applies to initially empty modes with $s = 0$.

We can estimate the maximum growth rate $(2\bar{\mu}/\hbar)$ for our experiment by using the average mean field energy across the condensate to obtain $(53 \mu\text{s})^{-1}$ for high and $(110 \mu\text{s})^{-1}$ for low mean field energy. The experimental data exhibit a somewhat slower growth rate of $(100 \mu\text{s})^{-1}$ and $(170 \mu\text{s})^{-1}$, respectively. This discrepancy is not surprising since our theoretical model does not take into account depletion and possible decoherence processes due to the finite size and inhomogeneity of a magnetically trapped condensate. We also observed that the angles of the Bragg beams and therefore the energy mismatch $\Delta\omega$ could be significantly varied without substantially affecting the four-wave mixing process, confirming the robustness [see Eq. (3)] of four-wave mixing.

In addition to the four distinct wave packets, Fig. 2 also shows a circular background of atoms that are scattered from the source waves \mathbf{k}_1 and \mathbf{k}_2 into other pairs of initially empty modes κ_1 and κ_2 ($\kappa_1 + \kappa_2 = \mathbf{k}_1 + \mathbf{k}_2$). The scattered atoms lie on a spherical shell in momentum space centered at $(\mathbf{k}_1 + \mathbf{k}_2)/2$ with a radius $|\mathbf{k}|$ close to $|\mathbf{k}_1 - \mathbf{k}_2|/2$ and a width $|\Delta\mathbf{k}| \sim m\sqrt{2\pi\bar{\mu}/t\hbar^3}/|\mathbf{k}|$ [13]. As time progresses, the thickness $|\Delta\mathbf{k}|$ narrows due to the exponential gain.

Eventually, the population of these background modes contributes to the depletion of the source waves. One can estimate the depletion time t_d of the source waves by comparing the total population in these modes to the original number of atoms. This sets a theoretical limit on the gain $G = e^{4\bar{\mu}t_d/\hbar}/4$ given by $4G/\sqrt{\ln(4G)} = \sqrt{2\pi}/|\mathbf{k}|a$. For

our geometry $|\mathbf{k}|a = 0.01$ and $G = 160$. In our condensate of 3×10^7 atoms, this maximum gain is achieved when all the atoms are scattered into the 9×10^4 pair modes in the momentum shell. With a 1% seed, the source waves are depleted earlier, leading to a maximum gain of 37, where we measured a gain of 20. For a 2% seed the measured gain was 10 (see Fig. 4).

In our experiment, we deliberately reduced the velocity between the two source waves to twice the speed of sound in order to increase G and also the overlap time between the two source waves. Under these circumstances, the thickness of the shell $|\Delta\mathbf{k}|$ becomes close to its radius, accounting for the uniform background of scattered atoms rather than the thin s -wave halo observed in Ref. [8]. For velocities around or below the speed of sound, the condensate will not separate from the other waves in ballistic expansion.

Once the amplified modes are populated, losses due to further collisions occur at a rate $\Gamma \sim 8\pi a^2 n \hbar |\mathbf{k}|/m$ per atom (n is the number density of atoms). In order to have net gain, the growth rate η should be greater than Γ , which is the case since $\eta/\Gamma = 1/|\mathbf{k}|a = 100 \gg 1$. Furthermore, we begin to lose squeezing when $s + 1$ atoms are lost from the mode pair that occurs approximately at a gain of $e^{4\mu t/\hbar}/4 = 1/|\mathbf{k}|a$. At this point, the condensate is already highly depleted. In our experiment, however, the shell of amplified modes is so thick that it includes many of the modes into which atoms are scattered and increases the scattering rate by bosonic stimulation. Ideally, the atomic beams should separate after maximum gain is achieved. However, for our condensate size, the waves overlap for a much longer time and suffer collisional losses. This is visible in Fig. 2, where 40% of the atoms were transferred to the seeded mode pair, but only $\sim 10\%$ survived the ballistic expansion.

The collisional amplification process studied here bears similarities to the superradiant Rayleigh scattering of light from a Bose condensate [9], where correlated photon-atom pairs are generated in the end-fire mode for the photons and the corresponding recoil mode for the atoms. However, there are significant differences between the two processes. In optical superradiance, the scattered photons leave the condensate very quickly, causing only the recoiled atoms to maintain the coherence and undergo exponential growth. This physical situation is reflected in the Markov approximation adopted in Refs. [6,15]. In contrast, the atoms move slowly in collisional amplification, and the Markov approximation does not hold (although it was applied in Ref. [6]). The energy uncertainty $\Delta E = \hbar/\Delta t$ for a process of duration Δt gives a longitudinal momentum width of $\Delta E/v$, where v is the speed of light for photons or the velocity of the scattered atoms. This shows that optical superradiance is much more momentum selective: The shell in momentum space is infinitesimally thin, and only the atomic modes with maximal overlap with this shell are selected. In contrast, the shell in collisional amplification is many modes thick and does not lead to strong mode

selection. Moreover, in optical superradiance the light is coherently emitted by the entire condensate, whereas collisional amplification reflects only local properties of the condensate, because the atoms do not move significantly compared to the size of the condensate. Therefore, features like growth rate, maximum amplification, and even whether mode pairs stay squeezed do not depend on global parameters such as size or shape.

In conclusion, we have observed high gain in atomic four-wave mixing and produced pair-correlated atomic beams. We have also identified some limitations for using collisions to create such twin beams, including loss by subsequent collisions, and competition between other modes with similar gain.

We thank Michael Moore for useful discussions and for sending us early drafts of his recent theory paper [16]. The conclusions of his paper agree with ours. We also thank James Anglin and Peter Zoller for helpful interactions, Jamil Abo-Shaeer for experimental assistance, and Jit Kee Chin for critical reading of the manuscript. This work was funded by ONR, NSF, ARO, NASA, and the David and Lucile Packard Foundation.

*Group website: http://cua.mit.edu/ketterle_group/

- [1] *Bose-Einstein Condensation in Atomic Gases*, Proceedings of the International School of Physics "Enrico Fermi," Course CXL, edited by M. Inguscio, S. Stringari, and C. E. Wieman (IOS Press, Amsterdam, 1999).
- [2] C. Orzel, A. K. Tuchman, M. L. Fenselau, M. Yasuda, and M. A. Kasevich, *Science* **291**, 2386 (2001).
- [3] D. Jaksch, H. J. Briegel, J. I. Cirac, C. W. Gardiner, and P. Zoller, *Phys. Rev. Lett.* **82**, 1975 (1999).
- [4] M. Greiner, O. Mandel, T. Esslinger, T. W. Hänsch, and I. Bloch, *Nature (London)* **415**, 30 (2002).
- [5] L.-M. Duan, A. Sørensen, J. I. Cirac, and P. Zoller, *Phys. Rev. Lett.* **85**, 3991 (2000).
- [6] H. Pu and P. Meystre, *Phys. Rev. Lett.* **85**, 3987 (2000).
- [7] A. Sørensen, L.-M. Duan, J. I. Cirac, and P. Zoller, *Nature (London)* **409**, 63 (2001).
- [8] A. P. Chikkatur, A. Görlitz, D. M. Stamper-Kurn, S. Inouye, S. Gupta, and W. Ketterle, *Phys. Rev. Lett.* **85**, 483 (2000).
- [9] S. Inouye, A. P. Chikkatur, D. M. Stamper-Kurn, J. Stenger, D. E. Pritchard, and W. Ketterle, *Science* **285**, 571 (1999).
- [10] L. Deng, E. W. Hagley, J. Wen, M. Trippenbach, Y. Band, P. S. Julienne, J. E. Simsarian, K. Helmerson, S. L. Rolston, and W. D. Phillips, *Nature (London)* **398**, 218 (1999).
- [11] M. Trippenbach, Y. B. Band, and P. S. Julienne, *Phys. Rev. A* **62**, 023608 (2000).
- [12] J. Stenger, S. Inouye, A. P. Chikkatur, D. M. Stamper-Kurn, D. E. Pritchard, and W. Ketterle, *Phys. Rev. Lett.* **82**, 4569 (1999).
- [13] V. A. Yurovsky, *Phys. Rev. A* **65**, 033605 (2002).
- [14] D. F. Walls and G. J. Milburn, *Quantum Optics* (Springer-Verlag, Berlin, 1995).
- [15] M. G. Moore and P. Meystre, *Phys. Rev. Lett.* **83**, 5202 (1999).
- [16] A. Vardi and M. G. Moore, cond-mat/0201590.

Appendix C

Formation of Quantum-Degenerate Sodium Molecules

This appendix reprints Ref. [118]: K. Xu, T. Mukaiyama, J.R. Abo-Shaeer, J.K. Chin, D.E. Miller, and W. Ketterle, *Formation of Quantum-Degenerate Sodium Molecules*, Phys. Rev. Lett. **91**, 210402 (2003).

Formation of Quantum-Degenerate Sodium Molecules

K. Xu, T. Mukaiyama, J. R. Abo-Shaeer, J. K. Chin, D. E. Miller, and W. Ketterle

*Department of Physics, MIT-Harvard Center for Ultracold Atoms, and Research Laboratory of Electronics, MIT,
Cambridge, Massachusetts 02139, USA*

(Received 1 October 2003; published 21 November 2003)

Ultracold sodium molecules were produced from an atomic Bose-Einstein condensate by ramping an applied magnetic field across a Feshbach resonance. More than 10^5 molecules were generated with a conversion efficiency of $\sim 4\%$. Using laser light resonant with an atomic transition, the remaining atoms could be selectively removed, preventing fast collisional relaxation of the molecules. Time-of-flight analysis of the pure molecular sample yielded an instantaneous phase-space density greater than 20.

DOI: 10.1103/PhysRevLett.91.210402

PACS numbers: 03.75.Nt, 32.80.Pj, 33.80.Ps, 34.20.Cf

Atomic Bose-Einstein condensates (BEC) provide a new window into macroscopic quantum phenomena [1]. A molecular condensate could lead to a host of new scientific explorations. These include quantum gases with anisotropic dipolar interactions, tests of fundamental symmetries such as the search for a permanent electric dipole moment, study of rotational and vibrational energy transfer processes, and coherent chemistry, where reactants and products are in coherent quantum superposition states. So far, the highly successful techniques for creating atomic BEC have not led to success for molecules. Laser cooling is difficult due to the complicated level structure of molecules [2], and evaporative cooling requires the preparation of a dense gas of molecules, where elastic collisions dominate inelastic collisions.

Alternative techniques, such as buffer gas loading [3] and Stark deceleration [4], have been successful in obtaining cold molecules. Yet these methods are still far from achieving the requisite phase-space density for BEC. The difficulty in cooling molecules directly can be circumvented by creating ultracold molecules from quantum-degenerate atomic samples. This requires molecule formation without release of energy, which can be accomplished either by photoassociation [5] or by “tuning” a molecular state via a Feshbach resonance [6] to be degenerate with the atomic state. A Feshbach resonance occurs when an applied magnetic field Zeeman shifts a molecular state to zero binding energy. By ramping an external field across a Feshbach resonance from negative to positive scattering length, translationally cold molecules in high vibrational states can be created adiabatically [7–9].

The first observation of a Feshbach resonance in ultracold atoms showed a high rate of atom loss [6,10]. Theories accounted for this loss by assuming the formation of ultracold molecules [7,8,11]. These molecules were predicted to decay vibrationally in less than $100 \mu\text{s}$ due to a two-body rate coefficient of order $10^{-10} \text{ cm}^3/\text{s}$. Because of this, no successful attempt was made to detect a molecular signature until atom-molecule beats were observed in ^{85}Rb , lasting about $100 \mu\text{s}$ [12]. Recent fermion experiments using magnetic field sweeps have ob-

served molecules with lifetimes approaching 1 s [13–16]. Until now, similar experiments with bosons have been carried out only during ballistic expansion [17,18]. According to theory, the decay of molecules composed of fermionic atoms is suppressed by Pauli blocking [19], whereas molecules composed of bosons decay rapidly. This could explain the low conversion efficiency of about 5% for bosons, compared to $> 50\%$ for fermions, where more adiabatic field ramps are possible.

If highly degenerate atoms (both fermionic and bosonic) are converted adiabatically to molecules, the molecules can be created at a phase-space density exceeding 2.6, the critical value at which a uniform, ideal Bose gas condenses [20]. Previous experiments [14,18,21] have measured or estimated conditions close to or around this critical phase-space density.

Here we report the production of trapped sodium molecules from an atomic BEC. The initial phase-space density of the molecular sample was measured in excess of 20. High phase-space density could only be achieved by rapidly removing residual atoms, before atom-molecule collisions caused trap loss and heating. This was accomplished by a new technique for preparing pure molecular clouds, where light resonant with an atomic transition selectively “blasted” unpaired atoms from the trap. In contrast to spatial separation via a Stern-Gerlach method [17,18], this technique can separate out the molecules faster and does not require a large difference in the magnetic moments of the atoms and molecules.

To generate the molecules, sodium condensates in the $|F = 1, m_F = -1\rangle$ state were prepared in an optical dipole trap. The radial and axial trap frequencies of $\omega_r = 2\pi \times 290 \text{ Hz}$ and $\omega_z = 2\pi \times 2.2 \text{ Hz}$, respectively, gave Thomas-Fermi radii of $R_r = 5 \mu\text{m}$ and $R_z = 650 \mu\text{m}$, and a peak density of $1.7 \times 10^{14} \text{ cm}^{-3}$ for 5×10^6 atoms. An adiabatic radio frequency sweep was used to transfer the atoms into the $|1, 1\rangle$ state, which has a 1 G wide Feshbach resonance at 907 G [6,22].

After 1 s equilibration in the optical trap, the molecules were generated using the field ramping scheme illustrated in Fig. 1(a). An applied magnetic field was ramped in $\sim 100 \text{ ms}$ to 4 G below the 907 G Feshbach resonance.

The field was generated using a pair of large bias and small antibias coils. Because molecules are only created when sweeping across the resonance from negative to positive scattering length, the field was stepped up to 913 G as quickly as possible ($\sim 1 \mu\text{s}$) to jump over the resonance with minimal atom loss. After allowing 2.5 ms for transient field fluctuation to damp out, the field was ramped down in time τ_{down} . Because of atom-molecule coupling, part of the atomic population was transferred into the molecular state following the Landau-Zener avoided crossing. With the given width of the resonance and the atomic density, we use a simple Landau-Zener model to calculate a ramp speed of $\sim 10^4 \text{ G/s}$ to transfer roughly half the atoms to the molecular state [7,8,11]. However, inelastic collisions led to fast decay for both the atoms and the molecules near the resonance. We found that a faster ramp speed of $\sim 10^5 \text{ G/s}$ (corresponding to $\tau_{\text{down}} = 50 \mu\text{s}$) gave optimal results. The conversion efficiency of atoms to molecules was $\sim 4\%$. Slower ramp speeds resulted in a similar number of molecules, but at higher temperature [see Fig. 1(e)].

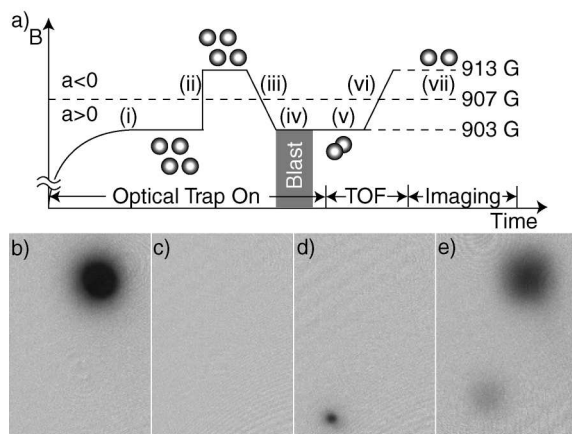


FIG. 1. (a) Experimental method for producing and detecting ultracold molecules. (i) Bose condensed atoms in an optical dipole trap are exposed to a magnetic field just below a Feshbach resonance. (ii) The field is quickly stepped through the resonance to minimize atom loss. (iii) The field is then swept back through the resonance, creating an atom-molecule mixture. (iv) Unpaired atoms are removed from the trap with resonant light, yielding a pure molecular sample. (v) The trap is switched off, allowing the molecules to expand ballistically. (vi) Finally, the magnetic field is swept back across the resonance to reconvert the molecules to atoms for imaging (vii). (b) Image of the *atomic* sample after ramping the field to produce molecules; (c) after the resonant light pulse has removed all unpaired atoms; (d) after the *molecules* ($\sim 10^5$) have been reconverted to atoms. (b),(c) were taken along the weak axis of the trap after 17 ms ballistic (time-of-flight-TOF) expansion. (e) An image showing both atomic (top) and molecular (bottom) clouds after 14 ms ballistic expansion, spatially separated by a magnetic field gradient. With 4 ms field ramp-down time, some molecules survived even without the blast pulse, but are much more heated. The field of view of each image is $1.8 \text{ mm} \times 1.3 \text{ mm}$.

The blast pulse was applied along the radial axis of the trap to minimize collisions between the escaping atoms and the molecules at rest. A $20 \mu\text{s}$ pulse of resonant light removed all atoms from the optical trap, leaving behind a pure molecular sample (see Fig. 1). At only 4 G below the Feshbach resonance, the light was still close to resonance with molecular photodissociation to low-velocity atoms, but the overlap matrix element was sufficiently diminished to leave the molecules unaffected. After a variable hold time, the optical trap was switched off and the molecules expanded ballistically for between 4 and 20 ms. The molecules were detected by converting them back to atoms with field ramp-up in $\tau_{\text{up}} = 100 \mu\text{s}$ at the end of expansion. Varying τ_{up} between $50 \mu\text{s}$ and 4 ms did not affect the recovered atom number, though shorter τ_{up} 's recovered atoms with larger kinetic energy [23]. Thus we assume all molecules are converted back to atoms. A resonant absorption image was taken after an additional $500 \mu\text{s}$, which allowed the imaging field to settle. The rapid conversion of molecules to atoms after a long expansion time ensured that the absorption images accurately depicted the momentum distribution of the *molecular cloud*.

Atoms and molecules were separated during the ballistic expansion by a Stern-Gerlach technique [Fig. 1(e)]. Because of trap imperfections, the large bias coils provided an additional radial gradient of the axial field of $\sim 2.8 \text{ G/cm}$ in the vicinity of the condensate. This value was determined from the trajectory of the falling atoms. Since the molecules have a different magnetic moment, they separate from the atoms during the ballistic expansion [Fig. 1(e)]. From the separation of the atomic and molecular clouds at different times, we determined the difference between atomic and molecular magnetic moments to be $3.2 \mu_B$ (μ_B is the Bohr magneton), in good agreement with theory [11].

For different ramp down times τ_{down} , the time-of-flight images of the molecular cloud exhibit drastically different momentum distribution. The coldest cloud was obtained with the fastest ramp down time possible, $\tau_{\text{down}} = 50 \mu\text{s}$ (Fig. 2). A Gaussian fit was used to determine the molecular temperature T_m and the phase-space density. Because of the rapid ramp down, the molecules had no time to adjust to the external trapping potential or any mean-field interactions. Therefore, we assume the molecules were *uniformly* created with the Thomas-Fermi profile of the original atomic BEC. The peak phase-space density is then given by

$$\text{PSD}_{\text{peak}} = \left(\frac{h}{\sqrt{2\pi k_B T_m M_m}} \right)^3 \frac{N_m}{\frac{8\pi}{15} R_r^2 R_z}, \quad (1)$$

where h is the Planck constant, k_B is the Boltzmann constant, M_m is the molecular mass, and N_m is the number of molecules. The second factor in the equation is the peak density for a Thomas-Fermi profile.

Figure 3(a) shows the phase-space densities obtained for different holding time in the optical trap. Phase-space

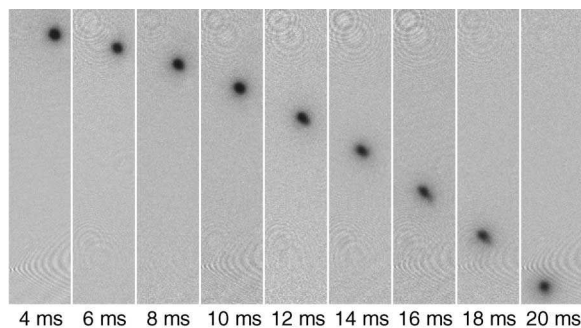


FIG. 2. Ballistic expansion of a pure molecular sample. Absorption images of molecular clouds (after reconversion to atoms) are shown for increasing expansion time after switching off the optical trap. The small expansion velocity corresponds to a temperature of ~ 30 nK, characteristic of high phase-space density. The images are taken along the weak axis of the trap. The field of view of each image is $3.0 \text{ mm} \times 0.7 \text{ mm}$.

densities in excess of 20 were observed, much larger than the critical value of 2.6. This demonstrates that a quantum-degenerate cloud of atoms can be transformed into a quantum-degenerate molecular gas.

The high initial phase-space density decayed rapidly (~ 2 ms), due to molecule loss and heating. For a pure molecular sample at a peak density of $4 \times 10^{12} \text{ cm}^{-3}$, the molecule number dropped by half in 5 ms and the apparent temperature doubled in 2 ms. Since the molecules are formed in a high vibrational state with quantum number $v = 14$, losses are most likely due to vibrational relaxation. The high loss rate of the molecules is consistent with theoretically predicted two-body relaxation rate coefficients of $10^{-10} \text{ cm}^3/\text{s}$ [9,24]. Because the loss of molecules is faster at the high densities near the bottom of the trap, it is accompanied by heating. This is in contrast to evaporative cooling, where the losses occur at the top of the trap. Such antievaporative heating gives a time con-

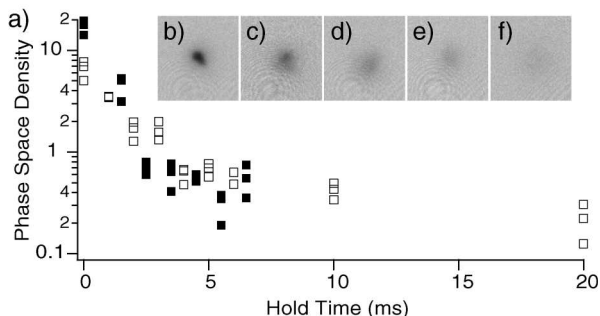


FIG. 3. Molecular phase-space density versus hold time. (a) The phase-space densities of the trapped molecules were observed to decrease significantly after a few milliseconds in the optical trap. The open and solid squares are data from two separate runs on different days. (b),(c) are absorption images of the molecular clouds after (b) 0 ms, (c) 2 ms, (d) 5 ms, (e) 10 ms, (f) 20 ms hold time in the trap. The field of view is $0.8 \text{ mm} \times 0.8 \text{ mm}$.

stant 4 times slower than the observed heating rate. We therefore believe that the rapid increase in the apparent temperature is due to the inward motion of the molecular cloud (see below), and possibly transfer of the vibrational energy of the molecules.

Our calculation of the phase-space density is conservative, since almost all errors lead to an underestimation of the value. The most critical quantity is the thermal velocity $v_{\text{therm}} = \sqrt{2k_B T_m / M_m}$ obtained from the Gaussian fit of the cloud, since the phase-space density scales with the third power of v_{therm} . We determined the velocity by simply dividing the size of the cloud by the time-of-flight, without correcting for imaging resolution and initial cloud size.

Correcting for the imaging resolution of $10 \mu\text{m}$ compared to the typical cloud size of $50 \mu\text{m}$ would increase the phase-space density measurement by 6%. In addition, radial excitation of the trapped cloud (shown in Fig. 4) contributed to the size of the cloud after the ballistic expansion. From the fits, the smaller of the two Gaussian radii was used to calculate v_{therm} , assuming that the larger size was caused by radial excitations. Yet since the radial excitation can occur in two orthogonal directions, we estimate that the extracted thermal velocities were still overestimated by $\sim 10\%$. We also considered magnetic focusing of the cloud due to residual field inhomogeneities. Because we use large coils (~ 17 cm in diameter and ~ 4 cm away from the condensate) to produce a homogeneous magnetic field, any residual radial curvature due to radial fields is calculated to be $\leq 0.1 \text{ G/cm}^2$. An upper bound for the radial curvature of the axial fields was obtained from trap frequency measurements and ballistic expansion measurements as $< 1 \text{ G/cm}^2$. This can only reduce the size of the cloud by less than 2% after a typical ballistic expansion time of 17 ms.

We assume resonant absorption in determining the number of atoms. Any systematic effect such as small detuning or saturation, would lower both N_m and the Thomas-Fermi volume (proportional to $N^{3/5}$, where N is the number of condensed atoms). The net effect is an underestimate of the phase-space density. In addition, because the molecular formation process is nonlinear in

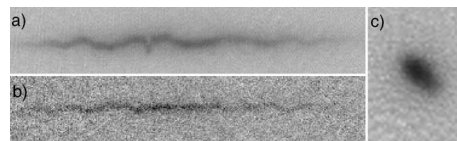


FIG. 4. Images of (a) atomic and (b) molecular clouds. These absorption images were taken after 7 ms ballistic expansion and show the axial extent of the clouds. Radial excitations in the optical trap resulting from the sudden switching of magnetic fields are manifest as snakelike patterns. Such excitations blur images (c) taken along the long axis of the trap (in 17 ms TOF), leading to an underestimate of the phase-space density. The fields of view are (a),(b) $0.6 \text{ mm} \times 3.2 \text{ mm}$, (c) $0.6 \text{ mm} \times 0.4 \text{ mm}$.

atomic density, the assumption of the atomic Thomas-Fermi volume for molecules is likely an overestimate. Furthermore, in the absence of strong mean-field repulsion (due to the much lower molecular density), the molecular cloud would not sustain the initial size of the atomic condensate [used in Eq. (1)], and shrink to a smaller size within a few milliseconds (\sim radial trap period). If we assume radial thermal equilibrium while keeping the axial length fixed (as the axial trap period is 500 ms), the phase-space density would be 2 to 4 times higher than is shown in Fig. 3. To sum up, the extracted peak phase-space densities are underestimated by $\geq 30\%$, and all other critical systematic effects would raise the value even further.

When a molecular cloud with high phase-space density equilibrates by elastic collisions, it should form a condensate. There is no prediction for the scattering length of the molecules, which are formed in the $|v = 14, l = 0\rangle$ state [25]. Assuming a prototypical scattering length of $100a_0$ (a_0 is the Bohr radius), we estimate the elastic collision rate between molecules to be 6 s^{-1} , which is smaller than our loss rate. Thus, the so-called ratio of good and bad collisions is smaller than 1.

Recent work on molecules composed of fermionic lithium [14,15] and potassium [26] atoms showed a dramatic increase in lifetime close to the Feshbach resonance. Theoretically, the rate of vibrational relaxation should decrease with the scattering length a_s as $\propto a_s^{-2.55}$ due to Pauli blocking [19]. In contrast, for molecules composed of bosonic atoms, the rate should increase proportionally to a_s [27]. On the other hand, the elastic collision rate is proportional to a_s^2 , so for large a_s one would expect the ratio of good-to-bad collisions to exceed one. However, if this condition is met at loss rates faster than the trap frequency, the cloud can only establish local, not global equilibrium.

Whether our molecular sample is a condensate depends on one's definition of BEC. If phase-space density in excess of 2.6 (corresponding to a diagonal matrix element of the single-particle density matrix larger than 1) is sufficient, then one may regard a short-lived atom-molecule superposition state [12] as a molecular BEC. However, following this definition, a small excited state admixture in an optically trapped BEC would qualify as BEC of electronically excited atoms. If one asks for the additional requirement of a pure molecular sample, we have achieved that in this work. Another definition would require phase coherence, which could again be observed even in short-lived samples. Should one also require a lifetime of the degenerate sample exceeding the collision time (to achieve local equilibrium), the trap period (to achieve global equilibrium), or the inverse mean-field energy (the typical dynamic timescale)? In our opinion, BEC requires thermal equilibrium. High phase-space density is necessary, but not sufficient.

In conclusion, we have created a quantum-degenerate gas of 10^5 cold sodium molecules with a phase-space

density >20 . This was achieved with a fast magnetic field sweep through a Feshbach resonance, followed by quick removal of the remnant atoms with resonant light. This purification was necessary to avoid heating and decay of the molecules through inelastic collision processes. These processes could also be avoided by loading the atomic BEC into an optical lattice in the Mott-insulator phase with a filling factor of 2 [28,29] which, after sweeping the magnetic field through the Feshbach resonance, would result in a long-lived sample of isolated molecules.

The authors would like to acknowledge M. Xue for experimental assistance with the project. We also thank A.E. Leanhardt and M.W. Zwierlein for their critical reading of the manuscript. This research is supported by NSF, ONR, ARO, NASA, and the David and Lucile Packard Foundation.

-
- [1] *Bose-Einstein Condensation in Atomic Gases*, Proceedings of the International School of Physics "Enrico Fermi," Course CXL, edited by M. Inguscio *et al.* (IOS Press, Amsterdam, 1999).
 - [2] J.T. Bahns *et al.*, *J. Chem. Phys.* **104**, 9689 (1998).
 - [3] J. D. Weinstein *et al.*, *Nature (London)* **395**, 148 (1998).
 - [4] H. L. Bethlem *et al.*, *Phys. Rev. Lett.* **83**, 1558 (1999).
 - [5] R. Wynar *et al.*, *Science* **287**, 1016 (2000).
 - [6] S. Inouye *et al.*, *Nature (London)* **392**, 151 (1998).
 - [7] F. H. Mies *et al.*, *Phys. Rev. A* **61**, 022721 (2000).
 - [8] F. A. van Abeelen and B. J. Verhaar, *Phys. Rev. Lett.* **83**, 1550 (1999).
 - [9] V. A. Yurovsky *et al.*, *Phys. Rev. A* **60**, R765 (1999).
 - [10] J. Stenger *et al.*, *Phys. Rev. Lett.* **82**, 2422 (1999).
 - [11] V. A. Yurovsky and A. Ben-Reuven, *Phys. Rev. A* **67**, 043611 (2003).
 - [12] E. Donley *et al.*, *Nature (London)* **417**, 529 (2002).
 - [13] C. A. Regal *et al.*, *Nature (London)* **424**, 47 (2003).
 - [14] J. Cubizolles *et al.*, cond-mat/0308018.
 - [15] S. Jochim *et al.*, cond-mat/0308095.
 - [16] K. E. Strecker *et al.*, *Phys. Rev. Lett.* **91**, 080406 (2003).
 - [17] S. Dürr *et al.*, cond-mat/0307440.
 - [18] J. Herbig *et al.*, *Science* **301**, 1510 (2003).
 - [19] D. S. Petrov *et al.*, cond-mat/0309010.
 - [20] K. Huang, *Statistical Mechanics* (Wiley, New York, 1987).
 - [21] R. Grimm, C. Salomon, and C. A. Regal, at EURESCO Conference on Bose-Einstein Condensation, San Feliu de Guixols, Spain, September 2003.
 - [22] F. A. van Abeelen and B. J. Verhaar, *Phys. Rev. A* **59**, 578 (1999).
 - [23] T. Mukaiyama *et al.* (to be published).
 - [24] P. Soldán *et al.*, *Phys. Rev. Lett.* **89**, 153201 (2002).
 - [25] A. J. Moerdijk, B. J. Verhaar, and A. Axelsson, *Phys. Rev. A* **51**, 4852 (1995).
 - [26] C. A. Regal *et al.*, cond-mat/0308606.
 - [27] D. S. Petrov (private communication).
 - [28] M. Greiner *et al.*, *Nature (London)* **415**, 39 (2002).
 - [29] D. Jaksch *et al.*, *Phys. Rev. Lett.* **89**, 040402 (2002).

Appendix D

Dissociation and Decay of Ultracold Sodium Molecules

This appendix reprints Ref. [177]: T. Mukaiyama, J.R. Abo-Shaeer, K. Xu, J.K. Chin, and W. Ketterle, *Dissociation and Decay of Ultracold Sodium Molecules*, Phys. Rev. Lett. **91**, 210402 (2003).

Dissociation and Decay of Ultracold Sodium Molecules

T. Mukaiyama, J. R. Abo-Shaeer, K. Xu, J. K. Chin, and W. Ketterle

*Department of Physics, MIT-Harvard Center for Ultracold Atoms,
and Research Laboratory of Electronics, Massachusetts Institute of Technology, Cambridge, Massachusetts 02139, USA*
(Received 24 November 2003; published 4 May 2004)

The dissociation of ultracold molecules was studied by ramping an external magnetic field through a Feshbach resonance. The observed dissociation energies directly yielded the strength of the atom-molecule coupling. They showed nonlinear dependence on the ramp speed. This was explained by a Wigner threshold law which predicts that the decay rate of the molecules above threshold increases with the density of states. In addition, inelastic molecule-molecule and molecule-atom collisions were characterized.

DOI: 10.1103/PhysRevLett.92.180402

PACS numbers: 03.75.Nt, 32.80.Pj, 33.80.Ps, 34.20.Cf

Recently, it has become possible to create ultracold molecular gases from precooled atomic samples [1–11]. Extending the ultralow temperature regime from atoms to molecules is an important step towards controlling the motion of more complicated objects. The complex structure of molecules may lead to new scientific opportunities, including the search for a permanent electric dipole moment, with sensitivity much higher than for heavy atoms [12], and the realization of quantum fluids of bosons and fermions with anisotropic interactions [13]. Furthermore, stable mixtures of atomic and molecular condensates are predicted to show coherent stimulation of atom-molecule or molecule-atom conversion, constituting quantum-coherent chemistry [14].

To date, all realizations of ultracold molecules (< 1 mK) have bypassed the need for direct cooling of the molecules, which is difficult due to the complicated rovibrational structure. Rather, molecules were formed from ultracold atoms using Feshbach resonances [2–11], where a highly vibrational excited molecular state is magnetically tuned into resonance with a pair of colliding atoms.

In this Letter, we study the dissociation and decay of such highly excited molecules. Figure 1 shows a schematic of the dissociation process. For magnetic fields above the Feshbach resonance, the molecular state crosses the free atomic states, shown here as discrete states in a finite quantization volume. The interaction between atoms and molecules turns these crossing into anticrossings. When the magnetic field is swept very slowly through the resonance, the molecules follow the adiabatic curve and end up in the lowest energy state of the atoms. For faster ramps, the molecular populations will partially cross some of the low-lying states, and the dissociation products will populate several atomic states. The stronger the coupling between the molecular state and the atomic states, the faster the molecules dissociate and the smaller the energy release in the dissociation. Observing the atom-molecule coupling in *one-body* decay (dissociation) is a new method to experimentally determine the strength

of a Feshbach resonance. Previous measurements used *two-* or *three-body* processes to characterize the Feshbach resonance and therefore required accurate knowledge of the atomic density distribution.

Collisional properties of the molecules were also studied. Inelastic collisions limit both the production of molecules and their lifetime. We observed loss of molecules by collisions both with atoms and other molecules. These two processes were studied by separating atoms and molecules with a short pulse of laser light [9].

To generate molecules, sodium condensates in the $|F, m_F\rangle = |1, -1\rangle$ state were prepared in an optical dipole trap. The trap frequencies of 290 Hz in the radial direction and 2.2 Hz in the axial direction yielded typical densities of $1.7 \times 10^{14} \text{ cm}^{-3}$ for 5×10^6 atoms. Atoms were then spin-flipped using an adiabatic radio frequency sweep to the $|1, 1\rangle$ state, where a 1 G wide Feshbach resonance exists at 907 G [15].

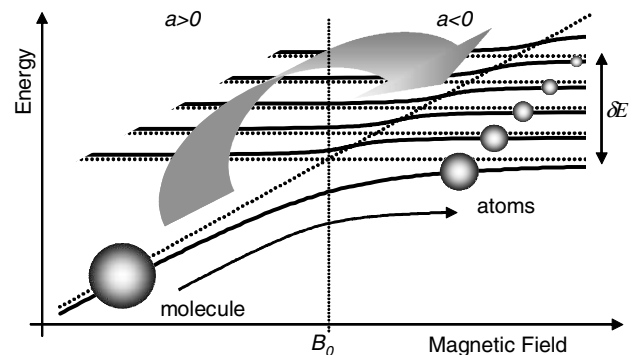


FIG. 1. Schematic diagram of energy levels for molecules and atoms. The diabatic energy levels are shown as dashed lines. The adiabatic curves (solid lines) include the atom-molecule coupling. When the magnetic field is swept from positive to negative scattering length, dissociated molecules end up in one or several atomic states, depending on the ramp rate of the magnetic field. The spheres represent the distribution of the population before and after the ramp.

The magnetic field sequence used to create and detect Na_2 molecules was identical to our previous work [9]. Briefly, the axial magnetic field was ramped to 903 G in 100 ms using two pairs of bias coils. In order to prepare the condensate on the negative scattering length side of the resonance, the field was stepped up to 913 G as quickly as possible ($\sim 1 \mu\text{s}$) to jump through the resonance with minimal atom loss. The field was then ramped back down to 903 G in 50 μs to form molecules. In order to remove nonpaired atoms from the trap, the sample was irradiated with a 20 μs pulse of resonant light. Because 903 G is far from the Feshbach resonance, the mixing between atomic and molecular states was small and therefore molecules were transparent to this “blast” pulse. By ramping the field back to 913 G molecules were converted back to atoms. Absorption images were taken at high fields (either at 903 or 913 G) after 10 to 17 ms ballistic expansion, with the imaging light incident along the axial direction of the condensate.

To study the momentum distribution of the back-converted atoms, the magnetic field was ramped up immediately after turning off the optical trap, or for a reference, at the end of the ballistic expansion. The difference between the energies of ballistic expansion is the released dissociation energy. Energies were obtained from the rms width of the cloud $\langle x^2 \rangle$ as $E = 3m\langle x^2 \rangle / 2t^2$, where t is the ballistic expansion time and m is the atomic mass. Figure 2 shows that faster field ramps created hotter atoms.

An earlier theoretical treatment assumes a constant predissociation lifetime of the molecules and predicts a linear relation between dissociation energy and field ramp rate [16]. This theory predicts a much faster dissociation (and therefore smaller dissociation energy) than was observed. Furthermore, our data show a nonlinear dependence. Linear behavior would be expected if the lifetime of the molecules was independent of the energy ϵ from the dissociation threshold. The fact that the slope be-

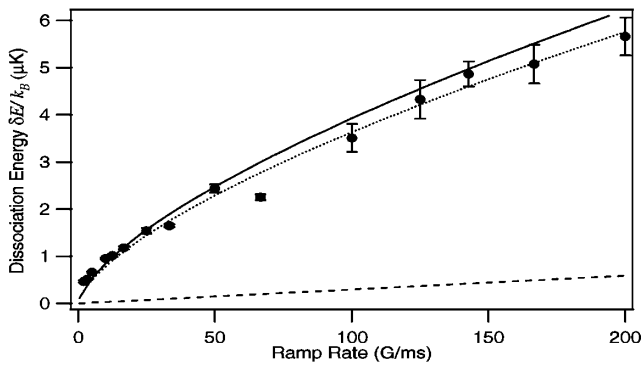


FIG. 2. Dissociation energy of molecules as a function of magnetic field ramp rate. The dashed line represents the linear relation described in Ref. [16], the solid line shows the result of our model using a theoretical value for $\Delta B = 0.98$ G and $a_{\text{bg}} = 3.4$ nm, and the dotted line shows a curve with the product $a_{\text{bg}}\Delta B$ as a fitting parameter.

comes smaller for increasing ramp rate indicates that the lifetime of molecules decreases with the ramp rate. As we show, this can be explained by an increase of the density of atomic states, leading to a $\sqrt{\epsilon}$ dependence of the molecular decay rate (Wigner threshold law [17]).

The decay rate $\Gamma(\epsilon)$ follows from Fermi's golden rule as $\hbar\Gamma(\epsilon) = 2\pi|V_{\text{ma}}(\epsilon)|^2 D(\epsilon)$ [18], where V_{ma} is the matrix element between atomic and molecular states, which to leading order is independent of ϵ . The density of states $D(\epsilon)$ is given by

$$D(\epsilon) = \frac{V}{(2\pi)^2} \left(\frac{m}{\hbar^2} \right)^{3/2} \epsilon^{1/2}, \quad (1)$$

where V is the quantization volume for free atomic states.

An expression for the matrix element V_{ma} is obtained by comparing the energy shift near a Feshbach resonance with second-order perturbation theory. Assuming two atoms in a volume V , the energy shift of the low-lying continuum states due to the coupling with a bound molecular state is

$$\delta(\epsilon) = \frac{|V_{\text{ma}}|^2}{\epsilon} = \frac{|V_{\text{ma}}|^2}{\Delta\mu(B - B_0)}, \quad (2)$$

where $\Delta\mu$ is the difference between atomic and molecular magnetic moments, B is the applied magnetic field, and B_0 is the position of the Feshbach resonance.

The energy shift can also be expressed in terms of the mean field energy $4\pi\hbar^2 a/mV$, where $a = a_{\text{bg}}\Delta B/(B - B_0)$ is the scattering length near the Feshbach resonance (a_{bg} is the background scattering length and ΔB is the resonance width [19]):

$$\delta(\epsilon) = \frac{4\pi\hbar^2 a_{\text{bg}}\Delta B}{mV(B - B_0)}. \quad (3)$$

Comparing Eqs. (2) and (3) yields

$$|V_{\text{ma}}|^2 = \frac{4\pi\hbar^2}{mV} a_{\text{bg}}\Delta\mu\Delta B. \quad (4)$$

If the entire population is initially in the molecular state, the fraction of molecules, $m(\epsilon)$, at energy ϵ follows the rate equation,

$$\frac{dm(\epsilon)}{d\epsilon} = \frac{dm(\epsilon)}{dt} \left(\frac{d\epsilon}{dt} \right)^{-1} = \Gamma(\epsilon)m(\epsilon) \left(\frac{d\epsilon}{dt} \right)^{-1} \quad (5)$$

$$= \frac{2\pi|V_{\text{ma}}(\epsilon)|^2 D(\epsilon)}{\hbar\Delta\mu|\dot{B}|} m(\epsilon). \quad (6)$$

Using Eqs. (1) and (4), we solve the differential equation for $m(\epsilon)$,

$$m(\epsilon) = e^{-(2/3)C\epsilon^{3/2}}, \quad C = \frac{2\Delta B}{\hbar\dot{B}} \sqrt{\frac{ma_{\text{bg}}^2}{\hbar^2}}. \quad (7)$$

In the laboratory frame, the atoms have kinetic energy $\epsilon/2$, and therefore the average energy of an atom after dissociation is

$$\delta E = \int_0^\infty \frac{\epsilon}{2} [-dm(\epsilon)] = 0.591 \left(\frac{\hbar^2}{ma_{\text{bg}}^2} \frac{\hbar \dot{B}}{2\Delta B} \right)^{2/3}. \quad (8)$$

Using theoretical values $a_{\text{bg}} = 3.4$ nm, $\Delta\mu/h = 3.65 \times 1.4$ MHz/G, and $\Delta B = 0.98$ G [20,21], the data show good agreement with our model. A fit of the product $a_{\text{bg}}\Delta B$ to our data results in $a_{\text{bg}}\Delta B = 3.64$ G nm $\pm 2\%$ (dotted line in Fig. 2). The discrepancy between the theoretical and fitted values is 4 times bigger than the statistical error, but within the systematic error of the measurement of the release energy.

Further experiments with ultracold sodium molecules will critically depend on their collision properties. Therefore we also studied heating and inelastic collision processes. As shown in Fig. 3, we observed monotonic heating of the pure molecular sample over ~ 30 ms. In addition, we observed short time scale oscillations (6 ms) in the fitted temperature (inset of Fig. 3). Such breathing oscillations were excited because the molecules were formed over the volume of the atomic condensate and started oscillations around their equilibrium volume. The equilibrium volume deduced from the observed released energy is much smaller than the initial volume. The absence of damping implies a collision time of at least 6 ms, or a molecular scattering length smaller than 17 nm (obtained using the expression for the collision rate $8\pi a^2 v_{\text{th}} n_m$, where v_{th} is the thermal velocity). It is unclear whether the oscillation disappeared due to collisions or limited signal-to-noise ratio.

The temperature of the molecular cloud saturated at ~ 250 nK after 15 ms. A possible explanation is the balance between heating due to inelastic molecular decay and the evaporative cooling caused by the finite trap depth (1.7 μ K). This would imply a collision time of 15 ms. However, we have no clear evidence that thermalization has occurred. Clearly, further studies of elastic collisions between ultracold molecules are necessary.

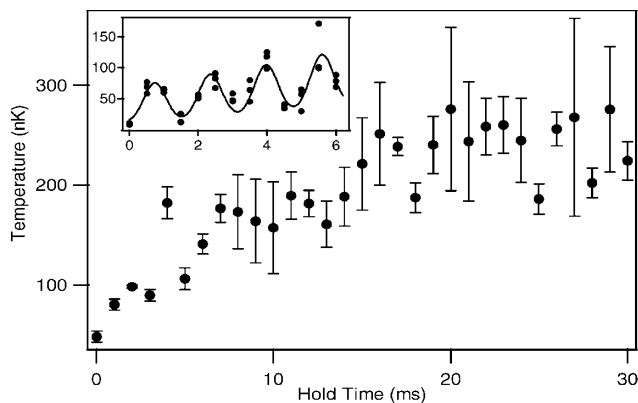


FIG. 3. Temperature of the molecular cloud. After 15 ms, the temperature saturates at ~ 250 nK. Error bars represent the statistical error (standard deviation). The inset shows finer resolution data for holding times up to 6 ms. The solid line is a guide to the eye.

Molecules formed via an s-wave Feshbach resonance are created in the rotational ground state, but in high vibrational states. Therefore, one expects vibrational relaxation to be a strong, inelastic decay mechanism.

Figure 4(a) shows the decay of a pure molecular sample. The decay was analyzed with the rate equation

$$\frac{\dot{N}_m}{N_m} = -K_{mm}n_m. \quad (9)$$

Here N_m, n_m is the number and the density of the molecules, respectively, and K_{mm} is the molecule-molecule collision rate coefficient. Because of the changing size and temperature of the molecular cloud during the first ~ 15 ms (Fig. 3), we fit data points only at later times, assuming a thermal equilibrium volume for the molecules. The decay at earlier times is slower, consistent with a larger molecular cloud. The fit yields a molecule-molecule collision coefficient of $K_{mm} \sim 5.1 \times 10^{-11}$ cm³/s, about 2 orders of magnitude larger than the typical values reported for fermions [4,5].

Inelastic collisions between molecules and atoms were also observed by keeping atoms in the trap [Fig. 4(b)]. The decay was analyzed assuming that the loss of

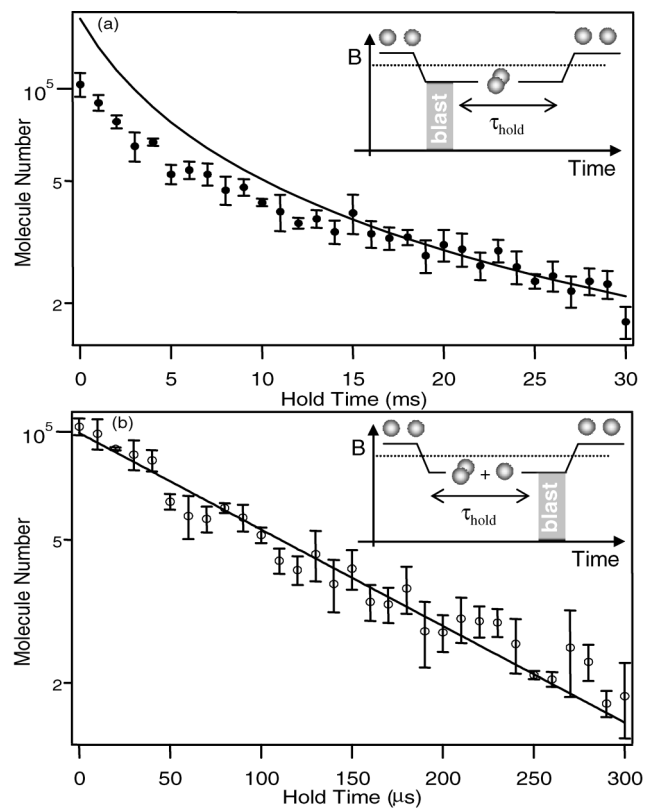


FIG. 4. Decay of ultracold molecules trapped alone (a) or together with atoms (b). The solid lines in (a) and (b) are fits to data, which assume vibrational relaxation in the collision of m molecules (a) or collisions between molecules and atoms (b). The insets illustrate the experimental sequences.

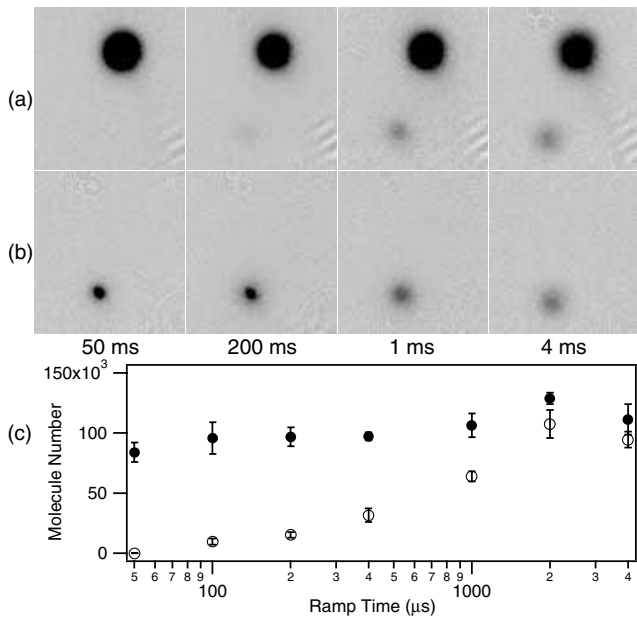


FIG. 5. Conversion of atoms to molecules for various ramp times. During a given time, the magnetic field was swept by 10 G. (a) and (b) show absorption images taken after 14 ms time of flight. The molecules (bottom) were radially separated from the atoms (top) by a field gradient of 2.8 G/cm. The molecules were converted back to atoms only 0.5 ms before imaging by ramping the magnetic field back across the Feshbach resonance. This time was chosen to be long enough for any transient field fluctuations to damp out, but short enough such that the size of the imaged cloud reflected the molecular temperature, not the dissociation energy. (a) The atoms remained in the trap. (b) The atoms were removed by a resonant laser pulse immediately after the magnetic field ramp. (c) Number of molecules as a function of ramp time for (a) (open circles) and (b) (closed circles).

molecules occurred mainly due to collisions with atoms, resulting in an exponential decay:

$$\frac{\dot{N}_m}{N_m} = -K_{am}n_a. \quad (10)$$

Here n_a is the density of atoms, and K_{am} is the atom-molecule collision rate coefficient. From the fit, we extract a lifetime of 106 μ s and a rate coefficient $K_{am} \sim 5.5 \times 10^{-11}$ cm³/s, which agrees well with theoretical predictions [21,22].

The inelastic losses determine the maximum conversion efficiency from atoms to molecules. For an adiabatic ramp, one expects close to 100% conversion efficiency. Indeed, in experiments with fermionic atoms, efficiencies up to 85% have been observed [5]. Figure 5 shows the results for magnetic field ramps of different durations. The two sets of images show that applying the blast pulse dramatically improved the molecular number and temperature. Without it, a slower ramp time (4 ms) appeared to be more favorable for molecule formation [open circles

in Fig. 5(c)]. No molecules were observed for a 50 μ s ramp time. However, with the blast pulse, a similar number of molecules was obtained for all ramp times between 50 μ s to 4 ms [closed circles in Fig. 5(c)].

We assume that these results reflect the interplay of two competing processes. The adiabatic condition requires a relatively slow field ramp for efficient conversion. However, this means that the atoms and molecules spend more time near or at the Feshbach resonance, where inelastic collision rates are enhanced. In contrast to Fig. 5(b), the absence of a molecular signal in Fig. 5(a) for 50 μ s ramp time reflects that the atomic density reduction due to the ballistic expansion is too slow for the molecules to survive the inelastic collisions with the atoms.

In conclusion, we observed a Wigner threshold behavior in the dissociation of ultracold molecules. We were able to characterize a Feshbach resonance using a one-body decay (dissociation) process. The rapid decay of the molecules due to collisions with atoms and other molecules imposes a severe limit to further evaporative cooling for bosons. This also explains the low conversion efficiency ($\sim 4\%$), in contrast to recent experiments with fermions.

The authors thank D. E. Miller for experimental assistance and A. E. Leanhardt, M. Saba, and D. Schneble for their critical reading of the manuscript. We also thank P. S. Julienne, B. J. Verhaar, and V. A. Yurovsky for useful discussion. This research is supported by NSF, ONR, ARO, and NASA.

-
- [1] R. Wynar *et al.*, *Science* **287**, 1016 (2000).
 - [2] E. A. Donley *et al.*, *Nature (London)* **417**, 529 (2002).
 - [3] C. A. Regal *et al.*, *Nature (London)* **424**, 47 (2003).
 - [4] S. Jochim *et al.*, *Phys. Rev. Lett.* **91**, 240402 (2003).
 - [5] J. Cubizolles *et al.*, *Phys. Rev. Lett.* **91**, 240401 (2003).
 - [6] K. E. Strecker *et al.*, *Phys. Rev. Lett.* **91**, 080406 (2003).
 - [7] S. Dürr *et al.*, *Phys. Rev. Lett.* **92**, 020406 (2003).
 - [8] C. Chin *et al.*, *Phys. Rev. Lett.* **90**, 033201 (2003).
 - [9] K. Xu *et al.*, *Phys. Rev. Lett.* **91**, 210402 (2003).
 - [10] M. Greiner *et al.*, *Nature (London)* **426**, 537 (2003).
 - [11] S. Jochim *et al.*, *Science* **302**, 2101 (2003).
 - [12] J. J. Hudson *et al.*, *Phys. Rev. Lett.* **89**, 23003 (2002).
 - [13] M. Baranov *et al.*, *Phys. Scr.* **T102**, 74 (2002).
 - [14] D. J. Heinzen *et al.*, *Phys. Rev. Lett.* **84**, 5029 (2000).
 - [15] S. Inouye *et al.*, *Nature (London)* **392**, 151 (1998).
 - [16] F. A. van Abeelen and B. J. Verhaar, *Phys. Rev. Lett.* **83**, 1550 (1999).
 - [17] E. P. Wigner, *Phys. Rev.* **73**, 1002 (1948).
 - [18] F. H. Mies *et al.*, *Phys. Rev. A* **61**, 022721 (2000).
 - [19] E. Timmermans *et al.*, *Phys. Rep.* **315**, 199 (1999).
 - [20] V. A. Yurovsky *et al.*, *Phys. Rev. A* **60**, R765 (1999).
 - [21] V. A. Yurovsky *et al.*, *Phys. Rev. A* **62**, 043605 (2000).
 - [22] V. A. Yurovsky and A. Ben-Reuven, *Phys. Rev. A* **67**, 043611 (2003).

Appendix E

Sodium Bose-Einstein Condensates in an Optical Lattice

This appendix reprints Ref. [139]: K. Xu, Y. Liu, J.R. Abo-Shaeer, T. Mukaiyama, J.K. Chin, D.E. Miller, and W. Ketterle, *Sodium Bose-Einstein condensates in an optical lattice*, Phys. Rev. A **72**, 043604 (2005).

Sodium Bose-Einstein condensates in an optical lattice

K. Xu,* Y. Liu, J. R. Abo-Shaer, T. Mukaiyama, J. K. Chin, D. E. Miller, and W. Ketterle[†]
*Department of Physics, MIT–Harvard Center for Ultracold Atoms, and Research Laboratory of Electronics, MIT, Cambridge,
 Massachusetts 02139, USA*

Kevin M. Jones
Department of Physics, Williams College, 33 Lab Campus Dr., Williamstown, Massachusetts 01267, USA

Eite Tiesinga
*Atomic Physics Division, National Institute of Standards and Technology, 100 Bureau Drive, Stop 8424, Gaithersburg, Maryland 20899,
 USA*

(Received 12 July 2005; published 10 October 2005)

The phase transition from a superfluid to a Mott insulator has been observed in a ^{23}Na Bose-Einstein condensate. A dye laser detuned ≈ 5 nm red of the $\text{Na } 3^2S \rightarrow 3^2P_{1/2}$ transition was used to form the three-dimensional optical lattice. The heating effects of the small detuning as well as the three-body decay processes constrained the time scale of the experiment. Certain lattice detunings were found to induce a large loss of atoms. These loss features were shown to be due to photoassociation of atoms to vibrational levels in the $\text{Na}_2(1)^3\Sigma_g^+$ state.

DOI: [10.1103/PhysRevA.72.043604](https://doi.org/10.1103/PhysRevA.72.043604)

PACS number(s): 03.75.Lm, 73.43.Nq, 33.20.Kf, 34.20.Cf

I. INTRODUCTION

Optical lattices have become a powerful tool to enhance the effects of the interaction in ultracold atomic systems to create strong correlations and probe many-body physics beyond the mean-field theory [1–7]. Simply through varying the depth of the lattice potential, one changes the tunneling rate as well as the on-site interaction energy by changing the confinement of the atoms. The strength of the atomic interaction can be directly tuned with a magnetic Feshbach resonance [8]. In comparison to ^{87}Rb , which has been used in almost all experiments on optical lattices, ^{23}Na has stronger and wider Feshbach resonances that are experimentally accessible [9,10]. One such resonance has been used to produce quantum degenerate Na_2 molecules [11]. Therefore, a sodium condensate loaded into an optical lattice would be a rich and flexible system for studying strong correlations.

So far, most optical lattice experiments have been performed with relatively heavy atomic species (e.g., rubidium and potassium) for which the recoil frequencies are lower and lasers are readily available to achieve trap depths of several tens of recoil frequencies at a few tens of milliwatts. For ^{23}Na , high-power single-mode lasers are necessary for similar experiments. In this work, we chose to use a dye laser red-detuned by ≈ 5 nm from the D lines of sodium (589 nm). The spontaneous scattering rate limited the time window of the experiment to less than 50 ms, but was still sufficient to satisfy the adiabaticity condition to explore the quantum phase transition from a superfluid to a Mott insulator. We also observed strong atom losses at various lattice laser detunings, which were interpreted as photoassociation transi-

tions. The particular molecular states responsible for these transitions were identified through theoretical calculations and previous experimental data.

II. EXPERIMENT SETUP

A ^{23}Na Bose-Einstein condensate containing up to 10^6 atoms in the $|F=1, m_F=-1\rangle$ state was first produced in a magnetic trap and subsequently loaded into a crossed optical dipole trap. The optical trap was derived from a single-mode 1064 nm infrared laser, with the horizontal and vertical beams detuned by 60 MHz through acousto-optic modulators. The number of condensed atoms was varied through three-body decay in a tight trap ($\omega_{x,y,z}=2\pi \times 200, 328, 260$ Hz), after which the trap was decompressed ($\omega_{x,y,z}=2\pi \times 110, 155, 110$ Hz) to allow further evaporation and rethermalization. A vertical magnetic field gradient was applied to compensate for gravity and avoid sagging in the weaker trap.

A dye laser operated at 594.710 nm was used to set up a three-dimensional optical lattice. The three beams were focused to a $1/e^2$ waist of $\sim 82 \mu\text{m}$ at the condensate, and retroreflected to form standing waves. The two horizontal beams were orthogonal to each other, while the third beam was slanted at $\sim 20^\circ$ with respect to the vertical axis due to limited optical access. The three beams were frequency shifted by ± 30 and 80 MHz to eliminate cross-interference between different beams.

The Gaussian profile of the lattice beams added an additional harmonic trapping potential, while the localization of atoms at the lattice sites increased the repulsive mean field interaction. At the maximum lattice depth, the trap frequencies due to the combined potentials of the optical dipole trap and the lattice beams were ~ 510 Hz for all three dimensions. The trap parameters were chosen such that during the

*Electronic mail: kwxu@mit.edu

[†]Website: cua.mit.edu/ketterle_group

ramping of the optical lattice potential, the overall size of the cloud (parametrized by Thomas-Fermi radii) remained approximately constant in order to minimize intraband excitations (the mean Thomas-Fermi radius is $\sim 14 \mu\text{m}$ for 10^6 atoms). The peak per-lattice-site occupancy numbers achieved in our experiment were between 3 to 5.

III. QUANTUM PHASE TRANSITION

Atoms held in a shallow optical lattice can tunnel freely from site to site and form a superfluid phase. As the lattice is made deeper, the atomic interaction is increased while the tunneling rate between lattice sites is exponentially suppressed. The system then undergoes a phase transition to an insulating phase—the Mott-insulator—in which each lattice site contains a definite fixed number of atoms. According to the mean-field theory for the homogenous systems of atoms in the lowest band of an optical lattice, the critical point for the phase transition from a superfluid to a Mott-insulator state with n atoms per lattice site is determined by [12–14]

$$U = z[2n + 1 + 2\sqrt{n(n+1)}]J, \quad (1)$$

where

$$U = \frac{4\pi\hbar^2 a_s}{m} \int d^3x |w(x)|^4 \quad (2)$$

is the on-site interaction energy;

$$J = \int d^3x w^*(x - \lambda_{\text{latt}}/2) \left(-\frac{\hbar^2}{2m} \nabla^2 + V_{\text{latt}}(x) \right) w(x) \quad (3)$$

is the tunneling rate between adjacent lattice sites; z is the number of nearest neighbors in the lattice (six for a cubic lattice); m is the atomic mass; a_s is the s -wave scattering length (2.75 nm for ^{23}Na); $w(x)$ is the Wannier function; λ_{latt} is the lattice wavelength; $V_{\text{latt}}(x)$ is the lattice potential.

Figure 1 shows U and $J_n = z[2n + 1 + 2\sqrt{n(n+1)}]J$ for a cubic lattice as a function of the lattice depth, obtained through a band-structure calculation. All energies are expressed in units of the recoil energy $E_{\text{recoil}} = \hbar^2 k_{\text{latt}}^2 / 2m$, where $k_{\text{latt}} = 2\pi/\lambda_{\text{latt}}$ is the lattice wave number. With this scaling J is independent of λ_{latt} . The peak occupancy number in our experiment was ≤ 5 . From Fig. 1, we find that the critical points are at a lattice depth of 14.2, 16.2, 17.6, 18.7, and 19.5 (all in units of E_{recoil}) for $n=1, 2, 3, 4,$ and 5 respectively. The inset of Fig. 1 shows that the ratio of U/J increases rapidly with an increasing lattice depth.

When a weak harmonic trap is present in addition to the lattice potential, as is the case for the experiment, the atomic density is not uniform. Nevertheless, Eqs. (1)–(3) can be used to estimate the lattice depth needed to observe the Mott-insulator phase transition at any point in the harmonic trap. Given the local density of the initial condensate, a local value of n can be estimated, and thus the local critical lattice depth can be read off from Fig. 1. Since the critical depth increases with n , one expects that as the lattice depth is increased, shells of different occupancies will undergo the transition to the Mott-insulator phase, starting from the edge of

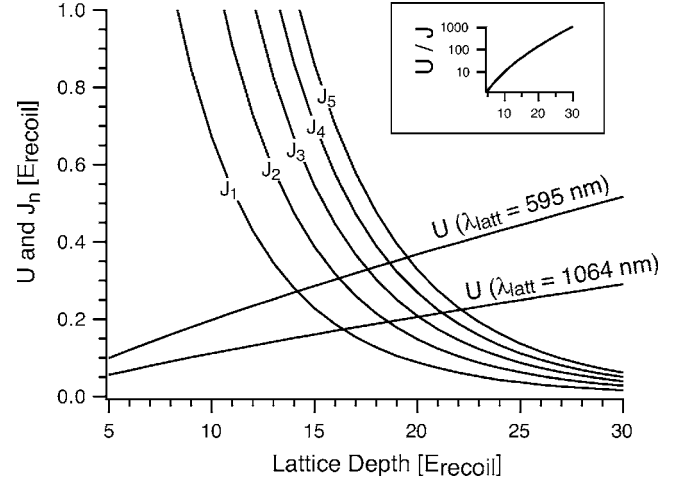


FIG. 1. A determination of the phase transition points: The phase transition at occupancy number n occurs when $J_n = z[2n + 1 + 2\sqrt{n(n+1)}]J$ as given by Eq. (1) equals U . The horizontal location of the crossing point where $J_n = U$ gives the critical lattice depth. The inset shows the ratio of U over J as a function of the lattice depth.

the density profile and moving in toward the center.

In our experiment, the optical lattice was linearly ramped up to a maximum potential of $20 E_{\text{recoil}}$ in a variable time τ_{ramp} ($E_{\text{recoil}} = \hbar 24.4 \text{ kHz}$ for our system). The lattice depth was calibrated by probing the energy difference between the first and the third band at zero quasimomentum with small-amplitude modulation of the lattice beams (see, e.g., [6]). After reaching the peak value, the lattice was ramped back down again in τ_{ramp} . The ramp sequence was stopped at different times when both the trap and the lattice were suddenly switched off (in $\lesssim 1 \mu\text{s}$). Absorption images were then taken after some time of flight, as shown in Fig. 2. The disappearance of the interference pattern as the lattice depth was increased indicated the loss of phase coherence and a transition from the superfluid state to the Mott insulator state [3]. The subsequent revival of the interference patterns as the lattice depth was reduced ensured that the system remained essentially in the ground state during the ramping process. Different τ_{ramp} 's were used to check the adiabaticity condition. The peak spontaneous light scattering rate was about 21 s^{-1} at the maximum intensity. Therefore for $\tau_{\text{ramp}} \leq 10 \text{ ms}$, less than 20% of the atoms spontaneously scattered a photon.

After the lattice was fully ramped down, most of the atoms ($> 80\%$) remained in the condensed fraction while the rest were heated and distributed across the first Brillouin zone. Based on the number of atoms that remained in the condensate after the lattice was fully ramped down, we conclude that $\tau_{\text{ramp}} \geq 1 \text{ ms}$ satisfies the intraband adiabaticity condition. In the following discussion, all measurements were performed for $\tau_{\text{ramp}} = 1, 5, 10 \text{ ms}$, but only the data for $\tau_{\text{ramp}} = 5 \text{ ms}$ are shown as representative of similar results unless otherwise noted (see Fig. 3).

To characterize the lifetime of the Mott-insulator phase, we held the lattice depth at the maximum level for various amounts of time before ramping the lattice down to $8 E_{\text{recoil}}$ (below the Mott-insulator transition point) and taking the

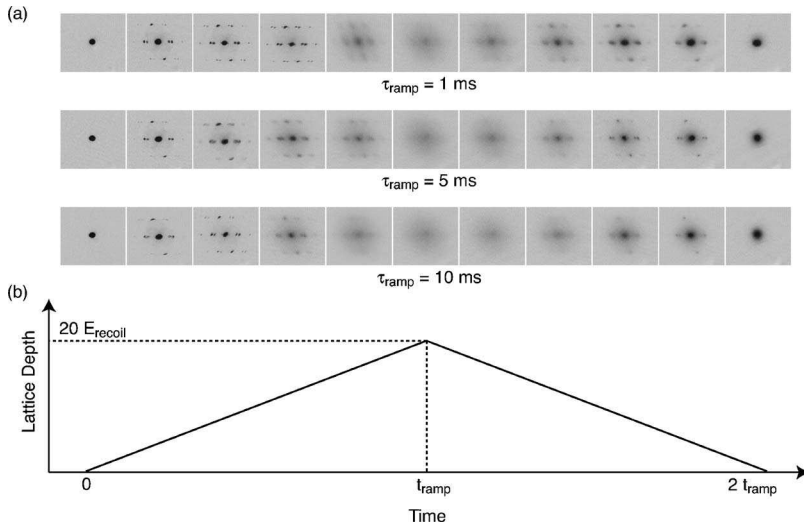


FIG. 2. (a) Observation of the superfluid to Mott insulator transition: The lattice depths for the sequence of images are from left to right 0, 4, 8, 12, 16, 20, 16, 12, 8, 4, 0 E_{recoil} . The time-of-flight is 7 ms and the field of view is $1000 \mu\text{m} \times 1200 \mu\text{m}$. The peak occupancy number n is 5 for these images, and the phase transition should occur between 14 and 20 E_{recoil} according to the mean-field calculation. (b) Time dependence of the lattice depth.

time-of-flight image. If the system remains in the ground state, the contrast of the interference pattern should be recovered, whereas additional heating populates the Brillouin zone and reduces the interference contrast. A cross section of the density profile was taken along the horizontal direction showing the interference peaks on top of a broad background (see Fig. 3). The five interference peaks and the broad background were fit by six gaussians. The ratio between the total integrated area of the peaks and the background was used as the contrast to quantify the heating of the system. The contrast gives a more sensitive measure of the heating compared to simply counting the recovered condensate atoms. As the atoms in the interference peaks quickly move apart, they are not as broadened by the mean-field expansion as a single condensate.

We performed the same measurement for two different peak occupancy numbers $n \approx 3$ and 5. Figure 3 shows the decay of the contrast and the lifetime τ was determined using an exponential fit. The fitting error on the lifetime was less than 17%. The lifetime was about 50% longer for $n=3$, implying that inelastic collision processes significantly contributed to the heating of the system. The three-body decay rate at the maximum lattice potential for the peak on-site atomic density ($\sim 10^{16} \text{ cm}^{-3}$ for $n=5$) is about 100 s^{-1} [15], consistent with the observed lifetimes of ~ 10 ms. The peak density of a condensate in a harmonic trap and therefore the peak occupancy number scales with $2/5$ power of the total number of atoms, and our method for varying the number of atoms (through three-body decay) was unable to consistently produce low enough atom numbers for peak occupancy ≤ 2 . The signal-to-noise ratio of our current imaging system also became marginal for such low atom numbers.

IV. PHOTOASSOCIATION RESONANCES

In this experiment, in addition to losses due to three-body recombination, we observed large losses of atoms for certain specific tunings of the lattice laser in the range 592 to 595 nm. A sample of such a loss feature is shown in Fig. 4. For this measurement, the same ramp sequence was used as before with $\tau_{ramp} = 1$ ms. The peak intensity is about

280 W/cm^2 in each lattice beam. Due to the intentional frequency shifts between the three lattice beams, the effective bandwidth of the lattice light as seen by the atoms is ≈ 100 MHz. For the narrow frequency scan range of Fig. 4, the relative frequency scale was determined to better than 25 MHz using a Fabry-Perot cavity with a 2 GHz free spectral range.

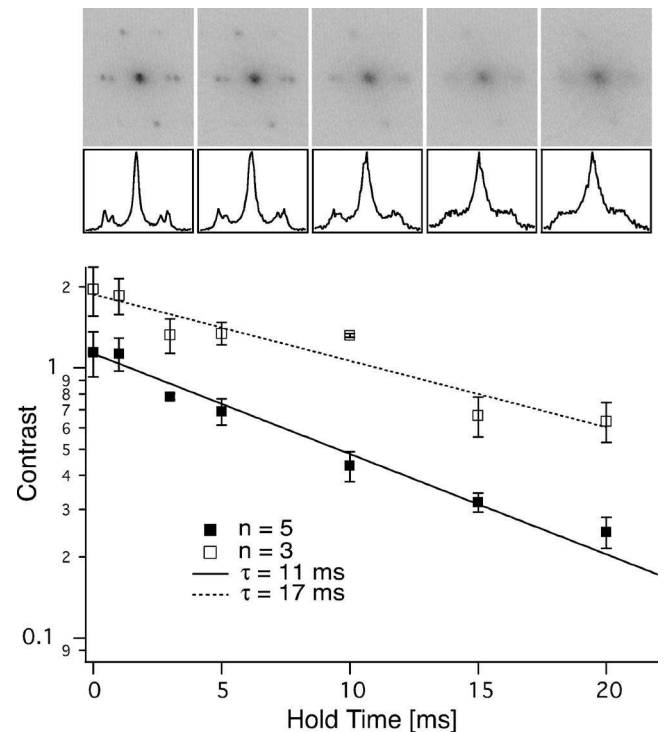


FIG. 3. Lifetime of the Mott insulator state: The top row of absorption images were taken for hold times 0, 5, 10, 15, 20 ms. The second row is the horizontal cross section of the atomic density profile taken at the center of the absorption images. The decay of the Mott insulator state is observed as the loss of contrast of the interference peaks. The curves are the simple exponential fits used to estimate the decay rate. The error bars in the graph are statistical standard deviation of multiple shots.

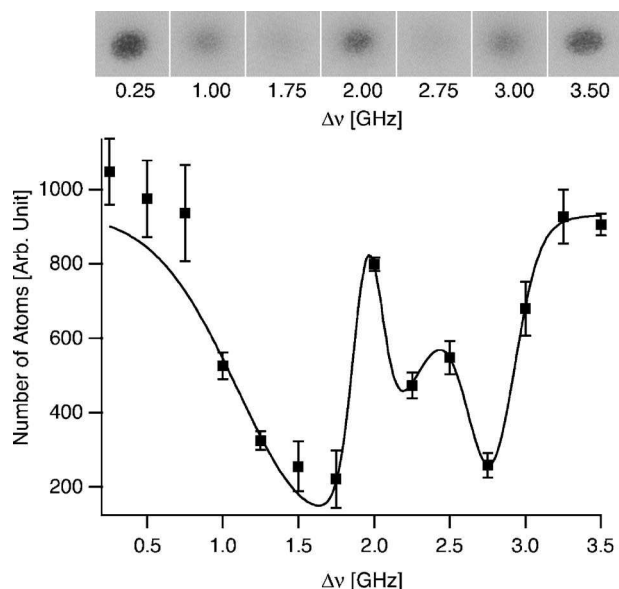


FIG. 4. Photoassociation resonances: Atom loss from the optical lattice as a function of the lattice laser detuning. The top row of images shows the remaining atom cloud after the lattice was turned off and the cloud expanded for 30 ms. The lower graph shows the remaining number of atoms for these and additional frequency points. The zero of the x axis corresponds to a laser wavelength of 594.490 nm as determined with a wave meter with accuracy ~ 1 GHz. The error bars are one standard deviation uncertainty. The line is only a guide and does not have a theoretical underpinning.

Single-photon photoassociations proved to have caused these losses. The lattice laser is tuned by ≈ 160 cm^{-1} to the red of the atomic $3^2S \rightarrow 3^3P_{3/2}$ transition and thus is in a spectral region where it might drive photoassociation transitions [16–18] to rovibrational levels in molecular states dissociating to either the $3^2S+3^2P_{1/2}$ or $3^2S+3^2P_{3/2}$ limits. Such a photoassociation transition, followed by the spontaneous radiative decay of the excited molecule into either a bound ground electronic-state molecule or into “hot” atoms, results in significant losses of atoms from the lattice. It is therefore important to identify the locations and strengths of these resonances and choose the appropriate lattice wavelength to avoid such losses.

There is an extensive body of knowledge on the photoassociation of ultracold alkali-metal atoms and the behavior of the molecular potentials dissociating to the $3^2S+3^2P_{1/2}$ or $3^2S+3^2P_{3/2}$ limits [16–18]. Figure 5 shows the relevant excited molecular potentials as a function of internuclear separation R . The ground electronic states of Na_2 are the $X^1\Sigma_g^+$ and $a^3\Sigma_u^+$ states and two colliding ground state atoms will be some mixture of these symmetries. To the extent that the excited states are well described as Σ or Π states, the $g \leftrightarrow u$ and $\Delta S=0$ selection rules imply that photoassociation transitions are allowed only to the two Σ states [$A^1\Sigma_u^+$ and $(1)^3\Sigma_g^+$].

Previous experiments have identified the locations of the strong transitions to the $A^1\Sigma_u^+$ state [19] and the weak transitions to the $(1)^1\Pi_g(1_g)$ state [20]. These are shown in Fig. 6. We looked for but failed to find any significant losses attributable to the weak $(1)^1\Pi_g(1_g)$ state resonances. We

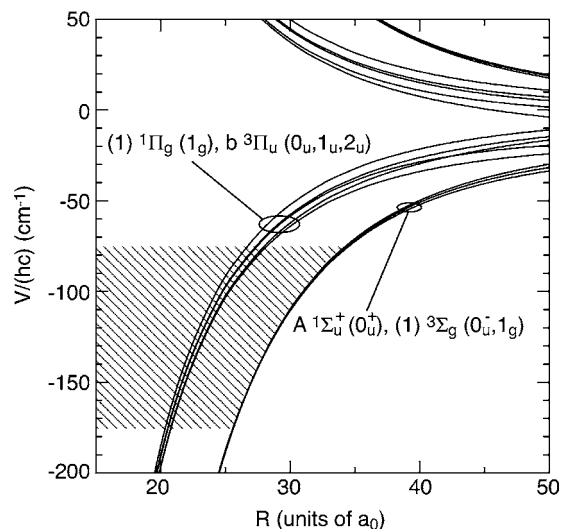


FIG. 5. Long-range molecular potentials near the Na_2 3^2S+3^2P separated atom limit ($1 a_0=0.0529$ nm): The zero of the vertical scale is the $3^2S+3^2P_{3/2}$ limit; the $3^2S+3^2P_{1/2}$ limit lies 17.2 cm^{-1} lower. The hatched region indicates the energy range explored in the experiment. The potentials are labeled by both Hund’s case (a) state labels of the form $^{2S+1}\Lambda_{g/u}^\pm$ and by Hund’s case (c) labels $\Omega_{g/u}^\pm$ given in parentheses after the case (a) label. For small R the curves labeled by a given case (a) label become degenerate, while for larger R , as the effect of spin-orbit coupling becomes increasingly important, the degeneracy is lifted.

were able to confirm one of the A-state resonances, indicated by the dot in Fig. 6. Since the primary goal of the present work was to avoid photoassociation losses, we did not investigate known A-state locations further. Our search focused on the strong resonances due to the $(1)^1\Sigma_g^+$ state that had not been previously observed in this spectral region. In 0.5 GHz steps, we scanned through a 30 GHz range around the theoretically predicted locations based on the model and auxiliary experimental data discussed below. In all but one such scans, we were able to observe between 1 to 3 dips in the remaining atom numbers within a range of $\lesssim 15$ GHz, including the loss feature shown in Fig. 4. As shown in Fig. 6 the agreement of the observed locations with the predictions and auxiliary measurements confirms that these loss features are due to photoassociation to the $(1)^3\Sigma_g^+$ state. The locations of the rovibrational levels of the $b^3\Pi_u$ state are not known in the current tuning range. Their spacing, however, should be equal to that of the $(1)^1\Pi_g$ levels and our observations are not consistent with such spacings.

The potential curves used in the calculation of the $(1)^3\Sigma_g^+$ vibrational levels were generated from an extended version of the model developed by Movre and Pichler for calculating the combined effects of the $1/R^3$ resonant dipole interaction and the atomic spin-orbit interaction. Such models have been extensively used to interpret photoassociation experiments [16–18]. To the long-range potentials generated by the Movre-Pichler-type calculation we append the results of *ab initio* calculations on the short-range molecular potentials (in the chemical bonding region). These short-range potentials are not sufficiently accurate to allow predictions of absolute vibrational positions. It is necessary to make slight adjust-

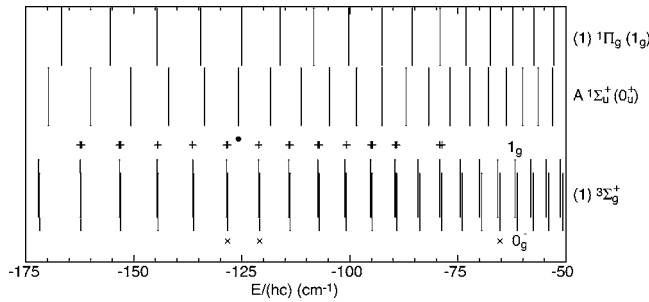


FIG. 6. A comparison of loss features (pluses and dot) observed in a Bose condensate trapped in an optical lattice, to known molecular level positions: The x axis is the binding energy of the molecular level relative to the $3^2S(f=2)+3^2P_{3/2}(f=3)$ atomic asymptote. If a loss feature, observed at a laser photon energy of E_{photon} , is due to the photoassociation of two $3^2S(f=1)$ Na atoms to a bound molecular level, then the molecular level is bound by $E_0 - E_{\text{photon}}$, where $E_0/(hc) = 16\,973.4636\text{ cm}^{-1}$. The laser tunings of observed loss features are plotted in this way (the pluses and the dot). The lines labeled $(1)^1\Pi_g(1_g)$ are binding energies of the $J=1$ rotational levels of vibrational levels in this potential measured in a magneto-optical trap (MOT) ([20] and unpublished work). The lines labeled $A\ 1\Sigma_u^+(0_u^+)$ are the energies reported in the RKR curve of [19] (nominally $J=0$ positions) shifted to agree with the photoassociation measurement of [21] corrected for rotation. The lines labeled $(1)^3\Sigma_g^+$ are from an extended Movre-Pichler model calculation calibrated to experimental data (the crosses) from a two-color photoassociation experiment in a MOT. The lines displaced upward (downward) are the 1_g (0_g^-) component of the $(1)^3\Sigma_g^+$ state. The crosses indicate the three calibration points that lie in this spectral range and are measurements of the $J=0$ levels of the 0_g^- component.

ments to these potentials to match experimentally measured vibrational positions, which were obtained through a separate photoassociation spectroscopy experiment in a dark-spot magneto-optical trap (MOT) containing Na $3^2S(f=1)$ atoms at about $300\ \mu\text{m}$, using a two-color ionization scheme and an ion detector [22,23]. The photoassociation spectra taken in the MOT have higher resolution than the loss features in the lattice experiment.

In the spectral region of interest for the lattice experiment, three vibrational levels of the $(1)^3\Sigma_g^+$ were identified by measurements in the MOT. The spectra show a 1_g component with a complicated hyperfine/rotational pattern, and, slightly higher ($\sim 0.3\text{ cm}^{-1}$) in energy, a 0_g^- component with a simpler nearly rotational pattern. This ordering of the 1_g and 0_g components is in agreement with the Movre-Pichler model.

For these levels, the $J=0$ feature of the 0_g^- component were found to be at $16\,845.155$, $16\,852.585$, and $168\,908.201\text{ cm}^{-1}$, calibrated to iodine lines with an estimated uncertainty of about 0.004 cm^{-1} and are shown in Fig. 6. This new data on the $(1)^3\Sigma_g^+$ was sufficient to calibrate our extended Movre-Pichler model without any further adjustable parameters. The predicted positions shown in Fig. 6 agree well with those of the loss features observed in the lattice experiment, thus identifying the loss features as photoassociation transitions to levels in the $(1)^3\Sigma_g^+$ state.

Based on this insight, we chose a wavelength of 594.710 nm for our lattice experiment (corresponding to -158.5 cm^{-1} in Fig. 6). This tuning lies $>45\text{ GHz}$ from the closest molecular resonance. Given the observed on-resonance photoassociation rate of 1 ms^{-1} in the lattice, photoassociative decay can be ignored at such detunings as the rate scales as the square of the ratio of the natural linewidth to the detuning [24].

V. CONCLUSIONS

In this paper, we explored the possibility of using a dye laser detuned $\approx 5\text{ nm}$ from the Na D lines to study many-body physics of a sodium BEC in an optical lattice, which could allow for an independent control of interaction using magnetic Feshbach resonances. The superfluid to Mott-insulator transition was observed in a Na Bose-Einstein condensate for the first time. The main technical difficulties are due to the heating from the spontaneous light scattering and three-body decay processes. In addition, several photoassociation resonances were observed and identified by means of auxiliary spectroscopy measurements combined with theoretical modeling. These resonances were avoided by choosing an appropriate lattice wavelength. In future experiments, we plan to use a high-power single-mode infrared laser at 1064 nm to eliminate atomic light scattering (Fig. 1 also shows the transition points for a 1064 nm lattice). Moreover, heating from three-body recombination can be avoided by using occupancy numbers less than three.

ACKNOWLEDGMENTS

The authors would like to thank Fredrik Fatemi and Paul Lett for their help in obtaining the MOT photoassociation data used here, and Widagdo Setiawan for experimental assistance. We also thank Carl Williams for initiating the communications regarding the photoassociation resonances. This research is supported by the NSF, ONR, ARO, and NASA.

- [1] F. S. Cataliotti, S. Burger, C. Fort, P. Maddaloni, F. Minardi, A. Trombettoni, A. Smerzi, and M. Inguscio, *Science* **293**, 843 (2001).
- [2] C. Orzel, A. K. Tuchman, M. L. Fenselau, M. Yasuda, and M. A. Kasevich, *Science* **291**, 2386 (2001).
- [3] M. Greiner, O. Mandel, T. W. Hänsch, I. Bloch, *Nature* **415**, 39 (2002).

- [4] M. Greiner, O. Mandel, T. W. Hänsch, and I. Bloch, *Nature* **419**, 51 (2002).
- [5] B. Paredes, A. Widera, V. Murg, O. Mandel, S. Fölling, I. Cirac, G. V. Shlyapnikov, T. W. Hänsch, and I. Bloch, *Nature (London)* **429**, 277 (2004).
- [6] C. Schori, T. Stoferle, H. Moritz, M. Kohl, and T. Esslinger, *Phys. Rev. Lett.* **93**, 240402 (2004).

- [7] M. Köhl, H. Moritz, T. Stoferle, K. Gunter, and T. Esslinger, *Phys. Rev. Lett.* **94**, 080403 (2005).
- [8] S. Inouye, M. R. Andrews, J. Stenger, H.-J. Miesner, D. M. Stamper-Kurn, and W. Ketterle, *Nature* **392**, 151 (1998).
- [9] J. Stenger, S. Inouye, M. R. Andrews, H. J. Miesner, D. M. Stamper-Kurn, and W. Ketterle, *Phys. Rev. Lett.* **82**, 2422 (1999).
- [10] A. Marte, T. Volz, J. Schuster, S. Durr, G. Rempe, E. G. M. van Kempen, and B. J. Verhaar, *Phys. Rev. Lett.* **89**, 283202 (2002).
- [11] K. Xu, T. Mukaiyama, J. R. Abo-Shaeer, J. K. Chin, D. E. Miller, and W. Ketterle, *Phys. Rev. Lett.* **91**, 210402 (2003).
- [12] M. P. A. Fisher, P. B. Weichman, G. Grinstein, and D. S. Fisher, *Phys. Rev. B* **40**, 546 (1989).
- [13] W. Krauth, M. Caffarel, and J. P. Bouchaud, *Phys. Rev. B* **45**, 3137 (1992).
- [14] D. Jaksch, C. Bruder, J. I. Cirac, C. W. Gardiner, and P. Zoller, *Phys. Rev. Lett.* **81**, 3108 (1998).
- [15] D. Stamper-Kurn, M. R. Andrews, and A. P. Chikkatur, *Phys. Rev. Lett.* **80**, 2027 (1998).
- [16] J. Weiner, V. Bagnato, S. Zilio, and P. Julienne, *Rev. Mod. Phys.* **71**, 1 (1999).
- [17] K. Jones, E. Tiesinga, P. Lett, and P. Julienne, *Rev. Mod. Phys.* (in review).
- [18] W. Stwalley and H. Wang, *J. Mol. Spectrosc.* **195**, 194 (1999).
- [19] E. Tiemann, H. Knöckel, and H. Richling, *Z. Phys. D: At., Mol. Clusters* **37**, 323 (1996). (Given our understanding of the implied dissociation limit for the RKR curve, the numbers in [19], and the $X^1\Sigma_g^+(v=0)$ energy in [24], we infer a dissociation limit that gives a binding energy ≈ 0.07 cm⁻¹ too low for the $v=135$ level when compared to the binding energy obtained directly from the photoassociation measurement in [21]. Even though [21] reported only the one line position as an incidental bit of information, other consistency tests suggest to us that it is better to use this line reported in [21] to fix the energy scale. This small difference is not important for the present work.)
- [20] L. P. Ratliff, M. E. Wagshul, P. D. Lett, S. L. Rolston, and W. D. Phillips, *J. Chem. Phys.* **101**, 2638 (1994). [While transitions to the two Π states are nominally forbidden, the residual effects of the fine structure interaction provide sufficient mixing that transitions are possible, even at these detunings. In particular, transitions to the $(1)^1\Pi_g(1_g)$ state played a prominent role in early photoassociation experiments, due largely to the fact that a single color laser cannot only produce molecules in this state but also readily ionizes them, making transitions to this state particularly easy to detect.]
- [21] C. McKenzie, J. H. Denschlag, H. Häffner, A. Browaeys, L. E. E. de Araujo, F. K. Fatemi, K. M. Jones, J. E. Simsarian, D. Cho, A. Simoni, E. Tiesinga, P. S. Julienne, K. Helmerson, P. D. Lett, S. L. Rolston, and W. D. Phillips, *Phys. Rev. Lett.* **88**, 120403 (2002).
- [22] K. Jones, S. Maleki, L. Ratliff, and P. Lett, *J. Phys. B* **30**, 289 (1997).
- [23] A. Amelink, K. M. Jones, P. D. Lett, P. van der Straten, and H. G. M. Heideman, *Phys. Rev. A* **61**, 042707 (2000).
- [24] K. M. Jones, S. Maleki, S. Bize, P. D. Lett, C. J. Williams, H. Richling, H. Knöckel, E. Tiemann, H. Wang, P. L. Gould, and W. C. Stwalley, *Phys. Rev. A* **54**, R1006 (1996).

Appendix F

Observation of Strong Quantum Depletion in a Gaseous Bose-Einstein Condensate

This appendix reprints Ref. [67]: K. Xu, Y. Liu, D.E. Miller, J.K. Chin, W. Setiawan and W. Ketterle, *Observation of Strong Quantum Depletion in a Gaseous Bose-Einstein Condensate*, *arXiv:cond-mat/0601184* (2006).

Observation of Strong Quantum Depletion in a Gaseous Bose-Einstein Condensate

K. Xu*, Y. Liu, D.E. Miller, J.K. Chin, W. Setiawan and W. Ketterle†

*Department of Physics, MIT-Harvard Center for Ultracold Atoms,
and Research Laboratory of Electronics, MIT, Cambridge, MA 02139*

(Dated: January 9, 2006)

We studied quantum depletion in a gaseous Bose-Einstein condensate. An optical lattice enhanced the atomic interactions and modified the dispersion relation resulting in strong quantum depletion. The depleted fraction was directly observed as a diffuse background in the time-of-flight images. Bogoliubov theory provided a semi-quantitative description for our observations of depleted fractions in excess of 50%.

PACS numbers: PACS 03.75.Hh, 03.75.Lm, 73.43.Nq

The advent of Bose-Einstein condensates (BEC) in 1995 extended the study of quantum fluids from liquid helium to superfluid gases with a 100 million times lower density. These gaseous condensates featured relatively weak interactions and a condensate fraction close to 100%, in contrast to liquid helium where the condensate fraction is only 10% [1]. As a result, the gaseous condensates could be quantitatively described by a single macroscopic wave function shared by all atoms which is the solution of a non-linear Schrodinger equation. This equation provided a mean-field description of collective excitations, hydrodynamic expansion, vortices and sound propagation [2].

The fraction of the many-body wavefunction which cannot be represented by the macroscopic wavefunction is called the quantum depletion. In a homogenous BEC, it consists of admixtures of higher momentum states into the ground state of the system. The fraction of the quantum depletion η_0 can be calculated through Bogoliubov theory: $\eta_0 = 1.505\sqrt{\rho a_s^3}$ where ρ is the atomic density and a_s is the s-wave scattering length [3]. For ^{23}Na at a typical density of 10^{14} cm^{-3} , the quantum depletion is 0.2%.

For the last decade, it has been a major goal of the field to map out the transition from gaseous condensates to liquid helium. Beyond-mean-field effects of a few percent were identified in the temperature dependence of collective excitations in a condensate [4, 5]. The quantum depletion increases for higher densities – however, at densities approaching 10^{15} cm^{-3} the lifetime of the gas is dramatically shortened by three-body collisions. Attempts to increase the scattering length near a Feshbach resonance were also limited by losses [6, 7]. Recently, deviations from mean-field behavior were seen in collective excitations of a molecular condensate near a Feshbach resonance [8, 9], but had a sign opposite to predictions. Therefore, the transition between a quantum gas and a

quantum liquid has been largely unexplored. Strongly correlated systems, which are no longer superfluid, were studied in 1D systems [10, 11], and in optical lattices [12, 13].

In this Letter, we report the first quantitative study of strong quantum depletion in a superfluid gas. Exposing atoms to an optical lattice enhances quantum depletion in two ways. First, the lattice localizes the atoms at the lattice sites and increases the atomic density. The increased density leads to enhanced interactions (by up to an order of magnitude in our experiment), ultimately limited by inelastic collisional losses. The second effect of the lattice is to modify the dispersion relation $T(k)$, which for free atoms is simply the kinetic energy $T(k) = \hbar^2 k^2 / 2m$. The effect of a weak lattice can be accounted for by an increased effective mass. For a deep lattice, when the width of the first band becomes comparable or smaller than the interaction energy, the full dispersion relation is required for a quantitative description.

In addition to enhancing the quantum depletion, an optical lattice also enables its direct observation in time-of-flight. For bare condensates in a harmonic trap, the quantum depletion cannot be observed during ballistic expansion in the typical Thomas-Fermi regime. Because the mean-field energy (divided by \hbar) is much greater than the trap frequency, the cloud remains locally adiabatic during the ballistic expansion. The condensate at high density transforms adiabatically into a condensate at low density with diminishing quantum depletion. Therefore, the true momentum distribution of the trapped condensate including quantum depletion and, for the same reason, phonon excitations can only be observed by in-situ momentum analysis such as Bragg spectroscopy [14, 15]. In an optical lattice, the confinement frequency at each lattice site far exceeds the interaction energy, and the time-of-flight images are essentially a snapshot of the frozen-in momentum distribution of the wavefunction at the time of the lattice switch-off, thus allowing for a direct observation of the quantum depletion.

The experiment setup is similar to that of our previous work [16]: A ^{23}Na BEC containing up to 5×10^5 atoms in the $|F = 1, m_F = -1\rangle$ state was loaded into a

*Contact Info: kwxu@mit.edu

†Website: cua.mit.edu/ketterle_group

crossed optical dipole trap. The number of condensed atoms was controlled through three-body decay in a compressed trap, after which the trap was relaxed to allow further evaporation and re-thermalization. A vertical magnetic field gradient was applied to compensate for gravity and avoid sagging in the weak trap. The final trap frequencies were $\omega_{x,y,z} = 2\pi \times 60, 60, 85$ Hz. The mean Thomas-Fermi radius was $\sim 12 \mu\text{m}$ for 1.7×10^5 atoms.

The lattice beams were derived from the same single-mode infra-red laser at 1064 nm used for the crossed optical dipole trap. All five beams were frequency-shifted by at least 20 MHz with respect to each other via acousto-optical modulator to eliminate cross interference between different beams. The three lattice beams had a $1/e^2$ -waist of $\sim 90 \mu\text{m}$ at the condensate, and were retro-reflected to form standing waves. The two horizontal beams were orthogonal to each other, while the third beam was tilted $\sim 20^\circ$ with respect to the vertical axis due to limited optical access. One and two dimensional lattices were formed using either one or both of the horizontal beams. The trap parameters were chosen such that during the ramping of the optical lattice potential, the overall Thomas-Fermi radii remained approximately constant in order to minimize intra-band excitations. All the measurements were performed at a peak lattice site occupancy number ~ 7 , as determined by a tradeoff between small three-body losses and good signal-to-noise ratio.

The optical lattice was linearly ramped up to a peak potential of $22 \pm 2 E_R$ in time τ_{ramp} , and then linearly ramped back down in the same amount of time. This ramp sequence was interrupted at various times by a sudden switch-off of all lattice and trapping potentials ($< 1\mu\text{s}$). Absorption images were taken after 10 ms time-of-flight, reflecting the momentum distribution of the system at the instant of release (Figure 1). Based on the number of atoms remaining in the condensate after the full ramping sequence ($\gtrsim 80\%$), we concluded that $\tau_{ramp} \gtrsim 1$ ms satisfies the intra-band adiabaticity condition. In the following discussion, all measurements were performed for $\tau_{ramp} = 50$ ms.

The loss and revival of the interference contrast, as illustrated in Figure 1, has been associated with the quantum phase transition from a superfluid state to a Mott-insulator state [12, 13]. The presence of sharp interference peaks indicates coherence and superfluid behavior, whereas the presence of a single broad peak indicates the insulating phase. However, as we show in this paper, even before the lattice depth exceeds the critical value for the phase transition, a diffuse background gradually emerges as a result of quantum depletion. The interference peaks represent the population in the zero quasi-momentum state, and the diffuse background represents the population in the rest of the Brillouin zone. We only account for the lowest energy band as the population in

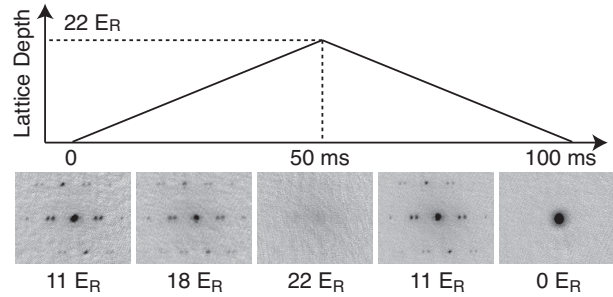


FIG. 1: Interference patterns in time-of-flight: The ramping sequence was interrupted as the lattice is ramped up (11, 18, 22 E_R) and back down (11, 0 E_R). The time-of-flight was 10 ms; the field of view is $861 \mu\text{m} \times 1075 \mu\text{m}$.

higher bands remains negligible for our parameters.

In the time-of-flight images, we masked off the sharp interference peaks and performed a two-dimensional gaussian fit on the diffuse background peak. After the lattice was fully ramped down, most of the atoms remained in the condensed fraction while a small fraction (up to 20%) were heated and distributed across the first Brillouin zone likely due to the technical noise and imperfect adiabaticity of the ramp. A linear interpolation was used to subtract this small heating contribution (up to 10% at the maximum lattice depth) and obtain the quantum depletion N_{qd}/N , where N_{qd} is the number of atoms in the diffuse background peak (quantum depletion) and N the total number.

We performed this measurement for one, two and three dimensional optical lattices, and the main results are shown in Figure 2. The quantum depletion became significant for lattice depths of $\gtrsim 10 E_R$ for a three dimensional lattice ($E_R = \hbar^2 k_{latt}^2 / 2m$, where $k_{latt} = 2\pi / \lambda_{latt}$ is the lattice wavenumber). Note that the Mott-insulator transition starts to occur only at lattice depths $\gtrsim 16 E_R$ (see below). N_{qd}/N remained small for one and two dimensional lattices.

A theoretical description of quantum depletion can be derived from the Bogoliubov theory which is the standard theory to describe the ground state properties of a weakly interacting system. The population in the (quasi-) momentum state k is given by [3, 17, 18]:

$$v_k^2 = \frac{T(k) + n_0 U - \sqrt{2T(k)n_0 U + T^2(k)}}{2\sqrt{2T(k)n_0 U + T^2(k)}} \quad (1)$$

where $T(k)$ is the kinetic energy, n_0 is the occupancy number [per cubic lattice cell of $(\lambda_{latt}/2)^3$] in the zero momentum state, and U is the on-site interaction energy [19–22]. Incidentally, v_k is one of the coefficients in the Bogoliubov transformation. The total occupancy number n is given by the sum of n_0 and the quantum depletion: $n = n_0 + \sum_{k \neq 0} v_k^2$. For a given density n , the quantum depletion can be obtained by using Eq. (1) and the appropriate dispersion relation $T(k)$.

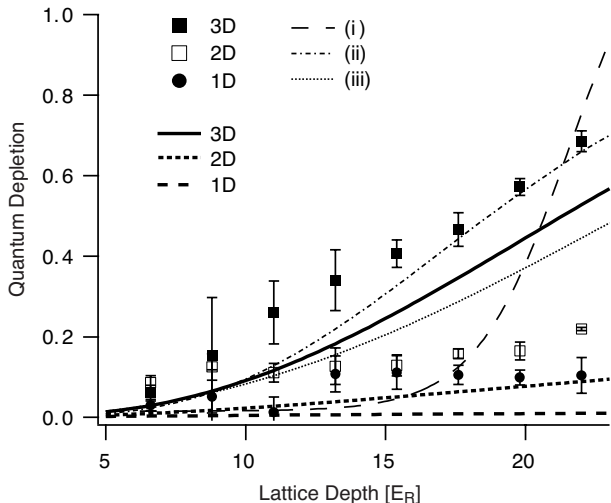


FIG. 2: Quantum depletion of a ^{23}Na BEC confined in a one, two and three dimensional optical lattice: the data points with statistical error bars are measured N_{qd}/N ; the three thick curves are the theoretical calculation of N_{qd}/N using Bogoliubov theory and local density approximation. For comparison, also shown are (thin curves): (i) the (smoothed out) Mott-insulator fraction N_{MI}/N based on a mean-field theory; (ii) the calculated quantum depletion for a *homogeneous* system of per-site occupancy number $n = 1$ and (iii) $n = 7$.

A band structure calculation was performed to obtain the on-site interaction U (and also the tunnelling rate J) as functions of the lattice depths, shown in Figure 3. In calculating U , we use a Wannier density function along the dimensions with a lattice, and a uniform density in the ones without. J is independent of the lattice wavelength or atomic mass for a given lattice depth (all energies measured in E_R).

The quantum depletion for a lattice of uniform occupation is obtained by integrating over the first Brillouin zone: $n = n_0 + \int v_{\mathbf{k}}^2 d\mathbf{k}$. For a sufficiently deep lattice ($\gtrsim 5 E_R$), the dispersion relation is given by:

$$T(\mathbf{q}) = 4J \sum_{i=1}^d \sin^2(q_i \pi) + 4E_R \sum_{i=d}^3 q_i^2. \quad (2)$$

where dimensions 1 through d are assumed to have a lattice present and $\mathbf{q} = \mathbf{k} \lambda_{latt}/4\pi$.

For an inhomogeneous system such as a harmonically confined condensate, we apply the result from the homogeneous system to shells of different occupancy numbers using the local density approximation (as the dependence of the quantum depletion on the occupancy number is slowly-varying). The calculated quantum depleted fractions are plotted in Figure 2, in reasonable agreement with the experimental observations. The remaining discrepancies may be due to unaccounted heating, a systematic overestimate of the background, and the inadequacies of Bogoliubov theory for large quantum depletion.

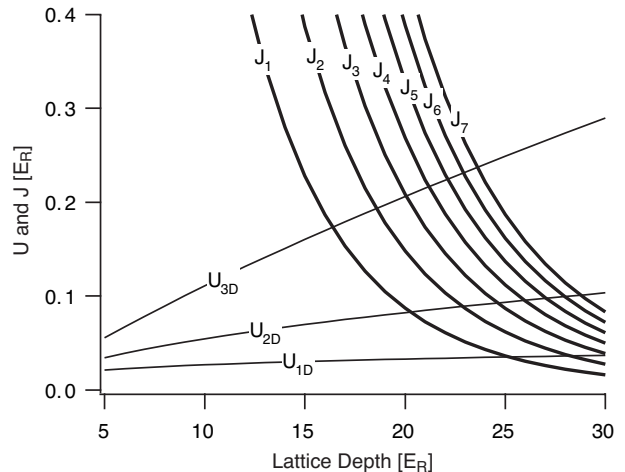


FIG. 3: On-site interaction U and tunnelling rate J for a ^{23}Na BEC in an optical lattice at 1064 nm: U_{dD} is for a d -dimensional lattice. In a three dimensional lattice, the superfluid to Mott-insulator transition for occupancy number n occurs when $J_n = 6(2n + 1 + 2\sqrt{n(n+1)})J$ equals U_{3D} [see Eq. (3)]. The horizontal locations of the crossing points where $J_n = U_{3D}$ are the critical lattice depths.

In free space, the dispersion curve is a continuous parabola. Both the number of populated states and the population in each state increases with the atomic density ρ , and the quantum depletion η_0 is proportional to $\rho^{3/2}$. This still holds for shallow lattices ($\lesssim 5 E_R$) where the quantum depletion (η) does not saturate the entire first Brillouin zone: $\eta = \eta_0 \left(\frac{\epsilon_{MF}^* m^*}{\epsilon_{MF} m} \right)^{3/2}$ (ϵ_{MF} and m are the free space mean-field energy and atomic mass; ϵ_{MF}^* and m^* are the lattice-enhanced mean-field energy and effective mass) [23].

The situation changes for deeper lattices as the interaction energy U becomes comparable to the width of the first energy band (approximately $4J$). In this regime, the quantum depletion starts to saturate the lowest band, but the higher bands remain virtually empty due to the large band gap. While the population N_{qd} in the lowest band continues to increase with the atomic density $\rho = n/(\lambda_{latt}/2)^3$, the quantum depleted fraction N_{qd}/N actually decreases with ρ [see Fig. 2 where the calculated quantum depletion is bigger for $n = 1$ than for $n = 7$ at large lattice depths ($\gtrsim 9 E_R$)].

The fact that the observed quantum depletion for one or two dimensional lattices remained small provides further evidence for our interpretation of the diffuse background as quantum depletion. In the dimension with a lattice present, the band width is proportional to the tunneling rate J which decreases exponentially with the lattice depth. The interaction energy U increases much slower with the lattice depth. Therefore the flattening of the dispersion relation contributes more significantly to the increased quantum depletion. Since this flattening

does not occur in the dimension without a lattice, the quantum depletion for one or two dimensional lattices is expected to increase much slower compared to three dimensional lattice, consistent with our observation.

Furthermore, one can show that in our regime, the observed quantum depletion far exceeds the fraction of atoms in the Mott-insulator phase. For the three dimensional lattice, the superfluid to Mott-insulator transition occurs as the lattice depth exceeds certain critical values. According to the mean-field theory in a homogenous bosonic lattice system [19–22], the critical value $(U/J)_c$ at which the phase transition occurs for occupancy number n is given by:

$$(U/J)_c = z(2n + 1 + 2\sqrt{n(n+1)}) \quad (3)$$

where z is the number of nearest neighbors ($z = 2d$ for a d -dimensional cubic lattice). For an inhomogeneous system such as a trapped condensate, shells of different occupancy numbers enter the Mott-insulator phase from outside as the lattice potential is increased and U/J exceeds the critical values.

In our experiment, the peak occupancy number is ~ 7 . We could divide the Thomas-Fermi profile of the condensate into 7 shells of average occupancy $n = 1, 2, \dots, 7$ and assume each shell enters the Mott-insulator phase as the lattice depth increases above the corresponding critical value. From Figure 3, the critical lattice depths in a three dimensional cubic lattice for $n = 1, 2, \dots, 7$ are 16.3, 18.5, 20.0, 21.2, 22.1, 22.9, 23.6 E_R respectively. The integrated Mott-insulator fraction N_{MI}/N as a function of lattice depths is plotted in Figure 2. Instead of a step function with jumps at each critical lattice depth, we use a smooth spline curve for N_{MI}/N , which is more realistic given the fluctuations associated with the atom numbers and lattice depths. N_{MI}/N clearly exhibits a much sharper transition as the lattice depth increases, in contrast to the gradual increase of the quantum depletion (particularly for lattice depths below the first critical value 16 E_R).

In the case of one and two dimensional lattices, a Mott-insulator transition would only occur for lattice depths much larger than those in our experiment. Note that Eq. (3) is not directly applicable as the dimensions without lattice beams in our system are only loosely confined and cannot be considered frozen[21]. In addition, n in Eq. (3) is the number of atoms *per lattice site* and far exceeds 7 for the lower-dimensional lattices.

In conclusion, we conducted the first quantitative study of quantum depletion in a gaseous BEC through the application of an optical lattice, and found reasonable agreement with a model based on Bogoliubov theory in the predominantly superfluid regime. A complementary study was recently reported by Gerbier *et al.* [24, 25] of the non-vanishing visibility of the interference peaks in a

Mott insulator as a result of the admixture of particle-hole states. The two works together give a complete description of the ground state in both the superfluid and insulating phases. More elaborate theoretical treatments for the intermediate case have been presented in Refs [26–28].

The authors would like to thank Jamil Abo-Shaeer and Takashi Mukaiyama for experimental assistances. This research is supported by NSF, ONR, ARO, and NASA.

-
- [1] A. Griffin, D. W. Snoke, and S. Stringari, *Bose Einstein Condensation* (Cambridge University Press, Cambridge, 1995).
 - [2] F. Dalfovo, S. Giorgini, L. P. Pitaevskii, and S. Stringari, *Rev. Mod. Phys.* **71**, 463 (1999).
 - [3] N. N. Bogoliubov, *J. Phys. (USSR)* **11**, 23 (1947).
 - [4] D. M. Stamper-Kurn *et al.*, *Phys. Rev. Lett.* **83**, 2876 (1999).
 - [5] S. Giorgini, *Phys. Rev. A* **61**, 063615 (2000).
 - [6] J. Stenger *et al.*, *Phys. Rev. Lett.* **82**, 2422 (1999).
 - [7] S. L. Cornish *et al.*, *Phys. Rev. Lett.* **85**, 1795 (2000).
 - [8] M. Bartenstein *et al.*, *Phys. Rev. Lett.* **92**, 203201 (2004).
 - [9] J. Kinast, A. Turlapov, and J. E. Thomas, *Phys. Rev. A* **70**, 051401 (2004).
 - [10] B. Paredes *et al.*, *Nature* **429**, 277 (2004).
 - [11] T. Kinoshita, T. R. Wenger, and D. S. Weiss, *Science* **305**, 1125 (2004).
 - [12] C. Orzel *et al.*, *Science* **291**, 2386 (2001).
 - [13] M. Greiner, I. Bloch, and T. W. Hänsch, *Phys. Rev. A* **63**, 031401 (2001).
 - [14] J. M. Vogels *et al.*, *Phys. Rev. Lett.* **88**, 060402 (2002).
 - [15] F. Zambelli, L. Pitaevskii, D. M. Stamper-Kurn, and S. Stringari, *Phys. Rev. A* **61**, 063608 (2000).
 - [16] K. Xu *et al.*, *Phys. Rev. A* **72**, 043604 (2005).
 - [17] D. van Oosten, P. van der Straten, and H. T. C. Stoof, *Phys. Rev. A* **63**, 053601 (2001).
 - [18] A. M. Rey *et al.*, *J. Phys. B: At. Mol. Opt. Phys.* **36**, 825 (2003).
 - [19] M. P. A. Fisher, P. B. Weichman, G. Grinstein, and D. S. Fisher, *Phys. Rev. B* **40**, 546 (1989).
 - [20] D. Jaksch *et al.*, *Phys. Rev. Lett.* **81**, 3108 (1998).
 - [21] W. Krauth, M. Caffarel, and J. P. Bouchard, *Phys. Rev. B* **45**, 3137 (1992).
 - [22] J. K. Freericks and H. Monien, *Phys. Rev. B* **53**, 2691 (1996).
 - [23] For very shallow lattices, one can obtain from perturbation theory: $m^*/m = 1 + E_{latt}^2/32$, $\epsilon_{MF}^*/\epsilon_{MF} = 1 + 3E_{latt}^2/32$, where E_{latt} is the lattice depth divided by E_R .
 - [24] F. Gerbier *et al.*, *Phys. Rev. Lett.* **95**, 050404 (2005).
 - [25] F. Gerbier *et al.*, *Phys. Rev. A* **72**, 053606 (2005).
 - [26] K. Sengupta and N. Dupuis, *Phys. Rev. A* **71**, 033629 (2005).
 - [27] J. J. García-Ripoll *et al.*, *Opt. Express* **12**, 42 (2004).
 - [28] C. Schroll, F. Marquardt, and C. Bruder, *Phys. Rev. A* **70**, 053609 (2004).

Bibliography

- [1] M.H. Anderson, J.R. Ensher, M.R. Matthews, C.E. Wieman, and E.A. Cornell. Observation of Bose-Einstein Condensation in a Dilute Atomic Vapor. *Science*, 269:198, 1995.
- [2] C.C. Bradley, C.A. Sackett, J.J. Tollet, and R.G. Hulet. Evidence of Bose-Einstein Condensation in an Atomic Gas with Attractive Interactions. *Phys. Rev. Lett.*, 75:1687, 1995.
- [3] K.B. Davis, M.-O. Mewes, M.R. Andrews, N.J. van Druten, D.S. Durfee, D.M. Kurn, and W. Ketterle. Bose-Einstein Condensation in a Gas of Sodium Atoms. *Phys. Rev. Lett.*, 75:3969, 1995.
- [4] F. Dalfovo, S. Giorgini, L.P. Pitaevskii, and S. Stringari. Theory of Bose-Einstein condensation in trapped gases. *Rev. Mod. Phys.*, 71:463, 1999.
- [5] Anthony J. Leggett. Bose-Einstein condensation in the alkali gases: Some fundamental concepts. *Rev. Mod. Phys.*, 73:307, 2001.
- [6] Anthony J. Leggett. Erratum: Bose-Einstein condensation in the alkali gases: Some fundamental concepts [Rev. Mod. Phys. 73, 307 (2001)]. *Rev. Mod. Phys.*, 75:1083, 2003.
- [7] D.G. Fried, T.C. Killian, L. Willmann, D. Landhuis, S.C. Moss, D. Kleppner, and T.J. Greytak. Bose-Einstein Condensation of Atomic Hydrogen. *Phys. Rev. Lett.*, 81:3811, 1998.

- [8] S.L. Cornish, N.R. Claussen, J.L. Roberts, E.A. Cornell, and C.E. Wieman. Stable ^{85}Rb Bose-Einstein condensates with widely tunable interactions. *Phys. Rev. Lett.*, 85:1795, 2000.
- [9] A. Robert, O. Sirjean, A. Browaeys, J. Poupard, S. Nowak, D. Boiron, C.I. Westbrook, and A. Aspect. A Bose-Einstein condensate of metastable atoms. *Science*, 292:461, 2001.
- [10] F. Pereira Dos Santos, J. Leonard, J. Wang, C.J. Barrelet, F. Perales, E. Rasel, C.S. Unnikrishmin, M. Leduc, and C. Cohen-Tannoudji. Bose-Einstein condensation of metastable helium. *Phys. Rev. Lett.*, 86:3459, 2001.
- [11] G. Modugno, G. Ferrari, G. Roati, R.J. Brecha, A. Simoni, and M. Inguscio. Bose-Einstein condensation of potassium atoms by sympathetic cooling. *Science*, 294:1320, 2001.
- [12] T. Weber, J. Herbig, M. Mark, H.-C. Nägerl, and R. Grimm. Bose-Einstein condensation of cesium. *Science*, 299:232, 2003.
- [13] Y. Takasu, K. Maki, K. Komori, T. Takano, K. Honda, M. Kumakura, T. Yabuzaki, and Y. Takahashi. Spin-singlet Bose-Einstein condensation of two-electron atoms. *Phys. Rev. Lett.*, 91:040404, 2003.
- [14] Axel Griesmaier, Jörg Werner, Sven Hensler, Jürgen Stuhler, and Tilman Pfau. Bose-Einstein condensation of chromium. *Phys. Rev. Lett.*, 94:160401, 2005.
- [15] B. DeMarco and D. S. Jin. Onset of Fermi degeneracy in a trapped atomic gas. *Science*, 285:1703, 1999.
- [16] A.G. Truscott, K.E. Strecker, W.I. McAlexander, G.B. Partridge, and R.G. Hulet. Observation of Fermi pressure in a gas of trapped atoms. *Science*, 291:2570, 2001.
- [17] D.M. Stamper-Kurn. *Peeking and poking at a new quantum fluid: Studies of gaseous Bose-Einstein condensates in magnetic and optical traps*. Ph.D., Massachusetts Institute of Technology, 1999.

- [18] Shin Inouye. *Manipulating Bose-Einstein condensates with laser light*. Ph.D., Massachusetts Institute of Technology, 2001.
- [19] S.N. Bose. Plancks Gesetz und Lichtquantenhypothese. *Z. Phys.*, 26:178, 1924.
- [20] A. Einstein. Quantentheorie des einatomigen idealen Gases. II. *Sitzungsberichte der preussischen Akademie der Wissenschaften*, Bericht 1:3, 1925.
- [21] Charles E. Hecht. Possible superfluid behavior of H atom gases and liquids. *Physica*, 25:1159, 1959.
- [22] W.C. Stwalley and L.H. Nosanow. Possible “new” quantum systems. *Phys. Rev. Lett.*, 36:910, 1976.
- [23] S. Chu. The manipulation of neutral particles. *Rev. Mod. Phys.*, 70:685, 1998.
- [24] C.N. Cohen-Tannoudji. Manipulating atoms with photons. *Rev. Mod. Phys.*, 70:707, 1998.
- [25] W.D. Phillips. Laser cooling and trapping of neutral atoms. *Rev. Mod. Phys.*, 70:721, 1998.
- [26] M.R. Andrews, C.G. Townsend, H.-J. Miesner, D.S. Durfee, D.M. Kurn, and W. Ketterle. Observation of interference between two Bose condensates. *Science*, 275:637, 1997.
- [27] S. Inouye, A.P. Chikkatur, D.M. Stamper-Kurn, J. Stenger, D.E. Pritchard, and W. Ketterle. Superradiant Rayleigh scattering from a Bose-Einstein condensate. *Science*, 285:571–574, 1999.
- [28] S. Inouye, T. Pfau, S. Gupta, A.P. Chikkatur, A. Görlitz, D.E. Pritchard, and W. Ketterle. Observation of phase-coherent amplification of atomic matter waves. *Nature*, 402:641–644, 1999.
- [29] M. Kozuma, Y. Suzuki, Y. Torii, T. Sugiura, T. Kuga, E.W. Hagley, and L. Deng. Phase coherent amplification of matter waves. *Science*, 286:2309–2312, 1999.

- [30] W. Ketterle, D.S. Durfee, and D.M. Stamper-Kurn. Bose-Einstein condensation in atomic gases. Proceedings of the International School of Physics Enrico Fermi, Course CXL, pages 67–176. IOS Press, Amsterdam, 1999.
- [31] Y. Castin and R. Dum. Bose-Einstein Condensates in Time Dependent Traps. *Phys. Rev. Lett.*, 77:5315, 1996.
- [32] M.-O. Mewes, M.R. Andrews, D.M. Kurn, D.S. Durfee, C.G. Townsend, and W. Ketterle. Output coupler for Bose-Einstein condensed atoms. *Phys. Rev. Lett.*, 78:582, 1997.
- [33] Immanuel Bloch, Theodor W. Hänsch, and Tilman Esslinger. Atom Laser with a cw Output Coupler. *Phys. Rev. Lett.*, 82:3008, 1999.
- [34] E. W. Hagley, L. Deng, M. Kozuma, J. Wen, K. Helmerson, S.L. Rolston, and W.D. Phillips. A Well-Collimated Quasi-Continuous Atom Laser. *Science*, 283:1706, 1999.
- [35] H. Hinderthür, F. Ruschewitz, H.-J. Lohe, S. Lecthe, K. Sengstock, and W. Ertmer. Time-domain high-finesse atom interferometry. *Phys. Rev. A*, 59:2216–2219, 1999.
- [36] Y. Torii, Y. Suzuki, M. Kozuma, T. Kuga, L. Deng, and E.W. Hagley. Mach-Zender Bragg interferometer for a Bose-Einstein condensate. *Phys. Rev. A*, 61:041602, 2000.
- [37] R. Dumke, T. Mütter, M. Volk, W. Ertmer, and G. Birkl. Interferometer-Type Structures for Guided Atoms. *Phys. Rev. Lett.*, 89:220402, 2002.
- [38] L. Deng, E.W. Hagley, J. Wen, M. Trippenbach, Y. Band, P.S. Julienne, J.E. Simsarian, K. Helmerson, S.L. Rolston, and W.D. Phillips. Four-wave mixing with matter waves. *Nature*, 398:218, 1999.
- [39] J.M. Vogels, K. Xu, and W. Ketterle. Generation of Macroscopic Pair-Correlated Atomic Beams by Four-Wave Mixing in Bose-Einstein Condensates. *Phys. Rev. Lett.*, 89:020401, 2002.

- [40] M.J. Holland and K. Burnett. Interferometric Detection of Optical Phase Shifts at the Heisenberg Limit. *Phys. Rev. Lett.*, 71:1355, 1993.
- [41] P. Bouyer and M.A. Kasevich. Heisenberg-limited spectroscopy with degenerate Bose-Einstein gases. *Phys. Rev. A*, 56:R1083, 1997.
- [42] R.A. Campos, Christopher C. Gerry, and A. Benmoussa. Optical interferometry at the Heisenberg limit with twin Fock states and parity measurements. *Phys. Rev. A*, 68:023810, 2003.
- [43] L.-M. Duan, A. Sørensen, J.I. Cirac, and P. Zoller. Squeezing and Entanglement of Atomic Beams. *Phys. Rev. Lett.*, 85:3991, 2000.
- [44] H. Pu and P. Meystre. Creating Macroscopic Atomic Einstein-Podolsky-Rosen States from Bose-Einstein Condensates. *Phys. Rev. Lett.*, 85:3987, 2000.
- [45] F. London. The λ -phenomenon of liquid helium and the Bose-Einstein degeneracy. *Nature*, 141:643, 1938.
- [46] F. London. On the Bose-Einstein Condensation. *Phys. Rev.*, 54:947, 1938.
- [47] L. Tisza. Transport Phenomena in Helium II. *Nature*, 141:913, 1938.
- [48] W.H. Keesom and M. Wolfke. Two liquid states of helium. *Konink. Akad. Wetensch. Amsterdam Proc.*, 31(190b):90, 1928.
- [49] L.D. Landau. The theory of superfluidity of helium II. *J. Phys. (USSR)*, 5:71, 1941.
- [50] L.D. Landau. Hydrodynamics of helium II. *J. Phys. (USSR)*, 8:1, 1944.
- [51] L.D. Landau. Theory of superfluidity of helium II. *J. Phys. (USSR)*, 11:91, 1947.
- [52] R.P. Feynman. Atomic Theory of Liquid Helium Near Absolute Zero. *Phys. Rev.*, 91:1301, 1953.

- [53] R.P. Feynman. Atomic Theory of the Two-Fluid Model of Liquid Helium. *Phys. Rev.*, 94:262, 1954.
- [54] Oliver Penrose and Lars Onsager. Bose-Einstein Condensation and Liquid Helium. *Phys. Rev.*, 104:576, 1956.
- [55] J. Bardeen, L.N. Cooper, and J.R. Schrieffer. Theory of Superconductivity. *Phys. Rev.*, 108:1175, 1957.
- [56] H.A. Feshbach. A unified theory of nuclear reactions. *II. Ann. Phys.*, 19:287, 1962.
- [57] S. Inouye, M.R. Andrews, J. Stenger, H.-J. Miesner, D.M. Stamper-Kurn, and W. Ketterle. Observation of Feshbach resonances in a Bose-Einstein condensate. *Nature*, 392:151–154, 1998.
- [58] J. Stenger, S. Inouye, M.R. Andrews, H.-J. Miesner, D.M. Stamper-Kurn, and W. Ketterle. Strongly enhanced inelastic collisions in a Bose-Einstein condensate near Feshbach resonances. *Phys. Rev. Lett.*, 82:2422–2425, 1999.
- [59] C. Orzel, A.K. Tuchman, M.L. Fenselau, M. Yasuda, and M.A. Kasevich. Squeezed States in a Bose-Einstein Condensate. *Science*, 291:2386, 2001.
- [60] M. Greiner, O. Mandel, T. Esslinger, T.W. Hänsch, and I. Bloch. Quantum phase transition from a superfluid to a Mott insulator in a gas of ultracold atoms. *Nature*, 415:39–44, 2002.
- [61] O. Mandel, M. Greiner, A. Widera, T. Rom, T.W. Hänsch, and I. Bloch. Controlled collisions for multi-particle entanglement of optically trapped atoms. *Nature*, 425:937, 2003.
- [62] M. Girardeau. Relationship between systems of impenetrable bosons and fermions in one dimension. *J. Math. Phys.*, 1:516, 1960.
- [63] Belén Paredes, Artur Widera, Valentin Murg, Olaf Mandel, Simon Fölling, Ignacio Cirac, Gora V. Shlyapnikov, Theodor W. Hänsch, and Immanuel Bloch.

- Tonks-Girardeau gas of ultracold atoms in an optical lattice. *Nature*, 429:277, 2004.
- [64] C. Ryu, X. Du, Emek Yesilada, Artem M. Dudarev, Shoupu Wan, Qian Niu, and D.J. Heinzen. Raman-induced oscillation between an atomic and a molecular quantum gas. 2005. arXiv:cond-mat/0508201.
- [65] Thilo Stöferle, Henning Moritz, Kenneth Günter, Michael Köhl, and Tilman Esslinger. Molecules of Fermionic Atoms in an Optical Lattice. *Phys. Rev. Lett.*, 96:030401, 2006.
- [66] G. Thalhammer, K. Winkler, F. Lang, S. Schmid, R. Grimm, and J. Hecker Denschlag. Long-Lived Feshbach Molecules in a Three-Dimensional Optical Lattice. *Phys. Rev. Lett.*, 96:050402, 2006.
- [67] K. Xu, Y. Liu, D.E. Miller, J.K. Chin, W. Setiawan, and W. Ketterle. Observation of Strong Quantum Depletion in a Gaseous Bose-Einstein Condensate. 2006. arXiv:cond-mat/0601184.
- [68] Dallin S. Durfee. *Dynamic Properties of Dilute Bose-Einstein Condensates*. Ph.D., 1999.
- [69] P.A.M. Dirac. *The Principles of Quantum Mechanics*. Oxford University Press, USA, 4th edition, 1982.
- [70] Kerson Huang. *Statistical Mechanics*. John Wiley & Sons, Inc., 2nd edition, 1987.
- [71] Claude Cohen-Tannoudji, Bernard Diu, and Frank Laloe. *Quantum Mechanics*. Wiley-Interscience, 1992.
- [72] R.K. Pathria. *Statistical Mechanics*. Butterworth-Heinemann, 2nd edition, 1996.
- [73] A.J. Moerdijk, B.J. Verhaar, and A. Axelsson. Resonances in ultracold collisions of ${}^6\text{Li}$, ${}^7\text{Li}$, and ${}^{23}\text{Na}$. *Phys. Rev. A*, 51:4852, 1995.

- [74] E. Tiesinga, B.J. Verhaar, and H.T.C. Stoof. Threshold and resonance phenomena in ultracold ground-state collisions. *Phys. Rev. A*, 47:4114, 1993.
- [75] H.M.J.M. Boesten, J.M. Vogels, J.G.C. Tempelaars, and B.J. Verhaar. Properties of cold collisions of ^{39}K atoms and of ^{41}K atoms in relation to Bose-Einstein condensation. *Phys. Rev. A*, 54:R3726, 1996.
- [76] J.M. Vogels, C.C. Tsai, R.S. Freeland, S.J.J.M.F. Kokkelmans, B.J. Verhaar, and D.J. Heinzen. Prediction of Feshbach resonances in collisions of ultracold rubidium atoms. *Phys. Rev. A*, 56:R1067, 1997.
- [77] P.O. Fedichev, Yu. Kagan, G.V. Shlyapnikov, and J.T. M. Walraven. Influence of Nearly Resonant Light on the Scattering Length in Low-Temperature Atomic Gases. *Phys. Rev. Lett.*, 77:2913, 1996.
- [78] A.J. Moerdijk, B.J. Verhaar, and T.M. Nagtegaal. Collisions of dressed ground-state atoms. *Phys. Rev. A*, 53:4343, 1996.
- [79] John L. Bohn and P.S. Julienne. Prospects for influencing scattering lengths with far-off-resonant light. *Phys. Rev. A*, 56:1486, 1997.
- [80] N.N. Bogoliubov. On the theory of superfluidity. *J. Phys. (USSR)*, 11:23, 1947.
- [81] J.K. Chin, J.M. Vogels, and W. Ketterle. Amplification of Local Instabilities in a Bose-Einstein Condensate with Attractive Interactions. *Phys. Rev. Lett.*, 90:160405, 2003.
- [82] R.P. Feynman. Progress in Low Temperature Physics. volume 1, page 17. North-Holland, Amsterdam, 1955.
- [83] I.M. Khalatnikov. *Introduction to the Theory of Superfluidity*. Benjamin, New York, 1965.
- [84] J. Wilks and D.S. Betts. *An Introduction to Liquid Helium*. Clarendon Press, Oxford, 1987.

- [85] P. Nozières and D. Pines. *The Theory of Quantum Liquids*. Addison-Wesley, Redwood City, CA, 1990.
- [86] A.J. Leggett. Superfluidity. *Rev. Mod. Phys.*, 71:S318, 1999.
- [87] C. Raman, M. Köhl, R. Onofrio, D.S. Durfee, C.E. Kuklewicz, Z. Hadzibabic, and W. Ketterle. Evidence for a Critical Velocity in a Bose-Einstein Condensed Gas. *Phys. Rev. Lett.*, 83:2502, 1999.
- [88] R. Onofrio, C. Raman, J.M. Vogels, J.R. Abo-Shaeer, A.P. Chikkatur, and W. Ketterle. Observation of Superfluid Flow in a Bose-Einstein Condensed Gas. *Phys. Rev. Lett.*, 85:2228, 2000.
- [89] C. Raman, R. Onofrio, J.M. Vogels, J.R. Abo-Shaeer, and W. Ketterle. Dissipationless Flow and Superfluidity in Gaseous Bose-Einstein Condensates. *J. Low Temp. Phys.*, 122:99, 2001.
- [90] David L. Feder, Anatoly A. Svidzinsky, Alexander L. Fetter, and Charles W. Clark. Anomalous Modes Drive Vortex Dynamics in Confined Bose-Einstein Condensates. *Phys. Rev. Lett.*, 86:564, 2001.
- [91] Juan J. García-Ripoll and Victor M. Pérez-García. Vortex nucleation and hysteresis phenomena in rotating Bose-Einstein condensates. *Phys. Rev. A*, 63:041603(R), 2001.
- [92] Makoto Tsubota, Kenichi Kasamatsu, and Masahito Ueda. Vortex lattice formation in a rotating Bose-Einstein condensate. *Phys. Rev. A*, 65:023603, 2002.
- [93] M.G. Moore and P. Meystre. Theory of Superradiant Scattering of Laser Light from Bose-Einstein Condensates. *Phys. Rev. Lett.*, 83:5202, 1999.
- [94] A. Vardi and M.G. Moore. Directional Superradiant Collisions: Bosonic Amplification of Atom Pairs Emitted from an Elongated Bose-Einstein Condensate. *Phys. Rev. Lett.*, 89:090403, 2002.

- [95] P.J. Martin, B.G. Oldaker, A.H. Miklich, and D.E. Pritchard. Bragg scattering of atoms from a standing light wave. *Phys. Rev. Lett.*, 60:515, 1988.
- [96] M. Kozuma, L. Deng, E.W. Hagley, J. Wen, R. Lutwak, K. Helmerson, S.L. Rolston, and W.D. Phillips. Coherent splitting of Bose-Einstein condensed atoms with optically induced Bragg diffraction. *Phys. Rev. Lett.*, 82:871, 1999.
- [97] J. Stenger, S. Inouye, A.P. Chikkatur, D.M. Stamper-Kurn, D.E. Pritchard, and W. Ketterle. Bragg spectroscopy of a Bose-Einstein condensate. *Phys. Rev. Lett.*, 82:4569, 1999.
- [98] A. Griffin. *Excitations in a Bose-condensed liquid*. Cambridge University Press, Cambridge, 1993.
- [99] D.M Stamper-Kurn and W. Ketterle. Spinor Condensates and Light Scattering from Bose-Einstein Condensates. In R. Kaiser, C. Westbrook, and F. David, editors, *Coherent Atomic Matter Waves*, Proceedings of the Les Houches Summer School, Course LXXII in 1999. Springer, NewYork, 2001. e-print arXiv:cond-mat/0005001.
- [100] J.M. Vogels, K. Xu, C. Raman, J.R. Abo-Shaeer, and W. Ketterle. Experimental Observation of the Bogoliubov Transformation for a Bose-Einstein Condensed Gas. *Phys. Rev. Lett.*, 88:060402, 2002.
- [101] A. Brunello, F. Dalfovo, L. Pitaevskii, and S. Stringari. How to Measure the Bogoliubov Quasiparticle Amplitudes in a Trapped Condensate. *Phys. Rev. Lett.*, 85:4422, 2000.
- [102] D.M. Stamper-Kurn, A.P. Chikkatur, A. Görlitz, S. Inouye, S. Gupta, D.E. Pritchard, and W. Ketterle. Excitation of phonons in a Bose-Einstein condensate by light scattering. *Phys. Rev. Lett.*, 83:2876–2879, 1999.
- [103] J. Steinhauer, R. Ozeri, N. Katz, and N. Davidson. Excitation Spectrum of a Bose-Einstein Condensate. *Phys. Rev. Lett.*, 88:120407, 2002.

- [104] R. Ozeri, J. Steinhauer, N. Katz, and N. Davidson. Direct observation of the phonon energy in a Bose-einstein condensate by tomographic imaging. *Phys. Rev. Lett.*, 88:220401, 2002.
- [105] D.F. Walls and G.J. Milburn. *Quantum Optics*. Springer, 1st edition, 1995.
- [106] J.A. Dunningham and K. Burnett. Phase resolution for Bose-Einstein condensates. *Phys. Rev. A*, 61:065601, 2000.
- [107] J.A. Dunningham, K. Burnett, and Stephen M. Barnett. Interferometry below the Standard Quantum Limit with Bose-Einstein Condensates. *Phys. Rev. Lett.*, 89:150401, 2002.
- [108] J. Fortagh, A. Grossmann, C. Zimmermann, and T.W. Hänsch. Miniaturized Wire Trap for Neutral Atoms. *Phys. Rev. Lett.*, 81:5310, 1998.
- [109] Johannes Denschlag, Donatella Cassettari, and Jörg Schmiedmayer. Guiding Neutral Atoms with a Wire. *Phys. Rev. Lett.*, 82:2014, 1999.
- [110] J.H. Thywissen, M. Olshanii, G. Zabow, M. Drndić, K.S. Johnson, R.M. Westervelt, and M. Prentiss. Microfabricated magnetic waveguides for neutral atoms. *Eur. Phys. J. D*, 7:361, 1999.
- [111] M. Key, I.G. Hughes, W. Rooijackers, B.E. Sauer, E.A. Hinds, D.J. Richardson, and P.G. Kazansky. Propagation of Cold Atoms along a Miniature Magnetic Guide. *Phys. Rev. Lett.*, 84:1371, 2000.
- [112] A.E. Leanhardt, A.P. Chikkatur, D. Kielpinski, Y. Shin, T.L. Gustavson, W. Ketterle, and D.E. Pritchard. Propagation of Bose-Einstein condensates in a magnetic waveguide. *Phys. Rev. Lett.*, 89:040401, 2002.
- [113] V. Vuletic, A.J. Kerman, C. Chin, and S. Chu. Observation of Low-Field Feshbach Resonances in Collisions of Cesium Atoms. *Phys. Rev. Lett.*, 82:1406, 1999.

- [114] John Weiner, Vanderlei S. Bagnato, Sergio Zilio, and Paul S. Julienne. Experiments and theory in cold and ultracold collisions. *Rev. Mod. Phys.*, 71:1, 1999.
- [115] Hendrick L. Bethlem, Giel Berden, and Gerard Meijer. Decelerating Neutral Dipolar Molecules. *Phys. Rev. Lett.*, 83:1558–1561, 1999.
- [116] Vladan Vuletic and Steven Chu. Laser Cooling of Atoms, Ions, or Molecules by Coherent Scattering. *Phys. Rev. Lett.*, 84:3787, 2000.
- [117] A. Marte, T. Volz, J. Schuster, S. Dürr, G. Rempe, E.G.M. van Kempen, and B.J. Verhaar. Feshbach Resonances in Rubidium 87: Precision Measurement and Analysis. *Phys. Rev. Lett.*, 89:283202, 2002.
- [118] K. Xu, T. Mukaiyama, J.R. Abo-Shaeer, J.K. Chin, D.E. Miller, and W. Ketterle. Formation of Quantum-Degenerate Sodium Molecules. *Phys. Rev. Lett.*, 91:210402, 2003.
- [119] S. Jochim, M. Bartenstein, A. Altmeyer, G. Hendl, S. Riedl, C. Chin, J. Hecker Denschlag, and R. Grimm. Bose-Einstein Condensation of Molecules. *Science*, 302:5653, 2003.
- [120] Markus Greiner, Cindy A. Regal, and Deborah S. Jin. Emergence of a molecular Bose-Einstein condensate from a Fermi gas. *Nature*, 426:537, 2003.
- [121] M.W. Zwierlein, C.A. Stan, C.H. Schunck, S.M.F. Raupach, S. Gupta, Z. Hadzibabic, and W. Ketterle. Observation of Bose-Einstein Condensation of Molecules. *Phys. Rev. Lett.*, 91:250401, 2003.
- [122] D.S. Petrov, C. Salomon, and G.V. Shlyapnikov. Weakly bound dimers of fermionic atoms. *Phys. Rev. Lett.*, 93:090404, 2004.
- [123] V.A. Yurovsky, A. Ben-Reuven, P.S. Julienne, and C.J. Williams. Atom loss from Bose-Einstein condensates due to Feshbach resonance. *Phys. Rev. A*, 60:R765, 1999.

- [124] V.A. Yurovsky, A. Ben-Reuven, P.S. Julienne, and C.J. Williams. Atom loss and the formation of a molecular Bose-Einstein condensate by Feshbach resonance. *Phys. Rev. A*, 62:043605, 2000.
- [125] Stephan Dürr, Thomas Volz, and Gerhard Rempe. Dissociation of ultracold molecules with Feshbach resonances. *Phys. Rev. A*, 70:031601(R), 2004.
- [126] C. Chin, T. Kraemer, M. Mark, J. Herbig, P. Waldburger, H.-C. Nägerl, and R. Grimm. Observation of Feshbach-Like Resonances in Collisions between Ultracold Molecules. *Phys. Rev. Lett.*, 94:123201, 2005.
- [127] Thomas Volz, Stephan Dürr, Niels Syassen, Gerhard Rempe, Eric van Kempen, and Servaas Kokkelmans. Feshbach spectroscopy of a shape resonance. *Phys. Rev. A*, 72:010704(R), 2005.
- [128] F. S. Cataliotti, S. Burger, C. Fort, P. Maddaloni, F. Minardi, A. Trombettoni, A. Smerzi, and M. Inguscio. Josephson Junction Arrays with Bose-Einstein Condensates. *Science*, 293:843, 2001.
- [129] S. Burger, F.S. Cataliotti, C. Fort, F. Minardi, M. Inguscio, M.L. Chiofalo, and M. P. Tosi. Superfluid and Dissipative Dynamics of a Bose-Einstein Condensate in a Periodic Optical Potential. *Phys. Rev. Lett.*, 86:4447, 2001.
- [130] O. Morsch, J.H. Müller, M. Cristiani, D. Ciampini, and E. Arimondo. Bloch Oscillations and Mean-Field Effects of Bose-Einstein Condensates in 1D Optical Lattices. *Phys. Rev. Lett.*, 87:140402, 2001.
- [131] D. Jaksch, C. Bruder, J.I. Cirac, C.W. Gardiner, and P. Zoller. Cold Bosonic Atoms in Optical Lattices. *Phys. Rev. Lett.*, 81:3108, 1998.
- [132] B. Laburthe Tolra, K.M. OHara, J.H. Huckans, W.D. Phillips, S.L. Rolston, and J.V. Porto. Observation of Reduced Three-Body Recombination in a Correlated 1D Degenerate Bose Gas. *Phys. Rev. Lett.*, 92:190401, 2004.

- [133] Toshiya Kinoshita, Trevor Wenger, and David S. Weiss. Local Pair Correlations in One-Dimensional Bose Gases. *Phys. Rev. Lett.*, 95:190406, 2005.
- [134] Charles Kittel. *Introduction to Solid State Physics*. Wiley, 7th edition, 1995.
- [135] Matthew P.A. Fisher, Peter B. Weichman, G. Grinstein, and Daniel S. Fisher. Boson localization and the superfluid-insulator transition. *Phys. Rev. B*, 40:546, 1989.
- [136] Werner Krauth, Michel Caffarel, and Jean-Philippe Bouchaud. Gutzwiller wave function for a model of strongly interacting bosons. *Phys. Rev. B*, 45:3137, 1992.
- [137] J.K. Freericks and H. Monien. Strong-coupling expansions for the pure and disordered Bose-Hubbard model. *Phys. Rev. B*, 53:2691, 1996.
- [138] Shlomo E. Sklarz, Inbal Friedler, David J. Tannor, Yehuda B. Band, and Carl J. Williams. Flat-phase loading of a Bose-Einstein condensate into an optical lattice. *Phys. Rev. A*, 66:053620, 2002.
- [139] K. Xu, Y. Liu, J.R. Abo-Shaeer, T. Mukaiyama, J.K. Chin, D.E. Miller, and W. Ketterle. Sodium Bose-Einstein condensates in an optical lattice. *Phys. Rev. A*, 72:043604, 2005.
- [140] J. Hecker Denschlag, J.E. Simsarian, H. Häffner, C. McKenzie, A. Browaeys, D. Cho, K. Helmerson, S.L. Rolston, and W.D. Phillips. A Bose-Einstein condensate in an optical lattice. *J. Phys. B: At. Mol. Opt. Phys.*, 35:3095, 2002.
- [141] Thilo Stöferle, Henning Moritz, Christian Schori, Michael Köhl, and Tilman Esslinger. Transition from a Strongly Interacting 1D Superfluid to a Mott Insulator. *Phys. Rev. Lett.*, 92:130403, 2004.
- [142] H. Ott, E. de Mirandes, F. Ferlaino, G. Roati, V. Türeċk, G. Modugno, and M. Inguscio. Radio Frequency Selective Addressing of Localized Atoms in a Periodic Potential. *Phys. Rev. Lett.*, 93:120407, 2004.
- [143] Gretchen Campbell, 2006 2006. Private Communication.

- [144] M.R. Matthews, B.P. Anderson, P.C. Haljan, D.S. Hall, C.E. Wieman, and E.A. Cornell. Vortices in a Bose-Einstein Condensate. *Phys. Rev. Lett.*, 83:2498, 1999.
- [145] K.W. Madison, F. Chevy, W. Wohlleben, and J. Dalibard. Vortex Formation in a Stirred Bose-Einstein Condensate. *Phys. Rev. Lett.*, 84:806, 2000.
- [146] J.R. Abo-Shaeer, C. Raman, J.M. Vogels, and W. Ketterle. Observation of Vortex Lattices in Bose-Einstein Condensates. *Science*, 292:476, 2001.
- [147] D.M. Stamper-Kurn, M.R. Andrews, A.P. Chikkatur, S. Inouye, H.-J. Miesner, J. Stenger, and W. Ketterle. Optical Confinement of a Bose-Einstein Condensate. *Phys. Rev. Lett.*, 80:2027, 1998.
- [148] M.R. Andrews, M.-O. Mewes, N.J. van Druten, D.S. Durfee, D.M. Kurn, and W. Ketterle. Direct, Non-Destructive Observation of a Bose Condensate. *Science*, 273:84–87, 1996.
- [149] Olaf Mandel, Markus Greiner, Artur Widera, Tim Rom, Theodor W. Hänsch, and Immanuel Bloch. Coherent Transport of Neutral Atoms in Spin-Dependent Optical Lattice Potentials. *Phys. Rev. Lett.*, 91:010407, 2003.
- [150] M. Bartenstein, A. Altmeyer, S. Riedl, R. Geursen, S. Jochim, C. Chin, J. Hecker Denschlag, and R. Grimm. Precise Determination of 6 Li Cold Collision Parameters by Radio-Frequency Spectroscopy on Weakly Bound Molecules. *Phys. Rev. Lett.*, 94:103201, 2005.
- [151] Harold J. Metcalf and Peter van der Straten. *Laser cooling and trapping*. Graduate Texts in Contemporary Physics. Springer-Verlag, 1999.
- [152] E.A. Donley, N.R. Claussen, S.T. Thompson, and C.E. Wieman. Atom-molecule coherence in a Bose-Einstein condensate. *Nature*, 417:529–533, 2002.
- [153] J. Herbig, T. Kraemer, M. Mark, T. Weber, C. Chin, H.-C. Nägerl, and R. Grimm. Preparation of a Pure Molecular Quantum Gas. *Science*, 301:1510–1513, 2003.

- [154] S.T. Thompson, E. Hodby, and C.E. Wieman. Ultracold Molecule Production via a Resonant Oscillating Magnetic Field. *Phys. Rev. Lett.*, 95:190404, 2005.
- [155] S.T. Thompson, E. Hodby, and C.E. Wieman. Spontaneous Dissociation of 85Rb Feshbach Molecules. *Phys. Rev. Lett.*, 94(020401), 2005.
- [156] E. Hodby, S.T. Thompson, C.A. Regal, M. Greiner, A.C. Wilson, D.S. Jin, E.A. Cornell, and C.E. Wieman. Production Efficiency of Ultracold Feshbach Molecules in Bosonic and Fermionic Systems. *Phys. Rev. Lett.*, 94:120402, 2005.
- [157] D.S. Petrov, C. Salomon, and G.V. Shlyapnikov. Scattering properties of weakly bound dimers of fermionic atoms. *Phys. Rev. A*, 71:012708, 2005.
- [158] J.P. D’Incao and B.D. Esry. Scattering Length Scaling Laws for Ultracold Three-Body Collisions. *Phys. Rev. Lett.*, 94:213201, 2005.
- [159] C.A. Regal, C. Ticknor, J.L. Bohn, and D.S. Jin. Creation of ultracold molecules from a Fermi gas of atoms. *Nature*, 424:47–50, 2003.
- [160] C.A. Regal, M. Greiner, and D.S. Jin. Lifetime of molecule-atom mixtures near a Feshbach resonance in ^{40}K . *Phys. Rev. Lett.*, 92:083201, 2004.
- [161] J. Cubizolles, T. Bourdel, S.J.J.M.F. Kokkelmans, G.V. Shlyapnikov, and C. Salomon. Production of Long-Lived Ultracold Li_2 Molecules from a Fermi gas. *Phys. Rev. Lett.*, 91:240401, 2003.
- [162] S. Jochim, M. Bartenstein, A. Altmeyer, G. Hendl, C. Chin, J. Hecker Denschlag, and R. Grimm. Pure Gas of Optically Trapped Molecules Created from Fermionic Atoms. *Phys. Rev. Lett.*, 91:240402, 2003.
- [163] Kevin E. Strecker, Guthrie B. Partridge, and Randall G. Hulet. Conversion of an Atomic Fermi Gas to a Long-Lived Molecular Bose Gas. *Phys. Rev. Lett.*, 91:080406, 2003.

- [164] K.M. O'Hara, S.L. Hemmer, M.E. Gehm, S.R. Granade, and J.E. Thomas. Observation of a Strongly Interacting Degenerate Fermi Gas of Atoms. *Science*, 298:5601, 2002.
- [165] C.A. Regal and D.S. Jin. Measurement of Positive and Negative Scattering Lengths in a Fermi Gas of Atoms. *Phys. Rev. Lett.*, 90:230404, 2003.
- [166] M. Bartenstein, A. Altmeyer, S. Riedl, S. Jochim, C. Chin, J. Hecker Denschlag, and R. Grimm. Crossover from a Molecular Bose-Einstein Condensate to a Degenerate Fermi Gas. *Phys. Rev. Lett.*, 92:120401, 2004.
- [167] C.A. Regal, M. Greiner, and D.S. Jin. Observation of Resonance Condensation of Fermionic Atom Pairs. *Phys. Rev. Lett.*, 92:040403, 2004.
- [168] M.W. Zwierlein, C.A. Stan, C.H. Schunck, S.M.F. Raupach, A.J. Kerman, and W. Ketterle. Condensation of Pairs of Fermionic Atoms near a Feshbach Resonance. *Phys. Rev. Lett.*, 92:120403, 2004.
- [169] T. Bourdel, L. Khaykovich, J. Cubizolles, J. Zhang, F. Chevy, M. Teichmann, L. Tarruell, S.J.J.M.F. Kokkelmans, and C. Salomon. Experimental Study of the BEC-BCS Crossover Region in Lithium 6. *Phys. Rev. Lett.*, 93:050401, 2004.
- [170] M. Bartenstein, A. Altmeyer, S. Riedl, S. Jochim, C. Chin, J. Hecker Denschlag, and R. Grimm. Collective Excitations of a Degenerate Gas at the BEC-BCS Crossover. *Phys. Rev. Lett.*, 92:203201, 2004.
- [171] C. Chin, M. Bartenstein, A. Altmeyer, S. Riedl, S. Jochim, J. Hecker Denschlag, and R. Grimm. Observation of the Pairing Gap in a Strongly Interacting Fermi Gas. *Science*, 305:1128, 2004.
- [172] A. Perali, P. Pieri, and G.C. Strinati. Quantitative Comparison between Theoretical Predictions and Experimental Results for the BCS-BEC Crossover. *Phys. Rev. Lett.*, 93:100404, 2004.

- [173] C.A. Regal, M. Greiner, S. Giorgini, M. Holland, and D.S. Jin. Momentum Distribution of a Fermi Gas of Atoms in the BCS-BEC Crossover. *Phys. Rev. Lett.*, 95:250404, 2005.
- [174] M.W. Zwierlein, C.H. Schunck, C.A. Stan, S.M.F. Raupach, and W. Ketterle. Formation Dynamics of a Fermion Pair Condensate. *Phys. Rev. Lett.*, 94:180401, 2005.
- [175] M. Greiner, C.A. Regal, and D.S. Jin. Probing the Excitation Spectrum of a Fermi Gas in the BCS-BEC Crossover Regime. *Phys. Rev. Lett.*, 94:070403, 2005.
- [176] M.W. Zwierlein, J.R. Abo-Shaeer, A. Schirotzek, C.H. Schunck, and W. Ketterle. Vortices and superfluidity in a strongly interacting Fermi gas. *Nature*, 435:1047, 2005.
- [177] T. Mukaiyama, J.R. Abo-Shaeer, K. Xu, J.K. Chin, and W. Ketterle. Dissociation and Decay of Ultracold Sodium Molecules. *Phys. Rev. Lett.*, 91:210402, 2003.